Quantum error correction in a compact ion-trap quantum computer

Doctoral thesis by

Ivan Pogorelov

Submitted to the faculty for
Mathematics, Computer Science and Physics
In partial fulfillment of the requirements for the degree of
Doctor of Philosophy (PhD)

Carried out under the supervision of
Dr. Thomas Monz, Dr. Philipp Schindler,
Dr. Martin Ringbauer and Dr. Christian Marciniak
in the Quantum Optics and Spectroscopy Group

Institute for Experimental Physics
University of Innsbruck
December 2024

Abstract

The field of quantum computing has been developing rapidly over the last decades, driven by the belief that quantum computing can provide computational advantage over devices of other computational paradigms. However, the aspect of scaling quantum computing hardware systems to sizes where computational advantage can be achieved remains the cornerstone problem of the field.

This thesis constitutes a step in the path towards scalable quantum systems. Specifically, the thesis describes the commissioning and operation of a trapped-ion quantum computing setup with modular design assembled in two 19-inch racks. The setup functions as a standalone device without a need for any special external infrastructure. The setup is capable of operating with 16 qubits in a highly-automated way with the ability to access the setup through a hardware-agnostic high-level interface. Details required for working with a 16-ion chain and the prospects of scaling the system further are discussed throughout the work.

The setup's performance is demonstrated via experimental implementation of quantum error correction, a major milestone on the way to scalable and practically-useful quantum computing. Various quantum error correction primitives were performed with logical qubits encoded using color codes. The primitives include encoding of the logical states, direct implementation of logical Clifford gates, and implementation of logical non-Clifford gates via magic state injection and code switching. These results represent one of the first experimental logical-level manipulations with encoded qubits.

Contents

Statement of contribution

A main result of my work at the University of Innsbruck as a part of Quantum Optics and Spectroscopy group lead by Prof. Rainer Blatt was commissioning a new quantum computing setup based on trapped ions. This setup was used in various projects in our group which led to the following publication where I played

a leading role:

[1] **I. Pogorelov**, T. Feldker, C. D. Marciniak, et al., 'Compact Ion-Trap Quantum Computing Demonstrator', PRX Quantum **2**, 020343 (2021)

[2] **I. Pogorelov**, F. Butt, L. Postler, et al., 'Experimental fault-tolerant code switching', Nature Physics **21**, 298 (2025)

a major role:

[3] L. Postler, S. Heußen, **I. Pogorelov**, et al., 'Demonstration of fault-tolerant universal quantum gate operations', Nature **605**, 675 (2022)

[4] S. Heußen, L. Postler, M. Rispler, **I. Pogorelov**, et al., 'Strategies for a practical advantage of fault-tolerant circuit design in noisy trapped-ion quantum computers', Physical Review A **107**, 042422 (2023)

[5] L. Postler, F. Butt, **I. Pogorelov**, et al., 'Demonstration of Fault-Tolerant Steane Quantum Error Correction', PRX Quantum **5**, 030326 (2024)

[6] N. Sadoune, **I. Pogorelov**, C. L. Edmunds, et al., 'Learning symmetry-protected topological order from trapped-ion experiments', arXiv.2408.05017 (2024)

a minor role:

[7] C. Sanz-Fernandez, R. Hernandez, C. D. Marciniak, **I. Pogorelov**, et al., 'Quantum portfolio value forecasting', arXiv.2111.14970 (2021)

[8] C. D. Marciniak, T. Feldker, **I. Pogorelov**, et al., 'Optimal metrology with programmable quantum sensors', Nature **603**, 604 (2022)

[9] L. O. Conlon, T. Vogl, C. D. Marciniak, **I. Pogorelov**, et al., 'Approaching optimal entangling collective measurements on quantum computing platforms', Nature Physics **19**, 351 (2023)

[10] J. Eisert, M. Ringbauer, M. Hinsche, T. Feldker, P. Faehrmann, J. Bermejo-Vega, C. Edmunds, L. Postler, R. Stricker, C. Marciniak, M. Meth, **I. Pogorelov**, et al., 'Verifiable measurement-based quantum random sampling with trapped ions', rs.3.rs-3936332/v1 (2024)

[11] D. Miller, K. Levi, L. Postler, A. Steiner, L. Bittel, G. A. L. White, Y. Tang, E. J. Kuehnke, A. A. Mele, S. Khatri, L. Leone, J. Carrasco, C. D. Marciniak, **I. Pogorelov**, et al., 'Experimental measurement and a physical interpretation of quantum shadow enumerators', arXiv.2408.16914 (2024)

Chapter 1

Introduction

Quantum computing emerged as a field in the 1980s after proposals to use quantum systems for computation supported by works of Paul Benioff [12], Yuri Manin [13], Richard Feynman [14], and others. This idea initially arose from the fact that some computational problems can not be solved on classical computers with a reasonable amount of resources despite the presence of an algorithm leading to the solution. For example, this is the case for simulations of some quantum systems with a classical computer where the required resources grow exponentially with the size of the problem making it intractable for large system size.

Since then, the field of quantum computing has been developing theoretically and experimentally. Currently, the main expectation from quantum computers is that they can solve certain problems more efficiently in terms of resource scaling than classical computers. A wide range of quantum algorithms achieving this advantage have been proposed [15] while many of them are based on three basic ideas: the factoring algorithm by Peter Shor proposed in 1994 [16], unstructured database search algorithm by Lov Grover introduced in 1996 [17] and the initial quantum system simulation idea proved by Seth Lloyd in 1996 [18].

Many physical platforms have been proposed and studied experimentally as potential hardware for quantum computers including photons, trapped atoms [19] and ions [20–24], molecular nuclear spins in liquid solutions [25], superconducting systems [26–33], and quantum dots [34–36]. These systems allowed to demonstrate basic quantum computing operations [37] and small-scale algorithms [38]. However, today's quantum computing systems are still too small and have too many errors in basic quantum computing operations to be practically useful for computation. Moreover, it is not yet clear which physical platform offers the best potential for scaling the size of quantum computers to achieve practically-useful quantum computing.

The errors present in quantum computers' hardware have been decreasing over the last decades but they can not be eliminated completely. As a consequence, the idea of quantum error correction was proposed by Peter Shor [39] and Andrew Steane [40] in 1996 inspired by error correction methods for classical computers. The hardware errors can be suppressed at the cost of redundant information encoding in quantum computers allowing large-scale quantum computation even in the presence of finite hardware errors.

Nowadays, experimental quantum computing is far from being practically useful and can only offer small- or medium-scale proof-of-principle demonstrations of quantum computing due to modest system sizes. Therefore, scaling the size of quantum computers is a necessary next step which represents the main priority for the field of quantum computing at the moment. At the same time, experimental quantum

error correction mechanisms should be developed and tested along with the system size increase as a vital part of large-scale quantum computing.

This work studies two aspects of quantum computing: the potential of increasing the system size and experimental quantum error correction. This work describes the construction of a novel trapped-ion quantum computing setup and experimental demonstrations of some basic quantum error correction mechanisms.

Structure outline

Ch. 2, 3, 4 provide some background knowledge about quantum information, quantum error correction and ion trapping respectively. Basics introduced there will be referred to in further parts of the work.

Ch. 5 describes the experimental setup created in this work.

Ch. 6 describes the approaches used in this work to operate the setup with long ion chains. In particular, the details about 16-ion chain are given.

Ch. 7 describes three quantum error correction projects carried out on the setup.

Chapter 2

Quantum information basics

Quantum information science is based on the idea that information can be encoded in quantum systems, e.g. individual atoms. The way information is stored and processed in 'quantum computers' is different to the widely-used 'classical computers'. Encoding information in quantum systems offers two unique features that are not present in conventional digital classical information processing, namely superposition states and entanglement. These two features open new paths for information processing and allow quantum computers to utilize novel algorithms that solve certain problems more efficiently than classical computers.

This chapter describes the concepts of encoding information in so-called 'qubits', manipulating this information using 'quantum gates' and introduces other basic terms and notations for the theory of quantum information. The reader can refer to Ref. 41 for a thorough review.

2.1 Qubits

Classical information processing usually operates with information encoded in elementary units of information called 'bits' (binary digit). A bit can take two possible states/values often labeled as 0 and 1. Physically, a bit can be represented by a physical system with two clearly distinguishable states, e.g. an electrical circuit with two distinct voltage levels. Such circuits can be merged to form a sequence of bits for information encoding. Whenever some information should be provided as an input for a computation, it can be converted to a binary encoding forming a string of bits. This bit string can be mapped to the voltages in the electrical circuit making it available for manipulation by a classical computer.

The principles of quantum computing follow similar ideas. Information in quantum computing is often encoded as qubits[1], the quantum analog of classical bits. A qubit can be represented by a two-level quantum system with states often denoted as $|0\rangle$ and $|1\rangle$. Here we use 'bra-ket' notation introduced by Dirac [43] for complex vector spaces, where $|v\rangle$ denotes a vector $\vec{v}$, $\langle f| = |f\rangle^\dagger$ denotes conjugate transpose of a vector $\vec{f}$ and $\langle f|v\rangle = |f\rangle^\dagger \cdot |v\rangle$ is the scalar product or the inner product of two vectors in the vector space.

[1] Qubits are not the only way to encode information for quantum computing. More generally, a qudit, a quantum system with d states $\{|0\rangle, \ldots, |d-1\rangle\}$ can be used [42]. In this work we will restrict our considerations to qubits, although many ideas can be generalized for the qudit case.

The state of a qubit can be described by a wave function $|\psi\rangle$:

$$|\psi\rangle = a\,|0\rangle + b\,|1\rangle = a\begin{pmatrix}1\\0\end{pmatrix} + b\begin{pmatrix}0\\1\end{pmatrix} = \begin{pmatrix}a\\b\end{pmatrix}, \tag{2.1}$$

where $a, b \in \mathbb{C}$ and $|a|^2 + |b|^2 = 1$. This is a superposition of the two states $|0\rangle$ and $|1\rangle$ forming an orthonormal basis in two-dimensional Hilbert space, often referred to as the 'computational basis'. Such superposition states are not possible with classical bits.

A qubit can be measured in the computational basis $\{|0\rangle, |1\rangle\}$. The probabilities to measure a qubit with the state $|\psi\rangle$ in the computational basis are given by the Born rule [44] as:

$$\begin{aligned} P(0) &= |\langle 0|\psi\rangle|^2 = |a|^2 \\ P(1) &= |\langle 1|\psi\rangle|^2 = |b|^2 = 1 - |a|^2. \end{aligned} \tag{2.2}$$

This motivates the normalization condition $|a|^2 + |b|^2 = 1$ since the total probability to observe the qubit in either of these states should be 1.

More generally, the outcome of a measurement can be described by a set of measurement operators M_i such that $\sum_i M_i^\dagger M_i = I$:

$$P(i) = \langle\psi| M_i^\dagger M_i |\psi\rangle . \tag{2.3}$$

Here the normalization condition ensures that the total probability to observe the qubit in one of the states amounts to 1, i.e $\sum_i P(i) = 1$. For the computational basis measurements operators are simply $M_0 = |0\rangle\langle 0|$ and $M_1 = |1\rangle\langle 1|$.

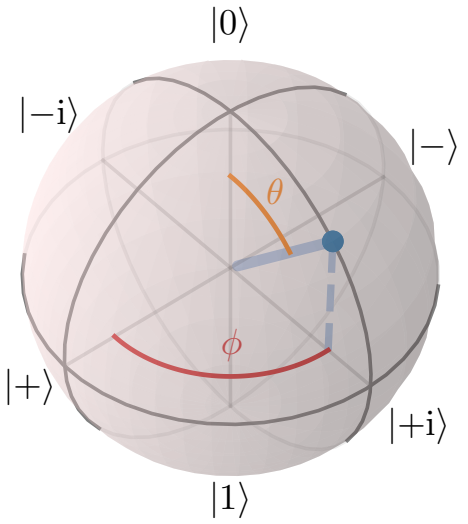

State	θ	ϕ
$\|0\rangle$	0	0
$\|1\rangle$	π	0
$\|+\rangle$	$\pi/2$	0
$\|-\rangle$	$\pi/2$	π
$\|+i\rangle$	$\pi/2$	$\pi/2$
$\|-i\rangle$	$\pi/2$	$-\pi/2$

Figure 2.1: Bloch sphere representation of single-qubit quantum states according to Eq. (2.4).

There is a useful geometrical interpretation of the qubit's state in Eq. (2.1). The wave function can be rewritten as follows with three parameters $\{\theta, \phi, \gamma\} \subset \mathbb{R}$:

$$e^{-i\gamma} |\psi\rangle = \cos\frac{\theta}{2} |0\rangle + e^{i\phi} \sin\frac{\theta}{2} |1\rangle , \tag{2.4}$$

where the parameter γ can be ignored since global phases are not observable for qubits, leaving us two real parameters θ and ϕ. This representation hints that a state can be mapped to the surface of a 3D sphere, called 'Bloch sphere', see Fig. 2.1.

Multiple qubits

All the information above can be generalized for multiple qubits. The computational basis states of a system with n qubits are tensor products of the single-qubit basis states, e.g $|0 \dots 0\rangle = |0\rangle \otimes \cdots \otimes |0\rangle$. The wave function of such a system can be written as follows:

$$|\psi\rangle = a_{0\dots0} |0 \dots 0\rangle + \cdots + a_{1\dots1} |1 \dots 1\rangle = \begin{pmatrix} a_{0\dots0} \\ \vdots \\ a_{1\dots1} \end{pmatrix} = \sum_i a_i |i\rangle , \tag{2.5}$$

where i goes thorough all possible bit strings of size n from $0 \dots 0$ to $1 \dots 1$. Sometimes the computational basis states can be labeled with their decimal representation instead of a bit string, e.g. $|1001\rangle = |9\rangle$ since 1001 in binary is equal to 9 in decimal.

2.2 Quantum gates

Logical states of qubits are mostly manipulated by applying operations called 'quantum logic gates' or 'quantum gates' analogously to classical logic gates. Quantum gates represent elementary building blocks quantum computing algorithms are assembled from. Quantum computing algorithms are often decomposed into single-qubit gates (acting on a single qubit) and two-qubit gates (acting on two qubits). Fig. 2.2 shows an example of a quantum algorithm represented as a quantum circuit diagram. The algorithm consists of qubit initialization, qubit state manipulation with quantum gates, and measurements.

The evolution of a closed quantum system can be described by a unitary operator U that satisfies $UU^\dagger = U^\dagger U = I$. Such operators preserve the unit length of the qubit's state vector. If a qubit in the state $|\psi\rangle$ undergoes an operation U, the resulting state of the qubit will be

$$|\psi'\rangle = U |\psi\rangle . \tag{2.6}$$

A quantum gate can be defined by a unitary matrix U describing what the gate does to the qubits' state, e.g. a 2×2 unitary matrix for a single-qubit gate.

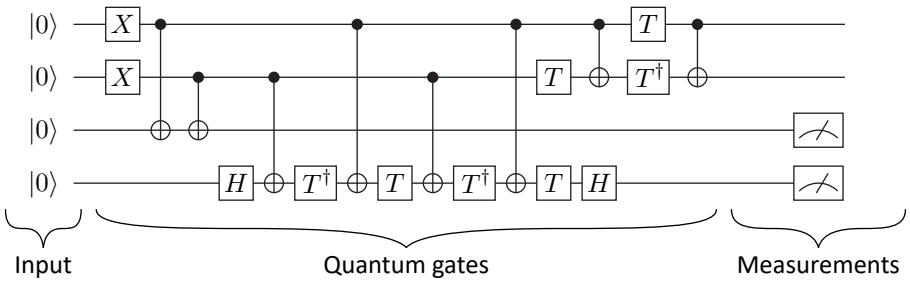

Figure 2.2: An example of a quantum algorithm represented as a quantum circuit diagram.

The list of quantum gates frequently used in this work and some of their properties will be introduced in this subsection since definitions and notations vary in the literature. The matrices describing the gates are given in the computational basis $\{|0\rangle, |1\rangle\}$. Fig. 2.3 shows how different gates will be depicted in quantum circuit diagrams in this work.

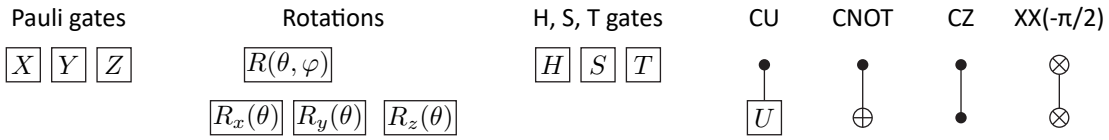

Figure 2.3: Circuit diagram representation of the basic quantum gates used in quantum circuit diagrams in this work. The definitions of the gates are given in Sec. 2.2.1 – 2.2.4

2.2.1 Single-qubit gates: Pauli gates

Pauli gates play an important role in many quantum information science descriptions. They are especially prominent in quantum error correction considerations since they generate a group called the Pauli group which will be discussed in more details in Sec. 3.2.

Pauli gates are defined by Pauli matrices $\{\sigma_x, \sigma_y, \sigma_z\}$ or $\{X, Y, Z\}$:

$$X = \begin{pmatrix} 0 & 1 \\ 1 & 0 \end{pmatrix}, \qquad Y = \begin{pmatrix} 0 & -i \\ i & 0 \end{pmatrix}, \qquad Z = \begin{pmatrix} 1 & 0 \\ 0 & -1 \end{pmatrix}. \tag{2.7}$$

The cardinal states of the Bloch sphere $\{|0\rangle, |1\rangle, |+\rangle, |-\rangle, |+i\rangle, |-i\rangle\}$ (see Fig.2.1)

$$|+\rangle = \frac{1}{\sqrt{2}}(|0\rangle + |1\rangle), \qquad |+i\rangle = \frac{1}{\sqrt{2}}(|0\rangle + i\,|1\rangle), \tag{2.8}$$
$$|-\rangle = \frac{1}{\sqrt{2}}(|0\rangle - |1\rangle), \qquad |-i\rangle = \frac{1}{\sqrt{2}}(|0\rangle - i\,|1\rangle)$$

are ± 1 eigenstates of the Pauli matrices:

$$\begin{aligned} Z|0\rangle &= +|0\rangle, & X|+\rangle &= +|+\rangle, & Y|+i\rangle &= +|+i\rangle, \\ Z|1\rangle &= -|1\rangle, & X|-\rangle &= -|-\rangle, & Y|-i\rangle &= -|-i\rangle. \end{aligned} \tag{2.9}$$

The X-gate and the Z-gate are often referred to as a bit flip and a phase flip respectively due to their effect on computational basis states:

$$\begin{aligned} X|0\rangle &= |1\rangle, & Z|0\rangle &= |0\rangle, \\ X|1\rangle &= |0\rangle, & Z|1\rangle &= -|1\rangle. \end{aligned} \tag{2.10}$$

The Y-gate can be seen as a combination of a phase flip and a bit flip:

$$Y = iXZ. \tag{2.11}$$

2.2.2 Single-qubit gates: rotation gates

The physical mechanisms of a system encoding qubits dictate the operations that can be performed on them. This is reflected in the notion of a 'native gate set', i.e. the set of gates that can be efficiently implemented in a certain hardware platform or in a given experimental setup. Rotation gates are important from the experimental perspective since they belong to native gate sets of many hardware platforms, including trapped ions.

The term 'rotation gates' usually refers to rotations around an axis of the Bloch sphere. In many platforms such as trapped ions it is sensible to divide rotation gates into two group according to their experimental implementations: rotations around an axis in the xy-plane of the Bloch sphere and rotations around the z-axis of the Bloch sphere.

A rotation around an axis in the xy-plane of the Bloch sphere is usually denoted as the R-gate. The gate is described by the following unitary matrix:

$$R(\theta, \phi) = \begin{pmatrix} \cos\frac{\theta}{2} & -ie^{-i\phi}\sin\frac{\theta}{2} \\ -ie^{i\phi}\sin\frac{\theta}{2} & \cos\frac{\theta}{2} \end{pmatrix}. \tag{2.12}$$

The rotation axis is set by the phase of the gate ϕ, while the rotation angle is θ.

There are two specific cases for the R-gate to mention: rotation around the x-axis R_x and rotation around the y-axis R_x

$$\begin{aligned} R_x(\theta) &= R(\theta, 0), \\ R_y(\theta) &= R(\theta, \frac{\pi}{2}). \end{aligned} \tag{2.13}$$

The X- and Y-gates can be implemented as the R_x-, and R_y-gates respectively:

$$\begin{aligned} X &= iR_x(\pi) = iR(\pi, 0), \\ Y &= iR_y(\pi) = iR(\pi, \frac{\pi}{2}). \end{aligned} \tag{2.14}$$

A rotation around the z-axis of the Bloch sphere is usually denoted as the R_z-gate. It is described by the following unitary matrix:

$$R_z(\theta) = \begin{pmatrix} 1 & 0 \\ 0 & e^{i\theta} \end{pmatrix}. \tag{2.15}$$

The R_z rotation by an angle π results in the Z-gate:

$$Z = R_z(\pi). \tag{2.16}$$

2.2.3 Single-qubit gates: H, S, T

The H, S and T gates are often used in theoretical considerations due to their mathematical properties and will be used throughout this work for quantum error correction theory.

H-gate

The H-gate or Hadamard gate is defined by the following matrix:

$$H = \frac{1}{\sqrt{2}} \begin{pmatrix} 1 & 1 \\ 1 & -1 \end{pmatrix}. \tag{2.17}$$

The Hadamard gate can be used to exchange the Z-basis and the X-basis:

$$X = HZH. \tag{2.18}$$

It is also often used to prepare an equal superposition of all computational basis states in the beginning of the quantum circuit:

$$H|0\rangle = \frac{1}{\sqrt{2}}(|0\rangle + |1\rangle), \tag{2.19}$$

$$H \otimes \cdots \otimes H |\underbrace{0 \ldots 0}_{n}\rangle = 2^{-n/2}(|0\rangle + |1\rangle) \otimes \cdots \otimes (|0\rangle + |1\rangle) = 2^{-n/2} \sum_{j=0}^{2^n-1} |j\rangle. \tag{2.20}$$

The following equalities are useful when implementing the Hadamard gate in practice:

$$H = XR_y\left(\frac{\pi}{2}\right), \tag{2.21}$$

$$H = R_y\left(-\frac{\pi}{2}\right)X, \tag{2.22}$$

$$H = ZR_y\left(-\frac{\pi}{2}\right), \tag{2.23}$$

$$H = R_y\left(\frac{\pi}{2}\right)Z. \tag{2.24}$$

In particular, Eq. (2.23 – 2.24) can be used to prepare the $|+\rangle$ state or perform a measurement in the X-basis (see Fig. 2.4). For example,

$$|+\rangle = H|0\rangle = R_y\left(\frac{\pi}{2}\right)Z|0\rangle = R_y\left(\frac{\pi}{2}\right)|0\rangle. \tag{2.25}$$

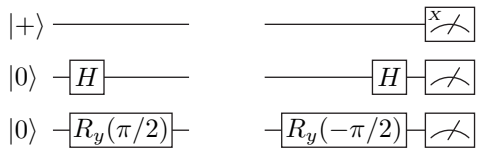

Figure 2.4: Circuits on the left are equivalent and circuits on the right are equivalent. The bottom circuits are usually used in the experiment to implement the desired logical result.

S-gate and T-gate

The S-gate and the T-gate are described by the following matrices:

$$S = \begin{pmatrix} 1 & 0 \\ 0 & i \end{pmatrix}, \qquad T = \begin{pmatrix} 1 & 0 \\ 0 & e^{i\pi/4} \end{pmatrix}. \tag{2.26}$$

They are specific cases of the R_z-gate:

$$S = R_z\left(\frac{\pi}{2}\right), \qquad T = R_z\left(\frac{\pi}{4}\right). \tag{2.27}$$

2.2.4 Two-qubit gates

Single-qubit gates can only act on one qubit while it is essential for universal computation to be able to change a qubit's (or a bit's) state based on the state of other qubits (bits). Such conditional operations can be realized with two-qubits gates, quantum analogs of classical logical two-bit gates (e.g. AND, OR, XOR) while multi-qubit gates can be constructed from two-qubit gates and single-qubit gates [45]. Additionally, two-qubit gates can create entanglement between qubits which is essential for most quantum information applications.

A widespread class of two-qubit gates is controlled gates. A controlled gate CU acting on two qubits can be written as follows:

$$\mathrm{C}U = \begin{pmatrix} 1 & 0 & 0 & 0 \\ 0 & 1 & 0 & 0 \\ 0 & 0 & & \\ 0 & 0 & & U \end{pmatrix}. \tag{2.28}$$

This gate applies U to the second (target) qubit if the state of the first qubit (control qubit) is $|1\rangle$ and applies the identity operation if the first qubit (control qubit) is in the $|0\rangle$ state. Therefore,

$$\begin{aligned} &\mathrm{C}U(a_1|0\rangle + b_1|1\rangle)(a_2|0\rangle + b_2|1\rangle) \\ &\qquad = a_1|0\rangle(a_2|0\rangle + b_2|1\rangle) + b_1|1\rangle U(a_2|0\rangle + b_2|1\rangle). \end{aligned} \tag{2.29}$$

Sometimes subscripts are used to indicate which qubit is the control qubit and which the target, e.g. $\mathrm{C}U_{1,2} = \mathrm{C}U$, especially in larger circuits where the two may be non-neighboring.

CNOT-gate and CZ-gate

The CNOT-gate (or CX-gate) and CZ-gate are frequently used in theory. They are both CU gates with $U = X$ and $U = Z$, respectively.

The CNOT-gate is defined by the following matrix:

$$\mathrm{CNOT} = \begin{pmatrix} 1 & 0 & 0 & 0 \\ 0 & 1 & 0 & 0 \\ 0 & 0 & \multicolumn{2}{c}{\multirow{2}{*}{X}} \\ 0 & 0 & & \end{pmatrix} = \begin{pmatrix} 1 & 0 & 0 & 0 \\ 0 & 1 & 0 & 0 \\ 0 & 0 & 0 & 1 \\ 0 & 0 & 1 & 0 \end{pmatrix}. \tag{2.30}$$

The CNOT-gate applies the X-gate (NOT-gate) to the target qubit if the control qubit is in the $|1\rangle$ state and applies the identity operation if the first qubit is in the $|0\rangle$ state. It can be used to create a maximally entangled state:

$$\mathrm{CNOT}\,|{+}0\rangle = \frac{1}{\sqrt{2}}(|00\rangle + |11\rangle). \tag{2.31}$$

This two-qubit state is called 'entangled' since it can not be represented as a tensor product of single-qubit states:

$$\frac{1}{\sqrt{2}}(|00\rangle + |11\rangle) \neq (a_1\,|0\rangle + b_1\,|1\rangle) \otimes (a_2\,|0\rangle + b_2\,|1\rangle), \qquad \forall a_1, b_1, a_2, b_2 \in \mathbb{C}. \tag{2.32}$$

Entangled states are another distinctive feature of quantum information processing since they do not appear in classical information processing.

The CNOT-gate can be used to create the CZ-gate since $HXH = Z$:

$$\mathrm{C}Z = H_2\mathrm{C}X_{1,2}H_2 = \begin{pmatrix} 1 & 0 & 0 & 0 \\ 0 & 1 & 0 & 0 \\ 0 & 0 & 1 & 0 \\ 0 & 0 & 0 & -1 \end{pmatrix} = \begin{pmatrix} 1 & 0 & 0 & 0 \\ 0 & 1 & 0 & 0 \\ 0 & 0 & \multicolumn{2}{c}{\multirow{2}{*}{Z}} \\ 0 & 0 & & \end{pmatrix}. \tag{2.33}$$

The CZ is symmetric with respect to target and control qubits:

$$\mathrm{C}Z_{1,2} = \mathrm{C}Z_{2,1}. \tag{2.34}$$

Therefore, its circuit diagram representation is also symmetric (see Fig. 2.3).

XX-gate

The CNOT-gate or the CZ-gate are not always easy to implement directly in a physical system. Sometimes other two-qubit gates are more favorable. This is often the case for trapped ions where the XX-gate belongs to the native gate set of the experimental system and can be implemented via the Mølmer-Sørensen interaction [46] (see Sec. 4.4.3). The XX-gate is defined by the following matrix:

$$XX(\theta) = \begin{pmatrix} \cos\frac{\theta}{2} & 0 & 0 & -i\sin\frac{\theta}{2} \\ 0 & \cos\frac{\theta}{2} & -i\sin\frac{\theta}{2} & 0 \\ 0 & -i\sin\frac{\theta}{2} & \cos\frac{\theta}{2} & 0 \\ -i\sin\frac{\theta}{2} & 0 & 0 & \cos\frac{\theta}{2} \end{pmatrix}. \tag{2.35}$$

$XX(-\pi/2)$ is equivalent to the CNOT-gate up to local rotations [47]. The circuit in Fig. 2.5 is used in this work to implement the CNOT-gate with the XX-gate.

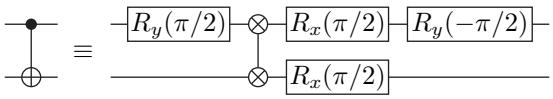

Figure 2.5: Circuit equivalence used to implement the CNOT-gate with the XX-gate in the experiment.

2.2.5 Universal gate set

Some of the gates listed above can be used to form a 'universal gate set'. The idea behind a universal gate set is that an arbitrary unitary operation on multiple qubits can be approximated with a desired precision by a sequence of operations from a finite set called 'universal gate set'. For example, $\{H, T, \text{CNOT}\}$ is a universal gate set.

The set of gates $\{H, T\}$ allows one to approximate an arbitrary single-qubit unitary gate to any required precision [48]. This is due to the fact that the $THTH$ operation implements a rotation by an angle θ which is an irrational multiple of π [41]. Therefore, $THTH$ repeated an appropriate number of times can be arbitrarily close to a desired rotation angle. Together with the CNOT-gate the universal gate set $\{H, T, \text{CNOT}\}$ allows for the approximation of an arbitrary unitary acting on multiple qubits [45].

The idea of a universal gate set eases the requirements for the experimental implementation of quantum computers: it is not necessary to be able to implement an arbitrary unitary gate experimentally but instead the experimental setup needs to be capable of performing only some finite but universal set of quantum gates with high quality. The same logic is valid for quantum error correction and fault-tolerance (see Sec. 3.7), i.e. only a finite set of logical operations needs be implemented in quantum error correcting codes.

2.3 Non-unitary evolution

Experimental systems do not follow perfect theoretical models describing qubits and their evolution. It is desired for the qubit system to be decoupled from the environment so it is isolated and does not change its state on its own, but it is never fully achievable. At the same time, some coupling to the environment is necessary to be able to manipulate the qubit state. In any case, the qubit system can not be treated as a closed system evolving unitarily. A larger system of qubits and environment together can be considered to recover the model description using state vectors and unitary matrices. The inseparability of the qubit system from the environment system is reflected in the fact that the state vector of the full system $|\Psi\rangle_{qubits+env}$ can not be represented as a tensor product of the smaller systems' state vectors, i.e. they are entangled:

$$|\Psi\rangle_{qubits+env} \neq |\psi_q\rangle_{qubits} \otimes |\psi_e\rangle_{env} \,. \tag{2.36}$$

The evolution of the full system can still be described by unitary matrices:

$$|\Psi'\rangle_{qubits+env} = U\,|\Psi\rangle_{qubits+env} \,. \tag{2.37}$$

However, an accurate modeling and description of the environment system is rarely possible and it is usually not of interest. Instead, the density matrix formalism can be used to describe an open system. We can introduce a density matrix for the full system:

$$\rho_{qubits+env} = |\Psi\rangle_{qubits+env} \langle\Psi|_{qubits+env} \,. \tag{2.38}$$

A density matrix can be seen as a classical mixture of 'pure' states, i.e. the states that can be represented by a state vector:

$$\rho = \sum_i p_i \,|\psi_i\rangle \langle\psi_i| \,. \tag{2.39}$$

If at least two $p_i \neq 0$, then the state is called a 'mixed' state. Any density matrix must be a positive semi-definite operator with a unit trace to describe a quantum system. In this case, $\rho_{qubits+env} = |\Psi\rangle_{qubits+env} \langle\Psi|_{qubits+env}$ is a pure state since $p_1 = 1$ and $|\psi_1\rangle = |\Psi\rangle_{qubits+env}$.

The qubit system can be described as a density matrix obtained by taking a partial trace over the environment system:

$$\rho_{qubits} = \mathrm{tr}_{env}(\rho_{qubits+env}). \tag{2.40}$$

The same logic can be applied to the evolution of a quantum system. One has to consider the evolution of the full system including the qubits and the environment to describe the evolution of the qubit system:

$$\begin{aligned} \rho'_{qubits+env} &= |\Psi'\rangle_{qubits+env} \langle\Psi'|_{qubits+env} \\ &= U\,|\Psi\rangle_{qubits+env} \langle\Psi|_{qubits+env} U^\dagger = U\rho_{qubits+env}U^\dagger. \end{aligned} \tag{2.41}$$

The state of the qubit system after the evolution is:

$$\rho'_{qubits} = \mathrm{tr}_{env}(U\rho_{qubits+env}U^\dagger). \tag{2.42}$$

It can be shown [41] that Eq. (2.42) can be rewritten as:

$$\rho' = \mathcal{E}(\rho) = \sum_k E_k \rho E_k^\dagger, \tag{2.43}$$

where ρ is the qubit system density matrix before the evolution and $\mathcal{E}(\rho)$ is the density matrix of the same system after the evolution under the process $\mathcal{E}$. This is called the 'operator sum representation'. The set of operators $\{E_k\}$ (also called 'Kraus operators') must fulfill $\sum_k E_k^\dagger E_k = I$ to preserve the trace of the density matrix.

The set of Kraus operators $\{E_k\}$ can be decomposed using the Pauli basis (see Sec. 3.2):

$$\mathcal{E}(\rho) = \sum_{i,j} \chi_{i,j} P_i \rho P_j, \qquad P_i, P_j \in \mathcal{P}_n. \tag{2.44}$$

The matrix χ here is called 'chi-matrix' and it is often used to describe quantum processes. Generally, the basis for the decomposition does not have to be the Pauli basis and any other bases can be used. However, the Pauli basis is often used for chi-matrices in the literature and will be used throughout this work. Such an approach allows to describe processes happening with open qubit systems. The chi-matrix fully describes an operation acting on an open system as unitary matrices describe processes happening in closed systems.

The chi-matrix representation is closely related to the Choi-Jamiołkowski isomorphism [49, 50]. The isomorphism is between quantum processes and density matrices of a special form in an extended space. Choi matrices are defined as follows:

$$\rho_{\mathcal{E}} = (\mathcal{E} \otimes I) \left|\Psi\right\rangle \left\langle\Psi\right|, \tag{2.45}$$

where $\left|\Psi\right\rangle = \frac{1}{\sqrt{d}} \sum_{i=1}^{d} \left|i\right\rangle \otimes \left|i\right\rangle$ is a maximally entangled state of two subsystems. The chi-matrix is equivalent to the Choi-matrix if they are represented in the same basis $\chi_{\mathcal{E}} \sim \rho_{\mathcal{E}}$.

2.4 Fidelity

Various experimental factors such as imperfect hardware control or coupling to the environment described above prevent experimental implementations from being exactly like the ideal operations. Therefore, it is desirable to have some kind of measure to estimate how well experimental operations match their theoretically desired counterparts, e.g. as described in Sec. 2.2. A quantity called 'fidelity' is often used in the literature for this purpose, but the definition can vary sometimes. Here we give

definitions for the fidelity between quantum states and between quantum processes used throughout this work.

The fidelity between two quantum states, represented by density matrices ρ, σ, is defined as follows (as opposed to the definition without a square in the end):

$$F_{st}(\rho, \sigma) = \left(\mathrm{tr} \sqrt{\sqrt{\rho} \sigma \sqrt{\rho}} \right)^2 . \tag{2.46}$$

For two pure states this is equivalent to:

$$F_{st}(|\psi_\rho\rangle, |\psi_\sigma\rangle) = |\langle \psi_\rho | \psi_\sigma \rangle|^2. \tag{2.47}$$

The fidelity between two quantum processes $\mathcal{E}, \mathcal{F}$ can be defined via the Choi-Jamiołkowski isomorphism and can be expressed as a state fidelity between the corresponding Choi-matrices or chi-matrices:

$$F_{pro}(\mathcal{E}, \mathcal{F}) = F_{st}(\rho_\mathcal{E}, \rho_\mathcal{F}) = F_{st}(\chi_\mathcal{E}, \chi_\mathcal{F}). \tag{2.48}$$

In the following text labels $_{st}$, $_{pro}$ will be omitted, assuming it is clear if we are talking about state or process fidelity.

Chapter 3

Quantum error correction basics

Practically useful quantum algorithms will require billions of operations to be applied to qubits [51]. The state of a qubit changes continuously and even a small error in quantum gates can add up and lead to incorrect results of the computation. At the same time, there is no way to make qubit manipulation perfect. Therefore, it is required to have a solution which allows quantum computation to work in the presence of finite errors.

One approach to make quantum computers resilient against errors is to perform quantum error correction (QEC). This chapter introduces some concepts of QEC important for the scope of this work. The reader can refer to Ref. 52, 53, 54 for a more thorough introduction.

3.1 Basic concept

The main idea of quantum error correction is to use several physical qubits to encode information redundantly into fewer logical qubits. Such an encoding can make logical information robust against certain errors. For example, we can consider a repetition code inspired by a classical repetition code. We encode one logical qubit using three physical qubits in the following way:

$$|0\rangle_L = |000\rangle\,, \qquad |1\rangle_L = |111\rangle\,. \tag{3.1}$$

These two states are called 'codewords' of the error-correcting code. This encoding will protect the logical state from a single X-error (bit flip) on any physical qubit. For example, if an X-error happens on qubit 1, the logical state can still be recovered as $|0\rangle_L$ since two other qubits remained in 0:

$$|0\rangle_L = |000\rangle \xrightarrow{X_1} |100\rangle \xrightarrow{\text{decoding}} |0\rangle_L\,. \tag{3.2}$$

Here a majority vote is applied to decode what logical state is encoded in physical qubits:

$$\begin{matrix} |000\rangle \\ |001\rangle \\ |010\rangle \\ |100\rangle \end{matrix} \xrightarrow{\text{decoding}} |0\rangle_L\,, \qquad \begin{matrix} |011\rangle \\ |101\rangle \\ |110\rangle \\ |111\rangle \end{matrix} \xrightarrow{\text{decoding}} |1\rangle_L\,. \tag{3.3}$$

However, if two X-errors happen the code will not be able to protect the logical information and the decoded state will be wrong:

$$|0\rangle_L = |000\rangle \xrightarrow{X_1X_2} |110\rangle \xrightarrow{\text{decoding}} |1\rangle_L . \tag{3.4}$$

This can be solved by increasing the redundancy of the encoding, e.g. five physical qubits can be used:

$$|0\rangle_L = |00000\rangle , \qquad |1\rangle_L = |11111\rangle . \tag{3.5}$$

This repetition code will protect from two bit flips but will fail if three bit flips happen.

The ability of an error-correcting code to protect from errors is closely related to the notion of distance of the code. The distance d of the code is defined as the number of bits (qubits) that must be affected to change one valid codeword to another.

$$|0\rangle_L = |000\rangle \xrightarrow{X_1X_2X_3} |111\rangle = |1\rangle_L \tag{3.6}$$

$$|0\rangle_L = |00000\rangle \xrightarrow{X_1X_2X_3X_4X_5} |11111\rangle = |1\rangle_L \tag{3.7}$$

The first code is the distance-3 repetition code and the second is the distance-5 repetition code. Usually, a code with distance d is robust against $t = \lfloor \frac{d-1}{2} \rfloor$ errors on different bits (qubits).

However, the codes we have considered above only protect against bit flip errors, while other errors can occur to qubits during quantum computation. Other QEC codes are also based on the idea of redundant encoding but encoding and decoding mechanisms are more sophisticated to make these codes robust against arbitrary errors. In the next sections we will introduce some mathematical framework before continuing with the QEC codes used in this work.

3.2 Pauli group and Pauli errors

It is convenient to work with the Pauli group to discuss errors that can happen to a logical state as argued in Ref. 52. The Pauli group is constructed using the Pauli matrices:

$$I = \begin{pmatrix} 1 & 0 \\ 0 & 1 \end{pmatrix}, \quad X = \begin{pmatrix} 0 & 1 \\ 1 & 0 \end{pmatrix}, \quad Y = \begin{pmatrix} 0 & -i \\ i & 0 \end{pmatrix}, \quad Z = \begin{pmatrix} 1 & 0 \\ 0 & -1 \end{pmatrix}. \tag{3.8}$$

These matrices form a basis of the vector space of 2×2 matrices.

The Pauli group on n qubits $\mathcal{P}_n$ can be defined as a group consisting of tensor products of Pauli matrices on n qubits with factors ± 1, $\pm i$:

$$\mathcal{P}_n = \left\{ \bigotimes_{i=1}^{n} P_i \mid P_i \in \{\pm I, \pm iI, \pm X, \pm iX, \pm Y, \pm iY, \pm Z \pm iZ\} \right\}. \tag{3.9}$$

Here, the index i denotes which qubit the element is applied to. The factors ± 1, $\pm i$ are needed to close the group under multiplication. It can also be said that the group is generated by the following elements:

$$\mathcal{P}_n = \left\langle \bigotimes_{i=1}^{n} P_i \mid P_i \in \{X, Y, Z\} \right\rangle, \tag{3.10}$$

where $\langle A, B, C \rangle$ denotes a group generated by A, B, C. This group has the following properties based on the properties of the Pauli matrices:

1. Elements of the group either commute or anticommute
   $\forall P, Q \in \mathcal{P}_n \Rightarrow$ either $[P, Q] = 0$ or $\{P, Q\} = 0$
2. The square of any element is $\pm I$
   $\forall P \in \mathcal{P}_n \Rightarrow P^2 \in \{+I, -I\}$
3. The group elements span the space of $2^n \times 2^n$ matrices, similarly to Pauli matrices spanning the space of 2×2 matrices

The number of non-identity elements of $P \in \mathcal{P}_n$ is called the weight of P or $\mathrm{wt}(P)$. For example, $P = I_1 \otimes X_2 \otimes I_3 \otimes Y_4 \equiv X_2 Y_4$ has weight 2.

It follows from property 3 that an arbitrary unitary error on n qubits can be decomposed into a linear combination of elements of the Pauli group $\mathcal{P}_n$ (Pauli errors). Moreover, it can be shown that if a QEC code can correct all weight-t Pauli errors, it can correct an arbitrary t-qubit error [55, 56]. Thus, in the following we will mostly talk about correcting Pauli errors.

3.3 Clifford group

Another group useful for quantum error correction is the Clifford group [52]. The Clifford group $\mathcal{C}_n$ on n qubits is defined as the group of unitaries normalizing the Pauli group $\mathcal{P}_n$, i.e. elements of this group map elements of $\mathcal{P}_n$ to other elements of $\mathcal{P}_n$:

$$\mathcal{C}_n = \{U \mid UPU^\dagger \in \mathcal{P}_n, \forall P \in \mathcal{P}_n\}. \tag{3.11}$$

It was shown that a quantum circuit starting in a computational basis state, containing only gates from the Clifford group and measurements in a Pauli basis can be efficiently simulated on a classical computer [57]. Therefore, a quantum computer should be capable of executing some gates not from the Clifford group to outperform classical computers.

Let us consider some of the basic gates from Sec. 2.2, namely H, S, CNOT, and T. The action of a quantum gate can be described in terms of its effect on the generating elements of the Pauli group $\mathcal{P}_n$ since it forms a basis for $2^n \times 2^n$ matrices.

The H-gate and the S-gate do not change the Pauli group under conjugation, so they belong to the Clifford group:

$$H: \quad X \to Z \qquad\qquad S: \quad X \to Y \tag{3.12}$$
$$Z \to X \qquad\qquad Z \to Z \tag{3.13}$$

The same is true for the CNOT-gate; it also belongs to the Clifford group:

$$\text{CNOT}: \quad I \otimes X \to I \otimes X \tag{3.14}$$
$$X \otimes I \to X \otimes X \tag{3.15}$$
$$I \otimes Z \to Z \otimes Z \tag{3.16}$$
$$Z \otimes I \to Z \otimes I \tag{3.17}$$

In fact, the Clifford group on n qubits is generated by H, S, and CNOT. However, the Clifford group alone is not enough to implement an arbitrary multi-qubit unitary gate, i.e. the Clifford group is not a universal gate set.

A universal gate set can be obtained if a non-Clifford gate is added to the Clifford group. For example, the T-gate can be added since $\{H, T, \text{CNOT}\}$ is a universal gate set as discussed in Sec. 2.2. The T-gate does not belong to the Clifford group since:

$$T: \quad X \to e^{-i\pi/4} \begin{pmatrix} 0 & 1 \\ i & 0 \end{pmatrix} \tag{3.18}$$
$$Z \to Z \tag{3.19}$$

Usually, one is interested in a QEC code that allows for a 'fault-tolerant' implementation of a universal gate set on the logical level as will be discussed in Sec. 3.7. However, the fault-tolerant implementation of non-Clifford gates is challenging in many QEC code popular nowadays while at least one of these gates is necessary for a universal gate set. On the other hand, some other QEC codes offer fault-tolerant non-Clifford gates but do no support a fault-tolerant implementation of the entire Clifford group.

3.4 Stabilizer codes

QEC codes can be constructed in various ways. Intuitively, a QEC code can be defined by the way logical states are mapped to physical states and vice versa, i.e. their encoder and decoder (see Sec. 3.1). For example, in the repetition code the encoding is given by Eq. (3.1) and the decoding is given by Eq. (3.3). However, there are other ways to define a QEC code, for example using stabilizer formalism which will be outlined below.

A stabilizer code $T(\mathcal{S})$ is defined by a set of stabilizers $\mathcal{S}$. The set of stabilizers $\mathcal{S}$ has the following properties:

1. The set $\mathcal{S}$ is a subset of the Pauli group $\mathcal{P}_n$
   $\mathcal{S} \subset \mathcal{P}_n$
2. The set $\mathcal{S}$ does not contain $-I$
   $-I \notin \mathcal{S}$
3. The set $\mathcal{S}$ is a group
   $\forall S_i, S_j \in \mathcal{S} \Rightarrow S_i S_j \in \mathcal{S}$
4. The group $\mathcal{S}$ is Abelian
   $\forall S_i, S_j \in \mathcal{S} \Rightarrow S_i S_j = S_j S_j$

The stabilizer group can describe a QEC code by defining its codespace, i.e. a subspace of the Hilbert space spanned by all possible codewords. The codespace of $T(\mathcal{S})$ is defined as the simultaneous $+1$ eigenstate of all stabilizers in $\mathcal{S}$:

$$T(\mathcal{S}) = \{|\psi\rangle \mid S|\psi\rangle = |\psi\rangle, \forall S \in \mathcal{S}\}. \tag{3.20}$$

The idea behind using stabilizers is that they can detect errors which anticommute with them. Let us assume we have an error $E \in \mathcal{P}_n$ and $\exists S \in \mathcal{S} \mid \{E, S\} = 0$. If this error E acts on the codestate $|\psi\rangle$, it brings it out of the codespace. The new state $|\psi'\rangle = E|\psi\rangle$ is no longer a valid codeword since it is not an eigenstate of the stabilizer S:

$$S|\psi'\rangle = SE|\psi\rangle = -ES|\psi\rangle = -E|\psi\rangle = -|\psi'\rangle. \tag{3.21}$$

The normalizer $\mathcal{N}(\mathcal{S})$ of the stabilzier group $\mathcal{S}$ can be considered to generalize this property and describe the class of errors that can be detected by a stabilizer code. The normalizer $\mathcal{N}(\mathcal{S})$ contains all the elements of the Pauli group $\mathcal{P}_n$ that commute with the group $\mathcal{S}$:

$$\mathcal{N}(\mathcal{S}) = \{N \in \mathcal{P}_n \mid [S, N] = 0, \forall S \in \mathcal{S}\}. \tag{3.22}$$

Three subsets of the Pauli group $\mathcal{P}_n$ naturally emerge here:

1. Stabilizer group $\mathcal{S}$

   These elements are stabilizers of any codeword, they act trivially on any codeword:

   $$S|\psi\rangle = |\psi\rangle, \qquad S \in \mathcal{S}. \tag{3.23}$$

2. Set difference of the normalizer and the stabilizer group $\mathcal{N}(\mathcal{S}) \setminus \mathcal{S}$

   The elements of this subset change the state, but it remains a valid codeword since these elements commute with all the stabilizers:

   $$SN|\psi\rangle = NS|\psi\rangle = N|\psi\rangle, \qquad N \in \mathcal{N}(\mathcal{S}) \setminus \mathcal{S}, S \in \mathcal{S}. \tag{3.24}$$

This means that the elements of this subset are logical operators of the code since they transform one valid logical state to another.

There is a certain freedom in how the logical operators are defined, i.e. what will be logical Z_L and X_L for the code. We can have a look at the factor group $\mathcal{N}(\mathcal{S})/\mathcal{S}$. Any maximal Abelian subgroup of $\mathcal{N}(\mathcal{S})/\mathcal{S}$ can be chosen to be the logical Z_L operators. After that, the appropriate elements of $\mathcal{N}(\mathcal{S})/\mathcal{S}$ can be chosen to be logical X_L operators to match the commutation relations with logical Z_L. For example, in the case of one encoded logical qubit the factor group will be generated by cosets of the logical Paulis and the stabilizer group $\mathcal{S}$:

$$\mathcal{N}(\mathcal{S})/\mathcal{S} = \langle iI\mathcal{S}, X_L\mathcal{S}, Z_L\mathcal{S}\rangle. \tag{3.25}$$

Generally, the factor group $\mathcal{N}(\mathcal{S})/\mathcal{S}$ is isomorphic to the Pauli group $\mathcal{P}_k$ action on k logical qubits. The stabilizer group $\mathcal{S}$ represents the identity operator of the Pauli group $\mathcal{P}_k$.

3. Set difference of the Pauli group and the normalizer $\mathcal{P}_n \setminus \mathcal{N}(\mathcal{S})$

   These elements are errors; they bring the state out of the codespace since there are stabilizers they anticommute with:

$$SE|\psi\rangle = -ES|\psi\rangle = -E|\psi\rangle, \qquad E \notin \mathcal{N}(\mathcal{S}), \exists S \in \mathcal{S}. \tag{3.26}$$

Summarizing, if the error $E \notin \mathcal{N}(\mathcal{S})$ it can be detected because it anticommutes with some stabilizers. If the error $E \in \mathcal{S}$ it is not really an error since it acts trivially on any codeword and does not change the logical state. Therefore, we can conclude that a stabilizer code can detect errors $E \notin \mathcal{N}(\mathcal{S}) \setminus \mathcal{S}$.

Now, let us discuss which errors a stabilizer code can correct, rather than just detect. The error E can be described by an error syndrome, i.e. a set of measurements identifying an error. For a stabilizer code $T(\mathcal{S})$ the list of measured eigenvalues of the generators of the stabilizer group $\mathcal{S}$ will be such an error syndrome. The code must be able to distinguish different errors to correct them, hence different errors should have different error syndromes. Once the error is identified based on the error syndrome, an appropriate correction procedure can be applied, e.g. $E^\dagger$. We write $E^\dagger$ to highlight that this is an inverse to E, but E is Hermitian since $E \in \mathcal{P}_n$, thus $E = E^\dagger$. Let us assume we have two errors E and F and they have the same error syndrome. It follows that they commute/anticommute with the same stabilizers:

$$[E, S_c] = 0, [F, S_c] = 0, \qquad \forall S_c \in \mathcal{S}_c \subset \mathcal{S}, \tag{3.27}$$

$$\{E, S_a\} = 0, \{F, S_a\} = 0, \qquad \forall S_a \in \mathcal{S}_a \subset \mathcal{S}. \tag{3.28}$$

This is equivalent to $E^\dagger F$ commuting with any stabilizer $S \in \mathcal{S}$ because such S either commutes or anticommutes with both errors:

$$E^\dagger F S_c = E^\dagger S_c F = S_c E^\dagger F \qquad \forall S_c \in \mathcal{S}_c \subset \mathcal{S}, \tag{3.29}$$

$$E^\dagger F S_a = -E^\dagger S_a F = S_a E^\dagger F \qquad \forall S_a \in \mathcal{S}_a \subset \mathcal{S}. \tag{3.30}$$

Consequently, errors E, F for which $E^\dagger F \in \mathcal{N}(\mathcal{S})$ have the same error syndromes and can not be distinguished.

However, we can say that a stabilizer code can correct a set of errors $\mathcal{E} \subset \mathcal{P}_n$ iff $E^\dagger F \notin \mathcal{N}(\mathcal{S}) \setminus \mathcal{S}, \forall E, F \in \mathcal{E}$. The errors $E, F \notin \mathcal{N}(\mathcal{S})$ can be distinguished and corrected according to their error syndromes. While the errors $E^\dagger F \in \mathcal{S}$ can not be distinguished, they act on codewords in the same way since $E^\dagger F = S \in \mathcal{S}$:

$$E\left|\psi\right\rangle = ES\left|\psi\right\rangle = EE^\dagger F\left|\psi\right\rangle = F\left|\psi\right\rangle. \tag{3.31}$$

The correction procedure for them is the same.

Summarizing, the stabilizer group $\mathcal{S}$ determines the error-correcting properties of the stabilizer code $T(\mathcal{S})$. The distance d of the stabilizer code is the minimal weight of an operator in $\mathcal{N}(\mathcal{S}) \setminus \mathcal{S}$ since that is the minimal number of qubits which should be affected by the operator to change one valid codeword to another. If a stabilizer code has n physical qubits and a stabilizer group $\mathcal{S}$ has s stabilizer generators then the code will encode $k = n - s$ logical qubits. Such a code is frequently denoted as $[[n, k, d]]$ code, where [[ ]] emphasizes that the code is a **quantum** error-correcting code as opposed to **classical** error-correcting codes denoted with [ ].

3.4.1 Stabilizer measurement

Experimentally, stabilizer eigenvalues of an encoded state $|\psi\rangle$ can be measured directly by measuring the state $|\psi\rangle$ in the computational basis. However, this will project the state $|\psi\rangle$ into one of the computational basis states and erase the encoded logical information. Such a procedure is only sensible at the end of the computation. Therefore, usually stabilizer eigenvalues are measured by mapping their values to auxiliary qubits with the Hadamard test. In the following we will refer to this procedure as 'stabilizer measurement' or 'stabilizer mapping'.

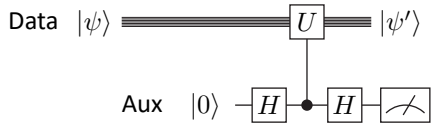

Figure 3.1: Quantum circuit for the Hadamard test.

Let us consider the circuit in Fig. 3.1 with a data state $|\psi\rangle$ and an auxiliary qubit; the operator U here is a unitary. The resulting state of the system right before the measurement of the auxiliary qubit can be written as:

$$\begin{aligned}|\Psi\rangle &= H_{aux}\mathrm{C}U_{aux,data}H_{aux}\left|0\right\rangle\left|\psi\right\rangle = \frac{1}{\sqrt{2}}H_{aux}\mathrm{C}U_{aux,data}(\left|0\right\rangle + \left|1\right\rangle)\left|\psi\right\rangle \\ &= \frac{1}{\sqrt{2}}H_{aux}(\left|0\right\rangle\left|\psi\right\rangle + \left|1\right\rangle U\left|\psi\right\rangle) = \frac{1}{2}\left[\left|0\right\rangle(I+U)\left|\psi\right\rangle + \left|1\right\rangle(I-U)\left|\psi\right\rangle\right].\end{aligned} \tag{3.32}$$

After the measurement of the auxiliary qubit, the data qubits will be in one of the states:

$$\left|\psi_0'\right\rangle = (I+U)\left|\psi\right\rangle, \tag{3.33}$$

$$\left|\psi_1'\right\rangle = (I-U)\left|\psi\right\rangle. \tag{3.34}$$

Both states are eigenstates of the unitary U:

$$U\left|\psi_0'\right\rangle = +\left|\psi_0'\right\rangle, \tag{3.35}$$

$$U\left|\psi_1'\right\rangle = -\left|\psi_1'\right\rangle. \tag{3.36}$$

If U is a stabilizer $U = S$, there are three cases possible:

1. There was no error
   $U\left|\psi\right\rangle = S\left|\psi\right\rangle = \left|\psi\right\rangle$
   $\left|\Psi\right\rangle = \left|0\right\rangle\left|\psi\right\rangle$
   The outcome of the auxiliary qubit measurement will be 0 and the state of the data qubits will be $\left|\psi\right\rangle$. No action needs to be taken.

2. There was an error E which anticommutes with the stabilizer $\{E, S\} = 0$
   $UE\left|\psi\right\rangle = SE\left|\psi\right\rangle = -E\left|\psi\right\rangle$
   $\left|\Psi\right\rangle = \left|1\right\rangle E\left|\psi\right\rangle$
   The outcome of the auxiliary qubit measurement will be 1 and the state of the data qubits will be $E\left|\psi\right\rangle$. The appropriate correction must be applied to cancel the error E.

3. There was an error E which commutes with the stabilizer $[E, S] = 0$
   $UE\left|\psi\right\rangle = SE\left|\psi\right\rangle = E\left|\psi\right\rangle$
   $\left|\Psi\right\rangle = \left|0\right\rangle E\left|\psi\right\rangle$
   The outcome of the auxiliary qubit measurement will be 0 and the state of the data qubits will be $E\left|\psi\right\rangle$. Such an error can only be detected by a different stabilizer.

The example circuits for $U \in \{X, Z\}$ are given in Fig. 3.2. The circuit for the Z measurement can be simplified since the CZ-gate is symmetric:

$$H_{aux}\mathrm{C}Z_{aux,data}H_{aux} = H_{aux}\mathrm{C}Z_{data,aux}H_{aux} = \mathrm{C}X_{data,aux} = \mathrm{CNOT}_{data,aux}. \tag{3.37}$$

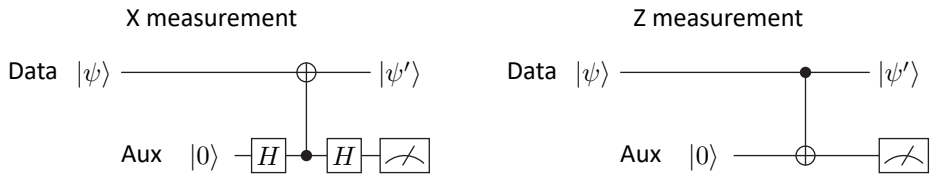

Figure 3.2: Quantum circuits for measuring X and Z operators with the Hadamard test.

Overall, based on the auxiliary qubit measurements outcome the error syndrome can be obtained when all stabilizer group generators are measured. This error syndrome allows one to find an appropriate correction procedure. However, the necessity to couple auxiliary qubits to data qubits for the stabilizer measurement induces problems which will be discussed in Sec. 3.7.

3.4.2 Logical state preparation

An important step for the QEC protocols is the logical state preparation. It is sufficient to consider only the codes encoding one logical qubit for the scope of this work. However, the logic provided in the following can be easily extended to codes encoding multiple logical qubits [54].

Any logical state $|\psi\rangle_L$ is a $+1$ eigenstate of all stabilizers S. However, there is still freedom in what logical information this state encodes. A logical state will be fully defined if we specify which logical operator it is an eigenstate of, e.g. $|0\rangle_L$ is a $+1$ eigenstate of Z_L and $|-\rangle_L$ is a -1 eigenstate of X_L. Therefore, for example, for $|0\rangle_L$:

$$S\,|0\rangle_L = |0\rangle_L\,, \qquad \forall S \in \mathcal{S}, \tag{3.38}$$

$$Z_L\,|0\rangle_L = |0\rangle_L\,. \tag{3.39}$$

We can consider the following state $|\psi\rangle$, where a is just a normalization factor:

$$|\psi\rangle = a \sum_{S\in\mathcal{S}} S\,|0\ldots0\rangle \tag{3.40}$$

This state contains a sum of all stabilizers from the group, so it is an eigenstate of any stabilizer:

$$S'\,|\psi\rangle = aS' \sum_{S\in\mathcal{S}} S\,|0\ldots0\rangle = a \sum_{S\in\mathcal{S}} S'S\,|0\ldots0\rangle = a \sum_{S''\in\mathcal{S}} S''\,|0\ldots0\rangle\,. \tag{3.41}$$

This means that $|\psi\rangle$ is a codeword. There is freedom in how the logical Z_L is chosen, and for many stabilizer codes it can be chosen in a way that $|0\ldots0\rangle$ is its $+1$ eigenstate (see Ch. 4.1, 4.2 in Ref. 54 for details):

$$Z_L\,|0\ldots0\rangle = |0\ldots0\rangle\,. \tag{3.42}$$

Then, the state $|\psi\rangle$ is the $|0\rangle_L$ state:

$$|0\rangle_L = a \sum_{S\in\mathcal{S}} S\,|0\ldots0\rangle\,. \tag{3.43}$$

This construction can be simplified a bit to give a better recipe for how this state can be prepared experimentally. The expression can be rewritten in a different from using the stabilizer group generators S_i of an $[[n, k, d]]$ code:

$$|0\rangle_L = a \prod_{i=1}^{n-k} (I + S_i)\,|0\ldots0\rangle\,. \tag{3.44}$$

Expressions in Eq. (3.43) and Eq. (3.44) are equivalent. This can be seen by noting that expanding the product will yield sums of all products of the generators, which produce by definition the entire group. Now it is clear that the state can be prepared experimentally by an application of $n - k$ consecutive operations.

The $|1\rangle_L$ state can be obtained by applying a logical X_L operator:

$$|1\rangle_L = X_L\,|0\rangle_L = aX_L \prod_{i=1}^{n-k} (I + S_i)\,|0\ldots0\rangle\,. \tag{3.45}$$

3.5 Subsystem codes

Another family of codes are subsystem codes [58, 59]. They share some features with stabilizer codes and can be considered a generalization of stabilizer codes.

A subsystem code is defined by its gauge group $\mathcal{G}$, a subgroup of the Pauli group $\mathcal{P}_n$. The group $\mathcal{G}$ does not have to be Abelian. The center of the group $\mathcal{G}$ is the stabilizer group $\mathcal{S}$. The center $\mathcal{S}$ contains all the elements which commute with every element of $\mathcal{G}$. A stabilizer code is a special case of a subsystem code when $\mathcal{S} = \mathcal{G}$, so $\mathcal{G}$ is Abelian. The codewords of a subsystem code are the $+1$ eigenstates of all elements of $\mathcal{S}$. Morever, codewords are considered equivalent if they differ by the application of a linear combination of elements from $\mathcal{G} \setminus \mathcal{S}$.

Stabilizer codes and subsystem codes can be generated in the following way [59]. We start with a Pauli group $\mathcal{P}_n$ for n physical qubits. It is generated by the following operators $\{iI, X_1, Z_1, \ldots, X_n, Z_n\}$[1], where X_i is an operator acting as X on qubit i and as I on other qubits. In some sense n physical qubits are defined by $2n$ Pauli operators $\{X_1, Z_1, \ldots, X_n, Z_n\}$. We can take a set of $2n$ different operators from $\mathcal{P}_n$ $\{X'_1, Z'_1, \ldots, X'_n, Z'_n\}$ such that they obey the same commutation relations among each other as in the initial set $\{X_1, Z_1, \ldots, X_n, Z_n\}$. The new operators define n new 'virtual' qubits; the states defining the virtual qubits are linear combinations of the states of the physical qubits. The new operators behave like the initial single qubit Pauli operators when acting on these virtual qubits. The new operators can be chosen in multiple ways and this will spawn different QEC codes. These new operators can be some combinations of X and Z operators acting on different physical qubits, e.g. $X'_1 = X \otimes Z \otimes X \otimes I \otimes \cdots \otimes I$. Analogously, the new virtual qubits are not the same physical qubits, they represent some 'combinations' of the physical qubits.

A stabilizer code can be formed by defining $s \leq n$ operators as stabilizers such that they commute and do not contain $-I$ to form a stabilizer group $\mathcal{S} = \langle S_1, \ldots, S_s \rangle$. One can pick first Z' operators as stabilizers $S_j = Z'_j$ for $j = 1, \ldots s$, without loss of generality. The stabilizer group 'fixes' s out of n virtual qubits. Now, there are $k = n - s$ logical qubits left. The logical operators for the k logical qubits are contained in the normalizer of the stabilizer group as discussed above (see Sec. 3.22):

$$\mathcal{N}(\mathcal{S}) = \langle iI, Z'_1, \ldots, Z'_s, Z'_{s+1}, \ldots Z'_n, X'_{s+1}, \ldots X'_n \rangle. \tag{3.46}$$

The operators $\langle iI, Z'_{s+1}, \ldots Z'_n, X'_{s+1}, \ldots X'_n \rangle$ generate the Pauli group for k logical qubits. However, operators multiplied by any stabilizer act in the same way on the logical qubits, e.g. $Z'_n \sim Z'_n S_1$. Hence, we can associate the factor group with the Pauli group $\mathcal{N}(\mathcal{S})/\mathcal{S} \cong \mathcal{P}_k$.

Now, one can introduce a gauge group $\mathcal{G}$ to form a subsystem code. $r \leq n - s$ more operators from the initial set can be added to the gauge group:

$$\mathcal{G} = \langle iI, S_1, \ldots, S_s, Z'_{s+1}, \ldots Z'_{s+r}, X'_{s+1}, \ldots, X'_{s+r} \rangle. \tag{3.47}$$

[1] The imaginary unit i in iI spans elements $\{\pm I, \pm iI\}$.

The gauge group made r qubits 'gauge' qubits and we have $k = n - s - r$ logical qubits left. The logical operators acting on these k qubits are

$$\mathcal{L} = \langle iI, Z'_{s+r+1}, \dots Z'_n, X'_{s+r+1}, \dots X'_n \rangle. \tag{3.48}$$

Similarly, the factor group $\mathcal{N}(\mathcal{S})/\mathcal{G} \cong \mathcal{P}_k$ can be associated with the Pauli group action on k logical qubits.

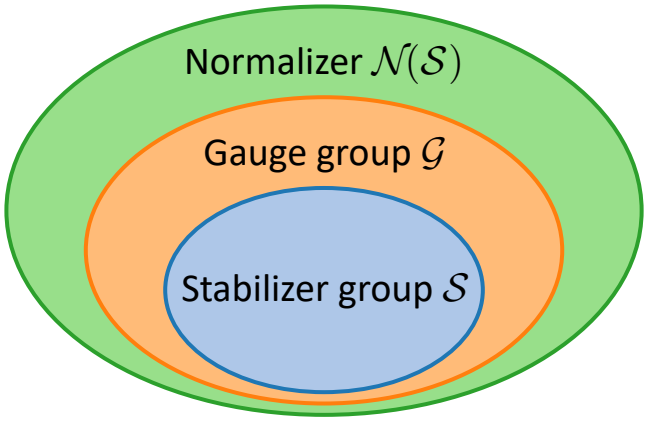

Figure 3.3: Group structure of a subsystem code. The code is defined by a gauge group $\mathcal{G}$, the stabilizer group $\mathcal{S}$ is the center of the gauge group.

Summarizing, we have a nested group structure $\mathcal{S} \subset \mathcal{G} \subset \mathcal{N}(\mathcal{S})$ (see Fig. 3.3). The stabilizer group $\mathcal{S}$ with s generator fixes the codespace with $n - s$ virtual qubits. Then, these $n - s$ virtual qubits are split into r gauge qubits and k logical qubits by the gauge group $\mathcal{G}$ with r additional generators[2]. It can be shown [59] that with the described properties of the gauge group any codeword can be split into a tensor product of gauge qubits and logical qubits:

$$|\psi\rangle = |l\rangle_L \otimes |g\rangle_G . \tag{3.49}$$

Operators from the stabilizer group act trivially on the codewords:

$$S\,|\psi\rangle = |\psi\rangle , \qquad S \in \mathcal{S}. \tag{3.50}$$

Operators from the gauge group act only on the gauge qubits:

$$G\,|\psi\rangle = |l\rangle_L \otimes G\,|g\rangle_G = |l\rangle_L \otimes |g'\rangle_G \qquad G \in \mathcal{G}. \tag{3.51}$$

The operators from $\mathcal{G} \setminus \mathcal{S}$ act non-trivially on the gauge qubits. The factor group $\mathcal{G}/\mathcal{S} \cong \mathcal{P}_r$ can be associated with the Pauli group acting on the gauge qubits, since operators $G \sim GS$ act in the same way.

Finally, operators from $\mathcal{L}$ act only on the logical qubits:

$$L\,|\psi\rangle = L\,|l\rangle_L \otimes |g\rangle_G = |l'\rangle_L \otimes |g\rangle_G \qquad L \in \mathcal{L}. \tag{3.52}$$

[2]Some stabilizer codes can be turned into subsystem codes if some stabilizer generators are replaced by gauge operators. A detailed example for the $[[9, 1, 3]]$ Shor code [55] can be found in Ref. 60.

These operators are called 'bare' logical gates. At the same time, operator $L \sim LG$ will act in the same way on the logical qubits but will change the gauge qubits as well.

$$LG\,|\psi\rangle = L\,|l\rangle_L \otimes G\,|g\rangle_G = |l'\rangle_L \otimes |g'\rangle_G \qquad L \in \mathcal{L}, G \in \mathcal{G}. \tag{3.53}$$

This is a 'dressed' logical gate. Overall, the factor group $\mathcal{N}(\mathcal{S})/\mathcal{G} \cong \mathcal{P}_k$ can be associated with the Pauli group acting on the logical qubits, since operators $L \sim LG$ act the same way on the logical qubits.

3.5.1 Code switching

Subsystem codes are important in the scope of this work because they can be used for code switching [61–64]. The idea of code switching is to coherently transfer encoded logical information from one code to another. Every QEC code has its advantages and disadvantages like robustness to certain types of errors or efficient implementations of certain logical gates. Code switching offers the option to use several QEC codes in a single quantum circuit to utilize the benefits of these codes and avoid their drawbacks. For example, using code switching two complimentary QEC codes can be combined to obtain a fault-tolerant implementation of a universal logical gate set, which is challenging to achieve in a single QEC code (see Sec. 3.7.3).

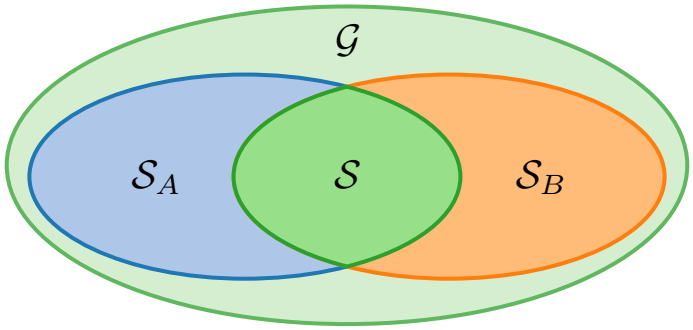

Figure 3.4: Group structure necessary for code switching between two stabilizer codes $\mathcal{S}_A, \mathcal{S}_B$ through a subsystem code $\mathcal{G}$.

In this work code switching will be performed between two stabilizer codes. Let us consider two stabilizer codes defined by stabilizer groups $\mathcal{S}_A, \mathcal{S}_B$ and a subsystem code define by a gauge group $\mathcal{G}$. These groups should be chosen in such a way that the stabilizer group of the subsystem code $\mathcal{S}$ is a subset of both stabilizer groups $\mathcal{S}_A, \mathcal{S}_B$ of the stabilizer codes (see Fig. 3.4):

$$\mathcal{S} \subset \mathcal{S}_A, \qquad \mathcal{S} \subset \mathcal{S}_B. \tag{3.54}$$

If this is true, a codeword of one of the stabilizer codes will also be a codeword of the subsystem code, since it is also stabilized by $\mathcal{S}$. Codewords of the stabilizer codes encoding logical state l (e.g. logical 0) can be represented in the following form:

$$|l\rangle_A = |l_A\rangle_L \otimes |g_A\rangle_G\,, \tag{3.55}$$
$$|l\rangle_B = |l_B\rangle_L \otimes |g_B\rangle_G\,. \tag{3.56}$$

Both states are codewords of the subsystem code, but they can differ by the state of the logical qubits $|l_A\rangle_L \neq |l_B\rangle_L$ and by the state of the gauge qubits $|g_A\rangle_G \neq |g_B\rangle_G$, even if they both encode the same logical information in the stabilizer codes.

However, we will also require logical operators $\mathcal{L}$ of all three codes to be the same. Then, the states $|l\rangle_A, |l\rangle_B$ representing the same logical state l for the stabilizer codes must have the same logical state in the subsystem code $l_A = l_B = l$ and the same state of the logical qubits in the subsystem code $|l_A\rangle_L = |l_B\rangle_L = |l\rangle_L$:

$$|l\rangle_A = |l\rangle_L \otimes |g_A\rangle_G , \tag{3.57}$$
$$|l\rangle_B = |l\rangle_L \otimes |g_B\rangle_G . \tag{3.58}$$

These two state only differ by the state of the gauge qubits $|g_A\rangle_G \neq |g_B\rangle_G$. Therefore, the logical information can be transferred from code A to code B, if the state of the gauge is changed $|g_A\rangle_G \to |g_B\rangle_G$. One can apply an element $G \in \mathcal{G} \setminus \mathcal{S}$, which only changes the state of the gauge qubits to do this:

$$G|l\rangle_A = |l\rangle_L \otimes G|g_A\rangle_G = |l\rangle_L \otimes |g_B\rangle_G = |l\rangle_B . \tag{3.59}$$

This is called 'gauge fixing'. The element G required for code switching $A \to B$ can be found by measuring stabilizer expectation values for $\mathcal{S}_B \setminus \mathcal{S}_A$ since $|l\rangle_A$ is not an eigenstate of these stabilizers but $|l\rangle_B$ is. We will call the outcome of this measurement 'switching syndrome'.

Summarizing, we start with a logical state encoded in code A, e.g. $|0\rangle_A$. This is also a codeword in the subsystem code since they share the stabilizer group $\mathcal{S}$. Moreover, the logical state is the same in the subsystem code since code A and the subsystem code share the logical operators, thus $|0\rangle_A = |0\rangle_L \otimes |g_A\rangle_G$. We can find a specific gauge operator G (based on the switching syndrome) such that $|g_A\rangle_G \to |g_B\rangle_G$ and thus $|0\rangle_A \to |0\rangle_B$: $|0\rangle_A = |0\rangle_L \otimes |g_A\rangle_G \xrightarrow{G} |0\rangle_L \otimes |g_B\rangle_G = |0\rangle_B$.

This describes the mathematical basis for code switching between two stabilizer codes through a subsystem code. More details and examples will be given in Sec. 7.3.

3.6 The [[7, 1, 3]] color code

After describing general ideas of the stabilizer codes in the previous sections, we will continue with the specific stabilizer code and the associated techniques used in this work. The main QEC code used in this work is the [[7, 1, 3]] 2D color code [65], also known as the Steane code [40]. This is the minimal instance of the color code family. The code is defined by stabilizers supported on three plaquettes as in Fig. 3.5.

There are six generators of the stabilizer group, three Z-stabilizers and three X-stabilizers. The [[7, 1, 3]] code is a Calderbank-Steane-Shor (CSS) code [40, 66], i.e. the set of stabilizer generators can be split into two sets: one containing only X-stabilizers and another containing only Z-stabilizers.

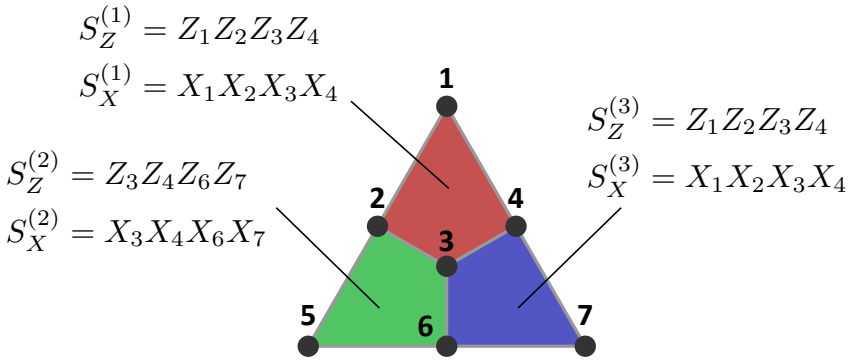

Figure 3.5: The [[7, 1, 3]] color code, its stabilizer generators, and logical Pauli operators.

The Z_L, X_L logical operators are supported on all seven qubits:

$$\begin{aligned} Z_L &= Z_1Z_2Z_3Z_4Z_5Z_6Z_7, \\ X_L &= X_1X_2X_3X_4X_5X_6X_7. \end{aligned} \tag{3.60}$$

The following operators are stabilizer-equivalent to the logical operators:

$$\begin{aligned} Z'_L &= S_Z^{(1)}Z_L = Z_5Z_6Z_7, \\ X'_L &= S_X^{(1)}X_L = X_5X_6X_7. \end{aligned} \tag{3.61}$$

These are the minimal weight logical operators, so the code has distance $d_Z = d_X = d = 3$. It encodes one logical qubit into seven physical qubits, thus it is a [[7, 1, 3]] code.

3.6.1 Logical gates

The logical Z_L and X_L can be implemented in a 'qubit-wise' fashion in the [[7, 1, 3]] code as in Eq. (3.60). Let us consider the implementation of other logical gates from the Clifford group. Any logical gate U_L should turn a valid codeword into another valid codeword, i.e. keep the state in the codespace. This statement can be reformulated in the language of stabilizers. If the state $|\psi\rangle$ is stabilized by the group $\mathcal{S}$, the state $U_L|\psi\rangle$ will be stabilized by the group $\mathcal{S}' = \{S' = U_L S U_L^\dagger, S \in \mathcal{S}\}$:

$$S|\psi\rangle = |\psi\rangle, \qquad \forall S \in \mathcal{S}, \tag{3.62}$$

$$S'U_L|\psi\rangle = U_L S U_L^\dagger U_L|\psi\rangle = U_L|\psi\rangle_L, \qquad \forall S' \in \mathcal{S}'. \tag{3.63}$$

If $\mathcal{S} = \mathcal{S}'$, then $U_L|\psi\rangle$ is still a valid codeword. Therefore, the logical gate U_L must not change the stabilizer group. Note that this conclusion is valid only for gates U_L from the Clifford group. Non-Clifford gates U_L will bring stabilizers out of the Pauli

group $U_L S U_L^\dagger \notin \mathcal{P}_n$, so $\mathcal{S}'$ can not coincide with the initial stabilizer group. In the case of non-Clifford gates the analysis of the logical gates can be done differently, and an example will be given in Sec. 7.3.

Additionally, a logical gate U_L must change the logical Pauli operators in the same way a physical gate U changes physical Pauli operators (see Eq. (3.12 – 3.19) in Sec. 3.3). For example, if a logical gate U_L is supposed to be a logical Hadamard gate H_L it should transform X_L and Z_L in the same was as H transforms X and Z:

$$H: \quad X \to Z \qquad\qquad U_L: \quad X_L \to Z_L \tag{3.64}$$

$$Z \to X \qquad\qquad Z_L \to X_L \tag{3.65}$$

The basic gates from the Clifford group can be implemented as follows in the [[7, 1, 3]] code:

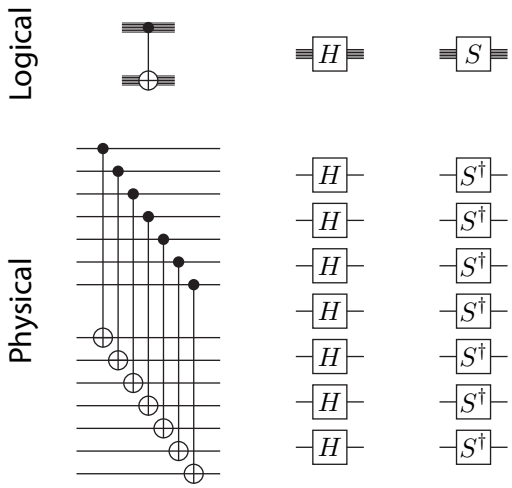

Figure 3.6: Implementation of the logical gates spanning the Clifford group for the [[7, 1, 3]] code.

1. **CNOT-gate**

   Let us consider a gate consisting of CNOT-gates applied to two logical qubits 'qubit-wise' (see Fig. 3.6):

   $$\mathrm{CNOT}_L = \mathrm{CNOT}_{1,1} \ldots \mathrm{CNOT}_{7,7}. \tag{3.66}$$

   Such a gate implements a logical CNOT-gate for any CSS code. In a CSS code stabilizer generators can be split into X and Z generators, thus the stabilizer group $\mathcal{S} \otimes \mathcal{S}$ is preserved under this gate:

   $$\mathrm{CNOT}_L: \quad I \otimes S_X^{(i)} \to I \otimes S_X^{(i)} \tag{3.67}$$

   $$S_X^{(i)} \otimes I \to S_X^{(i)} \otimes S_X^{(i)} \tag{3.68}$$

   $$I \otimes S_Z^{(i)} \to S_Z^{(i)} \otimes S_Z^{(i)} \tag{3.69}$$

   $$S_Z^{(i)} \otimes I \to S_Z^{(i)} \otimes I \tag{3.70}$$

where $S_X^{(i)}, S_Z^{(i)} \in \mathcal{S}$. The same is true for the logical X_L, Z_L operators:

$$\begin{aligned} \text{CNOT}_L: \quad & I \otimes X_1 \dots X_7 \to I \otimes X_1 \dots X_7 && (3.71)\\ & X_1 \dots X_7 \otimes I \to X_1 \dots X_7 \otimes X_1 \dots X_7 && (3.72)\\ & I \otimes Z_1 \dots Z_7 \to Z_1 \dots Z_7 \otimes Z_1 \dots Z_7 && (3.73)\\ & Z_1 \dots Z_7 \otimes I \to Z_1 \dots Z_7 \otimes I && (3.74) \end{aligned}$$

This means that the qubit-wise CNOT is indeed a logical CNOT for the [[7, 1, 3]] code. The qubit-wise implementation of a gate is also a 'transversal' implementation of a gate [52]. A transversal gate does not connect any physical qubits inside the same logical qubit with multi-qubit gates.

2. **H-gate**

The logical Hadamard can also be implemented as a transversal H-gate for the [[7, 1, 3]] code (see Fig. 3.6):

$$H_L = H_1 \dots H_7. \tag{3.75}$$

The transversal H-gate preserves the stabilizer group for any self-dual CSS code, i.e. the code where $X-$ and $Z-$stabilizers have the same support:

$$\begin{aligned} H_L: \quad & S_X^{(i)} \to S_Z^{(i)} && (3.76)\\ & S_Z^{(i)} \to S_X^{(i)} && (3.77) \end{aligned}$$

where $S_X^{(i)}, S_Z^{(i)} \in \mathcal{S}$. If $S_X^{(i)}$ and $S_Z^{(i)}$ act on the same qubits, the stabilizer group is preserved. The logical Pauli gates are changed accordingly:

$$\begin{aligned} H_L: \quad & X_1 \dots X_7 \to Z_1 \dots Z_7 && (3.78)\\ & Z_1 \dots Z_7 \to X_1 \dots X_7 && (3.79) \end{aligned}$$

Hence, the transversal Hadamard gate implements a logical Hadamard for the [[7, 1, 3]] code.

3. **S-gate**

The logical S-gate can be implemented transversally in the [[7, 1, 3]] code (see Fig. 3.6), however the implementation is slightly different from CNOT_L and H_L:

$$S_L = S_1^\dagger \dots S_7^\dagger. \tag{3.80}$$

Instead of applying S to every qubits, $S^\dagger$ must be applied.

It is important for the preservation of the stabilizer group that all the stabilizer generators are weight 4. The $S^\dagger$-gate changes X to $-Y = -iXZ$, so for the stabilizers we get:

$$\begin{aligned} S_L: \quad & S_X^{(i)} \to (-i)^4 S_X^{(i)} S_Z^{(i)} = S_X^{(i)} S_Z^{(i)} && (3.81)\\ & S_Z^{(i)} \to S_Z^{(i)} && (3.82) \end{aligned}$$

Logical Y_L for the [[7, 1, 3]] code can be written in the following form:

$$Y_L = iX_L Z_L = iX_1 Z_1 \dots X_7 Z_7. \tag{3.83}$$

The logical Paulis change accordingly:

$$S_L: \quad X_1 \dots X_7 \to (-i)^7 X_1 Z_1 \dots X_7 Z_7 = iX_1 Z_1 \dots X_7 Z_7 \tag{3.84}$$
$$Z_1 \dots Z_7 \to Z_1 \dots Z_7 \tag{3.85}$$

which is exactly what the logical S_L should do since the S-gate changes X to $Y = iXZ$. This is the reasons why the logical S_L actually consists of $S^\dagger$ gates.

Summarizing, the whole Clifford group can be implemented in the [[7, 1, 3]] as transversal gates (see Fig. 3.6). Transversal implementations are often easy to implement experimentally and are very useful for fault-tolerance aspects as will be discussed in Sec. 3.7.

3.6.2 Logical state preparation

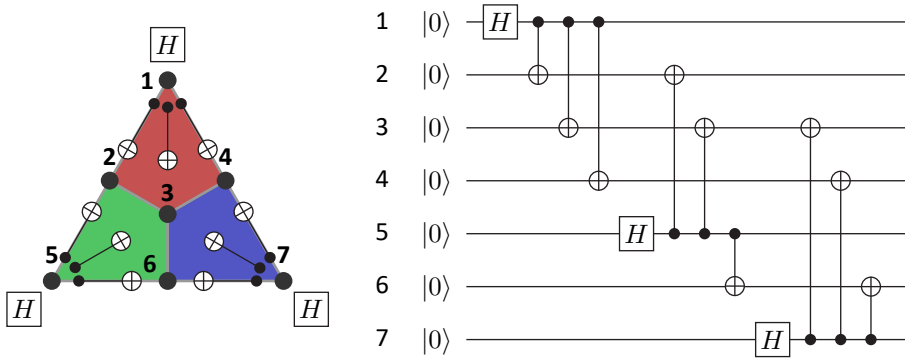

Figure 3.7: Quantum circuit used to prepare the $|0\rangle_L$ state for the [[7, 1, 3]] code.

We can use the method described in Sec. 3.4.2 to prepare the $|0\rangle_L$ state for the [[7, 1, 3]] code. If we apply Eq. (3.44) we get:

$$|0\rangle_L = a(I + S_X^{(1)})(I + S_X^{(2)})(I + S_X^{(3)})(I + S_Z^{(1)})(I + S_Z^{(2)})(I + S_Z^{(3)}) \, |0000000\rangle \, . \tag{3.86}$$

$|0000000\rangle$ is already a $+1$ eigenstate of any $S_Z^{(i)}$, so it is also a $+1$ eigenstate of $I + S_Z^{(i)}$:

$$|0\rangle_L = a'(I + S_X^{(1)})(I + S_X^{(2)})(I + S_X^{(3)}) \, |0000000\rangle \, . \tag{3.87}$$

The operation $I + X_1 \dots X_m$ can be implemented with gates in the following way:

$$\frac{1}{\sqrt{2}}(I + X_1 \dots X_m) \, |0 \dots 0\rangle = \frac{1}{\sqrt{2}}(|0 \dots 0\rangle + |1 \dots 1\rangle)$$
$$= \mathrm{CNOT}_{1,1} \dots \mathrm{CNOT}_{1,m} H_1 \, |0 \dots 0\rangle \, . \tag{3.88}$$

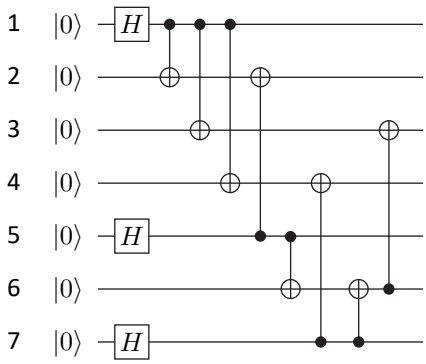

Figure 3.8: Simplified quantum circuit used to prepare the $|0\rangle_L$ state for the [[7, 1, 3]] code. The circuit is equivalent to the one in Fig. 3.7.

Finally, we can use the circuit in Fig. 3.7 to prepare $|0\rangle_L$ for the [[7, 1, 3]] code. This circuit can be simplified a bit to use one fewer CNOT-gate. The equivalent circuit is shown in Fig. 3.8. Other logical cardinal states can be obtained by applying the respective logical operations to $|0\rangle_L$:

$$\begin{aligned} |+\rangle_L &= H_L |0\rangle_L , & |+i\rangle_L &= S_L H_L |0\rangle_L , \\ |1\rangle_L = X_L |0\rangle_L , \quad |-\rangle_L &= Z_L H_L |0\rangle_L , & |-i\rangle_L &= S_L Z_L H_L |0\rangle_L . \end{aligned} \tag{3.89}$$

3.6.3 Error correction

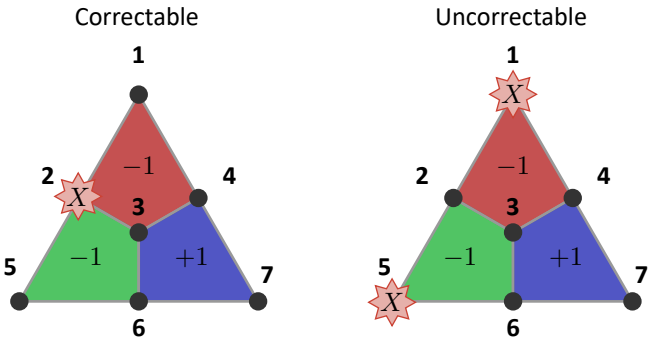

Figure 3.9: An example of a correctable and an uncorrectable error for the [[7, 1, 3]] code. Z-stabilizers yield the same error syndrome for both errors. Weight-1 errors can be corrected, weight-2 can not.

The error correction capabilities of the [[7, 1, 3]] code are defined by its stabilizer group. The following properties can be noted to simplify the considerations. The [[7, 1, 3]] code can correct an arbitrary weight-1 error as a distance-3 code. The [[7, 1, 3]] code is a CSS code: X- and Z-stabilizer generators are not mixed between each other. Therefore, X- and Z-errors can be treated separately: Z-stabilizers can detect X-errors and vice versa. Additionally, the [[7, 1, 3]] code is a self-dual CSS code, i.e. X- and Z-stabilizers have the same support. It follows that X- and Z-errors are treated analogously, hence it is enough to consider only one type of errors, e.g. X-errors.

Let us consider the examples in Fig. 3.9. If an X-error happens on qubit 2, it can be detected by stabilizers $S_Z^{(1)}, S_Z^{(2)}$ since they anticommute with the error, while the others commute. There is only one weight-1 error that can lead to this syndrome, thus it can be uniquely identified. The inverse of the error can be applied to correct it, i.e. X_2. The procedure for Z-errors and X-stabilizers is exactly the same. Other weight-1 errors can be identified and corrected according to the lookup table in Tab. 3.1.

However, a weight-2 X-error on qubits 1 and 5 leads to the same error syndrome. It can be misinterpreted as the X_2 error and, after the correction is applied, the total error will be $X_1X_2X_5$. This final error is stabilizer-equivalent to the logical $X_L = X_1X_2X_5S_X^{(3)}$ and the logical state will be corrupted. This illustrates that the [[7, 1, 3]] code can not correct some weight-2 errors.

Table 3.1: Lookup table for the [[7, 1, 3]] code. Z-stabilizers detect X-errors and vice versa.

Syndrome $(S_{Z/X}^{(1)}, S_{Z/X}^{(2)}, S_{Z/X}^{(3)})$	Error
$(1, 0, 0)$	X_1/Z_1
$(0, 1, 0)$	X_5/Z_5
$(0, 0, 1)$	X_7/Z_7
$(1, 1, 0)$	X_2/Z_2
$(1, 0, 1)$	X_4/Z_4
$(0, 1, 1)$	X_6/Z_6
$(1, 1, 1)$	X_3/Z_3

3.7 Fault tolerance

The idea behind QEC is to protect logical information from a noisy environment or faulty hardware control by doing some additional operations, e.g. redundant encoding, stabilizer measurements, and corrections. However, these operations can be faulty themselves since they are subject to the same noise. The idea of fault tolerance (FT) is to design the QEC procedures in such a way that QEC can be still beneficial despite the fact that error correction procedures can be erroneous themselves.

3.7.1 Error propagation

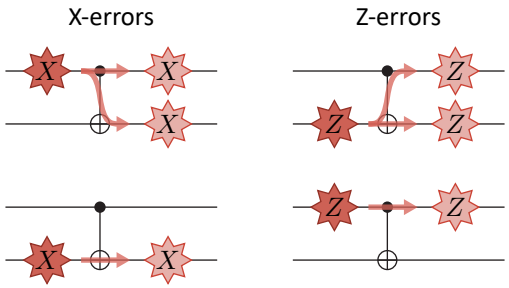

Figure 3.10: Error propagation for Pauli errors through a CNOT-gate.

Many challenges stem from the property of multi-qubit gates (and other operations, e.g. mid-circuit measurement) to proliferate errors. Let us have a look at the action of the CNOT-gate on Pauli errors (see Eq. (3.14) in Sec. 3.3). If a weight-1 Pauli error takes place before the CNOT-gate, it may result in a weight-2 error if we commute it through the CNOT-gate (see Fig. 3.10). This means that our additional actions taken to implement error correction can actually increase the error weight. Eventually, that can lead to uncorrectable errors if our code is incapable of dealing with higher-weight errors. FT protocols should be built in such a way that this error propagation does not lead to uncorrectable errors or at least this can be identified. In the following we will consider some examples of FT circuit design for the $[[7, 1, 3]]$ code.

3.7.2 Logical state preparation

The state preparation procedure for the $[[7, 1, 3]]$ code illustrated in Fig. 3.8 is vulnerable to dangerous error propagation. If a weight-1 X-error happens at one of the locations in Fig. 3.11, it will propagate to a weight-2 error which is not correctable for the $[[7, 1, 3]]$ code. One way to tackle this problem is so-called 'flag' qubits [67]. We can take an auxiliary qubit and map the logical $Z'_L = Z_2Z_4Z_6 = Z_L S_Z^{(1)} S_Z^{(2)} S_Z^{(3)}$ operator to this auxiliary qubit. If no errors occur, the prepared state $|0\rangle_L$ is an eigenstate of Z'_L so the auxiliary qubit will not be flipped. However, if one of the

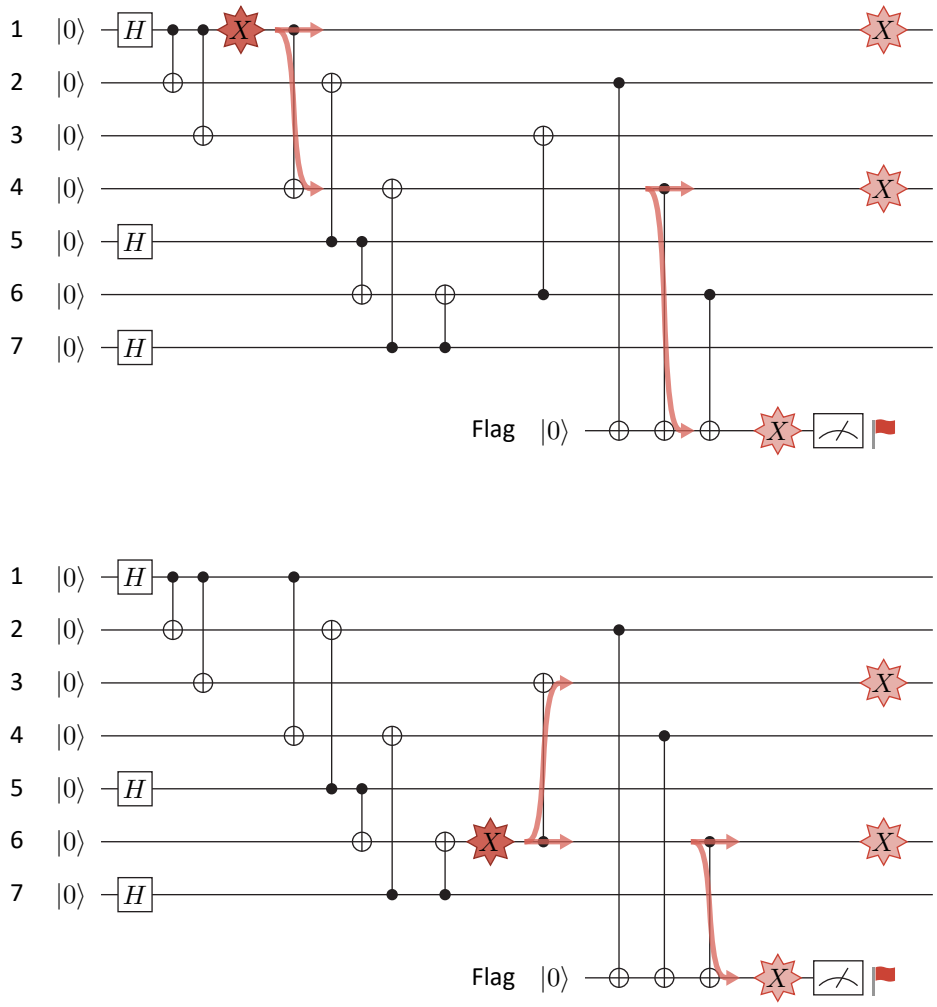

Figure 3.11: Modified version of the circuit in Fig. 3.8. The flag qubit catches dangerous error propagation with an additional Z_L measurement.

two errors in Fig. 3.11 happens, it will also propagate to the auxiliary qubit and flip it. The auxiliary qubit will flag a dangerous error, hence the name.

Once the auxiliary qubit flags, one can either discard the state and start over or perform additional measurements to figure out which dangerous error happened and correct it. In experimental results of this work whenever the circuit flags, the run is discarded and we start over.

3.7.3 Logical gates

Application of a logical gate can propagate errors and increase the error weight. However, if a logical gate implementation is transversal, there is no dangerous error propagation since there are no multi-qubit gates between physical qubits of the same logical qubit, e.g. all the physical gates are applied qubit-wise (see Fig. 3.12). The errors can still propagate in case of a two-qubit gate, but it will propagate to another logical qubit. For example in Fig. 3.12 both logical qubits will only have a weight-1

error on each, which is correctable for the $[[7, 1, 3]]$ code.

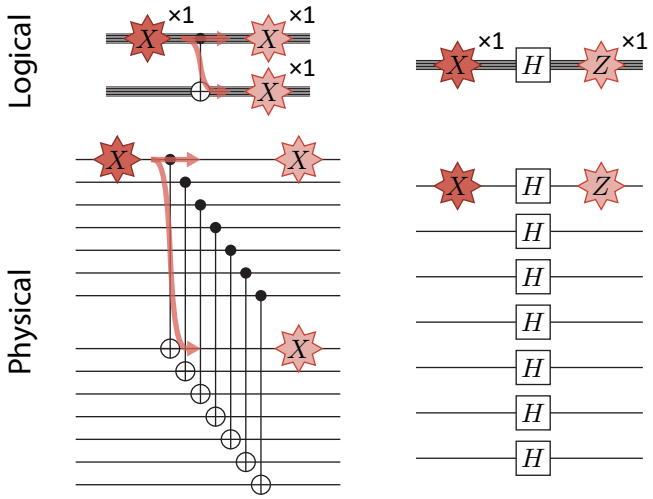

Figure 3.12: Error propagation for transversal implementations of logical gates.

Therefore, transversal logical gate implementations are preferable since they are intrinsically fault-tolerant. The $[[7, 1, 3]]$ code allows one to implement the entire Clifford group transversally, but the Clifford group is not enough for a universal gate set (see Sec. 3.3). The T-gate can be added to the Clifford group to form a universal gate set, but it does not have a transversal implementation for the $[[7, 1, 3]]$ code. Moreover, the Eastin-Knill theorem [68] states that no QEC code can have a transversal implementation of a universal gate set.

This means that at least one of the gates from the universal gate set must be implemented in a non-transversal fashion. There are various ideas how this can be done fault-tolerantly including magic state injection [69, 70], lattice surgery [71, 72] and code switching [61, 62]. All these approaches fulfill fault-tolerance requirements at the cost of large gate/qubit overhead. Experimental magic state injection and code switching results will be presented in this work in Sec. 7.

3.7.4 Stabilizer measurement

Error propagation problems also affect stabilizer measurements (see Sec. 3.4.1), which is one of the most common operations in QEC with stabilizer codes. Let us consider an example: measuring the $S_X^{(3)}$ stabilizer for the $[[7, 1, 3]]$ code with the Hadamard test (see Fig. 3.13). The auxiliary qubit is used to map the stabilizer expectation value, but an error on the auxiliary qubit can propagate back to the data qubits and results in an uncorrectable configuration. The same approach (see Sec. 3.7.2) with flag qubits [67] can be used here. One flag qubit can be added and connected to the auxiliary qubit for the stabilizer mapping to catch dangerous error propagation. If the flag qubit is flipped, the measurement should be discarded or additional measurements should be performed to determine which error happened exactly.

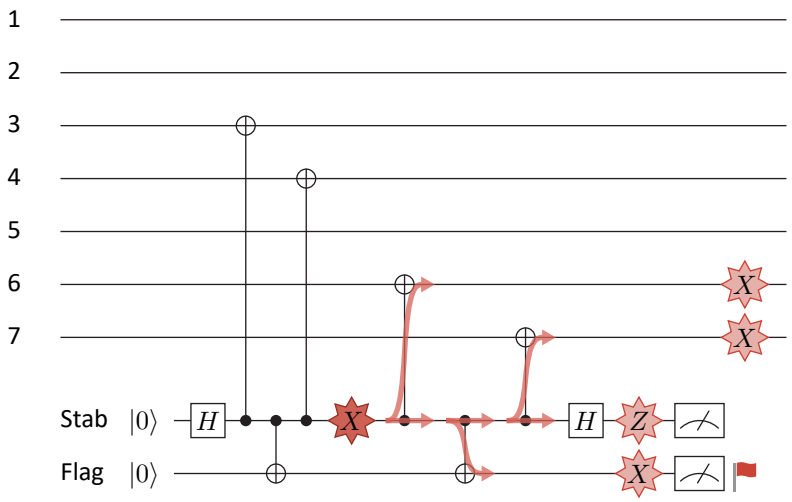

Figure 3.13: Error propagation for the measurement of the $S_X^{(3)}$ stabilizer for the $[[7, 1, 3]]$ code with the Hadamard test. The flag qubit catches dangerous error propagation.

In this particular example all the stabilizers needed for the error syndrome should be measured in the same way with flags. However, there are more sophisticated ways to measure an error syndrome in a fault-tolerant way, e.g. a self-flagging scheme [73] which is based on the same principle, but three stabilizers are measured simultaneously serving as flags for each other. This scheme requires fewer auxiliary qubits.

Chapter 4

Trapped ion basics

Various physical platforms can be used for quantum information processing [74]: superconducting quantum systems, trapped ions, neutral atoms, quantum dots, and many others. A physical platform encoding quantum information should possess certain features to make a good quantum computer [75] such as the following: the encoded information can be manipulated to perform required computations, the encoded information can be preserved when the system is left alone, and the information can be read out.

In this work, trapped ions are used as the physical basis for quantum information processing. Each trapped ion serves as a qubit and their electronic and motional states are manipulated with laser light. This chapter describes the main physical principles governing the behavior of trapped ions interacting with laser light and how they lead to the desired quantum computing operations.

4.1 Paul trap

The experimental setup used in this work features a blade Paul trap [76] for ion trapping. It consists of four blades and two end-caps (see Fig. 4.1). Two opposing blades are supplied with a radio frequency (RF) electric field while the two other blades are grounded. The frequency of the RF field usually lies in the range $[1, 100]$ MHz. The end-caps have a static voltage (DC) applied to them. The voltages are usually chosen such that the RF confinement is much stronger than the DC one. Therefore, ions align in a linear chain along the z-axis. A detailed description of Paul traps can be found in Ref. 76, 77, 78.

4.2 Normal modes of an ion chain

The number of ions (qubits) in a Paul trap can be scaled by loading more ions to the trapping potential. The ions trapped in a Paul trap in a single trapping potential will align along one of the axis of the trap forming an 'ion crystal' (also called 'ion chain') provided the trapping parameters are correct. The common motion of the ions in the ion chain is often used to mediate interaction between ions to implement two-qubit gates. Therefore, it is important to consider normal motional modes of the ion chain in a single trapping potential.

Let us consider a system of N ions of mass m and charge q in a harmonic trapping potential, which is an approximation for the real trapping potential created

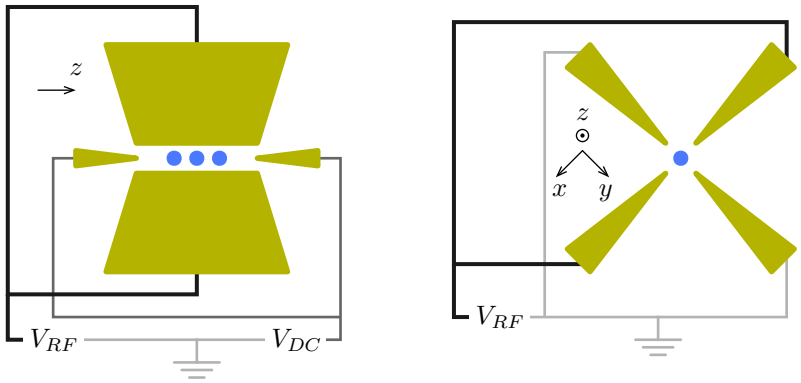

Figure 4.1: Sketch of a blade Paul trap. View along the bisector of the x-y-axes angle (left) and view along the z-axis (right).

in the experiment. The harmonic trapping potential is described by three frequencies $\omega_x, \omega_y, \omega_z$ along orthogonal axes. The confinement along the z-axis is assumed to be much weaker, i,e. $\omega_z \ll \omega_x, \omega_y$. We will also consider the confinement along the x- and y-axes to be equally strong $\omega_x = \omega_y \equiv \omega_{x/y}$. In the experiment $\omega_z \approx 2\pi \times 400\,\mathrm{kHz}$, while $\omega_{x/y} \approx 2\pi \times 3000\,\mathrm{kHz}$.

The potential energy V of the system can be described as follows [79]:

$$V = \frac{1}{2} m \sum_{j=1}^{N} \sum_{i \in \{x,y,z\}} \omega_i^2 {r_i^{(j)}}^2 + \frac{q^2}{8\pi\epsilon_0} \sum_{j \neq j'} \frac{1}{\sqrt{\sum\limits_{i \in \{x,y,z\}} (r_i^{(j)} - r_i^{(j')})^2}}, \tag{4.1}$$

where $r_i^{(j)}$ is a coordinate of ion j along the i-axis. Equilibrium positions $\bar{r}_i^{(j)}$ of the ions can be found from the following system of equations:

$$\frac{\partial V}{\partial r_i^{(j)}}\Big|_{\vec{r}=\vec{\bar{r}}} = 0, \qquad \forall i \in x, y, z, \forall j \in \{1, \ldots, N\}. \tag{4.2}$$

It is valid to assume that the ions will align along the z-axis due to the high anisotropy of the trapping potential [80, 81], i.e. $r_{x,y}^{(j)} = 0$. Dimensionless coordinates can be used for the sake of convenience:

$$u^{(j)} = \bar{r}_z^{(j)}/l, \qquad l = \left(\frac{q^2}{4\pi\epsilon_0 m \omega_z^2}\right)^{1/3}. \tag{4.3}$$

The dynamics of the system must be considered to describe the normal motional modes. The displacement of ion j from its equilibrium position $\xi_i^{(j)}$ can be introduced as follows:

$$r_i^{(j)}(t) = \bar{r}_i^{(j)} + \xi_i^{(j)}(t). \tag{4.4}$$

Then, the Lagrangian of the system can be written as:

$$L = T - V = \frac{1}{2}m\left[\sum_{j=1}^{N}\sum_{i\in\{x,y,z\}}\left(\dot{\xi}_i^{(j)}\right)^2 - \omega_i^2\left(\bar{r}_i^{(j)} + \xi_i^{(j)}\right)^2\right] - \frac{q^2}{8\pi\epsilon_0}\sum_{j\neq j'}\left[\sum_{i\in\{x,y,z\}}\left(r_i^{(j)} + \xi_i^{(j)} - r_i^{(j')} - \xi_i^{(j')}\right)^2\right]^{-1/2}. \quad (4.5)$$

After a Taylor expansion around the equilibrium positions the Lagrangian can be approximated as:

$$L \approx V_0 + \frac{1}{2}m\left[\sum_{j=1}^{N}\left(\dot{\xi}_z^{(j)}\right)^2 - \omega_z^2\sum_{j,j'=1}^{N}A_{jj'}\xi_z^{(j)}\xi_z^{(j')}\right] + \frac{1}{2}m\sum_{i\in x,y}\left[\sum_{j=1}^{N}\left(\dot{\xi}_i^{(j)}\right)^2 - \omega_z^2\sum_{j,j'=1}^{N}B_{jj'}\xi_i^{(j)}\xi_i^{(j')}\right] + \mathcal{O}\left(\xi^3\right), \quad (4.6)$$

with V_0 being the constant part of the potential energy and the coefficients $A_{jj'}, B_{jj'}$ calculated from the second partial derivatives of the potential energy V [79]:

$$A_{jj'} = \begin{cases} 1 + 2\sum_{k\neq j}\frac{1}{|u^{(j)} - u^{(k)}|^3}, & j = j' \\ -\frac{2}{|u^{(j)} - u^{(j')}|^3}, & j \neq j' \end{cases}, \quad (4.7)$$

$$B_{jj'} = \left(\frac{\omega_{x/y}^2}{\omega_z^2} + \frac{1}{2}\right)\delta_{jj'} - \frac{1}{2}A_{jj'}. \quad (4.8)$$

The matrix $A_{jj'}$ describing normal modes along the z-axis is real, symmetric and positive definite, and has positive eigenvalues μ_p and eigenvectors $c_p^{(j)}$:

$$\sum_{j'=1}^{N}A_{jj'}c_p^{(j')} = \mu_p c_p^{(j)}. \quad (4.9)$$

On the other hand, the matrix $B_{jj'}$ describing normal modes along the x- and y-axes has the same eigenvectors $c_p^{(j)}$, but different eigenvalues γ_p:

$$\sum_{j'=1}^{N}B_{jj'}c_p^{(j')} = \gamma_p c_p^{(j)}, \quad (4.10)$$

$$\gamma_p = \frac{\omega_{x/y}^2}{\omega_z^2} + \frac{1}{2} - \frac{\mu_p}{2}. \tag{4.11}$$

If one of the eigenvalues γ_p is negative, the ion chain configuration is unstable and a 'zig-zag' structure [82] (or other nonlinear structure) is formed.

We will refer to the normal modes along the z-axis as 'axial' modes and to the normal modes along the x- and y-axes as 'radial' modes. The mode frequencies can be calculated from the eigenvalues as follows:

$$\omega_{z,p} = \omega_z \sqrt{\mu_p}, \tag{4.12}$$
$$\omega_{x,p} = \omega_z \sqrt{\gamma_p}, \tag{4.13}$$
$$\omega_{y,p} = \omega_z \sqrt{\gamma_p}. \tag{4.14}$$

The spectrum of the motional modes of a 16-ion chain for $\omega_z = 2\pi \times 400\,\text{kHz}$ and $\omega_{x/y} = 2\pi \times 3000\,\text{kHz}$ is given in Fig. 4.2. The radial mode spectrum is particularly important for the two-qubit gate considerations in the experiment in Ch. 6.

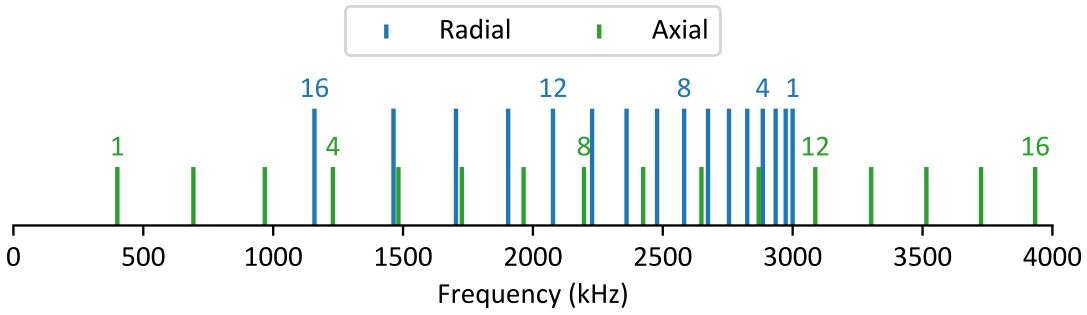

Figure 4.2: Spectrum of the motional modes of a 16-ion chain for $\omega_z = 2\pi \times 400\,\text{kHz}$ and $\omega_{x/y} = 2\pi \times 3000\,\text{kHz}$. Numbers above lines show mode indices.

4.3 $^{40}Ca^{+}$ ions

$^{40}Ca^{+}$ ions are trapped in the Paul trap in this work. The energy level structure of $^{40}Ca^{+}$ is shown in Fig. 4.3. The dipole-allowed transition $4^2S_{1/2} \leftrightarrow 4^2P_{1/2}$ at 397 nm is used for Doppler cooling and detection. 866 nm laser light can be used during Doppler cooling and detection to prevent population trapping in the $3^2D_{3/2}$ state.

The qubit is encoded in Zeeman sub-levels of the ground state $4^2S_{1/2}$ and the metastable $3^2D_{5/2}$ state ($|0\rangle = |4^2S_{1/2}, m_j = -1/2\rangle$, $|1\rangle = |3^2D_{5/2}, m_j = -1/2\rangle$) to ensure the lowest sensitivity of the qubit transition frequency to magnetic field fluctuations. The qubit transition is exited with narrow-line 729 nm laser light. 854 nm laser light allows for lifetime quenching of the $3^2D_{5/2}$ level resulting in a quick qubit 'reset'. Other Zeeman sub-levels can be used for optical pumping, resolved sideband cooling, and electron shelving techniques [83].

This type of qubit is called an 'optical qubit' since the qubit transition frequency lies in the optical domain. $^{40}Ca^{+}$ also allows for a 'Zeeman qubit', i.e. a qubit that is encoded in two Zeeman sub-levels of the ground level $4^2S_{1/2}$. Other species with non-zero nuclear spin also offer the option of 'hyperfine qubits' encoded in the sub-levels of the hyperfine structure of the respective ground states [84].

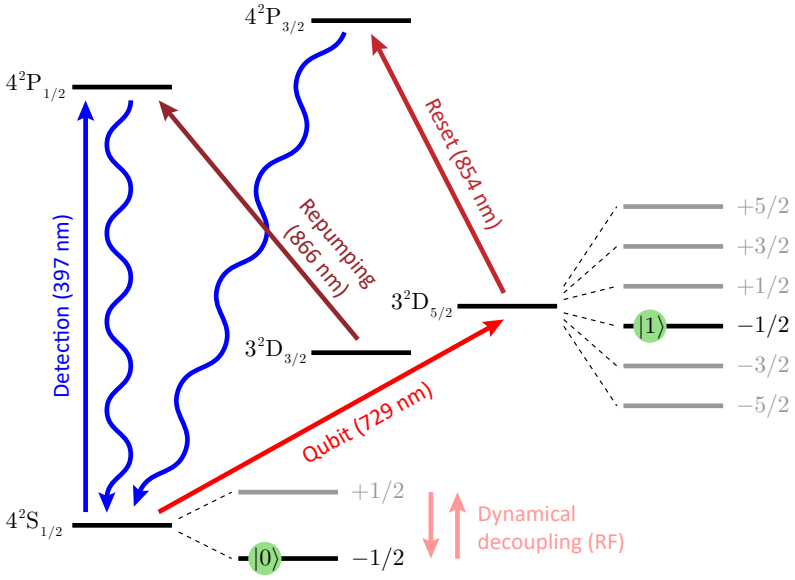

Figure 4.3: $^{40}Ca^{+}$ energy levels structure.

4.4 Qubit state manipulation

One of the central parts of quantum computing is qubits manipulation, i.e. changing the qubits' state in a controllable way. Optical qubits encoded in $^{40}Ca^{+}$ in our setup are manipulated with pulses of 729 nm laser light.

This section describes the theoretical background for the interaction between the ions in the trap and the laser light used to manipulate the ions [77]. Ions are considered as two-level systems, the trapping potential is assumed to be harmonic, and the laser light is treated as a classical planar wave throughout the section. The main goal of the section is to show how the models of the physical mechanisms governing the interaction lead to the desired gate operations with the qubits: single-qubit gates and two-qubit gates (see Sec. 2.2).

4.4.1 Laser-ion interaction

The Hamiltonion of the laser-ion system consists of two parts:

$$H_{L\text{-}i} = H_L + H_i. \tag{4.15}$$

The ion can be consider a qubit, i.e. a two-level system with energy separation $\hbar\omega_i$:

$$H_i = \frac{\hbar\omega_i}{2}\sigma_z. \tag{4.16}$$

The laser light is assumed to be a monochromatic planar wave with wave vector $\vec{k}$, frequency ω_L and phase ϕ_L. For now, the spatial component of the laser light can be omitted and the interaction with the ion can be described as follows:

$$H_L = \frac{1}{2}\hbar\Omega\left(\sigma_+ + \sigma_-\right)\left(e^{-i(\omega_L t+\phi_L)} + e^{i(\omega_L t+\phi_L)}\right), \tag{4.17}$$

where $\sigma_\pm = (\sigma_x \pm i\sigma_y)/2$ and Ω describes the coupling strength between the ion and the laser light. The coupling strength can be adjusted by regulating the intensity of the laser light.

The total Hamiltonian $H_{L\text{-}i}$ can be rewritten in the interaction picture using the ion Hamiltonian: $H^{int}_{L\text{-}i} = U_i^\dagger H_{L\text{-}i} U_i$ with $U_i = e^{-iH_i t/\hbar}$. The rotating wave approximation (RWA) can be applied, i.e. the terms rotating at high frequency $\omega_L + \omega_i$ are omitted. This results in the following Hamiltonian:

$$H^{int}_{L-i} = \frac{1}{2}\hbar\Omega\left(\sigma_+ e^{-i(\Delta t+\phi_L)} + h.c.\right), \tag{4.18}$$

where $\Delta = \omega_L - \omega_i$.

There are two relevant cases to consider here:

- **Resonant interaction**, $\Delta = 0$

  $$H^{int}_{L-i} = \frac{1}{2}\hbar\Omega\left(\sigma_x\cos\phi_L + \sigma_y\sin\phi_L\right) \tag{4.19}$$

  If the laser is resonant with the qubit transition, the evolution is identical to the action of the R-gate:

  $$R(\theta,\phi) = e^{-iH^{int}_{L-i}t/\hbar} = \begin{pmatrix} \cos\dfrac{\theta}{2} & -ie^{-i\phi}\sin\dfrac{\theta}{2} \\ -ie^{i\phi}\sin\dfrac{\theta}{2} & \cos\dfrac{\theta}{2} \end{pmatrix}, \tag{4.20}$$

  where $\theta = \Omega t$. This is a rotation around an axis in the x-y plane of the Bloch sphere. The axis is set by the phase of the laser pulse $\phi = \phi_L$, while the length of the pulse t sets the rotation angle θ. The laser pulse which results in $\theta = \pi$ is often called a 'π-pulse'.

  Resonant interaction will be used as a main mechanism for single-qubit X/Y-rotations.

- **Far off-resonant interaction**, $\Delta \gg \Omega$

  If the laser is detuned far from the qubit transition, the excitation of the qubit transition will be negligible, but the energy levels of the qubit will be shifted by an amount

  $$\Delta E = \pm\frac{1}{4}\hbar\frac{\Omega^2}{\Delta}. \tag{4.21}$$

This interaction results in an AC-Stark shift:

$$\Delta\omega_{AC} = \frac{1}{2}\frac{\Omega^2}{\Delta}. \tag{4.22}$$

The AC-Stark shift leads to an effective rotation around the z-axis of the Bloch sphere:

$$R_z(\theta) = \begin{pmatrix} 1 & 0 \\ 0 & e^{i\theta} \end{pmatrix}, \tag{4.23}$$

where $\theta = \Delta\omega_{AC}t$. This mechanism is important to consider when off-resonant laser interactions are hard to avoid, for example, when implementing a two-qubit gate with optical qubits.

However, using an AC-Stark shift to implement a single-qubit z-rotation will introduce some errors, as any physical operation will. Alternatively, one can change the phases of the subsequent R-gates instead of physically applying an R_z-gate [85]. This is based on the fact that

$$R_z(\theta_z)R(\theta,\phi)R_z^\dagger(\theta_z) = \begin{pmatrix} \cos\frac{\theta}{2} & -ie^{-i(\phi+\theta_z)}\sin\frac{\theta}{2} \\ -ie^{i(\phi+\theta_z)}\sin\frac{\theta}{2} & \cos\frac{\theta}{2} \end{pmatrix} = R(\theta,\phi+\theta_z). \tag{4.24}$$

Such 'virtual' rotation will be used as the main mechanism for single-qubit Z-rotations since this operations has near-perfect fidelity limited but the phase resolution of the control electronics.

4.4.2 Laser-ion-trap interaction

The fact that the ions are confined by the trapping potential can be taken into account by adding the harmonic potential of the trap to the Hamiltonian:

$$H_{L-i-t} = H_L^{trap} + H_i + H_t, \tag{4.25}$$

$$H_t = \hbar\omega_x\left(a^\dagger a + \frac{1}{2}\right), \tag{4.26}$$

where $a^\dagger, a$ are phonon creation and annihilation operators for the motional mode of the ion crystal, $n = a^\dagger a$ is the phonon number operator for the mode and ω_x is the mode frequency. Here the trapping potential is assumed to be one-dimensional along the x-axis and only one motional mode of the ion crystal is considered. The state of the system is now described as a joint state of the qubit system and the phonon mode $|\psi\rangle = |q,n\rangle$ with $q \in \{0,1\}$ and $n \in \{0\} \cup \mathbb{N}$.

The spatial component of the laser light along the x-axis should be taken into account due to the spatial dependency of the trapping potential and the Hamiltonian in Eq. (4.17) changes as follows:

$$H_L^{trap} = \frac{1}{2}\hbar\Omega\left(\sigma_+ + \sigma_-\right)\left(e^{-i(\omega_L t+\phi_L-k_x\hat{x})} + e^{i(\omega t+\phi_L-k_x\hat{x})}\right) \tag{4.27}$$

where $\hat{x} = x_0(a^\dagger + a)$, $x_0 = \sqrt{\frac{\hbar}{2m\omega_x}}$ and k_x is the projection of the wave vector onto the x-axis. If we introduce the Lamb-Dicke parameter $\eta = k_x x_0$, change to the interaction picture with $U_{i\text{-}t} = e^{-i(H_i+H_t)t/\hbar}$ and apply the RWA the Hamiltonian transforms into

$$H^{int}_{L-i-t} = \frac{1}{2}\hbar\Omega\left(\sigma_+ e^{-i(\Delta t+\phi_L)} e^{i\eta(a^\dagger e^{i\omega_x t}+ae^{-i\omega_x t})} + h.c.\right). \tag{4.28}$$

Typical values for the Lamb-Dicke parameter in the current experiment lie in [0.054, 0.078] for radial motional modes in a 16-ion chain and the addressing laser beam (729 nm) coming at a 90° angle. Therefore, it is reasonable to assume the Lamb-Dicke regime [77] ($\eta\sqrt{2n+1} \ll 1$) and use a Taylor expansion for the spatial part of the Hamiltonian:

$$H^{int}_{L-i-t} = \frac{1}{2}\hbar\Omega\left(\sigma_+ e^{-i(\Delta t+\phi_L)}\left(1 + i\eta\left(a^\dagger e^{i\omega_x t} + ae^{-i\omega_x t}\right) + \mathcal{O}\left(\eta^2\right)\right) + h.c.\right). \tag{4.29}$$

Three resonant transitions with different Rabi frequencies can be noted here, depending on the laser detuning:

1. **Carrier transition**, $\Delta = 0$, $|0,n\rangle \leftrightarrow |1,n\rangle$

   $H_{Car} = \frac{1}{2}\hbar\Omega\left(\sigma_+ e^{-i\phi_L} + \sigma_- e^{i\phi_L}\right)$

   $\Omega_{Car} = \Omega$

   The second order of the Taylor expansion gives the leading correction for the carrier transition Rabi frequency:

   $\Omega^{(2)}_{Car} = \Omega\left(1 - n\eta^2\right)$

2. **Red-sideband (RSB) transition**, $\Delta = -\omega_x$, $|0,n\rangle \leftrightarrow |1,n-1\rangle$

   $H_{RSB} = \frac{i}{2}\hbar\eta\Omega\left(\sigma_+ a e^{-i\phi_L} - \sigma_- a^\dagger e^{i\phi_L}\right)$

   $\Omega_{RSB} = \Omega\sqrt{n}\eta$

   If the motional mode is cooled to the ground state ($n = 0$), the RSB transition can not be excited.

3. **Blue-sideband (BSB) transition**, $\Delta = +\omega_x$, $|0,n\rangle \leftrightarrow |1,n+1\rangle$

   $H_{BSB} = \frac{i}{2}\hbar\eta\Omega\left(\sigma_+ a^\dagger e^{-i\phi_L} - \sigma_- a e^{i\phi_L}\right)$

   $\Omega_{BSB} = \Omega\sqrt{n+1}\eta$

4.4.3 Bichromatic light and MS gate

The Mølmer-Sørensen (MS) interaction [46] can be used to create entanglement between two (or more) ions. Let us consider a system with two ions in a harmonic trapping potential with mode frequency ω_x. The two ions are illuminated with a bichromatic laser beam with frequencies close (detuned by δ) to the RSB and BSB

transitions: $\Delta_- = -\omega_x - \delta$ and $\Delta_+ = +\omega_x + \delta$. The phases of the tones are ϕ_- and ϕ_+ respectively. These two tones lead to the respective Hamiltonians:

$$H_- = \frac{i}{2}\hbar\eta\Omega\left(\left(\sigma_+^{(1)} + \sigma_+^{(2)}\right) a e^{i(\delta t - \phi_-)} - \left(\sigma_-^{(1)} + \sigma_-^{(2)}\right) a^\dagger e^{-i(\delta t - \phi_-)}\right) \tag{4.30}$$

$$H_+ = \frac{i}{2}\hbar\eta\Omega\left(\left(\sigma_+^{(1)} + \sigma_+^{(2)}\right) a^\dagger e^{-i(\delta t + \phi_+)} - \left(\sigma_-^{(1)} + \sigma_-^{(2)}\right) a e^{i(\delta t + \phi_+)}\right) \tag{4.31}$$

The total Hamiltonian is a sum of these two:

$$H_{bichro} = H_- + H_+. \tag{4.32}$$

This expression can be conveniently split into qubit and motional components if we make a substitution:

$$\phi_+ = \phi_q + \phi_m - \frac{\pi}{2}, \qquad \phi_- = \phi_q - \phi_m - \frac{\pi}{2}. \tag{4.33}$$

Then the expression transforms into

$$H_{bichro} = -\frac{1}{2}\hbar\eta\Omega\left(\sigma_+^{(1)} e^{-i\phi_q} + \sigma_-^{(1)} e^{i\phi_q} + \sigma_+^{(2)} e^{-i\phi_q} + \sigma_-^{(2)} e^{i\phi_q}\right) \left(a e^{i(\delta t + \phi_m)} + a^\dagger e^{-i(\delta t + \phi_m)}\right) \tag{4.34}$$

$$H_{bichro} = -\frac{1}{2}\hbar\eta\Omega\left(\sigma_x^{(1)}\cos\phi_q + \sigma_y^{(1)}\sin\phi_q + \sigma_x^{(2)}\cos\phi_q + \sigma_y^{(2)}\sin\phi_q\right) \left(a e^{i(\delta t + \phi_m)} + a^\dagger e^{-i(\delta t + \phi_m)}\right) \tag{4.35}$$

$$H_{bichro} = -\frac{1}{2}\hbar\eta\Omega\left(\sigma_{\phi_q}^{(1)} + \sigma_{\phi_q}^{(2)}\right)\left(a e^{i(\delta t + \phi_m)} + a^\dagger e^{-i(\delta t + \phi_m)}\right), \tag{4.36}$$

where $\sigma_\phi^{(i)} = \sigma_x^{(i)}\cos\phi + \sigma_y^{(i)}\sin\phi$. Now, let us consider the configuration which is used for the MS gate, used as a two-qubit gate in the setup. The phases of the tones $\phi_\pm$ can be chosen such that $\phi_q = \pi$ and $\phi_m = 0$. Then the Hamiltonian becomes:

$$H_{MS} = \frac{1}{2}\hbar\eta\Omega\left(\sigma_x^{(1)} + \sigma_x^{(2)}\right)\left(a e^{i\delta t} + a^\dagger e^{-i\delta t}\right). \tag{4.37}$$

It can be shown [86, 87] that the evolution of the system under this Hamiltonian is described by the following unitary:

$$U_{MS}(t) = D(\alpha(t)S_x)e^{i\varphi(t)S_x^2}, \tag{4.38}$$

where $S_x = \sigma_x^{(1)} + \sigma_x^{(2)}$ and the displacement operator $D(\alpha) = e^{\alpha a^\dagger - \alpha^* a}$. Here

$$\alpha(t) = \frac{\eta\Omega}{2\delta}\left(e^{i\delta t} - 1\right), \tag{4.39}$$

$$\varphi(t) = \left(\frac{\eta\Omega}{2\delta}\right)^2 (\delta t - \sin\delta t). \tag{4.40}$$

The first component describes the qubit-state-dependent displacement of the motional mode. It has a periodicity of $T = 2\pi/\delta$. The state of the motional mode returns to its initial state at time $t_N = NT$, where N is an integer. This means that if the qubit-mode system state was separable in the beginning it will return to the separable state at $t_N = NT$. This is crucial for the two-qubit gate implementation since otherwise the resulting state of the qubit system will be entangled with the motional mode, which is not desired.

The second component describes the geometric phase accumulated by the qubit state during the interaction. It can also be shown that the accumulated phase is proportional to the area enclosed by the motional mode state trajectory in phase space [46].

If we now consider $t = T$, then $\varphi(T) = 2\pi \left(\frac{\eta\Omega}{2\delta}\right)^2$. The laser power can be chosen such that for a given gate time $t_{gate} = T$ and detuning from the motional mode δ, the accumulated phase $\varphi(t_{gate}) = \pi/8$. This will result in the following propagator:

$$U_{MS}(t_{gate}) = e^{i\frac{\pi}{4}\sigma_x^{(1)}\sigma_x^{(2)}} = \frac{1}{\sqrt{2}} \begin{pmatrix} 1 & 0 & 0 & i \\ 0 & 1 & i & 0 \\ 0 & i & 1 & 0 \\ i & 0 & 0 & 1 \end{pmatrix} = XX\left(-\frac{\pi}{2}\right). \tag{4.41}$$

This unitary is the $XX(-\pi/2)$-gate and it is equivalent to the CNOT-gate up to local rotations as discussed in Sec. 2.2.4.

The MS interaction will be used as the main mechanism for two-qubit gates.

4.4.4 MS gates with multiple motional modes

It is important to consider how the MS interaction changes when several motional modes are present in the ion chain. This becomes increasingly important when the number of ions in the chain grows, since the number of motional modes grows and they usually become closer to each other in frequency.

Let us consider a system of N ions (qubits) and M motional modes illuminated with a bichromatic beam [88–90]. The following Hamiltonian describes the system:

$$H(t) = i\hbar \sum_{j=1}^{N} \sigma_x^{(j)} \sum_{p=1}^{M} \left(\beta_p^{(j)}(t) a_p^\dagger - \beta_p^{(j)}(t)^* a_p\right), \tag{4.42}$$

where j indicates the qubit index, p indicates the mode index and coupling of ion j to mode p is described by

$$\beta_p^{(j)} = \frac{1}{2}\eta_p c_p^{(j)} \Omega(t) e^{i(\delta_p(t)t + \phi(t))}, \tag{4.43}$$

where η_p is the Lamb-Dicke parameter for mode p, $c_p^{(j)}$ is the eigenvector component describing participation of ion j in mode p and δ_p is the detuning of the bichromatic

tones from mode p. The bichromatic light parameters Ω, δ_p, ϕ can be modulated during the gate to ensure the required control when interacting with multiple motional modes.

The Hamiltonian above leads to a propagator (analogously to Eq. (4.38)):

$$U(t) = \exp\left(\sum_{j=1}^{N} \sigma_x^{(j)} B_j(t) + \frac{i}{2}\sum_{j=1}^{N}\sum_{k=1}^{j-1}\left(\varphi^{(j)(k)}(t) + \varphi^{(k)(j)}(t)\right)\sigma_x^{(j)}\sigma_x^{(k)}\right), \tag{4.44}$$

with

$$B_j(t) = \sum_{p=1}^{M} \alpha_p^{(j)}(t) a_p^\dagger - h.c., \tag{4.45}$$

$$\alpha_p^{(j)}(t) = \frac{1}{2}\eta_p c_p^{(j)} \int_0^t dt_1 \Omega(t_1) e^{i(\delta_p(t_1)t_1 + \phi(t_1))}, \tag{4.46}$$

$$\varphi^{(j)(k)}(t) = 2\,\mathrm{Im}\sum_{p=1}^{M}\int_0^t dt_1 \int_0^{t_1} dt_2 \beta_p^{(j)}(t_1)\beta_p^{(k)}(t_2)^*. \tag{4.47}$$

Here $\alpha_p^{(j)}(t)$ is the resulting displacement in phase space of mode p from the interaction with ion j and $\theta^{j\text{-}k}(t) = \varphi^{(j)(k)}(t) + \varphi^{(k)(j)}(t)$ is the geometric phase accumulated by ion pair j-k.

Ideally, for the purpose of the two-qubit gates only two ions with labels j_1 and j_2 participate in the interaction. There are two requirements to be met for a high fidelity XX-gate:

1. All the motional modes should be decoupled at the end of the interaction:
$$\alpha_p^{(j)}(t_{gate}) = 0, \qquad \forall j, p \tag{4.48}$$
2. The accumulated phase should match the desired XX-gate rotation, usually $\pm\frac{\pi}{2}$:
$$\theta^{j\text{-}k}(t_{gate}) = \pm\frac{\pi}{2} \tag{4.49}$$

Usually, some kind of bichromatic light parameters modulation strategy is used to achieve this goal [89–93]. The more modes that should be decoupled, the more complicated the modulation becomes since more free parameters are needed to satisfy all equations for the modes' decoupling. However, if the requirements in Eq. (4.48, 4.49) are met only approximately, the gate fidelity can be estimated as [90]:

$$F = \left[\cos\left(\theta^{j\text{-}k}\left(t_{gate}\right) \pm \frac{\pi}{2}\right)\left(1 - \sum_{p=1}^{M}\left(\alpha_p^{(j_1)}\left(t_{gate}\right)^2 + \alpha_p^{(j_2)}\left(t_{gate}\right)^2\right)\left(n_p + \frac{1}{2}\right)\right)\right]^2, \tag{4.50}$$

where n_p is an average phonon number in the mode p. The fidelity here is the process fidelity defined as in Eq. (2.48).

Interaction with multiple motional modes plays an important role in the experimental implementation of two-qubit gates in this work. The detailed experimental consideration for MS gates will be given in Ch. 6.

Chapter 5

Experimental setup

This chapter describes the experimental setup built in this work. The setup was jointly assembled and commissioned by myself, Thomas Feldker and Christian Marciniak. Many other people contributed to the maintenance and modifications of the setup including Lukas Postler, Michael Meth, Alex Steiner, Robert Freund and others. Some parts of the setup were designed in collaboration with Alpine Quantum Technologies GmbH (AQT), specifically Georg Jacob, Max Hettrich and Oliver Krieglsteiner. The software system controlling the setup was initially developed by Michael Meth and Philipp Schindler, and extended and modified later by myself, Lukas Postler, Michael Meth and others in collaboration with AQT.

5.1 AQTION setup

For a long time the main trapped-ion setup for quantum computing experiments in Innsbruck was the so-called 'LinTrap' setup. The setup was build around a macroscopic blade Paul trap which has been under vacuum since around 2002. The initial design of the setup is described in the PhD thesis of Stephan Gulde [94], while numerous modifications and upgrades have been made since then and can be found in other PhD theses [78, 95–98]. Currently, the LinTrap setup is still operated and can work with ion chains of up to about 10 ions.

A substantial part of this work was creating a new trapped-ion setup. This setup was built as a part of the EU project 'Advanced Quantum computing with Trapped IONs' (AQTION) and will be referred to as 'AQTION' setup. The AQTION setup can be considered as a successor of the LinTrap setup. Some design features of the LinTrap setup were revisited based on the experience obtained over almost 20 years of operation of the LinTrap setup.

Firstly, the AQTION setup features a different trap: the PINE trap from AQT (see Fig. 5.1). This trap is very similar to the one described in the PhD thesis of Michael Guggemos [99]. The main difference from the trap used in the LinTrap setup is that different materials are used. The blades are made of gold-plated titanium instead of stainless steel and sapphire is used for the trap holder instead of Macor. This allows us to achieve lower trap temperatures and get lower phonon heating rates.

Secondly, the compact design of the vacuum chanber in the AQTION setup allows us to place an objective for the optical addressing system $\approx 20\,\mathrm{mm}$ away from the ion chain compared to $\approx 50\,\mathrm{mm}$ in the LinTrap setup [98]. This results in a higher numerical aperture (≈ 0.6 vs ≈ 0.3) and better addressing performance. At this point, the numerical aperture in the AQTION setup in limited by the trap

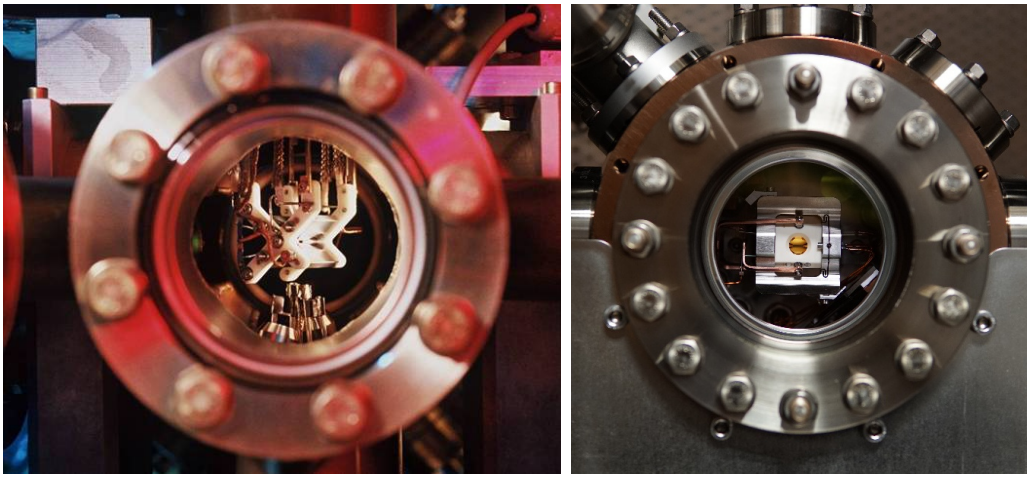

Figure 5.1: Traps inside vacuum chambers of the LinTrap setup (left) and the AQTION setup (right).

blades obstructing the view. Additionally, the addressing beam in the LinTrap setup comes at a 22.5° angle to the ion chain compared to 90° in the AQTION setup (see Fig. 5.2). The angle difference additionally decreases optical crosstalk in the new setup ($\approx 1.5\%$ vs $\approx 5\%$ [78]).

Figure 5.2: Single ion addressing geometry for the LinTrap setup (left) and the AQTION setup (right).

Finally, the AQTION setup features laser ablation loading of ions, which is a substantial 'quality of life' improvement thanks to a more precise control over the number of loaded ions. Therefore, the number of ions in the trap can be changed easier than in the LinTrap setup with oven loading. Additionally, ablation loading leads to fewer Ca atoms being deposited on the trap, less heating produced during the loading, and increased lifetime of the Ca source.

5.1.1 Rack concept

The AQTION setup is similar to the LinTrap setup from an ion-trapping perspective. However, it is quite different in other aspects. The idea of the AQTION project was to step away from the conventional lab environment toward industry standards. The main design goals were the following:

- The setup should be self-sufficient and should not depend on external devices.
- The on-site maintenance requirements for the device should be minimized.

Ideally, the device should be controlled remotely as much as possible, while the basic routines should be automated.

- The high-level access interface of the device should be hardware-agnostic. It should be possible for a non-expert in physics to be able to execute some quantum computing tasks on the device.
- The setup should be able to host many qubits and perform operations with them at the level sufficient for quantum error correction protocols (see Ch. 3). Therefore, the methods used for the operations and the calibration procedures should scale favorably with the number of qubits (ions).

These design goals led to the following architecture. The AQTION setup was assembled in two 19-inch racks (see Fig. 5.3). A 19-inch rack approach allows for modular structure of optical components and control electronics. Moreover, a lot of components are available in 19-inch format since it is a well established standard in industry. The two racks contain all the necessary components to trap and control ions for quantum computing purposes. This includes a vacuum chamber with the trap, lasers required to trap, cool and control ions, reference cavities for the lasers, all the control electronics for trapping and laser manipulation, and vibration isolation units to decouple the setup from the ground. Most of the modules are connected via an Ethernet interface, which allows for remote access.

Figure 5.3: The AQTION setup is assembled in two 19-inch racks.

5.2 Publication: Compact ion-trap quantum computing demonstrator

A thorough description and initial characterization of the AQTION setup is given in Ref. 1. The publication is provided below while some post-publication modifications are described in the following section.

Editors' Suggestion | Featured in Physics

Compact Ion-Trap Quantum Computing Demonstrator

I. Pogorelov,[1] T. Feldker,[1] Ch. D. Marciniak,[1] L. Postler,[1] G. Jacob,[2] O. Krieglsteiner,[2] V. Podlesnic,[1] M. Meth,[1] V. Negnevitsky,[3] M. Stadler,[3] B. Höfer,[4] C. Wächter,[4] K. Lakhmanskiy,[1,5] R. Blatt,[1,6] P. Schindler,[1] and T. Monz[1,2,*]

[1] *Institut für Experimentalphysik, 6020 Innsbruck, Austria*
[2] *Alpine Quantum Technologies (AQT), 6020 Innsbruck, Austria*
[3] *Institute for Quantum Electronics, ETH Zürich, 8093 Zürich, Switzerland*
[4] *Fraunhofer-Institut für Angewandte Optik und Feinmechanik IOF, 07745 Jena, Germany*
[5] *Russian Quantum Center, 121205 Moscow, Russia*
[6] *Institute for Quantum Optics and Quantum Information, 6020 Innsbruck, Austria*

(Received 28 January 2021; revised 12 April 2021; accepted 7 May 2021; published 17 June 2021; corrected 30 June 2021)

Quantum information processing is steadily progressing from a purely academic discipline towards applications throughout science and industry. Transitioning from lab-based, proof-of-concept experiments to robust, integrated realizations of quantum information processing hardware is an important step in this process. However, the nature of traditional laboratory setups does not offer itself readily to scaling up system sizes or allow for applications outside of laboratory-grade environments. This transition requires overcoming challenges in engineering and integration without sacrificing the state-of-the-art performance of laboratory implementations. Here, we present a 19-inch rack quantum computing demonstrator based on $^{40}Ca^{+}$ optical qubits in a linear Paul trap to address many of these challenges. We outline the mechanical, optical, and electrical subsystems. Furthermore, we describe the automation and remote access components of the quantum computing stack. We conclude by describing characterization measurements relevant to quantum computing including site-resolved single-qubit interactions, and entangling operations mediated by the Mølmer-Sørensen interaction delivered via two distinct addressing approaches. Using this setup, we produce maximally entangled Greenberger-Horne-Zeilinger states with up to 24 ions without the use of postselection or error mitigation techniques; on par with well-established conventional laboratory setups.

DOI: 10.1103/PRXQuantum.2.020343

I. INTRODUCTION

Quantum information processing as a computational paradigm has been proposed as an efficient means to tackle computational challenges throughout science and industry [1–6]. The rapid scaling of the computational potential with the number of quantum bits (qubits) is the basis for widespread interest in realizing a quantum information processor, or quantum computer. Tremendous progress has been made both experimentally and theoretically in exploring and demonstrating hallmark capabilities of quantum information processors in numerous architectures [7–12]. Among the most successful of these architectures are trapped atomic ions, which have already met many requirements for fault-tolerant [13] quantum computation [14–18].

With progressing capabilities among all platforms, the attention has recently shifted away from proof-of-principle implementations towards integration and scalability of architectures [7,8,14,19–23]. The shift in development of quantum computers from small-scale, expert-user devices to integrated, end-user-centric systems is analogous to the history of classical computation. It presents a host of new challenges such as manufacturing many, effectively identical qubits, and improving the scaling in a number of control and readout lines, while maintaining low error rates [24–26]. The minimization of resource overhead incurred in quantum control techniques or quantum error correction is an ongoing challenge across architectures [14]. These challenges are prominent examples of problems that need to be overcome as quantum devices scale to hundreds of qubits. It has become clear over the last decade that any device that can outperform classical

*thomas.monz@uibk.ac.at

high-performance computing for tasks relevant in industrial or applied science settings will require substantially more qubits than current architectures can sustain [27–31]. In addition to a large number of qubits, such a device should present the user with a hardware-agnostic interface, and require little to no maintenance by on-site personnel during standard operation. Meanwhile, all the basic routines should be automated and perform at the level sufficient for fault-tolerance requirements. Finally, the device should be deployable outside of well-controlled, low-noise laboratory conditions with purpose-built infrastructure. Demonstrating the capabilities of scalable architectures beyond laboratory implementations is therefore a crucial next step.

In this work we present the first phase of our efforts towards a compact, 50-qubit quantum computing demonstrator based on trapped ions as part of the AQTION (Advanced Quantum computation with Trapped IONs) collaboration. It features a 1.7×1 m^2 footprint with high mechanical stability, and scalable control electronics. We describe the hardware concept and integration, and characterize the initial system performance including the entangling gate operation necessary for quantum computation.

For a quantum computer to perform arbitrary computations, it is sufficient to implement arbitrary-pair, two-qubit entangling gates in addition to single-qubit rotations [32,33]. In a trapped-ion quantum computer these operations are typically the result of interactions with laser fields. Addressing individual qubits in a register with light beams is thus an essential component of universal quantum computation efforts in trapped ions [34,35]. Meeting the demands of state preparation and measurement [36–38] in a scalable fashion is therefore a major challenge in trapped-ion quantum computing. Consequently, the demonstrator leverages industrial expertise to accomplish scalable integration of light generation and delivery, in particular single-site addressing essential for the trapped-ion implementation. The demands of quantum control and algorithmic compiling on the software stack with increasing qubit and gate numbers are similarly challenging [39]. A detailed description of the holistic software stack of the AQTION platform, spanning device-specific control to hardware-agnostic end user algorithms, is beyond the scope of the present paper and will be covered in upcoming publications.

This manuscript is structured as follows. In Sec. II we present an overview of the physical qubit implementation, as well as the means of control, preparation, readout, and manipulation as necessary for computation. In Sec. III we describe the main subsystems by functional groups, including mechanical, optical, and electrical subsystems, as well as automation features of the demonstrator. In Sec. IV we turn to characterization measurements on the composite system. This manuscript concludes in Sec. V, where we outline near-term hardware integration goals to expand this setup into a fully self-contained, trapped-ion-based quantum computing demonstrator.

II. THE QUBIT SYSTEM

The choice of atomic species in a trapped-ion experiment is always based on trade-offs between beneficial physical properties of a given species, and technical implementation challenges associated with it. Broadly speaking, atomic qubits can be either optical qubits, Zeeman qubits, or hyperfine qubits. In optical qubits quantum information is encoded in two electronic states connected by an electric multipole transition with frequency in the optical domain, and the excited state is long lived or metastable. In Zeeman or hyperfine qubits the information is encoded in magnetic sublevels of electronic ground states with transition frequencies in the microwave to radiowave domain. A species may host several different types of qubit distinct in their implementation. Each species and qubit type offers advantages and disadvantages that may benefit certain applications more than others. At this stage no single species or qubit type has been identified as ultimately superior. The design goals and principles for our trapped-ion demonstrator are largely independent of the choice of ion species or qubit type to reflect the flexibility that this fact requires.

In our particular demonstrator we use optical qubits encoded in the electronic state of the valence electron in nuclear spin-free $^{40}Ca^+$ ions. This choice is motivated in part by technical considerations such as commercially available semiconductor laser sources and high-quality optics for all the required transitions. Transition wavelengths are in the blue, red, and infrared parts of the optical spectrum. Compared to transitions in the ultraviolet this has several advantages such as reduced charging of trap electrodes and substantially lower onset of solarization or photodarkening of optical components. Optical qubits can be directly interacted with using only a single beam compared to more complex beam geometries for Raman gates in Zeeman qubits or hyperfine qubits.

Specifically, the qubit $|1\rangle$ state is the $|4S_{1/2}, m_J = -1/2\rangle$ Zeeman state, which is coupled to the long-lived qubit $|0\rangle$ state $|3D_{5/2}, m_J = -1/2\rangle$. This excited state has a lifetime of $\tau = 1.168 \pm 0.007$ s [40], and decays via an electric quadrupole transition near 729 nm; see Fig. 1(a). This transition has the lowest magnetic field sensitivity in the manifold (5.6 MHz/mT) and is suitable for an effective two-level system as shown in Figs. 1(a) and 1(b).

The high magnetic field sensitivity compared to clock transitions in hyperfine qubits can be mitigated by proper magnetic shielding and stabilization [41]. A more fundamental limit of this optical qubit used is the lifetime of the upper qubit state $|3D_{5/2}, m_J = -1/2\rangle$. However, τ is about 4 orders of magnitude longer than typical 2-qubit operations (200 μs) and 5 orders of magnitude longer than

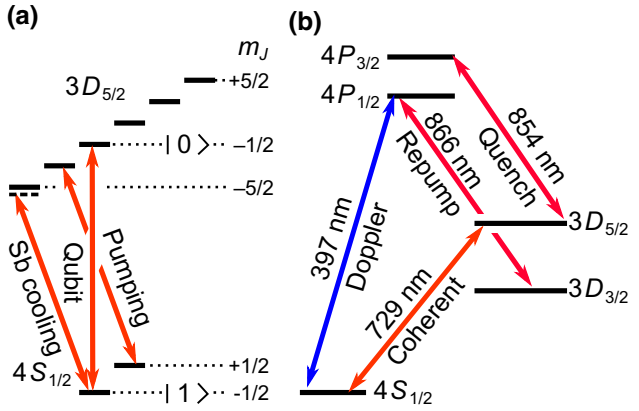

FIG. 1. Energy levels and relevant transitions in $^{40}Ca^+$ for the quantum computing demonstrator. (a) Ground and excited state fine structure manifold with electric quadrupole transitions for sideband (sb) cooling on the first red sideband, optical pumping, and the $\Delta m_J = 0$ qubit transition. (b) Ground, excited and auxiliary levels in $^{40}Ca^+$ with transitions for Doppler cooling and detection, repumping, and quenching of the excited state lifetime during sideband cooling.

single-qubit operations (15 μs). Thus, in the medium term, gate fidelity is not limited by the fundamental physical properties of the qubit but by the specifics of the technical implementation.

Preparation of the qubit system in our demonstrator entails two tasks. First, loading of ions into the trap is typically performed only when the qubit count has to be changed. Second, preparation of the electronic and motional states of the ions that is performed before every experiment.

A. Ion loading

$^{40}Ca^+$ is loaded into the trap either from a thermal source or via ablation from a target. Either method produces ions with temperatures ranging from hundreds to thousands of kelvin. Atomic ^{40}Ca features a low-lying excited state connected to the ground state via a dipole transition, which enables isotope-selective, resonantly enhanced two-photon photoionization at commercially available laser wavelengths near 423 and 375 nm. The ionization process takes place at the center of the trap, where ions are confined afterward by the trapping potential. The ions are then Doppler cooled via an electric dipole cycling transition from $4S_{1/2} \leftrightarrow 4P_{1/2}$ at 397 nm. A repumping laser near 866 nm prevents population trapping in the metastable $3D_{3/2}$ manifold. Doppler cooling alone may be sufficient to reach crystallization into a Coulomb crystal depending on the ion number and confining potential strength. Such Coulomb crystals of N ions support $3N$ bosonic motional modes, N of which are parallel to the weakly confining axial trap direction, and $2N$ perpendicular to that in the radial trap directions [42].

B. State preparation and readout

State preparation proceeds in four steps. First, ions are Doppler cooled at 397 nm and repumped near 866 nm. The motional modes of the ion cloud or Coulomb crystal after Doppler cooling will in general be in or close to the Lamb-Dicke regime [43]. Second, polarization gradient cooling (PGC) is employed using two counterpropagating, orthogonally polarized beams blue detuned from the $4S_{1/2} \leftrightarrow 4P_{1/2}$ transition [44]. Polarization gradient cooling results in a thermal state of all motional modes of typically a few quanta of motion for common trapping parameters much below the Doppler cooling limit [45]. Optical pumping of the qubit manifold on the $|3D_{5/2}, m_J = -3/2\rangle \rightarrow |4S_{1/2}, m_J = +1/2\rangle$ transition redistributes the electronic population from the initial mixed population of Zeeman sublevels to the $|4S_{1/2}, m_J = -1/2\rangle$ state. The final step of preparation is sideband cooling on selected motional modes close to the ground state. The targeted modes in sideband cooling may consist of subsets of the N axial modes, or of the $2N$ radial modes closest to the selected carrier transition that implements a gate operation. The cooling rate in sideband cooling is increased by quenching the lifetime of the $3D_{5/2}$ manifold through coupling to the short lived $4P_{3/2}$ level via excitation at 854 nm. State-selective readout is performed optically using fluorescence measurements on the Doppler cooling transition, either site resolved using a camera, or collectively (without spatial resolution) using an avalanche photodiode (APD).

C. State manipulation

The universal gate set employed [46] in the demonstrator is spanned by arbitrary single-qubit operations and the two-qubit entangling gate provided via the bichromatic Mølmer-Sørensen (MS) gate [14,47]. Both single- and two-qubit gates are implemented using laser light fields focused onto the ions. The effective Hamiltonian governing (near) resonant single-qubit interactions in the demonstrator is given by [48]

$$H = \hbar\Omega\sigma_+ e^{-i[(\omega-\omega_{\rm eg})t-\varphi]} e^{i\eta(ae^{-i\nu t}+a^\dagger e^{i\nu t})} + \text{H.c.},$$

where ω and φ denote the laser field frequency and phase, ν is the motional mode frequency, $\omega_{\rm eg}$ is the qubit transition frequency, and H.c. denotes the Hermitian conjugates. Furthermore, Ω denotes the Rabi frequency associated with the transition, η is the Lamb-Dicke parameter, $a^\dagger$ is the phonon creation operator, and σ_+ denotes the atomic (spin) raising operator. This Hamiltonian assumes a well-isolated two-level system for the interaction, uses the rotating wave approximation [43], and we neglect all other vibrational modes. This Hamiltonian in the first-order Lamb-Dicke

approximation leads to a single-qubit unitary propagator of the form

$$\hat{R}(\alpha) = e^{-i(\alpha/2)\vec{n}\cdot\vec{\sigma}},$$

where α is an angle that depends on the interaction strength and time, $\vec{n}$ is a unit vector, $\vec{\sigma} = \{\sigma_x, \sigma_y, \sigma_z\}$ is the Pauli spin vector, and $\vec{n}\cdot\vec{\sigma}$ quantifies the strength of the interaction along the three spin directions. In the atomic eigenbasis this can be expressed in spherical-coordinate form, assuming that $\omega = \omega_{\mathrm{eg}}$,

$$\hat{R}(\theta,\phi) = \begin{pmatrix} \cos\theta/2 & -ie^{-i\phi}\sin\theta/2 \\ -ie^{i\phi}\sin\theta/2 & \cos\theta/2 \end{pmatrix},$$

where θ and ϕ can be controlled via changing the amplitude or interaction time of the laser field, and its phase. The propagator lends itself to the interpretation of rotating the state of a qubit on the Bloch sphere, and single-qubit operations are consequently referred to as single-qubit rotations.

Qubit-qubit interactions in linear ion chains forming along the weakly confining trap axis are mediated via the bosonic bus of shared motional modes through spin-dependent optical dipole forces [49]. These forces are generated via a bichromatic laser field detuned slightly from the upper and lower sideband transitions of a selected vibrational mode. The effective Hamiltonian governing this interaction is given by

$$H = \sum_{j=j_1,j_2}\sum_{k=1,2} \hbar\Omega_{jk}\sigma_{j+}e^{-i[(\omega_k-\omega_{\mathrm{eg}})t-\varphi_k]} \times e^{i\eta_j(ae^{-i\nu t}+a^\dagger e^{i\nu t})} + \mathrm{H.c.},$$

where j enumerates ions and k enumerates the laser tones. Then, ω_k and φ_k denote frequencies and phases of the bichromatic laser field, ν the closest motional mode frequency, η_j the Lamb-Dicke parameter for this mode, ω_{eg} the frequency of the qubit transition, and Ω_{jk} the Rabi frequencies of the kth beam for the jth ion. As before, $a^\dagger$ is the phonon creation operator, σ_{j+} is the atomic (spin) raising operator. In the Lamb-Dicke approximation this leads to a two-qubit unitary propagator of the form

$$U_{\mathrm{MS}}(\chi) \approx e^{-i\chi S_x^2} = \begin{pmatrix} \cos\chi & 0 & 0 & -i\sin\chi \\ 0 & \cos\chi & -i\sin\chi & 0 \\ 0 & -i\sin\chi & \cos\chi & 0 \\ -i\sin\chi & 0 & 0 & \cos\chi \end{pmatrix},$$

where χ can be controlled with laser field power or interaction time and $S_x = \sum_j \sigma_{j,x}$ is the total spin along x. The bichromatic beam parameters should obey certain relations to guarantee that the motional state is disentangled from the ions' spin states at the end of the interaction [50,51].

III. TECHNICAL IMPLEMENTATION

Demonstrations of many of the requisite capabilities for quantum computation using trapped ions have been presented using laboratory setups [14–18]. However, different design constraints apply when constructing traditional laboratory setups or our modular approach. In the context of this work, we highlight the following. (i) The demonstrator needs to minimize footprint while maintaining mechanical stability to move towards scalability without sacrificing performance. (ii) Implementing modularity with flexible standard interconnects helps in reducing footprint and increasing rigidity, while also allowing replaceability and reconfiguration without major redesign, or manual realignment. (iii) The demonstrator needs to be self-contained and rely as little as possible on purpose-built infrastructure. This puts restrictions on external supplies like power, cooling, or environmental conditioning of the demonstrator location. (iv) Scalability inevitably requires standardization. Utilizing established standards to leverage industrial processes and interfaces is therefore desirable. (v) Hardware-agnostic design and scalability require the use of automation, as well as remote operability.

In this section we present our composite demonstrator's setup whose overall concept is shown in Fig. 2. The demonstrator setup is contained within two industry standard 19-inch racks. Connections between the modules inside each rack and between the two racks are achieved via electrical and optical patch cords, respectively. One of the two racks primarily houses modules related to generation, switching, and routing of the required optical frequencies and is hence designated the *optics rack*. The second houses the ion trap, associated infrastructure, and drive electronics, thus being designated the *trap rack*.

A. Mechanical assembly and environmental conditions

The primary mechanical assembly is composed of two industry standard 19-inch racks with a footprint of 0.85 × 1 m^2 each at a height of 2 m. Modules are largely free of moving parts to improve mechanical rigidity, and long-term stability. Modules that require manual alignment are equipped with self-arresting slide drawers, such that maintenance does not necessitate disassembly. The sole external supply to the racks is one standard 16 A/230 V connector per rack, for a total power consumption of less than 3.7 kW per rack. Temperature control inside the racks is provided by forced-air cooling and passive cooling fins throughout the modules. Air flow is restricted across free-space optical parts by appropriate enclosures. This prevents beam pointing instability and phase fluctuations induced by the moving air column. The racks are closed with doors in standard operation, improving directionality of air flow for better cooling, and protecting the equipment from dust.

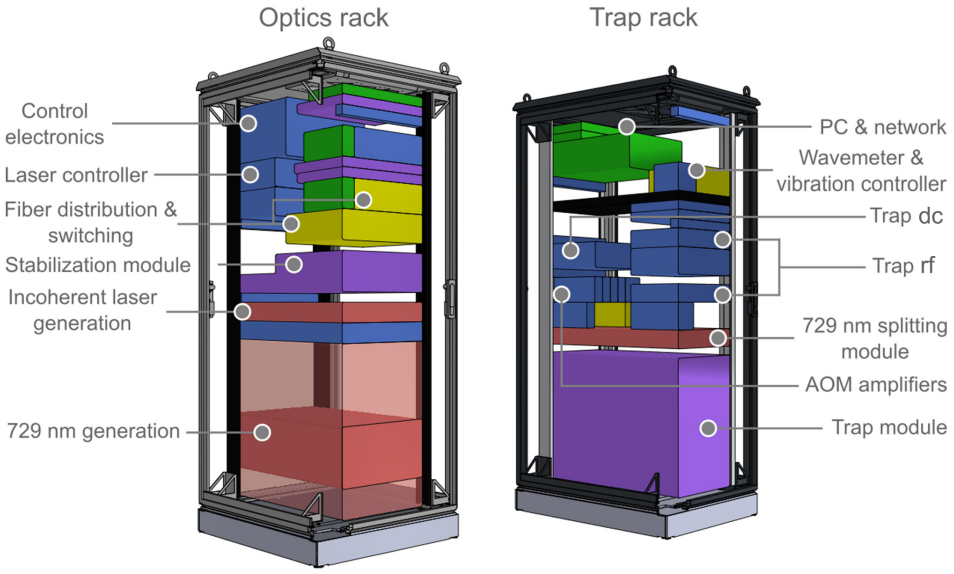

FIG. 2. Simplified scale model of the quantum computing demonstrator housed in two 19-inch racks with major components labeled. Modules in red correspond to optical systems, green for communication and readout, blue electronics and amplifiers, yellow fiber routing and switching, and purple for miscellaneous core modules. The "optics rack" contains primarily light generation, switching and routing modules with associated electronics. It additionally houses the coherent radio frequency (rf) and digital signal generation module. The "trap rack" houses the main trap module with associated drive electronics, as well as the communications and remote control hub. Interconnects between modules and racks via electrical and optical patch cords. Semitransparent red is the planned 729 nm light generation module.

1. Ion trap and vacuum apparatus

The $^{40}Ca^{+}$ ions are confined in a linear Paul trap (AQT Pine trap) consisting of electrodes machined from gold-plated titanium, and an alumina holder that serves as mounting and electrical isolation between the electrodes. The macroscopic trap design of the demonstrator consists of four blade electrodes and two endcaps, and is a variant of earlier designs employed previously in the Innsbruck ion trapping group [52,53]. The distance from the center of the trap to the surface of the blade electrodes is $r_0 = 0.57$ mm, while the endcap-endcap distance is $z_0 = 4.5$ mm.

Radio frequency voltage is applied to two opposing blade electrodes, and a positive static (dc) voltage to the endcaps. A set of additional electrodes allows for compensation of stray electric fields in order to reduce excess micromotion. The remaining two blade electrodes are held at a dc potential, but may be supplied with an out-of-phase rf potential for symmetric drive, if desired for complete cancelation of axial micromotion. The trap features a thermal calcium source (oven) for photoionization, as well as an ablation target. An *in vacuo* PT100 temperature sensor allows for temperature monitoring of the trap in operation.

The trap assembly uses exclusively nonmagnetic materials, specifically titanium, copper, alumina, and austenitic stainless steel (grade 1.4429 or equivalent) to minimize distortion of the magnetic environment.

The Paul trap itself is located inside a compact stainless steel spherical octagon vacuum chamber. Six diametrically opposing, nonmagnetic fused silica DN40 viewports with an antireflective coating allow for low numerical aperture (NA) optical access on the trap perimeter with NA ≈ 0.05. Additionally, a viewport with a clear aperture of 44.2 mm in the trap mounting flange provides optical access with a medium NA ≈ 0.29 for imaging of ions to an avalanche photodiode. From the opposing side of the vacuum chamber, a reentrance viewport with clear aperture of 71.2 mm at a distance of 18.3 mm to the trap center provides optical access via a NA $= 0.6$ objective lens (Photon Gear, 18WD Atom Imager Objective) for resolved ion imaging and illumination.

The trap mounting flange is equipped with feedthroughs for electrical connection to the trap electrodes, calcium oven, and the PT100 temperature sensor. Two nonevaporative getter pumps (SAES NexTorr Z200) provide the main pumping capacity to the chamber. A small ion getter pump (SAES CapaciTorr Z100) additionally pumps noble gases and provides pressure monitoring. Material selection for chamber construction is again restricted to low magnetic permeability, with the exception of permanent magnets required for pump operation.

Permanent magnets are further used in Halbach and Helmholtz configurations to provide the quantization field for the qubits. These are mounted directly to the vacuum chamber. The resulting homogeneous field in the

trap center has an angle of 66° and 34° to the trap axis and the imaging axis, respectively. The magnitude of the total field produced is $B_0 = 0.50$ mT. Temperature-compensated samarium cobalt magnets are employed to reduce magnetic field fluctuations to a minimum. Their relative change in magnetic field strength with temperature is $\delta_T B \approx 1 \times 10^{-5}$ K^{-1}. Furthermore, three sets of compensation coils along three orthogonal axes allow for control and stabilization of the magnetic field at the ion location in both absolute value and gradient.

2. Trap support infrastructure and environmental isolation

The Paul trap and accompanying vacuum chamber are the most critical components with respect to environmental disturbances like thermal, mechanical, or magnetic field fluctuations. The employed $^{40}Ca^{+}$ implementation maintains sensitivity to magnetic field noise that can limit attainable coherence times. Qubit operations depend on the amplitude, phase, and frequency of the interacting light fields. Therefore, any fluctuations on those quantities, as for example caused by beam pointing instabilities, will adversely affect operation fidelity. Consequently, these critical components are situated in an environmentally isolated housing, as shown in Fig. 3, which we refer to as the *trap drawer*. The drawer itself, designed at AQT, makes up the bottom layer of the trap rack, and is fastened to it via supports. The supports in turn connect to sliding rails on ball bearings through active vibration damping elements (Accurion Vario) based on preloaded springs and magnetic repulsion elements. Measurements of the isolators' magnetic fields show that their influence at the ions' position is below the ambient magnetic field level. The sliding drawer allows for easy access during installation and maintenance by clearing the main rack structure. The majority of the drawer footprint is enclosed in a μ-metal (ASTM A753 Alloy 4) shield (supplied by Magnetic Shield Ltd.) for magnetic isolation, which has a limited number of penetrations for electrical and optical access. Active instruments and electronics that can cause magnetic field noise are outside the shielded section wherever feasible.

B. Optical subsystems

Interaction with and readout of the qubits is primarily undertaken using optical fields in the presented demonstrator. The ability to manipulate and read out single qubits with light is thus central to its operation. Optical and optoelectronic subsystems consequently occupy an appreciable portion of the available space and complexity. In the following we discuss the generation and stabilization of the requisite lasers, present the light routing and addressing capabilities, and finally summarize the readout and detection components.

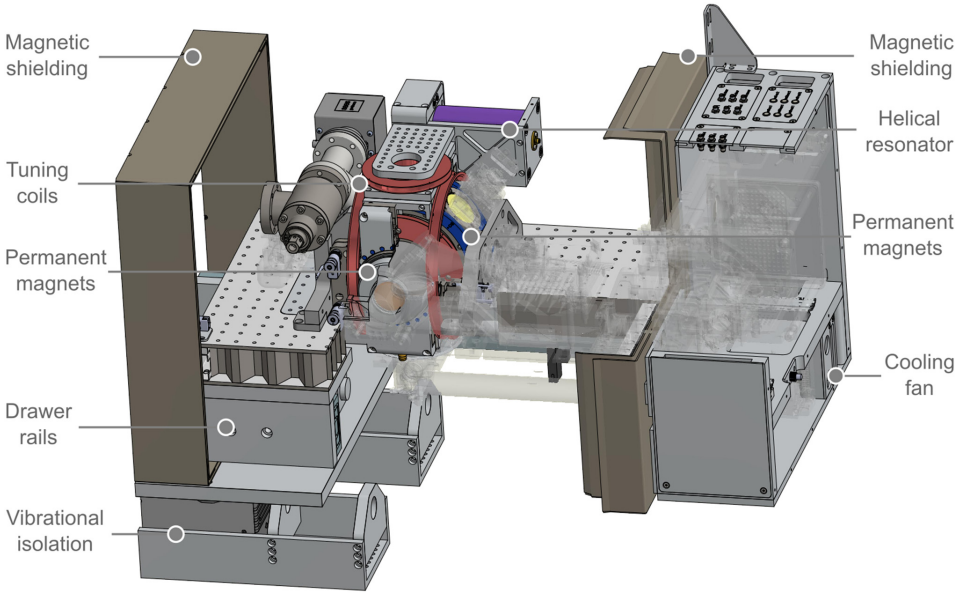

FIG. 3. Schematic of the trap drawer detail, focusing on the trap proper and mechanical components, displayed with extended (opened) drawer. Three sets of compensation coils each with a Helmholtz and anti-Helmholtz coil per holder (red) together with four sets of permanent magnets in Helmholtz (blue, left leader) and Halbach (blue, right leader) configurations define and compensate the magnetic environment. A μ-metal shielding encloses the trap setup except for penetrations allowing electrical and optical access. Active vibration isolation and thick honeycomb-lattice breadboards provide mechanical stability. A fan outside the shielding provides cooling for components close to the shield.

1. Laser light generation and stabilization

The demonstrator is equipped with three principal laser generation modules, as indicated in Fig. 4. First, a *Q*-switched (pulsed) laser (Coherent Flare NX) situated outside the magnetic shielding in the trap drawer emitting at 515 nm provides highly energetic pulses for ablation loading [54] of $^{40}Ca^{+}$ from the *in vacuo* target. Second, a multicolor diode laser (MDL) generation module (Toptica, MDL pro) provides light for all incoherently driven interactions: Doppler and polarization gradient cooling at 397 nm, line broadening ("lifetime quenching" for the qubit reset) at 854 nm, repumping at 866 nm, and 423 nm light used in the first (resonantly enhanced, isotope-selective) step for photoionization. This MDL setup is supplemented by a free-running laser diode (Toptica iBeam smart) providing light at 375 nm for the second (nonresonant) photoionization step to the continuum. The last major light generation module provides light at 729 nm for sideband cooling, optical pumping, and the coherent qubit control transition. Preliminary operation of this module uses a tapered amplifier (Toptica, TA pro), which is fed by seed light generated outside of the rack until the integrated laser source is installed. The seed light is derived from an ultrastable titanium sapphire (Ti:Sa) master oscillator (MSquared SolsTiS) locked to a high-finesse optical cavity, resulting in a linewidth of 3.6 ± 0.4 Hz [38]. The seed light is fed into the TA via an optical fiber with active fiber noise cancelation [55]. The TA has an output power of 500 mW at a seed level of 15 to 30 mW, which is sufficient to drive the amplifier gain into saturation. The bichromatic light fields required for the Mølmer-Sørensen interaction are generated by supplying a two-tone rf signal to the acousto-optic modulator (AOM) further downstream. Future hardware upgrades will be composed of a compact, diode-based laser system stabilized to a high-finesse cavity, which is completely contained in the rack. The pending system upgrade features a specified linewidth of less than 2 Hz and an output power of greater than 200 mW after fiber noise cancelation.

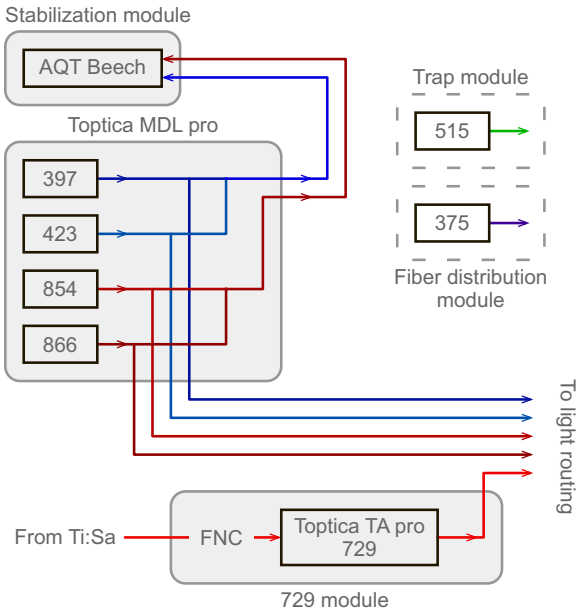

FIG. 4. Schematic of the principal light generation modules. A modified Toptica MDL pro unit produces four of the five laser colors needed for incoherently driven excitations. Their output is fiber coupled to a frequency stabilization module. A free-running laser diode is additionally installed downstream to provide the final incoherent excitation color. Laser colors within the qubit manifold are generated by a Toptica TA pro seeded by light from an ultrastable MSquared SolsTiS Ti:Sa master oscillator present in the laboratory.

Both ablation loading and photoionization inherently have no need for stringent frequency stabilization. On the other hand, all interactions with $^{40}Ca^{+}$ require precise control of the absolute frequency of the respective lasers to maintain efficient operation. The MDL unit has therefore been extended to provide two fiber-coupled feedback outputs combining all four frequencies on two patch cords, which are fed to a dedicated stabilization module. The stabilization unit should provide reliable low-noise frequency locking along with low long-term drift rates. In addition to these general requirements we need to comply with the demonstrator's design principles, which demand compactness, remote control access, and automation features. The module used here to comply with these requirements is the AQT Beech module. Inside, all lasers are locked to a reference cavity. The cavity in turn is stabilized via a transfer lock to an atomic transition in a gas cell. The details of this system will be presented in a separate publication.

2. Light delivery, switching, and addressing

The delivery subsystem handles the necessary routing and spatial distribution of the light colors throughout the setup. This includes collective delivery for all the lasers as well as site-selective (addressing) delivery for coherent qubit control. The system provides control over the temporal and intensity profile of the light fields via amplitude shaping, amplitude stabilization, and amplitude switching. The optical subsystems have been made modular whenever possible to provide replaceability and readjustment without disturbing other parts of the setup. Intermodule connection is achieved via fiber-optical patch cords in line with the requirements on stability and modularity. Polarization-maintaining single-mode optical fibers are used for delivery throughout due to the polarization sensitivity of optical transitions between Zeeman sublevels in the magnetic field. Typically, free-space optics outperform fiber optics in terms of transmission loss and polarization extinction ratio. This gap in performance grows

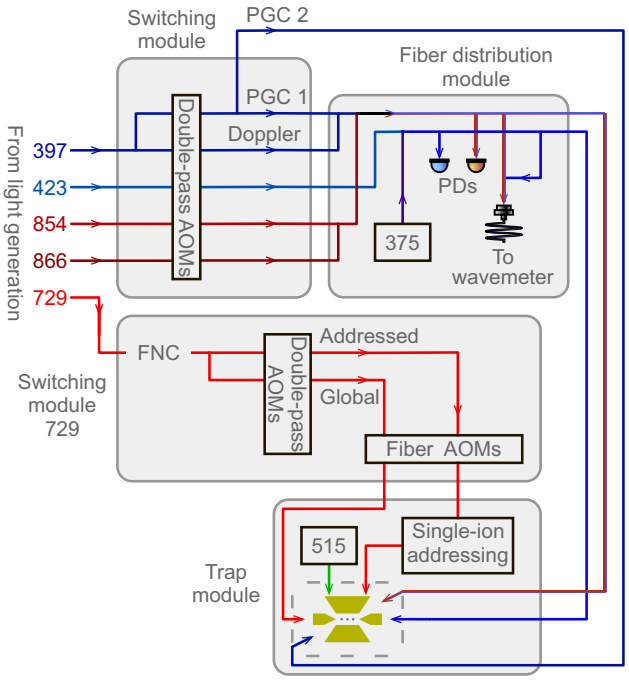

FIG. 5. Schematic of light delivery, switching, and addressing modules. Light is fiber delivered to dedicated switching modules utilizing free-space double-pass AOMs, after which overlapping and fiber routing to their final destination is handled on a fiber distribution module for incoherent interactions. Photodiodes (PDs) are placed throughout the beamline for continuous power monitoring. The qubit laser system has similar switching and routing capabilities, with the addition of fiber noise cancelation (FNC), and fiber AOMs for improved the on-off extinction ratio, bichromatic modulation for Mølmer-Sørensen interactions, and light field parameter control. One of two approaches is used to deliver addressed light; see Figs. 6 and 8.

for shorter wavelengths. Consequently, intermediate free-space optics are employed where fiber-based components perform insufficiently. Figure 5 shows a schematic of the delivery subsystem.

Four main delivery points for optical access are arranged orthogonal to the high-NA access ports of the vacuum chamber. Each of these is equipped with a fiber collimator for delivery. The collective qubit laser at 729 nm following the fiber-coupled AOM (FAOM) propagates through holes in the trap endcaps. On the opposing side is another single-mode fiber with the two photoionization colors. Delivery of all other collective beams happens at 45° to the trap axis. A large-mode-area photonic crystal fiber (NKT Photonics LMA-PM-5) delivers the superimposed Doppler cooling laser, refreeze laser, one of the two PGC lasers at 397 nm, as well as the repumping and quench lasers at 866 and 854 nm, respectively. A single-mode fiber on the opposing port delivers the remaining second PGC laser to complete the scheme. The high energy 515 nm light pulses for ablation loading are coupled free space into the trap from below. The four fiber access ports are each equipped with a fast and slow photodiode for monitoring power and stabilization close to the ion position.

Individual control over the amplitude of not only each color, but each laser beam, is required by nature of the gate-based interaction. Amplitude shaping is implemented via free-space double-pass AOMs. These shaping AOMs further provide the individual frequency offsets required to bridge the detuning between the frequency stabilization cavity resonance and required transition frequency. They are situated inside dedicated rack units as part of the switching module. An additional mechanical shutter is inserted in the Doppler cooling beam path, normally blocking the undiffracted zeroth order after the switching AOM. Opening the shutter gives access to a laser that is red detuned by approximately 300 MHz from the main cycling transition, and can be used to refreeze a molten ion crystal. The light switching modules are followed by a dedicated fiber distribution module, where free-space optics are used to overlap and fiber-couple beams into patch cords for final delivery. The fiber distribution and switching modules further incorporate photodiodes for continuous power monitoring on all colors throughout the beamline.

The beamline for the qubit manipulation laser is built analogously, with the addition of active fiber noise cancelation, preceding the switching module. The qubit laser is split on the switching board into two beams before passing a respective free-space double-pass AOM. The first goes directly into a FAOM and is sent to the trap along its symmetry axis for collective operations on all qubits simultaneously. The second is used for single-ion addressing. Light from an addressing unit is delivered to the ions via free space. For the addressing units, we trial two different approaches. The first uses a fixed number of fiber-coupled rigid waveguide channels with micro-optics that are imaged onto the ion. The second is based on two crossed acousto-optic deflectors (AODs) for positioning of the addressed beam [56]. An overview of these approaches is shown in Fig. 6. The arrangement of light fields arriving at the ion location is shown in Figs. 7 and 8.

For the micro-optics approach, light is sent to an additional splitting module with a fixed number of output channels, followed by individual FAOMs for light switching before being fed to the unit. The FAOMs have a center frequency of 150 MHz, an on/off extinction ratio of approximately 40 dB, and imprint the bichromatic sidebands onto the laser, as required for Mølmer-Sørensen interactions. The presence of an individual FAOM per ion has the further benefit of allowing individual control of the light field's parameters for each channel, to, e.g., interact with different motional modes for efficient coupling, to adjust each ion's Rabi rate, or to compensate for potential individual qubit frequency shifts. At the stage presented here, the splitting board is composed of a diffractive optic splitting the input light eightfold. The output fibers of the

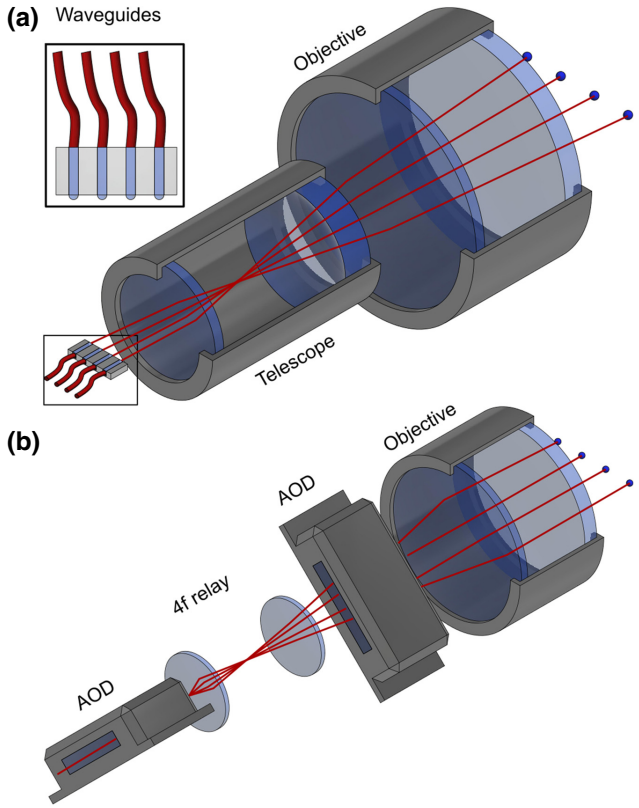

FIG. 6. Simplified illustration of the addressing approaches trialed, dimensions not to scale. (a) A fiber-coupled rigid waveguide with micro-optics delivers light via a shrinking telescope to the main objective and onto the ions. Beam separations are fixed. (b) A pair of crossed AODs with a relay telescope delivers light to the main objective and onto the ions. Beam separations are variable.

FAOMs are coupled into a waveguide and imaged onto the ion crystal via the main objective lens described in Sec. III B 3. This addressing unit is provided by Fraunhofer IOF. The details of this unit are beyond the scope of this paper and will be summarized in a forthcoming publication.

In the AOD approach on the other hand light is delivered via a single fiber. The two AODs are oriented at an angle of $\pm 45^\circ$ with respect to the ion string symmetry axis. Beam steering without incurring position-dependent frequency shifts is achieved by utilizing crossed pairs of AODs where the frequency up-shift from one unit (using the $+1$st diffraction order) is exactly canceled by the second (using the -1st diffraction order). Angular deflection through the AODs is converted to translation in the ion plane by action of the main imaging objective. Driving the AODs with multiple rf tones allows for simultaneous addressing of multiple ions at the cost of additional beams situated above and below the ion string. These beams have a nonzero frequency shift, and their number grows quadratically with the number of rf tones applied. Consequently, the power available per beam decreases quadratically with the number of tones as well.

3. Imaging optics

Optical readout can be performed in two ways. First, spatially resolved imaging of the ion string using an electron multiplying charge-coupled device camera through use of a near-diffraction-limited, high-NA objective. Second, not spatially discriminating (collective) light detection through a single-photon-counting avalanche photodiode and medium-NA optics. Both detection paths are situated orthogonally to the trap axis and the plane that contains all laser beams to minimize stray light onto the detectors. Additionally, this arrangement gives the largest possible numerical apertures through the vacuum chamber view ports for large collection efficiencies on the imaging systems. Both the APD and camera are placed outside of the magnetic shielding, where light exits through penetrations in the shield. Such an arrangement helps to minimize the amount of stray magnetic fields close to the trap chamber that may be caused by the readout electronics in the detectors.

Readout through the APD serves as a means of detection in trap characterization and system diagnostics, but is only suitable for small system sizes, and does not offer site selectivity. The imaging system employed for APD readout has a medium numerical aperture of NA ≈ 0.29, with a magnification of about $\times 1$, and a field of view of about 60 μm. A single ion driven far into saturation on the cycling transition with these parameters yields a photon flux of order 500 kcts/s on the APD given the NA, optical losses, and device quantum efficiency.

The primary imaging system features a high numerical aperture of NA ≈ 0.5 limited by the trap apertures. This system is used both for site-selective readout and manipulation of individual ions (single-site addressing). The system's main objective is a compound lens designed to operate near the diffraction limit for the detection light at 397 nm as well as for the addressing light at 729 nm. A dichroic mirror is used to overlap the two colors through this main objective, while compensation optics in the imaging path correct for abberations introduced by the dichroic mirror. Imaging design targets are a magnification of approximately $\times 29$ at a field of view of 150 μm to match the detector size. The design modulation transfer function exceeds 0.5 at a resolution of 0.5 μm over the full field of view, well in excess of what is required to resolve single ions with a typical spacing of $d_0 \geq 3$ μm.

The main objective's mounting provides five degrees of freedom for precisely aligning the optical axis with the ions necessary to achieving these tight specifications. First, translation perpendicular to the optical axis (X-Y translation) is achieved via flexure joints in

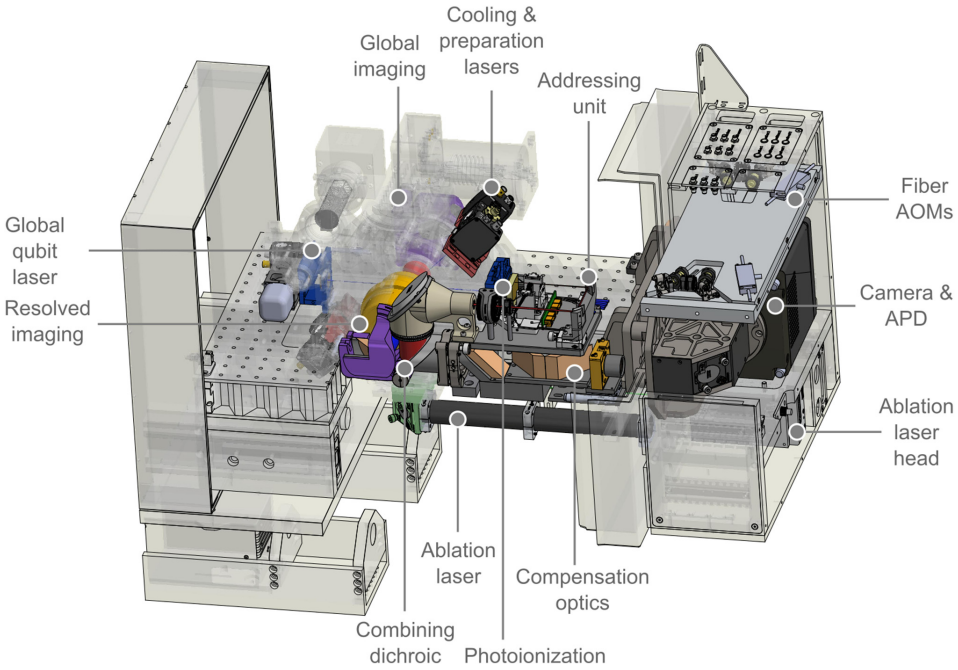

FIG. 7. Schematic of the trap drawer detail, focusing on optical and detection components, displayed with extended (opened) drawer. Optical interfacing with the ions is achieved via fiber delivery for Doppler cooling, polarization gradient cooling, quenching and repumping (red pair), as well as the collective qubit laser (blue, left) and photoionization (blue, right). Free-space delivery of the pulsed ablation laser is achieved via access from below (green). Single-site addressing lasers are steered by an addressing unit, and overlapped with the resolved detection path (high-NA objective, yellow) on a dichroic beam combiner (silver). Compensation optics for resolved light counter abberations introduced via the combiner. Collective imaging to an APD leaves at the back of the chamber (purple). Detection electronics and light sources are situated outside the μ-metal shielding. Fiber AOMs allow pulsing and imprinting of bichromatic sidebands onto the qubit lasers.

the objective's mounting plate, which are actuated via fine-pitch micrometers. Second, pitch and yaw can be adjusted using fine-pitch screws with a spring-loaded kinematic three-point mounting. Piezoelectric actuators allow for fine tuning the position on all three adjusters in addition to coarse alignment via thumbscrews. The final degree of freedom is translation along the optical axis (Z translation or focusing). Coarse alignment is achieved via the fine-pitch threading used to secure the objective lens. This thread is guided through a tight-fitting tube that affords high repeatability. Fine adjustment is achieved by using the kinematic mount's three piezoelectric transducers in tandem for pure translation. Realignment and refocusing using manual thumb screws is typically only necessary after making major changes to the system. Fine adjustment of the addressing using the piezo actuators is typically done once a day or after opening of the trap drawer.

C. Electronics, control, and automation

Access to and control of the experimental platform is managed by a rack-mounted desktop computer that is accessed via Ethernet. Both racks feature Ethernet switches that connect individual devices to the control computer.

The electronic outfitting of the demonstrator setup is based largely upon modular components. The demonstrator is controlled and driven by both analog and digital electronics. The trap blades providing radial confinement are driven by a dedicated rf signal generator (Rhode & Schwarz SMB100B) that is amplified via a helical resonator [57]. The ion's secular frequency is actively stabilized by a feedback circuit actuating on the supplied trap rf [58]. In addition, the demonstrator makes use of state-of-the-art phase-coherent digital signal generation, real-time control, and in-sequence decision making based on field programmable gate arrays (FPGAs) to perform digital (pulsed) operations.

1. Experimental control electronics

The laser pulses used for manipulating the states of the ions are controlled using acousto-optic modulators. These require radio frequency signals that are precisely timed and phase coherent (interpulse, interchannel, and intermodule). For typical rf pulses several microseconds in length, the timing resolution needs to be less than 10 ns

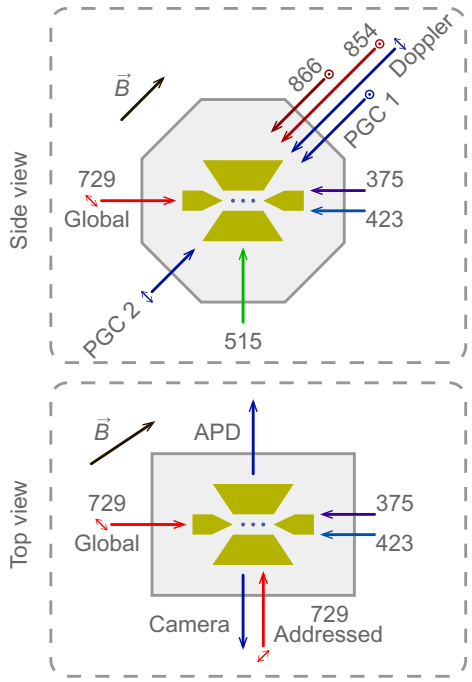

FIG. 8. Geometric arrangement of beam delivery; beam polarization indicated where required. The Doppler cooling beam, the repumping and quenching beams, as well as PGC beams enter the chamber at 45° to the trap axis. The collective 729 nm beam is delivered through a hole in the trap endcap. Photoionization beams enter through a hole in the opposing endcap. The medium-NA port is used for collective readout of the whole ion chain with an APD. The high-NA access port is used for single-ion addressing and readout with a camera.

to control pulse lengths to better than 1%, and the timing jitter must be below a few hundred picoseconds to ensure repeatability. Digital input/outputs (I/Os) with similar timing resolution and jitter are also required, both for triggering external devices such as rf switches, shutters, or arbitrary waveform generators, and for counting photon-arrival pulses from photomultipliers or APDs. These rf and digital signals are manipulated using a FPGA-based modular experimental control system developed at ETH Zurich, known as "Modular Advanced Control of Trapped IONs" (M-ACTION) [59]. It uses a "star" topology as shown in Fig. 9, with a central master control board that communicates with the control PC via a custom Ethernet protocol, and multiple peripheral boards providing rf output [60]. The peripheral boards communicate with the master via a low-level low-voltage differential-signaling-based protocol through a backplane into which all the boards are inserted.

The master board is a commercially available Avnet Zedboard extended with custom boards for digital I/O and board-to-board communication. It is centered around a Xilinx Zynq system on chip, which holds both a FPGA core used for low-level deterministic signal handling, and a dual core 667 MHz ARM A9 CPU suitable for higher-level control and real-time computations. These include Boolean decisions such as those in quantum error correction, as well as more sophisticated Bayesian decisions featuring feedback of a continuous parameter to the experimental hardware [59,61]. The FPGA core, on the other hand, monitors the peripheral rf boards, and controls the digital I/O that requires precise timing.

The rf peripheral boards each consist of four direct-digital synthesis (DDS) chips (Analog Devices AD9910), controlled by a standalone FPGA (Xilinx Spartan-6 XC6S150T) with sufficient memory and a pulse sequence processor to independently execute most typical experiments without intervention from the master [60]. In situations where intervention from the master board is required, such as when real-time feedback is being carried out, the latency between an input to the master and a change in pulse sequence on the peripheral cards is around 5 μs. Recent revisions of the rf board also feature two analog-to-digital converters, and support on-board servo regulators for intensity stabilization with sample and hold synchronous to the local pulse sequences. Proportional-integral-differential (PID) regulator gains and setpoints may be altered in sequence to help cope with external nonlinearities.

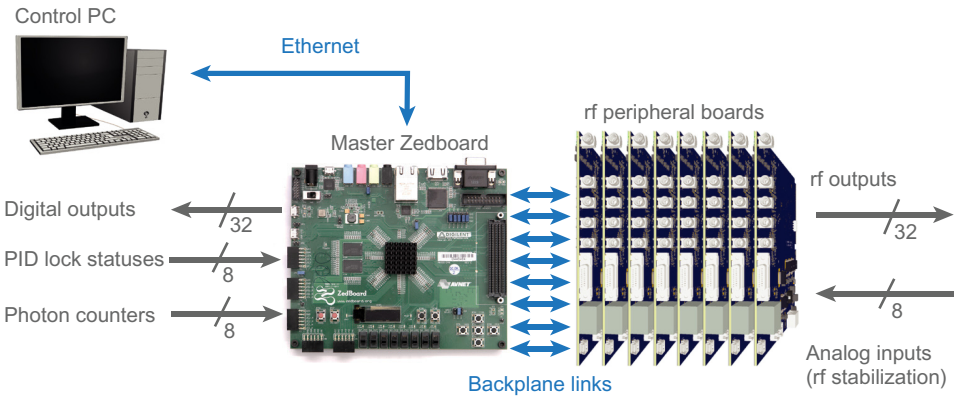

FIG. 9. M-ACTION experimental control system. The master board acts as the hub of the system, synchronously running experimental sequences involving the digital I/O and the rf peripheral boards, and managing communications with the control PC.

The aforementioned rf boards support a single-tone output per channel, requiring multiple channels to be added together for multitone quantum gates. Additionally, the complexity of a pulse is limited by the bandwidth of the interface between the FPGA and the DDS chips. A new rf generation board using 1 GSa/s DACs controlled directly by a more powerful FPGA, as well as 32 GB of local memory, is currently being developed to overcome these bottlenecks.

In-sequence decision making is performed based on predetermined conditional decisions or "branches". This predetermination allows FPGA memory management. Branches are subsequences that are executed if in-sequence detection fulfils the branch conditions. Photon count data from either a camera or APD are used directly on the FPGA to determine whether a branch condition is met.

A simple example would be of a state transfer $|S\rangle \rightarrow |D\rangle$ by means of a $\pi/2$ pulse. If at the decision making point $|S\rangle$ is measured, that is, many photons are scattered in the detection window, then the FPGA determines that the condition for state transfer to $|D\rangle$ is met, and executes a π-pulse to transfer the population into $|D\rangle$. If, on the other hand, $|D\rangle$ is detected, that is, few photons are scattered, then this additional pulse is not executed. A more complicated example is given in the literature [62], which uses the same hardware in a separate experiment.

2. Experimental control software

The experiment hardware is operated using two layers of control software. The lower layer, running on the master board, is written in C++ and provides access to the functionality of M-ACTION to a PYTHON-based higher layer running on the control PC. This higher layer is used for day-to-day experimental operation and programming, while the lower layer can be used to implement high-performance real-time computations, or extend the capabilities of M-ACTION.

A graphical user interface (UI) gives direct feedback to the operator, and is used for the majority of day-to-day experimental control tasks. Script-based implementations of pulse sequences allow for versatile extensions to low-level pulse patterns available from the UI. Automated routines for calibration, maintenance, and error handling, such as Rabi frequency tracking, frequency drift compensation, and string recrystallization, are supported to maintain the system at high fidelity without constant supervision. Quantum circuits are executed via a high-level language made in house, called PySeq, which acts as an intermediary between state-of-the-art frameworks like Cirq [63] and Qiskit [64] and close-to-hardware descriptions on the laser pulse level. PySeq is, similar to Qiskit, a PYTHON package and provides a convenient abstraction layer translating quantum circuit objects like rotations around an axis for a given angle to hardware instructions such as laser pulses with a certain power and duration. It is expected that this feature, in combination with remote access to the setup, will greatly improve the ease of use for collaborators.

IV. SYSTEM CHARACTERIZATION

We now turn to characterizing the demonstrator setup. A suite of common measures and experiments is used to evaluate the engineering approaches for the rack-based architecture. The section begins with outlining standard operation parameters for the ion trap. Measurements on the mechanical stability of the rack and the performance of the active vibration isolation system are presented. We show measurements on imaging system performance, as well as addressing capabilities using two different addressing unit devices. We finally turn to measurements pertaining to the operation of the demonstrator itself, such as characterization and compensation of the magnetic field gradients, coherence times, ion temperature and heating rates, and gate performance for single- and pairwise-qubit interaction.

A. Trapping parameters

The Paul trap's radial confinement voltage is supplied to a helical resonator, in order to filter and impedance match the rf drive to the trap [57] that results in a voltage step up at the trap side. The loaded resonator oscillates at a drive frequency of $\Omega_{\mathrm{rf}} \approx 2\pi \times 27.4$ MHz. It is driven with an input power of up to $P_{\mathrm{in,max}} = 10$ W. The trap endcaps are supplied with a voltage of up to $V_{\mathrm{ec}} \approx 1000$ V. An ion trapped in the trap will oscillate at the resulting pseudopotential's three fundamental trap frequencies ω_{ax}, and ω_{rad} that can be measured by external excitation with oscillating fields ("tickling") [65] or by sideband spectroscopy [66]. These trap frequencies are (nearly) identical to the center-of-mass motional excitations of ion clouds or crystals in the three trap directions. We determine the secular frequencies for a single $^{40}Ca^{+}$ of $\omega_{\mathrm{rad}} \approx 2\pi \times 3$ MHz in the radial direction with 10 W input power, and $\omega_{\mathrm{ax}} \approx 2\pi \times 1$ MHz along the trap axis at about 1000 V endcap voltage. *In situ* temperature measurements using a PT100 thermistor give a temperature of the trap that depends on the rf drive power. The temperature reaches about $T_{\mathrm{max}} \approx 100\,^{\circ}\mathrm{C}$ after sustained operation at $P_{\mathrm{in,max}} = 10$ W. The pressure in the vacuum chamber as measured by the pump's gauge is 1.5×10^{-11} mbar. The pressure reading does not depend on the drive power, indicating little outgassing from adsorbed contaminants on the trap surfaces.

The ion gauge's pressure measurement is performed at the pump location instead of the ion location. Differential pressures in ultralow vacuum conditions can thus lead to an underestimation of the pressure at the ion location. Consequently, we independently determine the pressure at the ion location via collision rate measurements [67,68].

Collisions with residual thermal atoms melt the ion crystal and thus limit the stability of ion crystals in the trap. We distinguish between two different types of collision event: those that melt the crystal and cause ions to change sites in the refrozen crystal, and those that lead to molecule formation via chemical reactions that changes the number of (bright) ions. Detection of reconfiguration events is done by observing the position of nonfluorescing, cotrapped ions (defect hopping). We measure a collision rate of $\Gamma_{\mathrm{col}} = 0.0025 \pm 0.0011\ \mathrm{s}^{-1}$ per ion by observing reconfiguration events in a three-ion crystal consisting of two bright $^{40}Ca^{+}$ and one dark, cotrapped ion, which corresponds to a pressure of $p_{\mathrm{ion}} = (9.7 \pm 4.2) \times 10^{-11}$ mbar assuming collisions with H_2 [68]. This means that even a 50-ion chain is unlikely to experience a collision during the qubit coherence time of 100 ms. Ion loss may occur when collisions are sufficiently strong to lead to unstable ion trajectories, or when chemical reactions cause formation of dark ions. By observing an ion crystal of 32 bright $^{40}Ca^{+}$ ions over the course of 12 h we observe the loss of only one ion from the trap.

B. Mechanical stability and active damping

Mechanical instability affects quantum computing fidelity via a multitude of avenues from light field amplitude fluctuation, lowering of the signal-to-noise ratio through blurring or defocusing in the detection system, to light field dephasing noise [69–73]. We measure the vibrational stability of the setup using piezoelectric shear accelerometers (Endevco 7703A-1000) at various locations in the setup. Time series data from the detectors is recorded and Fourier transformed to voltage power spectral densities in an audio spectrum analyzer (Stanford Research Systems SR1). Voltage spectra are converted to displacement spectral densities via the accelerometer sensitivity calibration. The measurement is limited by the electronic noise floor of the signal conditioner (Endevco 133) below about 2 Hz. Displacement spectral densities recorded simultaneously in the horizontal and vertical directions are shown in Fig. 10, along with a reference spectrum obtained on an empty, broadband-damped, honeycomb-lattice optical table in close proximity. Root-mean-square displacements over the full measurement bandwidth are shown in Table I with the electronic background subtracted.

The overall vibrational stability of the system is similar to traditional optical setups situated on dedicated optical tables. Spectra do show a clear influence of the operation of cooling fans used in the rack construction. The majority of root-mean-square displacement is contributed at low frequencies below 10 Hz. Notably, these frequencies are also well below the fan rotation frequencies, indicating that they do not simply originate from vibrations of the fans or modulations at the 50 Hz motor drive. Determining the origin of excess vibrations caused by the fans and the structured noise at low frequencies is part of future upgrade efforts, including dc-drive fans and improved air flow direction. The performance is comparable to the empty reference table in spite of the compact, towerlike construction in active operation, and validates engineering approaches used in the demonstrator.

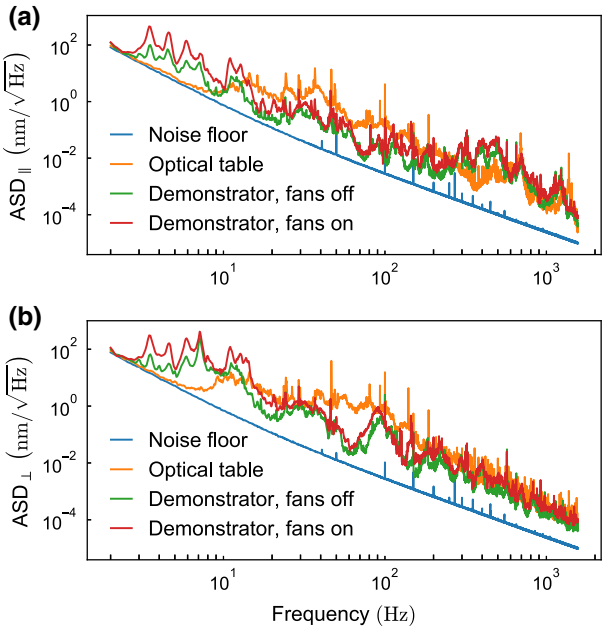

FIG. 10. Displacement (amplitude) spectral densities (ASDs) (a) parallel to the floor (horizontal) and (b) perpendicular to the floor (vertical) calculated from time series data obtained with piezoelectric shear accelerometers. Traces show equivalent displacement spectral densities of the electronic noise floor (blue), a typical optical table setup in close proximity (orange), and the demonstrator setup with cooling fans turned off (green) and on (red).

C. Imaging and detection performance

Characterizing the performance of the primary imaging system provides information about the achievable signal-to-noise ratio in readout, and the minimal achievable spot size and crosstalk for addressing light. After

TABLE I. Root-mean-square (RMS) displacements over the full measurement bandwidth for vibration measurements shown in Fig. 10. Electronic background subtracted pointwise from spectra.

	Noise	Optical table	Full w/o fans	Full w/ fans
$\mathrm{RMS}_{\mathrm{hor.}}$ (nm)	54	21	61	275
$\mathrm{RMS}_{\mathrm{vert.}}$ (nm)	50	33	139	335

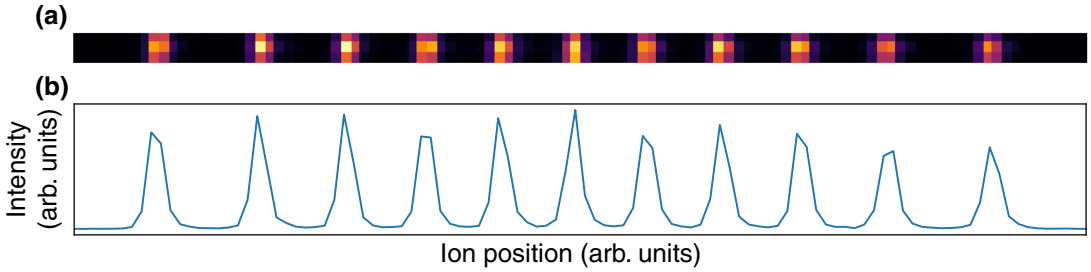

FIG. 11. Detection performance. (a) Fluorescence image of a linear string containing 11 ions. The axial trap frequency is $\omega_{ax} = 2\pi \times 450$ kHz, corresponding to a distance between the two center ions of 4 μm. (b) Integration over pixel columns shows well-separated ions.

optimization of the objective alignment we resolve well-separated ions in a 50-ion linear crystal. A typical image of an 11-ion crystal with minimal ion-ion separation of approximately 4 μm is shown in Fig. 11(a) recorded at the detection wavelength of 397 nm. We determine the achieved imaging system magnification to be $\times 29.9$ from the known pixel dimensions and calculated ion spacings for the used trap parameters. This is slightly larger than the design magnification of $\times 29$. The high-NA readout optics enable camera detection times down to 300 μs at a fidelity of about 99.9%.

We determine the detection fidelity by preparing an ion string either in the bright $4S_{1/2}$, or in the dark $3D_{3/2}$ manifold by turning off the repumping laser at 866 nm. We elect to pursue this method over creation of the dark state via excitation using the 729 nm laser to avoid conflating operational infidelities in qubit manipulation with detection infidelities. After a cooling period we perform a projective measurement and detect each ion individually on a camera. From the counting statistics in each ion detection region we determine the probability of measuring the prepared state for a given measurement time, that is, measure many (no) photons for the ion prepared in the bright (dark) state. We estimate the detection crosstalk by determining the probability of measuring a bright state in a detection region in between two bright ions spaced at 5.9 μm. Detecting light above the background in this empty region of space comes solely from detection crosstalk. At a measurement time of 300 μs we detect no events above the background threshold out of 10 000. Consequently, we conclude that detection crosstalk during our measurement windows is negligible.

D. Single-ion addressing performance

Addressing capabilities are crucial for the quantum computing scheme we pursue. This capability is routinely quantified in terms of the ability to resolve individual sites along with the crosstalk between individual channels. In the following, characterization measurements of the micro-optics addressing unit and AOD addressing units are presented.

At this stage we utilize only four of the channels on the micro-optics addressing unit. The beams from these channels are fixed in position, and measuring the beam profile proceeds by moving a single ion electrostatically along the trap axis through the beams by scanning the endcap voltages. At each position the light intensity is obtained by measuring the oscillation frequency of Rabi oscillations. The Rabi frequency is proportional to the electric field at a given position. Figure 12(a) shows the estimated light intensity along the trap axis obtained in this fashion. From a Gaussian fit to a higher-resolution scan shown in Fig. 12(b) we calculate a beam waist of $w_0 = 0.81 \pm 0.01$ μm for all spots. Different coupling efficiencies through FAOMs and waveguides lead to peak heights varying across channels.

We further measure the resonant crosstalk between channels as defined by the ratio of the Rabi frequencies, $\Omega_{\text{adjacent}}/\Omega_{\text{addressed}}$, when exciting a single ion. For the four active channels, we measure resonant crosstalk between 1.9% and 3.4%, as shown in Fig. 12(c). This is much larger compared to what we would expect from a Gaussian beam with $w_0 = 0.81$ μm or Airy fringes arising from the finite aperture, and implies that the crosstalk is limited by optical aberrations.

For the AOD addressing unit, we scan the addressing beam over a string of ions by changing the AOD drive frequency. In this measurement we use laser pulses of a fixed power and duration such as to produce a pulse area of less than π at the center of the beam. Scanning the beam across an ion will thus produce Rabi oscillations with maximal population in the excited state coinciding with maximal intensity. We calibrate the deflection per drive frequency increment obtained from the AODs by comparing the population profile to the known ion distances at a given axial center-of-mass mode frequency. The calibration yields a deflection slope of 4.9 ± 0.1 μm/MHz.

A measurement for a 16-ion string with a minimal ion distance of approximately 3.4 μm and a total length of approximately 60 μm is shown in Fig. 13(a). The intensity

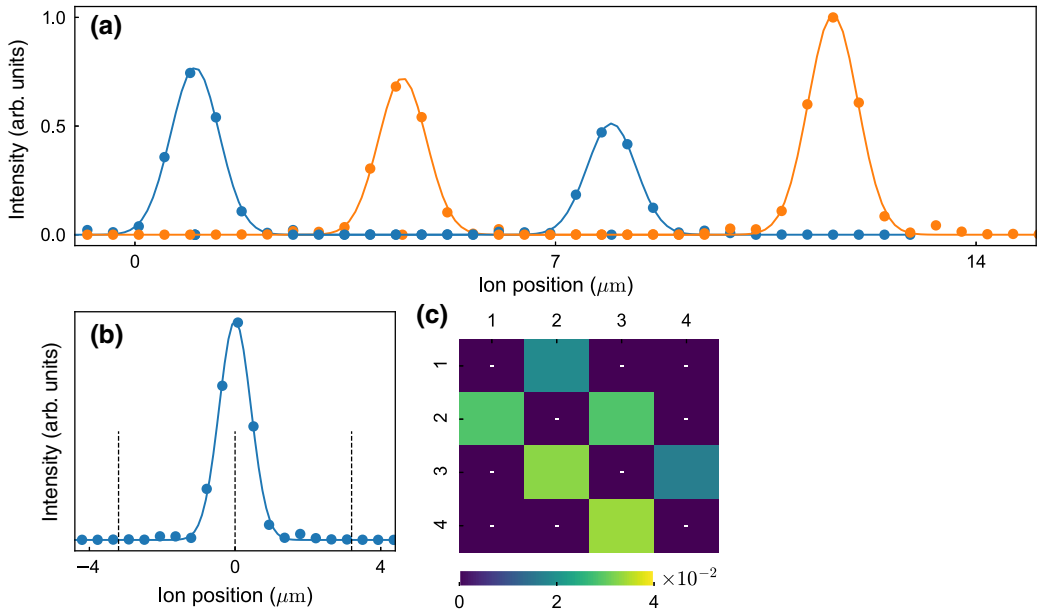

FIG. 12. Micro-optics addressing unit performance. (a) A single ion's position is scanned electrostatically along the trap axis by varying the endcap voltages. The square of the Rabi frequency is plotted as a function of this position for four active channels at a distance of 3.4 μm. Solid lines are Gaussian fits to data, alternating colours for clarity. (b) Same as (a) with higher resolution for spot size measurement of the focused addressing beam at 729 nm. By fitting a Gaussian distribution to the data we obtain a beam width of $w_0 \approx 0.8$ μm. Dashed black lines indicate the nearest neighbors for a 50-ion crystal at the minimal distance of approximately 3.2 μm. (c) Estimates of resonant crosstalk from intensity profiles in (a). The dashed entries in (c) are not assessed.

profile shown in Fig. 13(b) is measured analogously to that of the micro-optics addressing unit, yielding a beam waist of $w_0 \approx 1.09 \pm 0.02$ μm. Next, we characterize the resonant and off-resonant crosstalk in a ten-ion string with a minimal inter-ion distance of 3.5 μm. The ratio of the Rabi frequencies of the nonaddressed ions to the addressed ion is plotted in Fig. 13(c). We obtain an average resonant crosstalk of 0.2% with a maximum of 1% on ion 5 when addressing ion 4. The average nearest-neighbor crosstalk is 0.5%. This is significantly lower than in the micro-optics addressing unit. The difference may at least partly be attributed to the better overall optical quality of macroscopic precision optics used in the AOD approach, rather than micro-optical prototype components.

Figure 13(d) shows the results of off-resonant crosstalk measurements. For this measurement, we perform a resonant collective $\pi/2$ pulse, followed by an addressed ac-Stark pulse of variable length, followed by a collective $-\pi/2$ pulse. These composite pulses, sometimes referred to as $U(3)$ pulses, are used to reduce the effect of crosstalk. The ac-Stark shift is proportional to the light field intensity $I \propto E^2$ while the Rabi frequency is proportional to the electric field $\Omega \propto \sqrt{I} \propto E$. Consequently, we expect the $U(3)$ pulses to produce significantly smaller crosstalk. The maximum crosstalk measured is 2.6×10^{-4}, 20 times lower compared to the resonant crosstalk. The average crosstalk on nearest neighbors is 1.3×10^{-4}.

E. Coherence properties and magnetic fields

Qubit coherence times are affected by a multitude of sources. Two common technical sources of decoherence in state-of-the-art trapped-ion setups are phase noise from the driving fields and magnetic field noise. Phase noise may originate either directly from laser frequency instability, that is, finite linewidth, or can be imparted through, e.g., fiber noise or optical path length noise. Magnetic field noise modulating the energy splitting in the qubit manifold often originates from mains or its harmonics, switching power supplies, or ground loops.

Phase noise in the driving field is ultimately limited by the linewidth of the stabilized laser. Vibrational isolation, rigid construction principles, fixing of flexible (fiber optics) paths, and air current control in free space are implemented throughout the setup to prevent adding excess phase noise. Additionally, fiber noise cancelation is used up to the double-pass switching AOM; see Sec. III B 2.

The influence of magnetic field noise depends on two factors: the noise present and the sensitivity of the utilized transition to it. The qubit transition $|4S_{1/2}, m_J = -1/2\rangle \leftrightarrow |3D_{5/2}, m_J = -1/2\rangle$ is the least sensitive to magnetic field fluctuations out of the $S_{1/2} \leftrightarrow D_{5/2}$ manifold, with a slope of 5.6 MHz/mT. This is orders of magnitude higher than in clock transitions of hyperfine qubits [74], and therefore magnetic field stability as well as homogeneity have to be

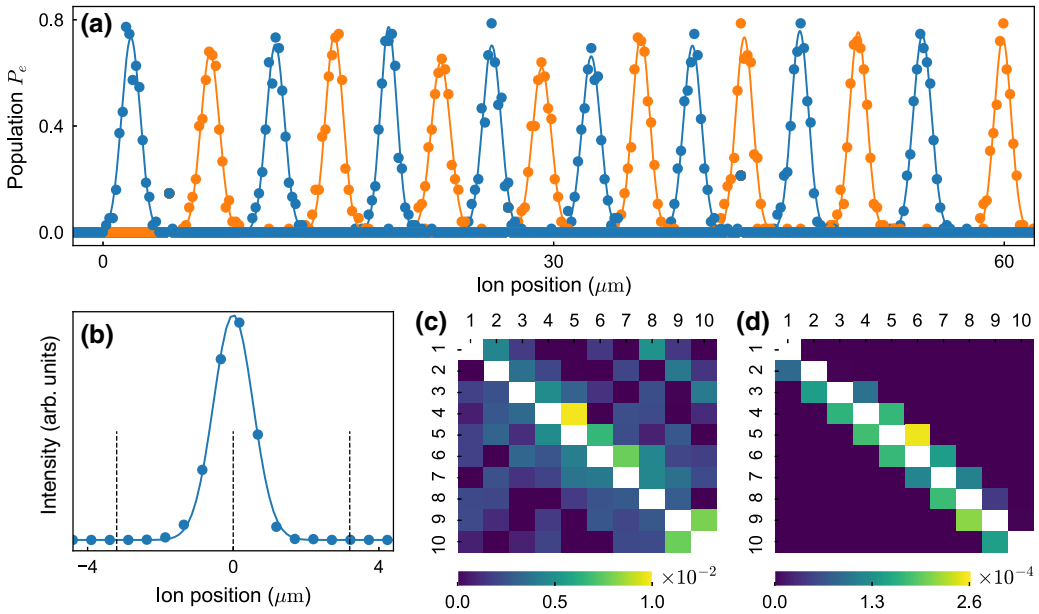

FIG. 13. AOD addressing unit performance. (a) Scan of the addressing beam over a 16-ion crystal. The population P_e is used as a proxy for the signal intensity; see the main text. Solid lines are Gaussian fits to data, alternating colours for clarity. (b) Spot size measurement of the focused addressing beam at 729 nm. A single ion's position is scanned electrostatically along the trap axis by varying the endcap voltages. The square of the Rabi frequency is plotted as a function of this position. By fitting a Gaussian distribution to the data we obtain a beam width of $w_0 \approx 1.1$ μm. Dashed black lines indicate the nearest neighbors for a 50-ion crystal at the minimal distance of approximately 3.2 μm. (c) Resonant crosstalk measurements in a ten-ion crystal with minimal inter-ion distance of 3.5 μm. Plotted are the ratios of Rabi frequencies of ions relative to the addressed ion (white on the diagonal). (d) Same as (c) but using off-resonant, compensating $U(3)$ pulses; see the main text. Ions where Rabi oscillations are too slow to fit reliably are set to 0 in the plot to avoid a spurious structure.

precisely controlled in order to reach sufficient coherence times of the order of $T_2 \approx 100$ ms or better.

We characterize the temporal magnetic field stability by performing Ramsey spectroscopy on the *ground state qubit* $|4S_{1/2}, m_J = -1/2\rangle \leftrightarrow |4S_{1/2}, m_J = +1/2\rangle$ transition in a single ion. This transition has a 5 times increased sensitivity to the magnetic field with respect to the qubit transition, with a gradient of 28.0 MHz/mT. The optical pulse sequence to access this transition begins with a $\pi/2$ pulse, which creates an equal superposition state between $|0\rangle$ and $|1\rangle$. A π pulse then coherently transfers the population from the optical qubit $|0\rangle$ state to the $|4S_{1/2}, m_J = +1/2\rangle$ state. After the Ramsey waiting time the sequence is reversed, which implements the Ramsey time evolution of an effective magnetic dipole transition. This sequence yields a significant decrease in sensitivity to optical noise sources, thus isolating the influence of the magnetic field. Performing Ramsey spectroscopy with a closed μ-metal shield on the ground state qubit and optical qubit yields respective coherence times of $T_2^{\mathrm{GS}} = 18 \pm 1$ ms and $T_2^{\mathrm{opt}} = 90 \pm 30$ ms, as shown in Figs. 14(b) and 14(c). This is sufficient to execute about 400 two-qubit gates or 4000 single-qubit gates during the coherence time.

Furthermore, we measure no influence of the vibration isolation elements on the coherence time of our qubit. The initial decay of fringe contrast is consistent with coherence times in excess of the $T_2^{\mathrm{opt}} = 90 \pm 30$ ms. However, for waiting times longer than 25 ms, we observe accelerated contrast decay that limits the coherence time to the value above, and causes substantial uncertainty. The source of this enhanced decay is the subject of ongoing investigation, but may be caused by magnetic field noise induced by switching magnets in neighboring experiments, or mains noise. This is further supported by two observations. First, neighboring ion trap experiments implementing feedforward to cancel mains noise see a substantial improvement in coherence times. Second, a similar experiment being set up in a neighboring building with overall worse environmental control but almost no other occupants causing magnetic field noise also shows increased coherence times.

In addition, the spatial homogeneity of the magnetic field needs to be investigated to maintain coherence across an extended ion register. Small deviations in the positioning of the employed Halbach and Helmholtz configurations may cause a gradient or curvature across the trap axis. Likewise, the permanent magnet of the ion getter pump may cause a magnetic field gradient across the ion string.

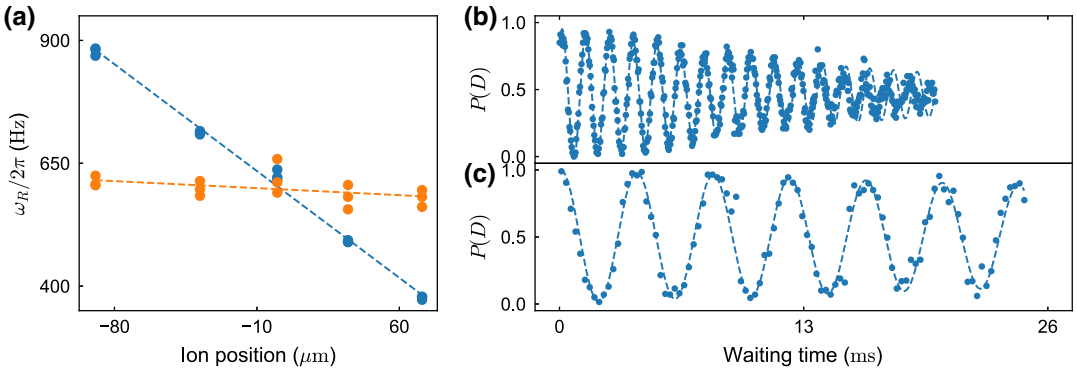

FIG. 14. (a) Magnetic field gradient before compensation (blue, 3.2 ± 0.1 Hz/μm) and after compensation (red, 0.2 ± 0.1 Hz/μm) on the ground state qubit as seen from the Ramsey fringe frequency ω_R for a fixed detuning as a function of ion position, corrected for linear frequency drift at fixed position. (b) Decay of Ramsey fringes of the dark state population $P(D)$ for the ground state qubit over time, resulting in a coherence time of $T_2^{\mathrm{GS}} = 18 \pm 1$ ms. (c) Same for the optical qubit transition. The sensitivity to magnetic fields is 5 times lower, leading to less impact from magnetic field noise. We determine $T_2^{\mathrm{opt}} = 90 \pm 30$ ms.

We measure a gradient $\partial_z B = 0.111 \pm 0.002$ mT/m by performing Ramsey spectroscopy on the ground state qubit and then shifting the equilibrium position of a single ion electrostatically. The gradient leads to a frequency shift on the ground state qubit transition of 3.1 ± 0.1 Hz/μm. Applying appropriate currents to the compensation coils reduces this axial gradient by an order of magnitude to 0.2 ± 0.1 Hz/μm. For the 5 times less sensitive optical qubit transition, this means a gradient of 0.041 ± 0.021 Hz/μm, corresponding to an end-to-end frequency difference of approximately 8 Hz in a 200 μm chain of 50 ions, as shown in Fig. 14(a).

F. Ion temperature and motional heating rates

High-fidelity gate operations typically require the ions to retain coherence in their motional degrees of freedom [16,75–77]. Motional coherence is ultimately limited by the motional heating rate. We therefore measure the ion temperature, that is, phononic mode occupation, and from that, the heating rates with sideband thermometry [78]. Sideband thermometry can be applied for an average phonon occupation $\bar{n} \lesssim 2$. Comparison of the Rabi oscillations on the red and blue sidebands of the qubit transition yields the average phonon occupation [48]. After sideband cooling a single ion, we obtain a phonon number of $\bar{n}_{\mathrm{ph,\,ax}} = 0.02 \pm 0.01$ (at $\omega_{\mathrm{ax}} = 2\pi \times 1.05$ MHz) in the axial direction, and $\bar{n}_{\mathrm{ph,\,rad}} = 0.06 \pm 0.02$ (at $\omega_{\mathrm{rad}} = 2\pi \times 2.5$ MHz) in the radial direction. By increasing the time between sideband cooling and temperature measurement we obtain a heating rate of 0.221 ± 0.007 s^{-1} in the axial direction [see Fig. 15(a)] and 0.3 ± 0.1 s^{-1} in the radial direction. These heating rates compare favorably with values obtained in other traps operated at room temperature [79] (see, in particular, Fig. 8). Measuring heating rates for axial trap frequencies between $\omega_{\mathrm{ax}} = 2\pi \times 0.15$ MHz and $\omega_{\mathrm{ax}} = 2\pi \times 1.05$ MHz, we obtain a power-law dependency $1/\omega_{\mathrm{ax}}^{\alpha}$ with $\alpha \approx 1.7$; see Fig. 15(b).

G. Single-qubit gates

Arbitrary single-qubit rotations are part of the complete gate set we chose to implement for universal quantum computation capabilities. Qubit rotations are implemented differently depending on the sets of qubits required, and on the axis of rotation chosen. For many applications, rotating all qubits collectively is required. This can be efficiently implemented using a single, collective beam traveling axially along the spine of the trap, colinearly with the ion string. The single-site-resolving addressing units described in Sec. IV D are used instead if only subsets of qubits need to be rotated.

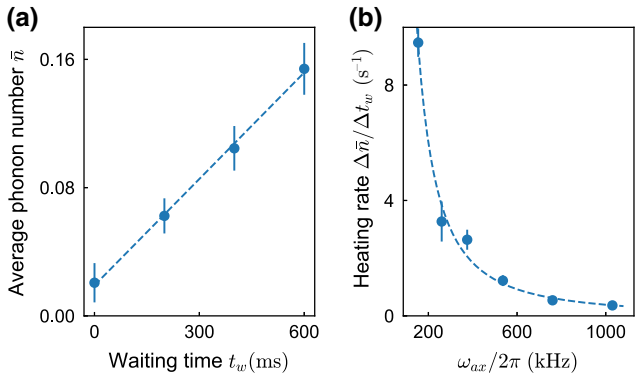

FIG. 15. Axial heating rates. (a) We calculate the heating rate of $\Delta\bar{n}/\Delta t_w = 0.221 \pm 0.007$ s^{-1} at $\omega_{\mathrm{ax}} = 1.05$ MHz by fitting the increase in $\bar{n}$ over the waiting time t_w, where $\bar{n}$ is determined from sideband thermometry. (b) Heating rates are determined as in (a) as a function of the trap frequency. The dashed line is a power-law fit $1/\omega_{\mathrm{ax}}^{\alpha}$, where $\alpha \approx 1.7$.

The mechanism to drive the rotation itself is additionally different depending on the axis chosen. A rotation around an axis in the Bloch sphere's equatorial plane, that is, between $\hat{R}_x$ and $\hat{R}_y$, can be implemented via resonant excitation on the 729 nm qubit transition. An optical phase imparted using the FAOMs is used to define the axis of rotation relative to the first pulse in a sequence, which may be defined arbitrarily. The remaining axis, $\hat{R}_z$, is instead driven by off-resonant ac-Stark pulses. Typically, we perform $\pi/2$ rotations in 15 μs, limited by our current control electronics.

In order to characterize the fidelity of these single qubit rotations we perform randomized benchmarking on a single qubit [80], assuming uncorrelated noise. A number of n Clifford gates is executed, where each Clifford gate incurs an average cost of 1.875 $\hat{R}_x(\pi)$. At the end of the sequence the Clifford gate that inverts the sequence is added, thus creating an identity operation if not for gate errors. Here, we concatenate up to 100 Clifford gates and fit an exponential decay of the form $A \times p^n + 0.5$ to the population of the initial state. We assume that the population will decay to a value of 0.5 for a large number of gates. Then $A + 0.5$ is the fidelity of state initialization. The error per Clifford gate is calculated as $R_{\mathrm{Clif}} = (1-p)(1-1/d)$, with $d = 2$ denoting the dimension of the Hilbert space for a single qubit.

First we characterize qubit rotations when using the global, axially-aligned beam that drives collective rotations. We obtain a Clifford gate fidelity of $F_{\mathrm{Clif}} = 99.83\% \pm 0.01\%$ or $F_{\mathrm{gate}} = 99.91\% \pm 0.01\%$ per single-qubit rotation. We perform the same measurement on a single ion with the tightly focused beam from the micro-optics addressing unit, and obtain $F_{\mathrm{Clif}} = 99.75\% \pm 0.02\%$ and $F_{\mathrm{gate}} = 99.86\% \pm 0.01\%$, respectively.

H. Mølmer-Sørensen gate and entanglement generation

The ability to generate entanglement in a deterministic way is key for quantum computation [81–83], and the missing component to our complete gate set. Different types of entangling gates have been proposed and demonstrated for trapped-ion qubits [49,84,85]. Here, we utilize the Mølmer-Sørensen gate [47,50] that generates entanglement through spin-dependent forces generated by a bichromatic light field slightly detuned from a vibrational mode. However, quantifying the degree and depth of entanglement in many-body quantum systems generated by any means remains a challenging task [86]. Entanglement witnesses [87,88] are often used, where the observable crossing a given threshold guarantees multipartite entanglement of a given depth. Greenberger-Horne-Zeilinger (GHZ) states are a class of maximally entangled Schrödinger's cat states that have the fortunate features of being natively implemented by the Mølmer-Sørensen gate,

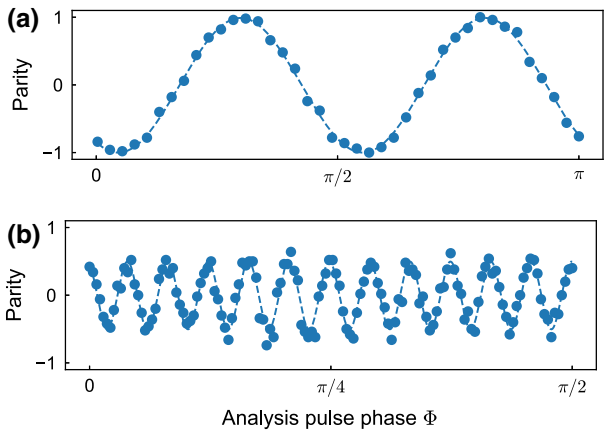

FIG. 16. (a) Parity oscillations after a Mølmer-Sørensen gate on two ions followed by an evaluation pulse with phase Φ. The amplitude of the parity oscillations is $C_2 = 0.995 \pm 0.011$ with 100 measurements per data point. Together with populations $P_2(SS, DD) = 0.9988 \pm 0.0005$ we determine a fidelity of $F_2 = 0.997 \pm 0.006$. (b) Parity oscillations of a 24-ion GHZ state with 100 measurements per data point. The parity contrast drops to $C_{24} = 0.501 \pm 0.013$, the population to $P_{24}(S\cdots S, D\cdots D) = 0.588 \pm 0.006$. We obtain a fidelity of $F_{24} = 0.544 \pm 0.007$; more than 6 standard deviations above the 24-partite entanglement threshold of 0.5. Measurement uncertainties are smaller than the marker size.

and providing a particularly easy-to-measure entanglement witness. Furthermore, GHZ states are highly susceptible to errors and decoherence [89–91], and as such, provide a sensitive probe for characterizing the performance of our compound system.

First, we implement Mølmer-Sørensen gates using a collective, axially oriented beam on ion strings from 2 to 24 ions. The state fidelity F after the entangling operation provides the entanglement witness with $F > 0.5$, guaranteeing full-depth entanglement. We characterize the operation using a two-ion crystal. The fidelity is directly inferable from the populations in the $|S, S\rangle = |1, 1\rangle$ and $|D, D\rangle = |0, 0\rangle$ states with $P_2(SS, DD) = 0.9988 \pm 0.0005$, as shown in Fig. 16(a), as well as their coherences [89]. The coherences are obtained from observing the oscillations in the state's parity as the phase of an analysis $\pi/2$ pulse is varied before projective measurement. Measuring the amplitude of this oscillation yields $C_2 = 0.995 \pm 0.011$ [89,92]. From those we calculate a single-gate state fidelity $F_2 = (P_2 + C_2)/2$ with $F = 0.997 \pm 0.006$. This fidelity includes all errors from state preparation and measurement (SPAM) and in particular is achieved without postselection. A single two-ion Mølmer-Sørensen gate typically takes 200 μs. Sustaining the interaction for odd-integer multiples of this duration implements repeated Mølmer-Sørensen gates. Measuring the fidelity after different numbers of gates, and fitting an

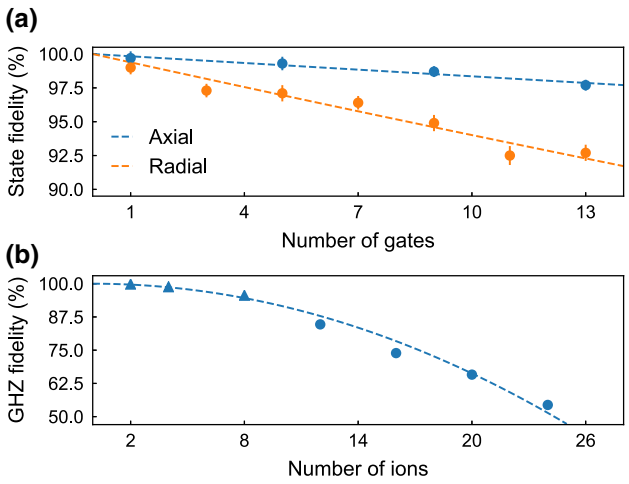

FIG. 17. Mølmer-Sørensen gate performance. (a) Decay of overall state fidelity after repeated, odd-integer application of approximately 200 μs Mølmer-Sørensen interactions for axial and radial two-ion gates. We infer a single-gate state fidelity of 0.9983 ± 0.0001 per axial gate and 0.9936 ± 0.0003 per radial gate. (b) Axial Mølmer-Sørensen gates on a linear ion string for different ion numbers. Pairs of ions are successively added to the existing string and the measurement repeated. Blue circles represent measurements performed at an axial center-of-mass mode frequency of $\omega_{ax} = 2\pi \times 234$ kHz, to ensure the formation of a linear string for a large number of ions, and are taken consecutively. Blue triangles represent measurements performed at an axial center-of-mass mode frequency of $\omega_{ax} = 2\pi \times 200$ to 1000 kHz on different days. Measurement uncertainties are smaller than the marker size.

exponential decay as shown in Fig. 17(a) yields a simple estimator of the state fidelity with 0.9983 ± 0.0001 per gate.

Larger multipartite entangled states are subsequently produced by applying a single Mølmer-Sørensen gate to multiple ions. We demonstrate the generation of GHZ states up to 24 qubits. Measured fidelities are plotted in Fig. 17(b), where pairs of ions are successively added to the existing string and the measurement is repeated. For 24 ions, we measure $P_{24}(S\cdots S, D\cdots D) = 0.588 \pm 0.006$, $C_{24} = 0.501 \pm 0.013$, and $F_{24} = 0.544 \pm 0.007$, which is again not corrected for SPAM errors and without postselection, and is more than 6 standard deviations above the threshold for 24-partite entanglement [89]. The parity oscillations are plotted in Fig. 16(b). To the best of our knowledge, this is the largest GHZ state as well as the largest fully entangled state that has been generated in any system without error mitigation or postselection.

In the data shown above Mølmer-Sørensen gates were carried out on the axial modes of vibration. In order to create a fully programmable system, we use the radial modes of vibration for arbitrary-pair, addressed entangling operations on specific qubits in long ion strings. Characterizing the creation of states with addressed operations naturally

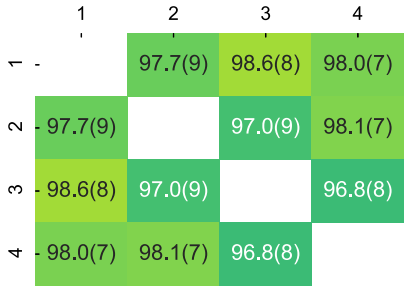

FIG. 18. Full register overlap fidelity of states produced using the AOD addressing unit in a four-ion crystal. There is no meaningful distinction between pair (1,4) and (4,1) as opposed to in single-site addressing. Consequently, the matrix is symmetric.

leads to the question of the fidelity metric, with two prominent candidates. The first is the fidelity of, say, GHZ state production where the nonaddressed subregister is ignored. This will quantify the action of an entangling gate, but is oblivious to what this operation does to the rest of the register. The second, more stringent choice, would be to determine the fidelity of performing an entangling operation on the addressed qubits without affecting the idling qubits. This is then the overlap of the full register state with the ideal register state, rather than subregisters. Given that crosstalk is unavoidable we elect to chose the second metric.

Initial tests are carried out with the micro-optics addressing unit, addressing the two outer ions of a three-ion crystal. The Mølmer-Sørensen gate with the radially oriented addressing beam yielded a register overlap fidelity of $F_2 = 0.989 \pm 0.005$ for a single gate. Again, concatenating multiple gates and fitting an exponential decay yields a fidelity of $F_2' = 0.9936 \pm 0.0003$ per gate as plotted in Fig. 17(a). Here F_2 is the fidelity of the Mølmer-Sørensen gate including SPAM errors, while F_2' is approximately the pure fidelity per gate operation without SPAM errors.

With the AOD addressing unit we measure all pairwise-entangling gates in a four-ion crystal. We calibrate the gate on the two outer ions and use the same set of parameters for all gates. The register overlap fidelities are shown in Fig. 18. We achieve fidelities in the range from 0.969(7) to 0.986(8). Cumulative population in the nominally nonaddressed subregister for these measurements is below 0.2%.

We anticipate that further improvements in the radial mode stability, cooling of radial modes, addressing unit and mode disentanglement [93–95] should increase the fidelity of the addressed gates.

V. CONCLUSION

In this manuscript we have provided a detailed description of the experimental implementation of a compact, trapped-ion quantum computing demonstrator situated in

two 19-inch racks. We have presented mechanical, optical, and electrical systems along with characterizing experiments. This experimental platform improves upon conventional hardware implementations in terms of modularity, integration, and remote control. In our characterization measurements we find the system performance to be on par with conventional, laboratory-based hardware implementations in terms of experimentally relevant performance criteria. We find that mechanical stability, optical readout and addressing performance, heating rates, coherence times, and Mølmer-Sørensen entangling fidelities in the current implementation do not suffer relative to traditional optical table setups. Using the compound system, we are able to produce maximally entangled Greenberger-Horne-Zeilinger states with up to 24 qubits with a fidelity of $54.4\% \pm 0.7\%$. To our knowledge, this is the largest maximally entangled state yet generated in any system without the use of error mitigation or postselection, and demonstrates the capabilities of our system.

In addition, we presented site-selective qubit operations to implement a complete gate set for universal quantum computation using two distinct approaches to addressing: a micro-optics approach with fixed, rigid waveguides, and an acousto-optic deflector approach. Both of these approaches offer advantages over the other in particular settings.

The micro-optics approach readily offers itself for simultaneous multisite addressing without producing off-axis spots that can lead to resonant and off-resonant crosstalk. The power scaling in such a scenario is linear in the number of channels, assuming a suitable power distribution system is at hand. Parallel radial sideband cooling is one direct beneficiary of such capabilities, as is direct generation of interaction between more than two qubits. Individual control over amplitude, phase, and frequency of each channel is a fundamental advantage of this approach but requires one FAOM per qubit. The positional stability is not affected by the oscillator stability of rf sources, and extension to larger registers are not limited by the speed of sound or similar quantities such as in AOD-based devices.

The AOD approach on the other hand is technologically simpler, thus offering superior performance at this stage. Optical quality of macroscopic components is often also superior to micro-optics, in particular in prototyping scenarios such as here, which reduces abberations. The addressing is inherently flexible, such that it can be adjusted for qubit registers from 2 ions to 40 ions in our configuration. Adjustment of power and optical phase of individual channels is possible without an optical modulator per ion, which significantly reduces the technological overhead compared to the micro-optics approach. This unit is fed by a single fiber, and no prior power distribution capabilities are required. The switching speed in AODs is limited ultimately by the speed of sound in the deflecting crystal, which therefore also limits the speed at which operations can be performed. The quadratic power loss for multisite addressing, and off-axis spots limit this technology to the simultaneous addressing of a small number of ions.

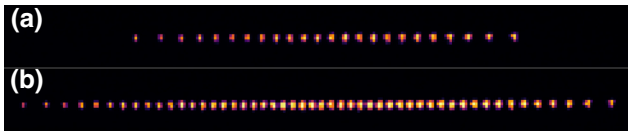

FIG. 19. Ion images of (a) 24 and (b) 50 ions in the demonstrator. The 24-ion chain is used to demonstrate 24-partite entanglement within the setup without the use of postselection or error mitigation. Fifty-ion chains are the midterm control target and can already be trapped and cooled. Nonuniform brightness stems from the finite size of the detection beam.

With both of these approaches we demonstrate single-qubit and pairwise-entangling gates on registers up to 10 ions. From randomized benchmarking we obtain a fidelity of $F_{\text{gate}} = 99.86\% \pm 0.01\%$ per addressed single-ion gate. Measurements of resonant crosstalk are shown to be below 1% across the entire ten-ion register with the AOD approach, while nonresonant crosstalk is measured to be less than 1.25×10^{-4} in the same string. Together with the pairwise-entangling operations with fidelities between 97% and 99% we show all the basic operations for a fully programmable quantum system. Benchmarking of larger registers, and with more complete suites of benchmarking tools [96] will be undertaken as part of the next round of hardware integration and software improvements.

These near- and midterm upgrades to the hardware and software stacks will further improve upon the demonstrator's capabilities. Use of an external master oscillator to generate the narrow-linewidth qubit laser will no longer be required after installation of the compact diode-laser source that is currently under construction as part of the AQTION collaboration. Similarly, single-site addressing capabilities will be improved in mode quality and the number of channels. This will allow the setup to implement more complex algorithms by moving from axial gates to radial quantum gates enhanced by established quantum control techniques [97,98]. Upgrades to M-ACTION, as well as complimentary developments to the control and remote access software stack will enable easier access to the demonstrator capabilities in a hardware-agnostic fashion.

Already, the device presented is capable of operating with qubit numbers on par with state-of-the-art conventional laboratory setups. An image of such a qubit register is shown in Fig. 19(a). The midterm upgrades should enable us to increase this number to the AQTION control target of 50 qubits and beyond. We have already demonstrated basic capabilities of control in larger qubit chains as shown in Fig. 19(b), with a 50-ion chain already crystallized in our trap. In the long term, we hope that the demonstrator's features and engineering solutions mean

that ion-trap-based quantum computers may be situated in any space with reasonable environmental stability and vibrational level. Quantum computation with a qubit count exceeding 100 is feasible based on our architecture and this characterization of its first implementation.

ACKNOWLEDGMENTS

We gratefully acknowledge funding from the EU H2020-FETFLAG-2018-03 under Grant Agreement No. 820495. We also acknowledge support by the Austrian Science Fund (FWF), through the SFB BeyondC (FWF Project No. F7109), and the IQI GmbH. This project has received funding from the European Union's Horizon 2020 research and innovation programme under the Marie Skłodowska-Curie Grant Agreement No. 840450. P.S. and M.M. acknowledge support from the Austrian Research Promotion Agency (FFG) contract 872766. P.S., T.M., and R.B. acknowledge funding from the Office of the Director of National Intelligence (ODNI), Intelligence Advanced Research Projects Activity (IARPA), via US ARO Grants No. W911NF-16-1-0070 and No. W911NF-20-1-0007, and the US Air Force Office of Scientific Research (AFOSR) via IOE Grant No. FA9550-19-1-7044 LASCEM. All statements of fact, opinions, or conclusions contained herein are those of the authors and should not be construed as representing the official views or policies of the funding agencies.

[1] D. Deutsch and R. Jozsa, in *Proceedings of the Royal Society of London, Series A* (The Royal Society, 1992), Vol. 439.

[2] P. W. Shor, in *Proceedings of the 35th Annual Symposium on Foundations of Computer Science, NM, Nov. 20–22* (IEEE Computer Society Press, Santa Fe, 1994), p. 124.

[3] M. H. Yung, J. Casanova, A. Mezzacapo, J. McClean, L. Lamata, A. Aspuru-Guzik, and E. Solano, From transistor to trapped-ion computers for quantum chemistry, Sci. Rep. **4**, 3589 (2014).

[4] J. Preskill, Quantum Computing in the NISQ era and beyond, Quantum **2**, 79 (2018).

[5] S. McArdle, S. Endo, A. Aspuru-Guzik, S. C. Benjamin, and X. Yuan, Quantum computational chemistry, Rev. Mod. Phys. **92**, 015003 (2020).

[6] B. Bauer, S. Bravyi, M. Motta, and G. K. L. Chan, arXiv: 2001.03685 (2020).

[7] F. Arute *et al.*, Quantum supremacy using a programmable superconducting processor, Nature **574**, 505 (2019).

[8] J. Zhang, G. Pagano, P. W. Hess, A. Kyprianidis, P. Becker, H. B. Kaplan, A. V. Gorshkov, Z. X. Gong, and C. Monroe, Observation of a many-body dynamical phase transition with a 53-qubit quantum simulator, Nature **551**, 601 (2017).

[9] H. Bernien *et al.*, Probing many-body dynamics on a 51-atom quantum simulator, Nature **551**, 579 (2017).

[10] X. L. Wang *et al.*, 18-Qubit Entanglement with Six Photons' Three Degrees of Freedom, Phys. Rev. Lett. **120**, 260502 (2018).

[11] C. H. Yang *et al.*, Operation of a silicon quantum processor unit cell above one kelvin, Nature **580**, 350 (2020).

[12] J. J. Pla, K. Y. Tan, J. P. Dehollain, W. H. Lim, J. J. L. Morton, D. N. Jamieson, A. S. Dzurak, and A. Morello, A single-atom electron spin qubit in silicon, Nature **489**, 541 (2012).

[13] P. Shor, in *37th Annual Symposium on Foundations of Computer Science (FOCS '96)* (IEEE, 1996), Vol. 00, p. 56.

[14] J. Benhelm, G. Kirchmair, C. F. Roos, and R. Blatt, Towards fault-tolerant quantum computing with trapped ions, Nat. Phys. **4**, 463 (2008).

[15] D. Nigg, M. Müller, E. A. Martinez, P. Schindler, M. Hennrich, T. Monz, M. A. Marting-Delgado, and R. Blatt, Quantum computations on a topologically encoded qubit, Science **345**, 302 (2014).

[16] C. J. Ballance, T. P. Harty, N. M. Linke, M. A. Sepiol, and D. M. Lucas, High-Fidelity Quantum Logic Gates Using Trapped-Ion Hyperfine Qubits, Phys. Rev. Lett. **117**, 060504 (2016).

[17] J. P. Gaebler, T. R. Tan, Y. Lin, Y. Wan, R. Bowler, A. C. Keith, S. Glancy, K. Coakley, E. Knill, D. Leibfried, and D. J. Wineland, High-Fidelity Universal Gate Set for $^{9}Be^{+}$ Ion Qubits, Phys. Rev. Lett. **117**, 060505 (2016).

[18] S. Zhang, Y. Lu, K. Zhang, W. Chen, Y. Li, J.-N. Zhang, and K. Kim, Error-mitigated quantum gates exceeding physical fidelities in a trapped-ion system, Nat. Commun. **11**, 1 (2020).

[19] T. Monz, D. Nigg, E. A. Martinez, M. F. Brandl, P. Schindler, R. Rhines, S. X. Wang, I. L. Chuang, and R. Blatt, Realization of a scalable shor algorithm, Science **351**, 1068 (2016).

[20] C. Figgatt, A. Ostrander, N. M. Linke, K. A. Landsman, D. Zhu, D. Maslov, and C. Monroe, Parallel entangling operations on a universal ion-trap quantum computer, Nature **572**, 368 (2019).

[21] C. Hempel, C. Maier, J. Romero, J. McClean, T. Monz, H. Shen, P. Jurcevic, B. P. Lanyon, P. Love, R. Babbush, A. Aspuru-Guzik, R. Blatt, and C. F. Roos, Quantum Chemistry Calculations on a Trapped-Ion Quantum Simulator, Phys. Rev. X **8**, 031022 (2018).

[22] K. K. Mehta, C. Zhang, M. Malinowski, T.-L. Nguyen, M. Stadler, and J. P. Home, Integrated optical multi-ion quantum logic, Nature **586**, 533 (2020).

[23] R. J. Niffenegger, J. Stuart, C. Sorace-Agaskar, D. Kharas, S. Bramhavar, C. D. Bruzewicz, W. Loh, R. T. Maxson, R. McConnell, D. Reens *et al.*, Integrated multi-wavelength control of an ion qubit, Nature **586**, 538 (2020).

[24] A. Crippa *et al.*, Gate-reflectometry dispersive readout and coherent control of a spin qubit in silicon, Nat. Commun. **10**, 1 (2019).

[25] M. C. Jarratt, A. Jouan, A. C. Mahoney, S. J. Waddy, G. C. Gardner, S. Fallahi, M. J. Manfra, and D. J. Reilly, arXiv:1903.07793 (2019).

[26] D. J. Reilly, in *2019 IEEE International Electron Devices Meeting (IEDM)* (IEEE, San Fransisco, 2019), p. 31.

[27] C. R. Clark, T. S. Metodi, S. D. Gasster, and K. R. Brown, Resource requirements for fault-tolerant quantum

simulation: The ground state of the transverse ising model, Phys. Rev. A **79**, 062314 (2009).
[28] D. Wecker, B. Bauer, B. K. Clark, M. B. Hastings, and M. Troyer, Gate-count estimates for performing quantum chemistry on small quantum computers, Phys. Rev. A **90**, 022305 (2014).
[29] T. Takeshita, N. C. Rubin, Z. Jiang, E. Lee, R. Babbush, and J. R. McClean, Increasing the Representation Accuracy of Quantum Simulations of Chemistry Without Extra Quantum Resources, Phys. Rev. X **10**, 011004 (2020).
[30] R. Babbush, D. W. Berry, J. R. McClean, and H. Neven, Quantum simulation of chemistry with sublinear scaling in basis size, npj Quantum Inf. **5**, 1 (2019).
[31] N. Moll, A. Fuhrer, P. Staar, and I. Tavernelli, Optimizing qubit resources for quantum chemistry simulations in second quantization on a quantum computer, J. Phys. A **49**, 295301 (2016).
[32] R. K. Brylinski and G. Chen, *Mathematics of Quantum Computation* (CRC Press, 2002).
[33] M. J. Bremner, C. M. Dawson, J. L. Dodd, A. Gilchrist, A. W. Harrow, D. Mortimer, M. A. Nielsen, and T. J. Osborne, Practical Scheme for Quantum Computation with Any Two-Qubit Entangling Gate, Phys. Rev. Lett. **89**, 247902 (2002).
[34] H. C. Nägerl, D. Leibfried, H. Rohde, G. Thalhammer, J. Eschner, F. Schmidt-Kaler, and R. Blatt, Laser addressing of individual ions in a linear ion trap, Phys. Rev. A **60**, 145 (1999).
[35] U. Warring, C. Ospelkaus, Y. Colombe, R. Jördens, D. Leibfried, and D. J. Wineland, Individual-Ion Addressing with Microwave Field Gradients, Phys. Rev. Lett. **110**, 173002 (2013).
[36] S. Mavadia, J. F. Goodwin, G. Stutter, S. Bharadia, D. R. Crick, D. M. Segal, and R. C. Thompson, Control of the conformations of ion coulomb crystals in a penning trap, Nat. Commun. **4**, 1 (2013).
[37] J. F. Goodwin, G. Stutter, R. C. Thompson, and D. M. Segal, Resolved-Sideband Laser Cooling in a Penning Trap, Phys. Rev. Lett. **116**, 143002 (2016).
[38] R. Stricker, Master's thesis, Universität Innsbruck, 2017.
[39] F. T. Chong, D. Franklin, and M. Martonosi, Programming languages and compiler design for realistic quantum hardware, Nature **549**, 180 (2017).
[40] P. A. Barton, C. J. S. Donald, D. M. Lucas, D. A. Stevens, A. M. Steane, and D. N. Stacey, Measurement of the lifetime of the 3d2D5/2 state in 40Ca+, Phys. Rev. A **62**, 032503 (2000).
[41] T. Ruster, C. T. Schmiegelow, H. Kaufmann, C. Warschburger, F. Schmidt-Kaler, and U. G. Poschinger, A long-lived Zeeman trapped-ion qubit, Appl. Phys. B **122**, 1 (2016).
[42] R. C. Thompson, Ion Coulomb crystals, Contemp. Phys. **56**, 63 (2015).
[43] D. Leibfried, R. Blatt, C. Monroe, and D. Wineland, Quantum dynamics of single trapped ions, Rev. Mod. Phys. **75**, 281 (2003).
[44] S. Ejtemaee and P. C. Haljan, 3D Sisyphus Cooling of Trapped Ions, Phys. Rev. Lett. **119**, 043001 (2017).
[45] Y. Castin, H. Wallis, and J. Dalibard, Limit of Doppler cooling, J. Opt. Soc. Am. B **6**, 2046 (1989).
[46] D. Maslov, Basic circuit compilation techniques for an ion-trap quantum machine, New J. Phys. **19**, 023035 (2017).
[47] A. Sørensen and K. Mølmer, Quantum Computation with Ions in Thermal Motion, Phys. Rev. Lett. **82**, 1971 (1999).
[48] H. Häffner, C. F. Roos, and R. Blatt, Quantum computing with trapped ions, Phys. Rep. **469**, 155 (2008).
[49] J. I. Cirac and P. Zoller, Quantum Computations with Cold Trapped Ions, Phys. Rev. Lett. **74**, 4091 (1995).
[50] A. Sørensen and K. Mølmer, Entanglement and quantum computation with ions in thermal motion, Phys. Rev. A **62**, 022311 (2000).
[51] C. F. Roos, Ion trap quantum gates with amplitude-modulated laser beams, New J. Phys. **10**, 013002 (2008).
[52] M. Guggemos, D. Heinrich, O. A. Herrera-Sancho, R. Blatt, and C. F. Roos, Sympathetic cooling and detection of a hot trapped ion by a cold one, New J. Phys. **17**, 103001 (2015).
[53] P. Schindler *et al.*, A quantum information processor with trapped ions, New J. Phys. **15**, 123012 (2013).
[54] K. Sheridan, W. Lange, and M. Keller, All-optical ion generation for ion trap loading, Appl. Phys. B **104**, 755 (2011).
[55] L. S. Ma, P. Jungner, J. Ye, and J. L. Hall, Time-domain measured resonant absorption-induced change in group delay of erbium-doped silica fibers, Opt. Lett. **19**, 177 (1994).
[56] S. Kim, R. R. McLeod, M. Saffman, and K. H. Wagner, Doppler-free, multiwavelength acousto-optic deflector for two-photon addressing arrays of rb atoms in a quantum information processor, Appl. Opt. **47**, 1816 (2008).
[57] J. D. Siverns, L. R. Simkins, S. Weidt, and W. K. Hensinger, On the application of radio frequency voltages to ion traps via helical resonators, Appl. Phys. B **107**, 921 (2012).
[58] K. G. Johnson, J. D. Wong-Campos, A. Restelli, K. A. Landsman, B. Neyenhuis, J. Mizrahi, and C. Monroe, Active stabilization of ion trap radiofrequency potentials, Rev. Sci. Instrum. **87**, 053110 (2016).
[59] V. Negnevitsky, Ph.D. thesis, ETH Zurich, 2018.
[60] B. Keitch, V. Negnevitsky, and W. Zhang, arXiv: 1710.04282 (2017).
[61] B. de Neeve, Master's thesis, ETH Zurich, 2017.
[62] R. Stricker, D. Vodola, A. Erhard, L. Postler, M. Meth, M. Ringbauer, P. Schindler, T. Monz, M. Müller, and R. Blatt, Experimental deterministic correction of qubit loss, Nature **585**, 207 (2020).
[63] Cirq website, https://cirq.readthedocs.io/en/stable/.
[64] Qiskit website, https://qiskit.org/.
[65] K. Dholakia, G. Z. K. Horvath, D. M. Segal, and R. C. Thompson, Photon correlation measurement of ion oscillation frequencies in a combined trap, J. Mod. Opt. **39**, 2179 (1992).
[66] S. Mavadia, G. Stutter, J. F. Goodwin, D. R. Crick, R. C. Thompson, and D. M. Segal, Optical sideband spectroscopy of a single ion in a penning trap, Phys. Rev. A **89**, 032502 (2014).
[67] C. Hempel, Ph.D. thesis, Universität Innsbruck, 2014.
[68] H. A. Fürst, Ph.D. thesis, University of Amsterdam, 2019.
[69] P. Micke *et al.*, Closed-cycle, low-vibration 4 K cryostat for ion traps and other applications, Rev. Sci. Instrum. **90**, 065104 (2019).

[70] T. Kessler, C. Hagemann, C. Grebing, T. Legero, U. Sterr, F. Riehle, M. J. Martin, L. Chen, and J. Ye, A sub-40-mHz-linewidth laser based on a silicon single-crystal optical cavity, Nat. Photonics **6**, 687 (2012).
[71] J. G. Hartnett, N. R. Nand, and C. Lu, Ultra-low-phase-noise cryocooled microwave dielectric-sapphire-resonator oscillators, Appl. Phys. Lett. **100**, 183501 (2012).
[72] K. Somiya, Detector configuration of KAGRA: The Japanese cryogenic gravitational-wave detector, Class. Quantum Gravity **29**, 124007 (2012).
[73] C. P. Aguirre *et al.*, Dark matter search with CUORE-0 and CUORE, Phys. Procedia **61**, 13 (2015).
[74] N. C. Brown and K. R. Brown, Comparing Zeeman qubits to hyperfine qubits in the context of the surface code: 174Yb+ and 171Yb+, Phys. Rev. A **97**, 052301 (2018).
[75] Q. A. Turchette, C. J. Myatt, B. E. King, C. A. Sackett, D. Kielpinski, W. M. Itano, C. Monroe, and D. J. Wineland, Decoherence and decay of motional quantum states of a trapped atom coupled to engineered reservoirs, Phys. Rev. A **62**, 053807 (2000).
[76] M. Brownnutt, M. Kumph, P. Rabl, and R. Blatt, Ion-trap measurements of electric-field noise near surfaces, Rev. Mod. Phys. **87**, 1419 (2015).
[77] I. Talukdar, D. J. Gorman, N. Daniilidis, P. Schindler, S. Ebadi, H. Kaufmann, T. Zhang, and H. Häffner, Implications of surface noise for the motional coherence of trapped ions, Phys. Rev. A **93**, 043415 (2016).
[78] R. J. Epstein, S. Seidelin, D. Leibfried, J. H. Wesenberg, J. J. Bollinger, J. M. Amini, R. B. Blakestad, J. Britton, J. P. Home, W. M. Itano, J. D. Jost, E. Knill, C. Langer, R. Ozeri, N. Shiga, and D. J. Wineland, Simplified motional heating rate measurements of trapped ions, Phys. Rev. A **76**, 033411 (2007).
[79] M. Brownnutt, M. Kumph, P. Rabl, and R. Blatt, Ion-trap measurements of electric-field noise near surfaces, Rev. Mod. Phys. **87**, 1419 (2015).
[80] E. Knill, D. Leibfried, R. Reichle, J. Britton, R. B. Blakestad, J. D. Jost, C. Langer, R. Ozeri, S. Seidelin, and D. J. Wineland, Randomized benchmarking of quantum gates, Phys. Rev. A **77**, 012307 (2008).
[81] R. Penrose, in *Philosophical Transactions of the Royal Society of London, Series A: Mathematical, Physical and Engineering Sciences* (The Royal Society, 1998), Vol. 356, p. 1927.
[82] R. Jozsa and N. Linden, in *Proceedings of the Royal Society of London, Series A: Mathematical, Physical and Engineering Sciences* (The Royal Society, 2003), Vol. 459, p. 2011.
[83] A. Datta and G. Vidal, Role of entanglement and correlations in mixed-state quantum computation, Phys. Rev. A **75**, 042310 (2007).
[84] P. Staanum, M. Drewsen, and K. Mølmer, Geometric quantum gate for trapped ions based on optical dipole forces induced by Gaussian laser beams, Phys. Rev. A **70**, 052327 (2004).
[85] K. Kim, C. F. Roos, L. Aolita, H. Häffner, V. Nebendahl, and R. Blatt, Geometric phase gate on an optical transition for ion trap quantum computation, Phys. Rev. A **77**, 050303(R) (2008).
[86] L. Amico, R. Fazio, A. Osterloh, and V. Vedral, Entanglement in many-body systems, Rev. Mod. Phys. **80**, 517 (2008).
[87] M. Bourennane, M. Eibl, C. Kurtsiefer, S. Gaertner, H. Weinfurter, O. Gühne, P. Hyllus, D. Bruß, M. Lewenstein, and A. Sanpera, Experimental Detection of Multipartite Entanglement Using Witness Operators, Phys. Rev. Lett. **92**, 087902 (2004).
[88] A. S. Sørensen and K. Mølmer, Entanglement and Extreme Spin Squeezing, Phys. Rev. Lett. **86**, 4431 (2001).
[89] T. Monz, P. Schindler, J. T. Barreiro, M. Chwalla, D. Nigg, W. A. Coish, M. Harlander, W. Hänsel, M. Hennrich, and R. Blatt, 14-Qubit Entanglement: Creation and Coherence, Phys. Rev. Lett. **106**, 130506 (2011).
[90] A. Omran *et al.*, Generation and manipulation of Schrödinger cat states in Rydberg atom arrays, Science **365**, 570 (2019).
[91] G. J. Mooney, G. A. L. White, C. D. Hill, and L. C. L. Hollenberg, arXiv: 2101.08946 (2021).
[92] D. Leibfried *et al.*, Creation of a six-atom 'Schrödinger cat' state, Nature **438**, 639 (2005).
[93] A. R. Milne, C. L. Edmunds, C. Hempel, F. Roy, S. Mavadia, and M. J. Biercuk, Phase-Modulated Entangling Gates Robust to Static and Time-Varying Errors, Phys. Rev. Appl. **13**, 024022 (2020).
[94] Y. Shapira, R. Shaniv, T. Manovitz, N. Akerman, and R. Ozeri, Robust Entanglement Gates for Trapped-Ion Qubits, Phys. Rev. Lett. **121**, 180502 (2018).
[95] R. Blümel, N. Grzesiak, N. H. Nguyen, A. M. Green, M. Li, A. Maksymov, N. M. Linke, and Y. Nam, arXiv: 2101.07887 (2021).
[96] K. Wright, K. Beck, S. Debnath, J. Amini, Y. Nam, N. Grzesiak, J.-S. Chen, N. Pisenti, M. Chmielewski, C. Collins *et al.*, Double-slit photoelectron interference in strong-field ionization of the neon dimer, Nat. Commun. **10**, 1 (2019).
[97] J. Werschnik and E. Gross, Quantum optimal control theory, J. Phys. B **40**, R175 (2007).
[98] K. Khodjasteh and L. Viola, Dynamically Error-Corrected Gates for Universal Quantum Computation, Phys. Rev. Lett. **102**, 080501 (2009).

Correction: Incorrect source information appeared in Ref. [20] and has been fixed.

5.3 Additional hardware details

Some details were omitted in the publication for the sake of limited interest to the general reader and therefore will be provided here. This section contains additional hardware details important for the future considerations in this work.

5.3.1 Light frequency control

It is worth mentioning some details of the frequency control of the laser light used to address ions (see Fig. 5.4). The laser light is generated by a diode laser designed by Toptica as a part of the AQTION collaboration ('Toptica 1 Hz system'). The laser is locked to a high-finesse cavity providing a linewidth ≈ 1 Hz. The laser light goes through a series of acousto-optical modulators (AOMs) and acousto-optical deflectors (AODs) before reaching the ion chain.

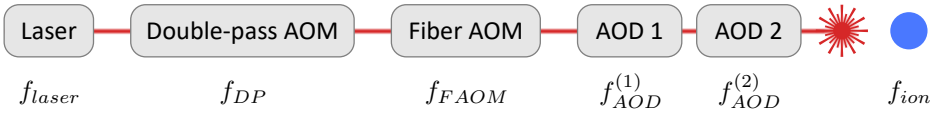

Figure 5.4: Schematic of the AOMs used to adjust the laser light frequency.

The frequency of the laser light after all the AOMs/AODs should be resonant with the qubit transition posing the following condition for the frequencies applied to the AOMs/AODs:

$$f_{laser} + 2f_{DP} + f_{FAOM} + f^{(1)}_{AOD} - f^{(2)}_{AOD} = f_{ion}. \tag{5.1}$$

Typical values for these frequencies are given in Tab. 5.1.

Every acousto-optical device in this chain plays a specific role which sets some limitations to the frequencies that are supplied to the device. The role of each device will be briefly discussed below.

Laser

The frequency of the light produced by the laser is fixed by the cavity lock:

$$f_{laser} = f_{cavity}(t). \tag{5.2}$$

However, if left undisturbed, the cavity shows a slow long-term length change resulting a in frequency drift ≈ 3 kHz/d on average. This drift must be compensated by other AOMs/AODs to satisfy condition in Eq. (5.1) at all times.

Fiber AOM

The fiber AOM is responsible for creation of multichromatic laser light required for two-qubit gates. For example, single qubit gates require a monochromatic light and

only one tone is supplied to the fiber AOM. On the other hand, MS gates require bichromatic light (see Sec. 4.4.3) and two tones are supplied to the fiber AOM.

The bichromatic light for MS gates should have equal power for both tones for a high fidelity gate. The two tones' frequencies can be chosen symmetrically around the central frequency f_c of the fiber AOM efficiency profile $I_{FAOM}(f)$:

$$I_{FAOM}(f_c - \Delta f) = I_{FAOM}(f_c + \Delta f), \tag{5.3}$$

where Δf is the frequency detuning from the carrier transition required for an MS gate.

Therefor, for a single-tone light the fiber AOM is supplied with one tone

$$f_{FAOM} = f_c, \tag{5.4}$$

while for the two-tone light it is supplied with two tones

$$\begin{aligned} f^{-}_{FAOM} &= f_c - \Delta f, \\ f^{+}_{FAOM} &= f_c + \Delta f. \end{aligned} \tag{5.5}$$

Addressing AODs

Two crossed acousto-optical deflectors (AODs) are used for single-ion addressing as described in Ref. 1. The AODs diffract to opposite sides resulting in opposite sign frequency shifts Eq. (5.1).

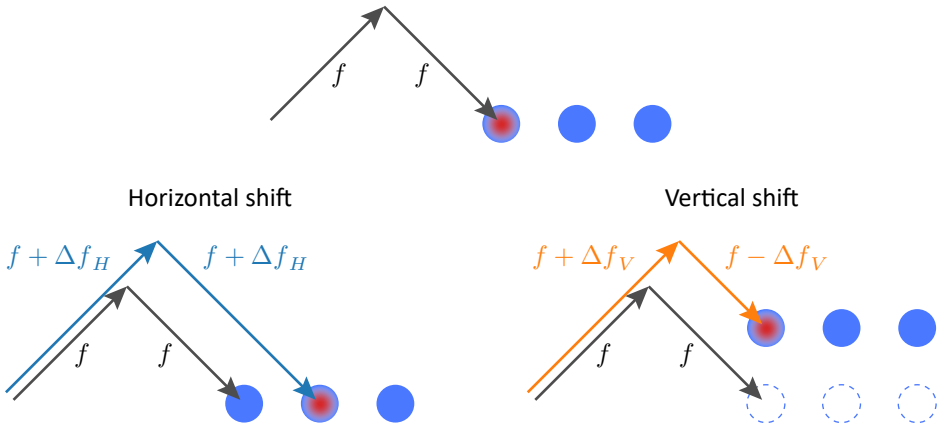

Figure 5.5: Principal scheme of the crossed AODs addressing unit.

The addressing system is aligned in a way that changing both AODs frequencies by the same value Δf_H results in a horizontal shift of the addressed spot (see Fig. 5.5). The frequencies required to address each ion can be calibrated by sweeping the frequency of both AODs simultaneously. After the calibration we get a lookup table for addressing frequencies $\{f_j\}$ for each ion. The AODs are supplied with the following frequencies to address ion j:

$$\begin{aligned} f^{(1)}_{AOD} &= f_j, \\ f^{(2)}_{AOD} &= f_j. \end{aligned} \tag{5.6}$$

However, sometimes the 'addressed line' can shift vertically relatively to the ion chain due to long-term temperature drifts and fluctuations. This can be compensated by changing the AOD frequencies by a small amount Δf_V with opposite sign:

$$f_{AOD}^{(1)} = f_j + \Delta f_V, \qquad (5.7)$$
$$f_{AOD}^{(2)} = f_j - \Delta f_V.$$

This leads to a vertical shift of the addressed spot which can compensate the vertical drift. However, the frequency shift introduced by the addressing system is no longer 0, but instead $f_{AOD}^{(1)} - f_{AOD}^{(2)} = 2\Delta f_V$ and should be accounted for to satisfy condition in Eq. (5.1).

Double-pass AOM

The double-pass (DP) AOM is responsible for pulse shaping of the laser light. Other AOMs/AODs are constantly supplied with fixed RF power during the pulse sequence to keep the temperature of the crystals at the same level and avoid unpredictable behavior due to thermalization processes. On the contrary, the RF power supplied to the DP AOM is varied depending on the required Rabi frequency and timed precisely to provide the necessary interaction time, e.g. for a π-pulse.

Moreover, the DP AOM is used to bridge the frequency gap between the laser light frequency and the qubit transition (see Eq. (5.1)). Changes in frequency of the laser or other AOMs/AODs like the cavity drift (see Eq. (5.2)) or AOD vertical shift (see Eq. (5.7)) can be compensated by the DP AOM frequency f_{DP}. Different Zeeman sub-levels or motional sidebands can be excited by changing the frequency of the DP AOM as well.

Table 5.1: Typical values for the laser and the AOM/AOD frequencies.

	Frequency (MHz)
f_{laser}	$\approx$ 411 041 699
f_{DP}	$[185, 210]$
f_{FAOM}	146.85
f_{AOD}	$[100, 120]$

5.3.2 Addressing system performance

The addressing system plays a crucial role in the implementation of single-qubit and two-qubit gates in the AQTION system. One of the error sources for these gates is the optical crosstalk coming from the addressing system delivering the laser light. The problem is more pronounced for optical qubits than for Zeeman or hyperfine qubits since the latter are often driven with Raman beams. The coupling of Raman beams to a qubit of these types is proportional to the square of the electric field

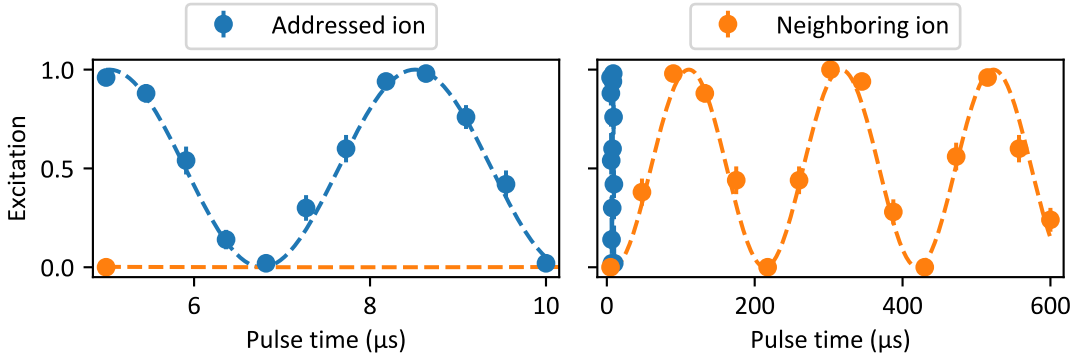

Figure 5.6: An example of crosstalk in 16-ion chain. The Rabi flops of the addressed ion, ion 8 (left) and the Rabi flops of the neighboring ion, ion 9 (right).

amplitude $\Omega_{Raman} \sim E^2$, while a single optical beam driving an optical qubit has a coupling $\Omega_{optical} \sim E$. This is also true for the crosstalk, thus, the requirements for an addressing setup for an optical qubit are more stringent.

The AOD addressing unit crosstalk characterization in Ref. 1 was extended to 16- and 50-ion chains. An example of crosstalk in 16-ion chain is shown in Fig. 5.6: ion 8 is addressed, while ion 9 experiences Rabi flops with ≈ 60 times lower Rabi frequency.

The crosstalk characterization data for 16- and 50-ions chains is shown in Fig. 5.7. Crosstalk amplitude is defined as the ratio of the Rabi frequency the crosstalk ion experiences to the Rabi frequency of the target ion

$$\varepsilon = \frac{\Omega_{crosstalk}}{\Omega_{target}}. \tag{5.8}$$

Some values are given in Tab. 5.2. The larger crosstalk values for the 50-ion chain can be explained by a lower inter-ion distance compared to the 16-ion chain. This is a result of weaker axial confinement since it requires undesirably high RF power to keep the 50-ion chain out of zig-zag configuration with the same axial confinement as for the 16-ion chain. However, the mean crosstalk for the neighbors in only slightly higher for the 50-ion chain. It indicates that the addressing system performance should not limit the setup's performance when working with 50 ions. It will be discussed in the Ch. 6 that the main limitation for increasing the number of ions is the two-qubit gate performance degradation due to the complexity of the motional mode spectrum, but not the addressing system.

Table 5.2: Some crosstalk values for the 16- and 50-ion chains.

	16 ions	50 ions
Max. crosstalk (%)	1.65(3)	3.29(5)
Mean next-neighbor crosstalk (%)	0.9(5)	1.0(8)

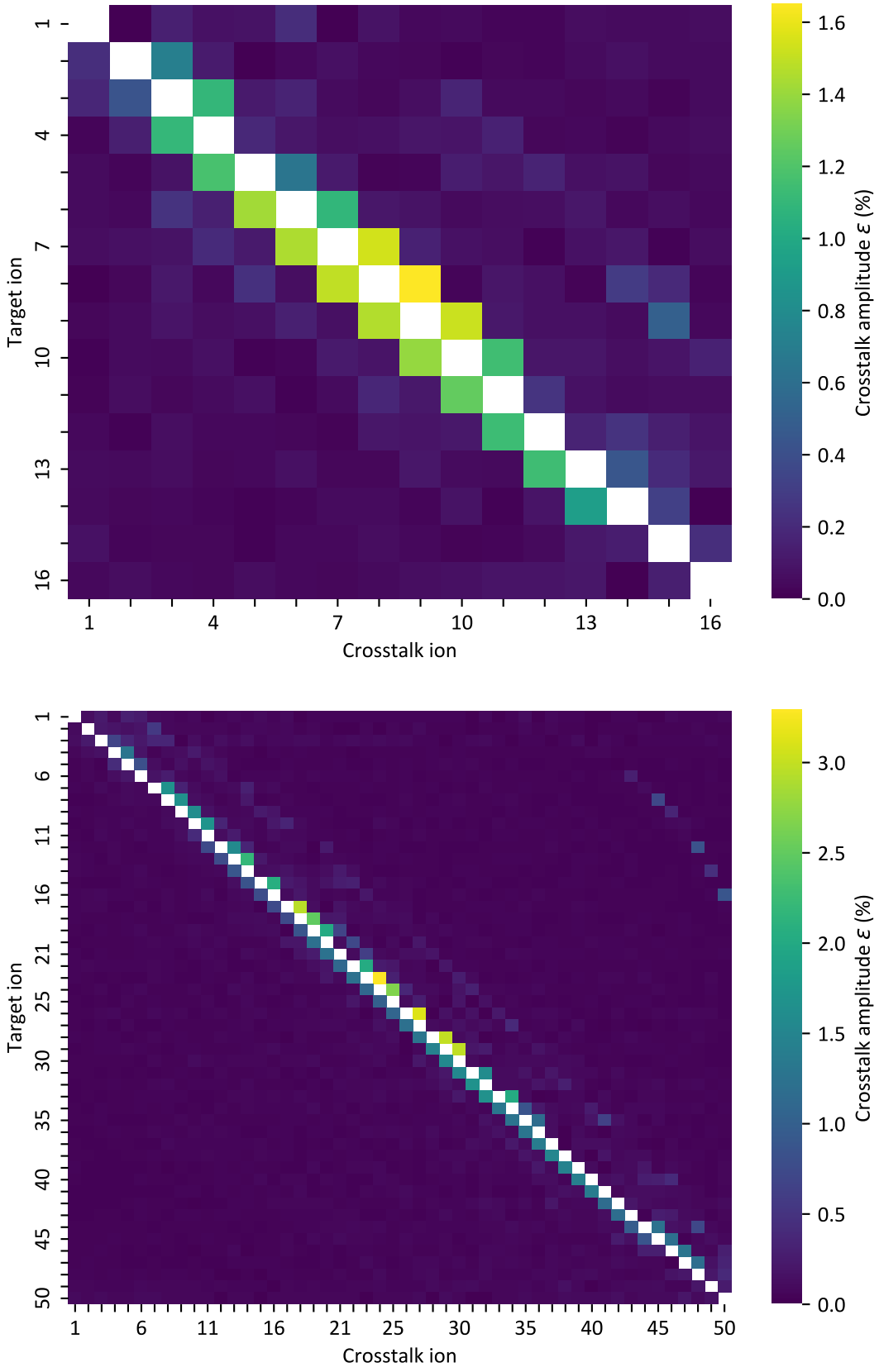

Figure 5.7: Crosstalk characterization matrices for a 16-ion chain (top) and a 50-ion chain (bottom).

Chapter 6

Working with long ion chains

The AQTION project aimed at operating with medium-sized qubit registers, i.e. working with medium-long ion chains in a single potential well. The complexity of the system increases significantly when the numbers of ions in the potential well is increased. A lot of details have to be taken into account to retain the same level of performance when increasing the number of ions.

Our system has been calibrated, tested and operated mostly with 16 ions. This chapter describes the details of operating the setup with a 16-ion chain. Various aspects and problems stemming from the complexity of the motional spectrum are discussed. Most of the ideas and principles also apply to longer chains.

6.1 MS gates in long chains

One of the main challenges for scaling the number of qubits in trapped-ion systems with a single potential well is two-qubit gates. There are two main issues to address here.

Firstly, the complexity of the motional mode spectrum plays an important role. Two-qubit gates in trapped-ion systems usually utilize common motional modes of the ion crystal (see Sec. 4.2 and Sec. 4.4.3). The number of the motional modes involved in two-qubit gates increases with the number of ions in the chain. It often follows that performing a high-fidelity MS gate becomes more challenging because there are more conditions to satisfy as discussed in Sec. 4.4.4.

Secondly, it would be ideal to be able to perform a two-qubit gate between any two ions in the chain for better connectivity. This might require tuning a two-qubit gate for every ion pair individually making calibration efforts for the two-qubit gates scale rapidly with the number of ions in the chain. However, the implementation of MS gates can be tailored to mitigate the required calibration efforts. More details on the calibration procedures are given in Sec. 6.2.

This section discusses the implementation of MS gates in the AQTION setup with the focus on maintaining high gate fidelity in long chains while keeping the number of calibration parameters low.

6.1.1 Radial modes

Two-qubit gate interaction in the AQTION setup is mediated through the radial motional modes of the crystal due to the specifics of the single ion addressing setup.

The addressing system is arranged such that the addressing laser beam comes at 90° angle to the ion chain. This means that the wave vector $\vec{k}$ has negligible overlap with the axial modes (along the chain), but has a substantial overlap with the radial modes (perpendicular to the chain). The radial modes are made non-degenerate by applying a $V_{bias} = 1.5\,\mathrm{V}$ bias voltage to the DC blades of the Paul trap (see Fig. 6.1). This splits the radial spectrum into two sets of modes along perpendicular axes, the x-axis and the y-axis. We will refer to these sets as radial-x modes and radial-y modes, respectively. The radial-y modes experience higher confinement than the radial-x modes due to the bias voltage. Hence, the radial-y mode spectrum is shifted higher in frequency by around 80 kHz relatively to the radial-x spectrum. The overlap of the addressed beam wave vector with the radial-x and the radial-y modes is close to equal.

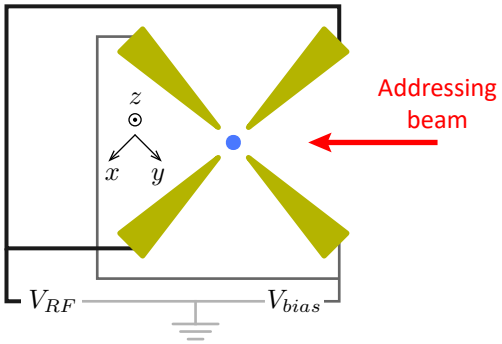

Figure 6.1: Sketch of the trap blades' orientation relatively to the addressing beam. The ion chain is aligned along the z-axis.

A typical motional mode spectrum for realistic experimental parameters is shown in Fig. 6.2. The spectrum was calculated using Eq. (4.12 – 4.14). The γ_p coefficient in Eq. (4.11) can be calculated separately for x and y modes to account for the shift from the bias voltage. The following parameters were used:

$$\begin{aligned} f_z &= 380\,\mathrm{kHz}, \\ f_x &= 3080\,\mathrm{kHz}, \\ f_y &= 3160\,\mathrm{kHz}. \end{aligned} \tag{6.1}$$

These values are close to the ones observed in the experimental setup.

Different modes have different coupling to different ions. This is described by the eigenvector $c_p^{(j)}$ corresponding to mode p (see Eq. (4.10)). Some eigenvectors for the 16-ion chain are shown in Fig. 6.3. We will refer to mode 1 as the COM-mode (center-of-mass) since all the ions move together as one because they have the same coupling to mode 1. It should be noted that some modes can only be excited if specific ions are addressed, e.g. mode 2 can barely be excited while addressing ions 8 or 9 since they have negligible coupling to this mode.

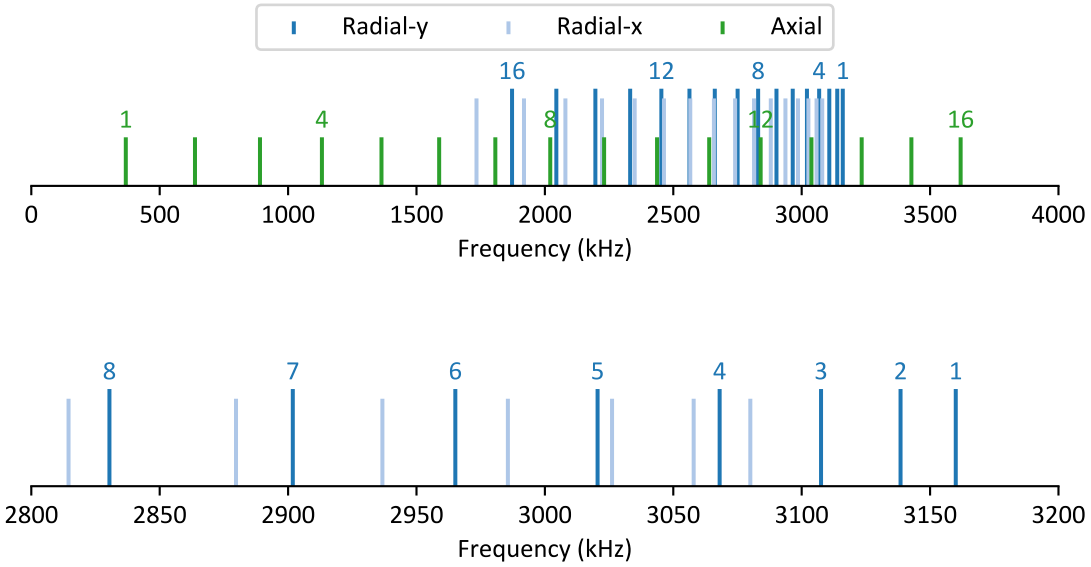

Figure 6.2: Spectrum of the motional modes of the 16-ion chain with the parameters specified in Eq. (6.1). Numbers above lines show mode indices (see Fig. 6.3).

6.1.2 Radial spectrum in the experiment

The real experimental spectrum of the radial modes can be measured by scanning the frequency of the DP AOM around the qubit transition and exciting BSB transitions of the radial modes. We address two ions subsequently, namely ion 1 and ion 8, to measure the spectrum since it is hard to probe all modes with the same ion. Using an outer ion and a middle ion is quite convenient when identifying high-frequency radial modes, because the spectrum is crowded in that frequency region. For example, mode 2 is coupled to ion 1 and almost not coupled to ion 8 which allows one to identify it in the scan (see Fig. 6.4).

The axial modes can also be seen in the scan. This might happen due to the addressing beam being not perfectly perpendicular to the ion chain or because of the not perfectly aligned addressed beam creating transversal gradient having a projection on the axial direction. Nevertheless, the frequencies of the COM modes can be determined from the scan, including the axial COM mode:

$$\begin{aligned} f_z &= 368.7\,\mathrm{kHz}, \\ f_x &= 3082.4\,\mathrm{kHz}, \\ f_y &= 3164.8\,\mathrm{kHz}. \end{aligned} \tag{6.2}$$

However, if these values are used to calculate the rest of the spectrum both radial-y mode 16 and radial-x mode 16 will be off by about 360 kHz. This might be due to the fact that the model used for the calculations assumes a symmetric potential and does not take micromotion compensation electrodes into account. Certainly, a more complicated model can be employed, but we decided to replace the actual axial COM mode frequency with an 'effective' $f_z^{(eff)}$ and use it for calculations instead of

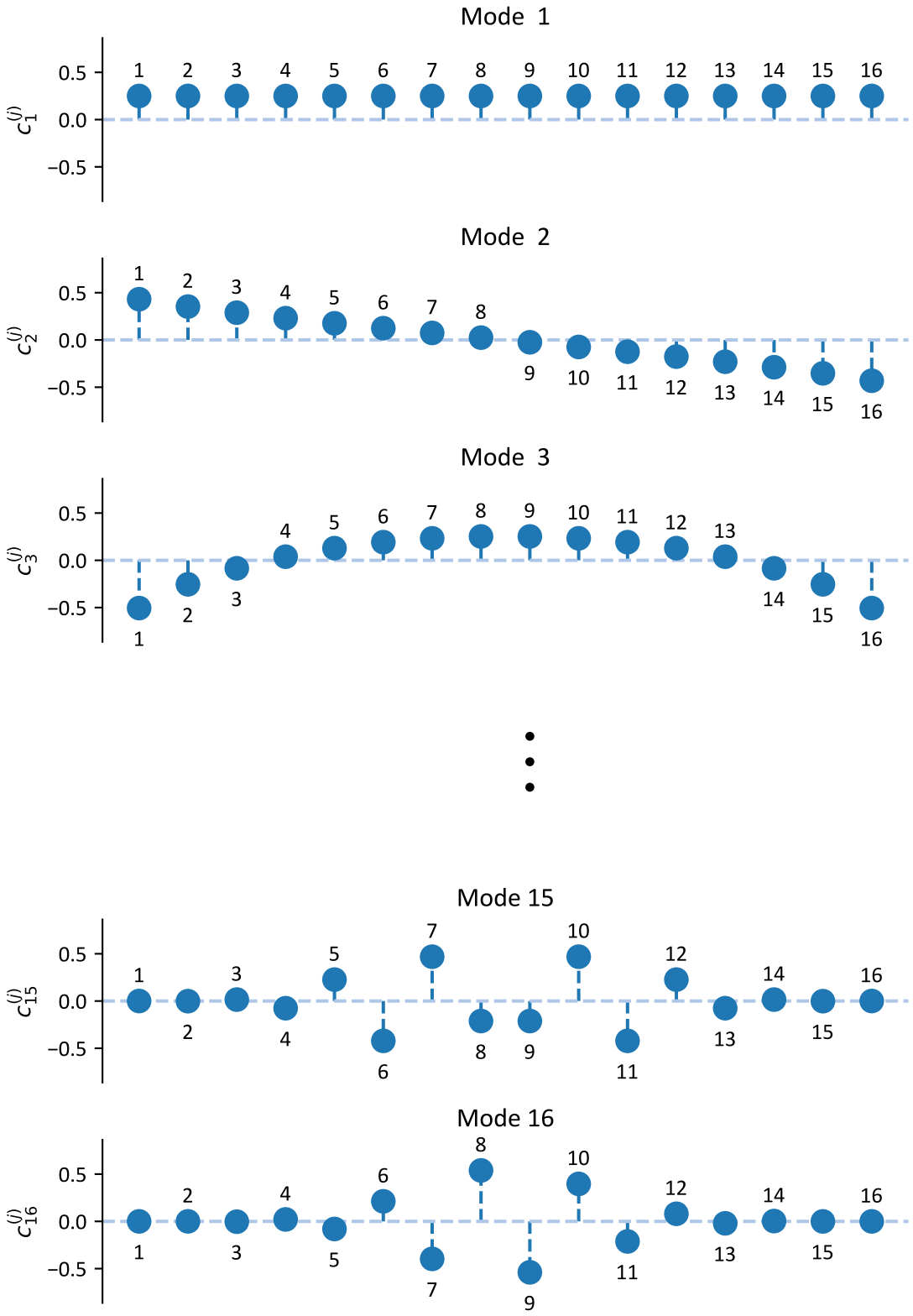

Figure 6.3: Eigenvectors of the motional modes of the 16-ions chain. The eigenvectors define the coupling of each ion to a specific mode.

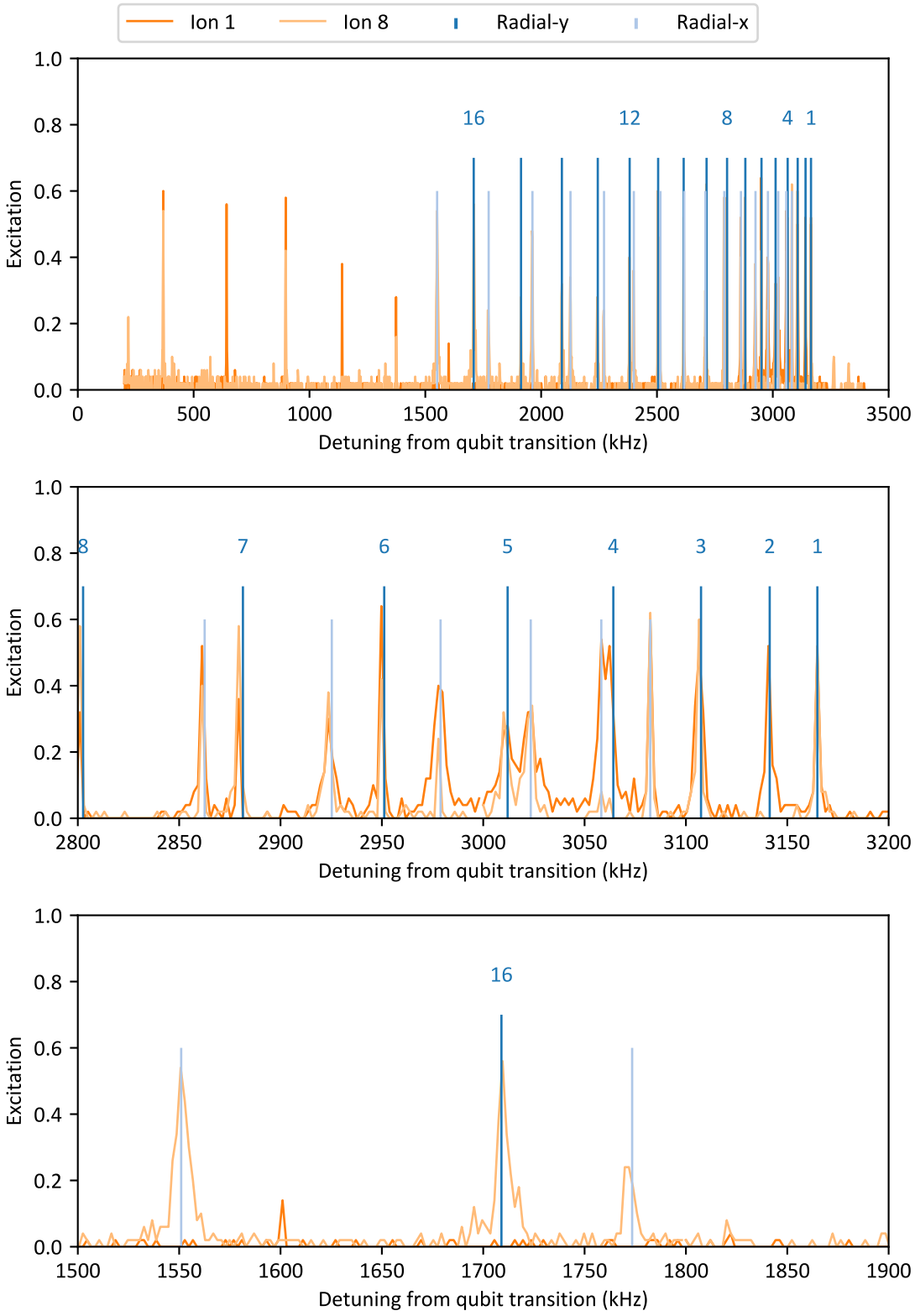

Figure 6.4: Experimentally measured spectrum of the motional modes of a 16-ion chain. The radial mode frequencies are predicted using COM mode values from Eq. (6.3). Numbers above the lines indicate mode numbers (see Fig. 6.3).

the real one. The value is chosen such that radial-x mode 16 matches the measured experimental value:

$$\begin{aligned} f_z^{(eff)} &= 385.06\,\text{kHz} \\ f_x &= 3082.4\,\text{kHz}, \\ f_y &= 3164.8\,\text{kHz}. \end{aligned} \tag{6.3}$$

The resulting prediction of the spectrum matches the measured spectrum within a few kHz which is enough for our goals (see Fig. 6.4). These values can fluctuate from day to day and calibration procedures are performed to keep track of these values. We will use approximate values for the future calculations throughout this work:

$$\begin{aligned} f_z^{(eff)} &= 384\,\text{kHz} \\ f_x &= 3080\,\text{kHz}, \\ f_y &= 3160\,\text{kHz}. \end{aligned} \tag{6.4}$$

The frequencies of the axial modes are not important for considerations in this work due to the small overlap of the addressing beam with them.

6.1.3 MS gates with radial modes

One of the goals of this work is to be able to perform a high-fidelity two-qubit MS gate with any pair of ions. The addressing beam geometry dictates the usage of radial motional modes for this purpose. In principle, an MS-type interaction can be mediated through any motional mode both ions of the pair have non-zero coupling to. In this work we use the radial-y COM mode for MS gates but other scenarios are also possible. An advantage of COM modes is that all ions are equally coupled to it. This means that MS gate parameters for different pairs will be the same if only a COM mode participates in the interaction. In reality they do vary because of the presence of the other modes[1]. Nevertheless, the radial-y COM mode has spectator motional modes only at lower frequencies while there are no radial motional modes at higher frequencies (see Fig. 6.2). This makes the radial-y COM mode preferable over the radial-x COM mode.

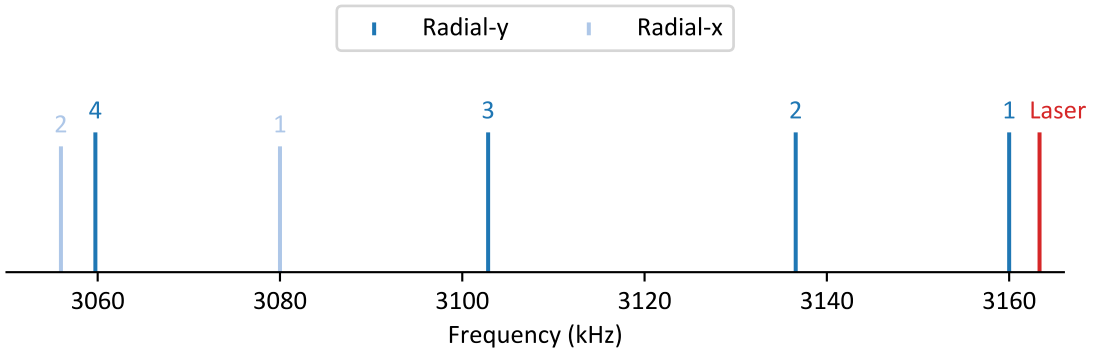

Figure 6.5: Spectral configuration of the radial motional modes of a 16-ion chain and the blue component of the bichromatic laser light used for MS gates.

Bichromatic light for an MS gate should be spectrally close to the motional mode used to mediate interaction, i.e. the radial-y COM mode in our case. The exact frequency of the bichromatic tones depends on the gate time of the MS gate as described in Sec. 4.4.3. In this work we mostly use MS gates with gate time $t_{gate} = 300\,\mu s$. The choice of this gate time is mostly determined by the contribution of the other motional modes[1]. For a 'single-loop' MS gate the detuning of the bichromatic tones from the motional mode should be $\delta = 1/t_{gate} \approx 3.3\,kHz$. A 'single-loop' gate means that the motional mode experiences only one period of oscillation[2] (see Eq. (4.39)).For our experiment the blue component of the bichromatic laser light is shown in Fig. 6.5. The laser line is close in frequency to the radial-y COM mode and much further away from other motional modes. Hence, mostly the radial-y COM mode is excited during the gate, while the effect of the other modes is small. Radial-y mode 2 has the second largest contribution to gates fidelity[1]. One

[1]The effect of the other motional modes on MS gates will be quantitatively discussed in Sec. 6.1.6
[2]Here and in the following we will be talking about mode oscillations as periodic trajectories in the ions' phase space (see Eq. (4.38)) in the rotating frame (see Eq. (4.28)), not their laboratory-frame oscillations.

can see that using the radial-x COM mode as the main mode for MS gates is more difficult since radial-y modes 3 and 4 are very close to the radial-x COM and will affect the gate as well as other motional modes (radial-y mode 2 and radial-x mode 2).

Using a COM mode has its challenges. Firstly, a COM mode often has higher heating rates than other modes due to its higher overlap with typical spatial distribution of the electromagnetic field noise. Secondly, the radial spectrum is much more 'crowded' around COM modes than e.g. around radial-y mode 16 (see Fig. 6.2). This means that a lot of modes are involved in the process which makes MS gates harder to implement correctly. The heating rate problem is not that crucial for the AQTION setup since we have very low heating rates as shown in Ref. 1.

However, the problem of mode crowding is important and gets more prominent with more ions in the chain. Other modes can be used for MS gates but COM modes are the only modes which can be used to entangle any pair of ions due to their uniform coupling profile. Any other approach would require picking different main motional modes for MS gates for different ion pairs. This has not been explored experimentally in the AQTION setup yet but has been demonstrated in other setups around the world [93, 100, 101].

6.1.4 Sideband cooling

Theoretically, MS gates can achieve high fidelities even if the motional mode mediating the interaction is not ground-state cooled. Practically, implementing an MS gate with hot motional modes makes calibration of the gate parameters harder and increases the sensitivity to miscalibrations [87]. In the AQTION setup we near-ground-state cool all radial motional modes as a part of the initialization of the ion chain.

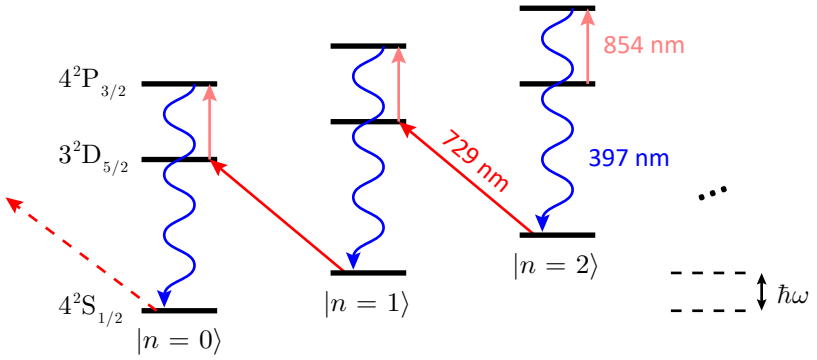

Figure 6.6: Scheme of the sibeband cooling technique.

We use the sideband cooling technique (SBC) [83, 102] to cool radial motional modes (see Fig. 6.6). SBC has a low cooling limit but it is relatively slow and has a relatively narrow bandwidth compared to other cooling techniques. For example, in the AQTION setup the radial-y COM mode is cooled to $n = 0.02(1)$ phonons which would take three cooling cycles $\approx 500\,\mu s$ each with $\approx 100\,kHz$ cooling bandwidth.

Other radial modes have to be cooled separately due to the narrow bandwidth of SBC.

There are other promising cooling techniques like polarization gradient cooling or electromagnetically induced transparency cooling. These techniques allow for faster, higher-bandwidth cooling at the cost of a higher cooling limit. They can be applied before SBC to significantly reduce overall cooling time. More details on these cooling techniques can be found in Ref. 78, 103. Unfortunately, space restrictions and available beam geometries in the AQTION setup make it difficult to implement either of these techniques in a conventional way.

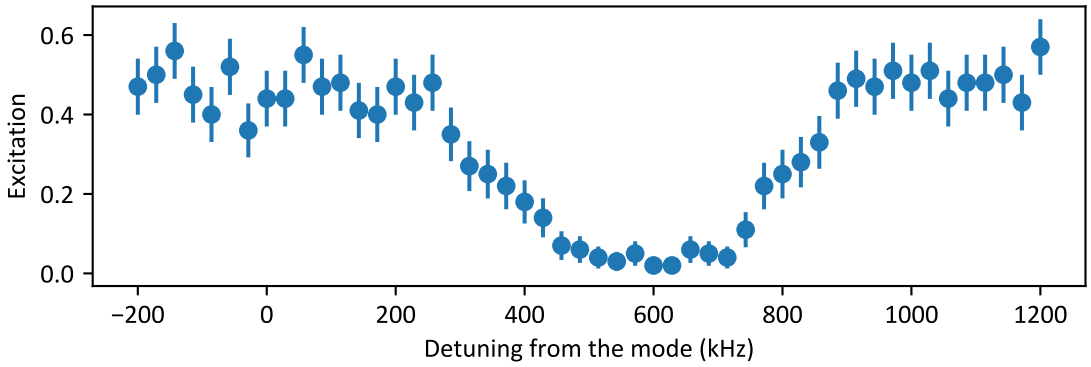

Figure 6.7: SBC of the radial-y COM mode. Laser light detuning is varied while the RSB of the mode is probed.

The time required to cool all the radial modes with SBC can be optimized if several motional mode can fit into the cooling bandwidth. First of all, we characterized the cooling bandwidth while cooling a single radial mode. The detuning of the 729 nm laser light used for cooling was varied while the RSB transition of the cooled radial mode was probed (see Fig. 6.7). Low excitation of the RSB transition indicates that the mode is close to the ground state (see Fig. 6.6). The optimal frequency of the cooling light is different from the RSB transition frequency by around 600 kHz due to the AC Stark shift of the transition. Cooling performance can vary from day to day resulting in variations of the width of the dip in Fig. 6.7. Therefore, we conservatively estimate our cooling bandwidth as at least 100 kHz.

As a consequence, we can assume that when we cool with laser light of a certain frequency we cool all the modes in a 50 kHz vicinity. We arrange our cooling light frequencies in a way that it covers the most modes. Cooling pulses of different frequencies are applied sequentially. The distribution of the cooling frequencies can be seen in Fig. 6.8. Radial-y modes 1 and 2 are cooled separately due to their high involvement in MS gates. This scheme allows us not to cool every mode separately and save some time.

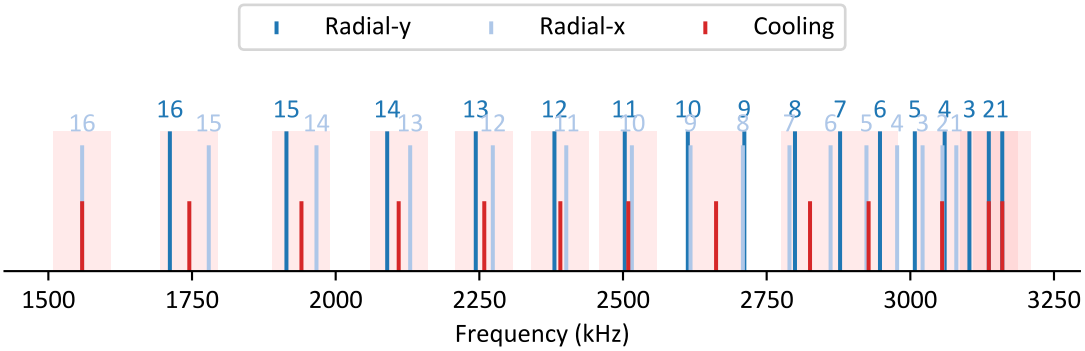

Figure 6.8: Distribution of cooling frequencies to cool all radial modes. Light red patches illustrate cooling bandwidth of 100 kHz.

MS gates with partial cooling

It was mentioned above that it is easier to achieve higher fidelities for MS gates when the motional modes involved are cold. The first radial modes are involved the most in MS gates operations close to the radial-y COM mode. Hence, cooling of the first radial modes is the most crucial and has the highest effect on the fidelity of the MS gates. However, we also observe a substantial effect of the cooling of the last modes. The effect varies depending on the ion pair, e.g. ion pair 1-16 should not be influenced by a radial mode 16 while ion pair 8-9 should due to their couplings to the modes (see Fig. 6.3).

The experimentally measured fidelities for MS gates for different cooling settings are given in Tab. 6.1. Cooling of radial-y mode 16 and radial-x mode 16 has a high impact on pair 8-9 but not on pair 1-16. Pair 1-16 mostly suffers when radial-y mode 2 is not cooled. We believe that the influence of the modes which are far away in frequency might happen due to higher order components in the Taylor expansion in the Lamb-Dicke parameter η in Eq. (4.29), i.e. second orders of the motional modes or mode intercombinations. These second orders or intercombinations might end up close in frequency to the bichromatic tones and be involved in the MS gate according to their coupling to an ion pair. However, this effect is substantially suppressed when modes are cold. We conclude that cooling of all radial modes is necessary to achieve high fidelities for MS gates on various pairs.

6.1.5 MS gates with three tones

In the experiment, spectral considerations for MS gates discussed in Sec. 6.1.3 should be extended by taking into account the AC Stark shift induced by off-resonant bichromatic light. The two tones are detuned from the qubit transition as follows:

$$\begin{aligned} f_{\mathrm{MS}}^{+} &= f_q + f_{\mathrm{y,COM}} + \delta \\ f_{\mathrm{MS}}^{-} &= f_q - f_{\mathrm{y,COM}} - \delta. \end{aligned} \tag{6.5}$$

Table 6.1: MS gate fidelities for ion pairs 1-16 and 8-9 for different cooling settings.

SBC cooled radial modes x / y	MS gate fidelity (%)	
	Pair 1-16	Pair 8-9
None / None	45.4 ± 1.5	54.0 ± 1.5
None / 1	85.6 ± 1.1	50.2 ± 1.8
None / 1–2	90.8 ± 1.7	53.0 ± 1.7
1–14 / 1–15	96.0 ± 1.4	75.8 ± 1.9
1–16 / 1–16	98.0 ± 1.1	96.0 ± 1.1

Here f_q is the combination of AOM frequencies required to resonantly excite the qubit transition (see Sec. 5.3.1), $f_{\mathrm{y,COM}}$ is the frequency of the radial-y COM mode and δ is the detuning chosen for MS gates (see Sec. 6.1.3). The latter two are supplied to the FAOM.

These two off-resonant tones lead to an AC Stark shift of the qubit transition $f'_q = f_q + \Delta f_{AC}$ (see Eq. (4.22)). The total shift is a combination of AC Stark shifts from different transitions, mainly between Zeeman sub-levels of $4^2\mathrm{S}_{1/2}$ and $3^2\mathrm{D}_{5/2}$:

$$\Delta f_{AC} = \sum_{m_j^{(S)}} \sum_{m_j^{(D)}} \Delta f_{m_j^{(S)} \to m_j^{(D)}}. \tag{6.6}$$

The shift of the qubit transition leads to the two tones of the laser light being shifted relatively to the motinal mode spectrum. Thus, the detunings of the two tones from the RSB and BSB of the radial-y COM mode are incorrect (and unequal) (see Fig. 6.5). The AC Stark shift of the qubit transition must be mitigated in some way for MS gates to work as intended (see Fig. 6.9).

Centerline detuning

One of the ways to solve this is what we call 'centerline detuning'. Both tones can be adjusted in frequency to account for the AC Start shift:

$$\begin{aligned} f'^{+}_{\mathrm{MS}} &= f^{+}_{\mathrm{MS}} + \Delta f_{AC} \\ f'^{-}_{\mathrm{MS}} &= f^{-}_{\mathrm{MS}} + \Delta f_{AC}. \end{aligned} \tag{6.7}$$

Therefore, the detuning from the qubit transition will be back to the desired value for MS gates:

$$\begin{aligned} f'^{+}_{\mathrm{MS}} - f'_q &= f^{+}_{\mathrm{MS}} - f_q = +f_{\mathrm{y,COM}} + \delta \\ f'^{-}_{\mathrm{MS}} - f'_q &= f^{-}_{\mathrm{MS}} - f_q = -f_{\mathrm{y,COM}} - \delta. \end{aligned} \tag{6.8}$$

A major problem of this technique for long ions chains (N ions) is that MS gates for different ions pairs might require slightly different optical powers of the tones. Hence,

gates for different ion pairs will have different AC Stark shift values Δf_{AC} since it depends on power of the tones. This will lead to $\sim N^2$ calibration parameters to make all MS gates in the chain work. Such an approach seems infeasible for long chains given the calibration overhead. The following approach can solve this problem.

Third tone

One can introduce a third tone to the previously bichromatic light. The idea of the third tone is adding more AC Stark shift $\Delta f_{AC}^{(3)}$ and canceling the AC Stark shift from the previous two tones entirely, i.e. $\Delta f_{AC} = \Delta f_{AC}^{(1+2)} + \Delta f_{AC}^{(3)} = 0$. In the end, the following three tones are supplied to the FAOM during an MS gate:

$$f_{\mathrm{MS}}^{+} = f_q + f_{\mathrm{y,COM}} + \delta \tag{6.9}$$

$$f_{\mathrm{MS}}^{-} = f_q - f_{\mathrm{y,COM}} - \delta \tag{6.10}$$

$$f_{\mathrm{MS}}^{(3)} = f_q + f^{(3)}. \tag{6.11}$$

The exact frequency of this tone does not matter that much. We choose it such that it sits away from any motional mode frequencies: $f^{(3)} = 550\,\mathrm{kHz}$. The power of the third tone should be adjusted such that the total AC Stark shift for the qubit transitions is zero: $\Delta f_{AC} = 0$.

The issue with the power for different ion pairs is solved automatically here. The power adjustment for different ion pairs happens at the DP AOM (see Sec. 5.3.1). The power is changed for all three tones simultaneously since the tones are combined in the FAOM. Consequently, all AC Stark shifts are scaled in the same way and the resulting shift is kept at zero: $\Delta f_{AC} = 0$. Moreover, this makes MS gates with the third tone more robust against optical power fluctuations. However, there is still a need to use different DP AOM powers for different ion pairs, which will be discussed in Sec. 6.1.6.

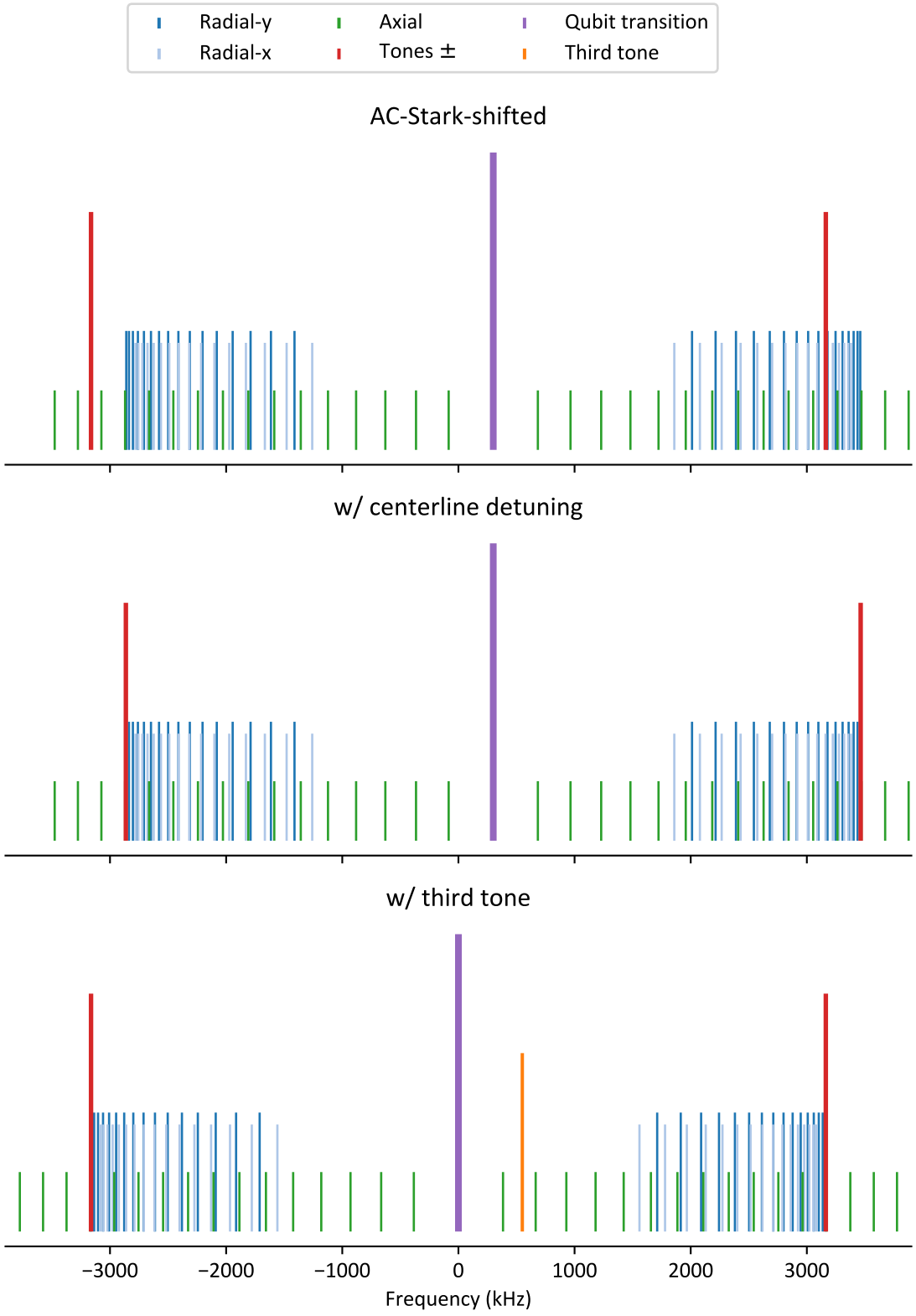

Figure 6.9: (top) Spectrum is displaced due to the AC Stark shift induced by the bichromatic light for an MS gate. The MS gate does not work. (center) Both tones are shifted together to match the AC Stark shift. The MS gate works. (bottom) Third tone is introduced to compensate the AC Stark shift. The MS gate works.

6.1.6 Effect of spectator modes on MS gates

MS gates in the AQTION setup use the radial-y COM mode (see Sec. 6.1.3). The tones of the bichromatic light for an MS gate are set close to the radial-y COM mode in frequency as in Fig. 6.5. The frequency of the tones is always set further from the qubit transition than the radial-y COM mode frequency to reduce the involvement of the other radial modes in MS gates. Nevertheless, other radial modes affect the behavior of MS gates.

A general MS interaction should satisfy conditions in Eq. (4.48 – 4.49) to implement a maximally entangling XX-gate. Essentially, this means that:

1. All motional modes should be decoupled from the qubit system at the end of the interaction (see Eq. (4.48))
2. The geometric phase accumulated during the interaction should be $\pm\frac{\pi}{2}$ (see Eq. (4.49))

If condition 1 is satisfied, condition 2 can be satisfied by scaling the overall optical power[3] of the light used for MS interaction until the geometric phase is equal to $\pm\frac{\pi}{2}$.

Let us imagine for now that there is only one motional mode to interact with – the radial-y COM mode with the frequency $f_{\mathrm{y,COM}}$. The tones of the bichromatic light are detuned from the mode by δ (see Eq. (6.9 – 6.10)). The oscillation of the mode population during the MS gate will happen at frequency δ. Condition 1 would require any motional mode to return back to the state it was before the gate. The radial-y COM mode will be decoupled from the qubit state at the following moments of time after the MS interaction starts:

$$t_{\mathrm{y,COM}}(k) = k\frac{1}{\delta}, \qquad k \in \mathbb{N}. \tag{6.12}$$

The number k indicates how many periods of oscillation the mode has experienced during the gate. We usually do a 'single-loop' gate, i.e. $k = 1$. The necessity to decouple the mode sets a dependence between the gate time t_{gate} and the detuning from the mode δ:

$$t_{gate} = \frac{1}{\delta}. \tag{6.13}$$

[3] In the following we will use 'gate amplitude' to refer to the variable Ω quantifying the coupling strength between the light and the ions, e.g. in Hamiltonians in Eq. (4.18) and Eq. (4.37). Gate amplitude is equivalent to the Rabi frequency of the oscillations between qubit states for the case of resonant excitation in a ground-state-cooled ion chain. However, for the case of two-qubit gates the term 'Rabi frequency' is rarely used and the term 'gate amplitude' seems more appropriate. In this work we drive the qubit transition with a single optical beam, thus gate amplitude Ω is proportional to the amplitude of the optical field E: $\Omega \sim E \sim \sqrt{I} \sim \sqrt{P}$, where I is the intensity of the light and P is the optical power of the beam.

The numerical values for the gate amplitude will be given in arb.u. since all optical power adjustments in the control software are given in some dimensionless parameters. Most of the gate amplitude calibrations are done via scanning these dimensionless parameters and the physical parameters of the light like intensity or field amplitude are not measured.

A constant-amplitude-constant-detuning MS gate has three parameters: amplitude Ω, detuning δ, gate time t_{gate}. Eq. (6.13) and condition 2 pose two restriction on these three parameters leaving one degree of freedom. For example, one can choose any gate time t_{gate} and it will set the detuning to be $\delta = 1/t_{gate}$ and the amplitude Ω such that the absolute value of the geometric phase matches $\pi/2$. Generally, shorter gate times would require larger detuning and higher amplitude.

Now, let us assume we have a second radial mode with frequency $f_{\mathrm{y},2}$. The detuning of the tones from this mode would be $\delta_2 = \delta + f_{\mathrm{y,COM}} - f_{\mathrm{y},2}$. The mode population will oscillate at this frequency and the mode will be decoupled at the following moments of time:

$$t_{\mathrm{y},2}(k_2) = k_2 \frac{1}{\delta_2}, \qquad k_2 \in \mathbb{N}. \tag{6.14}$$

We want both modes to be decoupled so the following should hold to satisfy condition 1:

$$t_{gate} = t_{\mathrm{y,COM}}(1) = t_{\mathrm{y},2}(k_2). \tag{6.15}$$

This assumes a single loop on radial-y COM mode, while radial-y mode 2 can have any natural number of loops k_2. For the detuning δ it means:

$$\frac{1}{\delta} = \frac{k_2}{\delta + f_{\mathrm{y,COM}} - f_{\mathrm{y},2}}, \tag{6.16}$$

$$\delta(k_2) = \frac{f_{\mathrm{y,COM}} - f_{\mathrm{y},2}}{k_2 - 1} \qquad k_2 > 1, k_2 \in \mathbb{N}. \tag{6.17}$$

The gate time can be determined accordingly $t_{gate} = 1/\delta(k_2)$ and the amplitude Ω should again match the geometric phase to be $-\pi/2$. Now the gate time can not be chosen freely anymore as before; it can only take certain values defined by $t_{gate} = 1/\delta(k_2)$.

In general, if more modes are considered only very high k (and large gate times) will satisfy condition 1 to decouple all the motional modes while doing a constant-amplitude-constant-detuning MS gate. However, parameters of an MS gate can be modulated to get more degrees of freedom [89–93]. For example, if the gate amplitude is modulated $\Omega = \Omega(t)$, there are more gate parameters available. Hence, more restrictions can be satisfied and condition 1 can be fulfilled again for reasonably low gate times.

On the other hand, theoretically condition 2 can always be satisfied unless the accumulated geometric phase is exactly 0. For any given non-zero geometric phase θ the amplitude Ω can be scaled accordingly since $\theta \sim \Omega^2$. If the initial geometric phase was θ and the amplitude was Ω then the scaled amplitude Ω' would make the new geometric phase $\theta' = -\pi/2$:

$$\Omega' = \Omega\sqrt{\frac{\theta'}{\theta}} = \sqrt{-\frac{\pi}{2\theta}}. \tag{6.18}$$

However, practically the required amplitude can sometimes require higher optical power than what is experimentally available, e.g. when the gate time is too low. This fact should be taken into account when choosing gate parameters.

Choosing gate time

Only two motional modes can be easily decoupled at the end of the MS gate as shown in the previous section. Therefore, it is reasonable to satisfy condition 1 for the two radial modes closest to the laser tones in frequency, i.e. the radial-y COM mode and radial-y mode 2 (see Fig. 6.5). This is motivated by the fact that the displacement of mode p from interaction with ion j in the end of the gate is proportional to the inverse of the detuning of the laser tones from the mode δ_p (see Eq. (4.39, 4.46)):

$$\alpha_p^{(j)} \sim c_p^{(j)} \frac{\Omega}{\delta}. \tag{6.19}$$

The gate time t_{gate} can be chosen according to Eq. (6.15) to decouple the two closest modes. There is still freedom in the choice of k_2. It can be used to mitigate the effect of the other radial modes which are not decoupled, i.e. condition 1 is not satisfied for them.

The effect of the other radial modes on the infidelity of an MS gate can be estimated using Eq. (4.50). The fidelity of the MS gate as a function of gate time is shown in Fig. 6.10. The detuning from the radial-y COM mode δ is always chosen according to Eq. (6.13), i.e. condition 1 is always satisfied for the radial-y COM mode, the closest radial mode. Condition 2 is always satisfied by scaling the gate amplitude Ω according to Eq. (6.18). Different plots illustrate the effect of the closest $M \in \{2, 3, 32\}$ modes for different ion pairs illuminated by the laser light.

There are several thing to point out in this figure:

- The infidelity in these plots is due to condition 1 not being satisfied, i.e. some modes are not decoupled in the end of the MS gate. Condition 2 is always satisfied.

- The plots for different ion pairs look different because different ions have different coupling to different modes. The contribution of mode p to the infidelity is higher if the couplings $c_p^{(j)}$ of the ions from the pair are higher.

  For example, ions $1, 16$ have very high coupling to radial-y mode 2, while coupling of ions $8, 9$ to this mode is negligible. If only the radial-y COM mode and radial-y mode 2 are considered (top plot), pair 8-9 should have near-perfect fidelity for any gate time since the displacement of radial-y mode 2 $\alpha_{\mathrm{y},2}^{(7)}, \alpha_{\mathrm{y},2}^{(8)}$ can be neglected. On the other hand, pair 1-16 experiences fidelity oscillations due to the coupling to radial-y mode 2. The fidelity is the highest if Eq. (6.15) is satisfied, i.e. radial-y mode 2 is decoupled (dashed orange lines).

- The middle plot shows the fidelity when three modes are taken into account: the radial-y COM mode, radial-y mode 2 and radial-y mode 3. Fidelity oscillation coming from the displacement of radial-y mode 3 can be seen compared to the top plot. Again, the effect is stronger for the pair 1-16 since it has the highest coupling to radial-y mode 3. Orange dashed lines indicate gate times when radial-y mode 3 is decoupled. These gate times can be close to the gate times when radial-y mode 2 is decoupled but they do not match exactly, e.g.

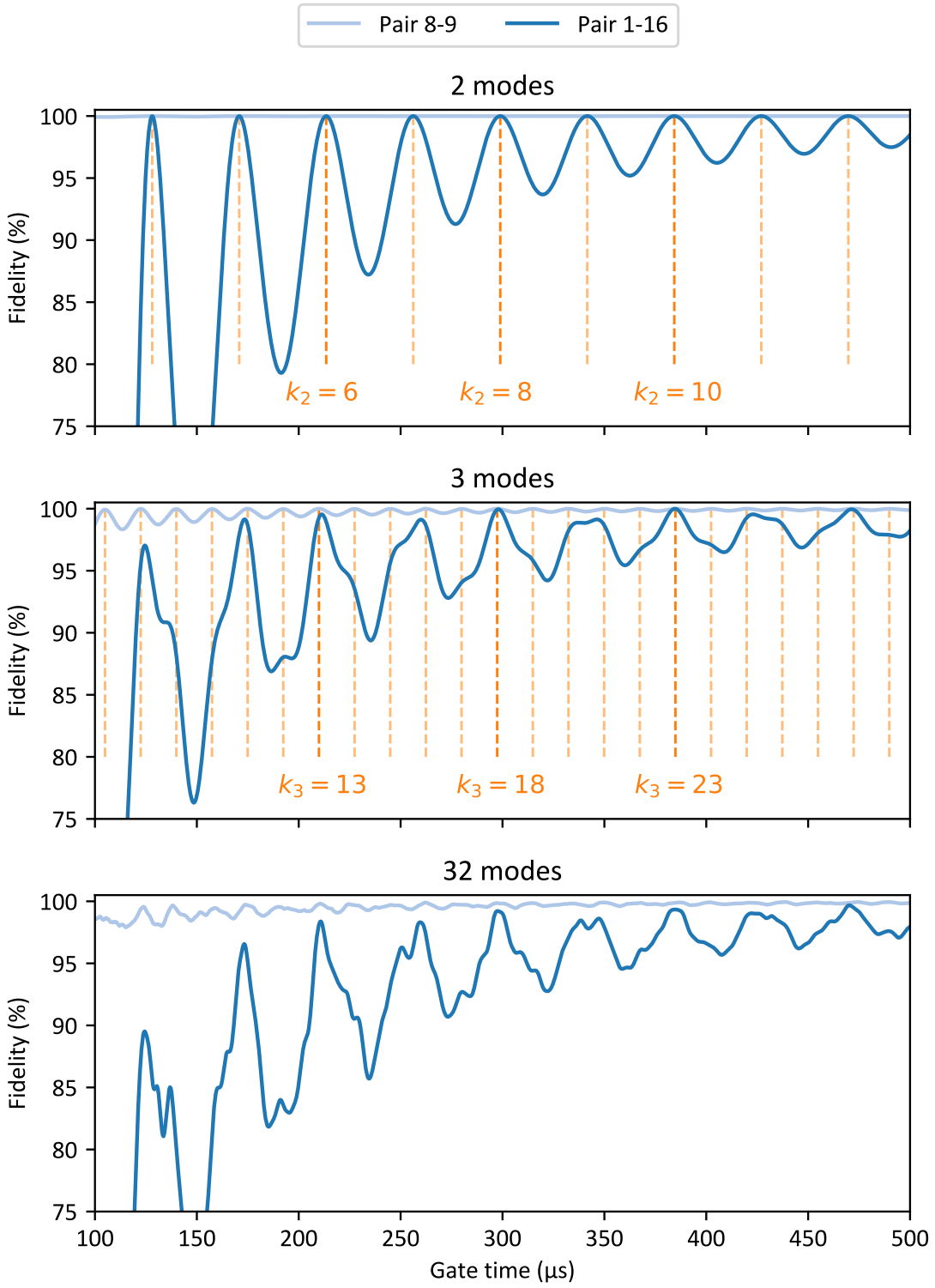

Figure 6.10: Fidelity of the MS gate as a function of gate time. The detuning from the radial-y COM mode δ is always chosen according to Eq. (6.13), i.e. condition 1 is always satisfied for the radial-y COM mode, the closest radial mode. Condition 2 is always satisfied by scaling the gate amplitude Ω according to Eq. (6.18). Different plots illustrate the effect of the closest $M \in \{2, 3, 32\}$ modes for different ion pairs illuminated by the laser. Dashed lines indicate gate times where a certain motional mode is decoupled: radial-y mode 2 for the top plot and radial-y mode 3 for the middle plot.

$t_{gate}(k_2 = 8) \approx 298.9\,\mu s \neq 297.4\,\mu s \approx t_{gate}(k_3 = 18)$. The fidelity behavior is still mostly dominated by the displacement of radial-y mode 2 since the detuning from this mode δ_2 is smaller.

- The bottom plot takes into account all 32 radial modes of the 16-ion chain. Oscillation stemming from the displacements of the other modes can be seen, but their effect is smaller than from the first modes. However, the effect of the other spectator modes does not allow to achieve gate fidelity above 99% for any gate time below 295 µs.

- Pair 1-16 has the highest coupling to all modes with mode number below 6. Therefore, it is enough to consider the fidelity behavior for this pair since the main contributions come from the low-mode-number modes. Pair 8–9 is shown to illustrate the difference between ion pairs.

It was decided to choose $t_{gate} = 300\,\mu s$ as the gate time for MS gates with radial modes. This is close to the shortest gate time allowing one to achieve gate fidelity higher than 99%. The RF confinement can be slightly adjusted as well to shift the radial mode spectrum and provide the highest fidelity at $t_{gate} = 300\,\mu s$ instead of $t_{gate} \approx 297\,\mu s$ as in Fig. 6.10.

It is important to note that this simulation does not take into account various factors present in the experimental setup, e.g. off-resonant qubit transition excitation, gate parameter fluctuations, 'smooth' amplitude change in the beginning and in the end of MS gates, and decoherence effects. Moreover, all motional modes are assumed to be ground-state-cooled and have no heating rate. Nevertheless, the model captures the main features of the interaction with spectator modes.

The experimental data shows similar behavior to the one predicted by the model (see Fig. 6.11). The fidelity is highest for the gate time close to 300 µs, while fidelity for the lower gate time is lower than for the higher gate time.

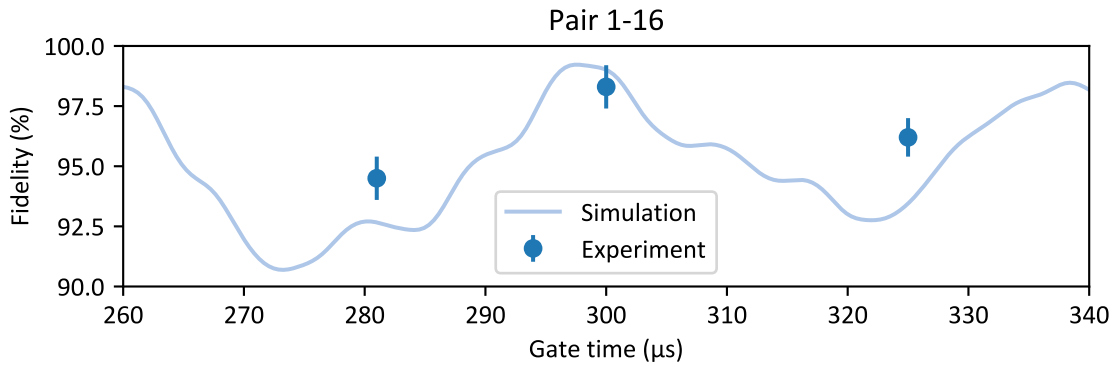

Figure 6.11: Fidelity of the MS gate as a function of gate time. The detuning from the radial-y COM mode δ is always chosen according to Eq. (6.13). Condition 2 is always satisfied by scaling the gate amplitude Ω according to Eq. (6.18). All 32 radial modes are taken into account for the simulation.

Power corrections

Condition 1 fixes the gate time $t_{gate} = 300\,\mu s$ and the detuning from the radial-y COM mode $\delta = 3.33\,kHz$ as it follows from the previous consideration. The gate amplitude Ω should be adjusted to satisfy condition 2. However, gate amplitude is different for different ion pairs.

The total geometric phase accumulated during the gate θ is a sum of contributions from different modes θ_p:

$$\theta = \sum_p \theta_p. \tag{6.20}$$

The contribution from mode p interacting with ion pair j_1-j_2 is proportional to couplings $c_p^{(j_1)}, c_p^{(j_2)}$ to this mode

$$\theta_p \sim c_p^{(j_1)} c_p^{(j_2)} \frac{\Omega^2}{\delta_p} t_{gate}. \tag{6.21}$$

Therefore, different ion pairs require different gate amplitudes $\Omega_{j_1\text{-}j_2}$ to satisfy condition 2.

Experimentally, gate amplitude is adjusted by changing the RF signal amplitude A_{DP} supplied to the DP AOM (see Sec. 5.3.1). The gate amplitude Ω depending on the DP amplitude A_{DP} can be measured experimentally via Rabi oscillations of a single qubit, the result is shown in Fig. 6.12. Theoretically, it is expected to behave as [104]

$$\Omega = a \sin^2(bA_{DP}), \tag{6.22}$$

which matches experimental data (a, b are fit parameters). However, we find that two-qubit gate amplitudes for different pairs $\Omega_{j_1\text{-}j_2}$ are better described if we use the power law instead of the sine law[4]:

$$\Omega = a' A_{DP}^{1.8}. \tag{6.23}$$

The required DP AOM amplitude for different ions pairs is found by scanning it and finding the value which provides the best gate fidelity. However, such a scan would be required for all $C_{16}^2 = 120$ ion pairs. Calibrating all available pairs is time consuming and it clearly scales poorly with system size. Instead, the required amplitudes can be predicted using simulations. The required gate amplitudes can be calculated for any pair $\Omega_{j_1\text{-}j_2}$ based on the radial mode spectrum. We find it more practical to measure the DP AOM amplitude for one ion pair and scale amplitudes for other pairs according to the simulation rather than predict all the amplitudes. For example, the DP AOM amplitude $A_{DP,\ 8\text{-}9}$ required to achieve the correct gate amplitude $\Omega_{8\text{-}9}$ for pair 8-9 can be measured by scanning it. After that, other amplitudes can be

[4]Both formulas (Eq. (6.22) and Eq. (6.23)) provide a decent approximation of the experimental data in Fig. 6.12 with the sine law giving a better fit. On the other hand, the final goal of this fit was to predict the DP AOM amplitudes for the gates as in Eq. (6.24). Using the power law in Eq. (6.24) provides a better match with the experimentally measured DP AOM power giving the best gate fidelities than if the sine law is used in Eq. (6.24): the total deviation of the amplitudes for all ion pairs is 4% lower for the power law.

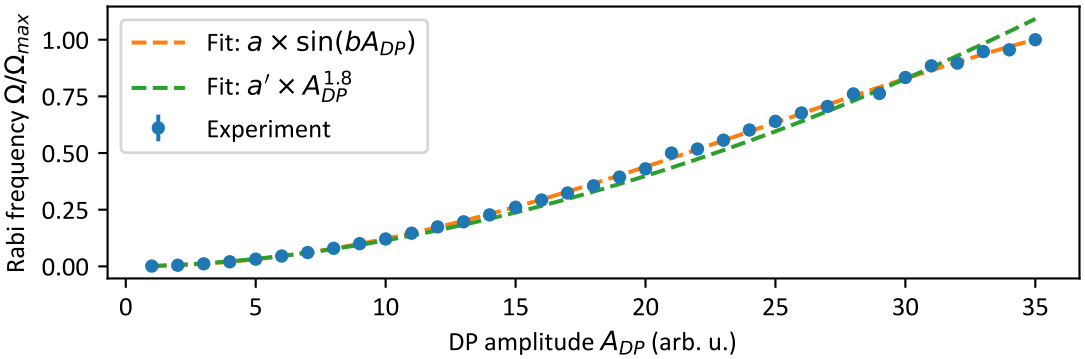

Figure 6.12: Normalized Rabi frequency for ion 1 in a 16-ion chain for different DP AOM amplitudes.

found based on the simulated values for gate amplitudes combined with the AOM response curve in Eq. (6.23):

$$A_{DP,\ j_1\text{-}j_2} = \left(\frac{\Omega_{j_1\text{-}j_2}}{\Omega_{8\text{-}9}}\right)^{1/1.8} A_{DP,\ 8\text{-}9}. \tag{6.24}$$

This 'power correction matrix' can be calculated once for the given spectrum of radial modes to significantly reduce calibration efforts. The matrix for the spectrum defined by Eq. (6.4) is given in Fig. 6.13. Note, that the power correction matrix should be recalculated if the radial spectrum changes, e.g. when the number of ions in the chain changes.

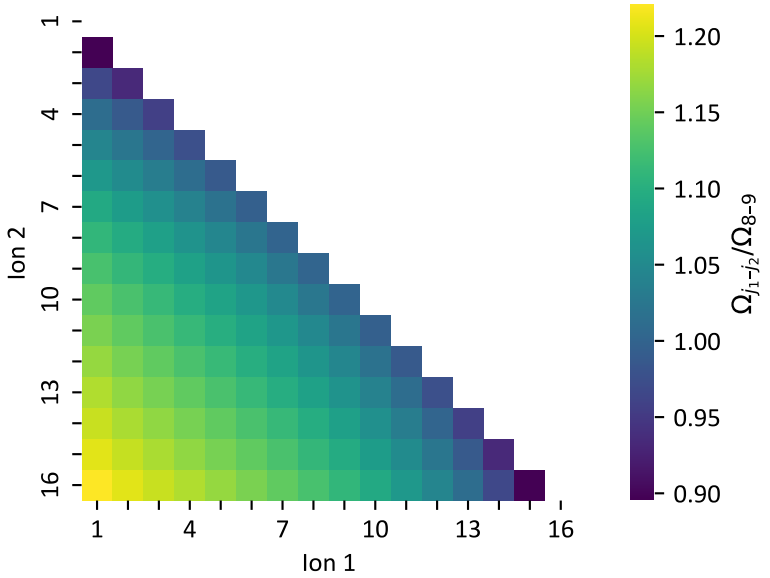

Figure 6.13: Power correction matrix for 300 µs MS gates for 16-ion chain. All 32 radial modes are taken into account for the simulation.

6.2 Automated calibration

An experimental quantum computing system should be able to execute quantum circuits composed of quantum gates. Performing a high-fidelity gate requires initial calibration of control pulses, such as gate time, RF amplitude for AOMs and so on, similar to the ones described in the previous section. Moreover, any experimental system can be susceptible to hardware parameter fluctuations. These fluctuations can affect the performance of the setup, e.g. gate fidelities, which would lead to deterioration of the output of the quantum computation.

One way to tackle the problem of fluctuations[5] is to recalibrate crucial setup parameters periodically (in addition to the initial calibration) to account for the change in hardware parameters due to fluctuations. Such an approach, combined with sufficient passive stability of the hardware parameters, can keep the performance of the setup above some set threshold providing consistent computation outcomes.

One of the goals of the AQTION project was to decrease the maintenance effort of the setup. Therefore, it would be beneficial to fully automate all routines required for recalibration. Moreover, calibration procedures should scale favorably with the number of ions. Otherwise, the setup will spend most of its time calibrating itself, even though everything is automated. For example, it requires a lot of time to calibrate gate amplitude for all 120 ion pairs in the 16-ion chain. That is why we use power corrections based on simulations to minimize calibration efforts as discussed in the previous section (Sec. 6.1.6) and effectively calibrate the gate amplitude for one ion pair only. In this section, we will describe the main calibration procedures in the setup.

6.2.1 Parameters to recalibrate

Mainly, fluctuations of the following hardware parameters affect the performance of the setup:

- Qubit laser (729 nm) power and frequency
- Magnetic field amplitude
- Temperature

All these parameters can affect standard qubit manipulation operations: state preparation, single-, and two-qubit gates. For example, magnetic field amplitude fluctuations affect the qubit transition frequency through the Zeeman splitting, while temperature fluctuations can cause the addressing system to misalign, changing AOD frequencies required to address different qubits.

[5] Here we imply that the change in hardware parameters is slow enough for calibration procedures to be useful. Typical calibration repetition periods of 10-30 min can help fight slow processes such as daily temperature drifts or slow magnetic field change. Fast processes, e.g. 50 Hz magnetic field noise from the AC mains, can not be mitigated with recalibrations.

Predominantly, precise control of the qubit state is realized through laser light shaped with AOM/AOD modules supplied with electric pulses. Therefore, calibration is mostly required for amplitudes and frequencies of those pulses. Let us have a look at the Hamiltonians underlying single- and two-qubit gates in Eq. (4.18, 4.37) to understand what needs to be calibrated:

$$H_{sq}^{(j)} = \frac{1}{2}\hbar \overbrace{\Omega_j}^{②}(\sigma_+^{(j)} e^{-i(\overbrace{\Delta}^{①} t+\phi_L)} + h.c.), \tag{6.25}$$

$$H_{tq}^{(j_1)(j_2)} = \frac{1}{2}\hbar\eta \overbrace{\Omega_{j_1-j_2}}^{⑤}(\sigma_x^{(j_1)} + \sigma_x^{(j_2)})(a e^{i\overbrace{\delta}^{③} t} + h.c.) + \frac{1}{2}\hbar \overbrace{\Delta\omega_{AC}}^{④}(\sigma_z^{(j_1)} + \sigma_z^{(j_2)}), \tag{6.26}$$

where the last component includes the problem of AC Stark shifts discussed in Sec. 6.1.5. The numbers in circles highlight the parameters requiring calibration. These numbers suggest the order in which the parameters should be calibrated. Let us briefly describe these parameters:

① **Detuning of the laser from the qubit transition: Δ**

This affects almost every operation with qubits, so it crucial to have this well calibrated. Mainly, fluctuations come from the instability of the magnetic field and the drift of the qubit laser reference cavity (see Eq. (5.2)).

② **Gate amplitude for single-qubit gates: Ω_j**

Generally, different ions might have different optical powers illuminating them when addressed. It is important to calibrate Rabi frequencies for each ion such that a desired qubit rotation can be implemented. This parameter is ion-dependent. Mainly, fluctuations come from laser power fluctuations or temperature-related addressing system misalignment.

③ **Detuning of the bichromatic tones from the motional sidebands: δ**

This desired value for this parameter is essentially fixed as discuss in Sec. 6.1.6. Thus, it is important to keep this value constant. Once parameter 1 is calibrated, it is only required to know the radial-y COM mode frequency to set δ. Therefore, the main fluctuations come from RF power fluctuations modulating the radial confinement.

④ **AC Stark shift induced by the bichromatic beam: $\Delta\omega_{AC}$**

We add a third tone to the bichromatic light to cancel the AC Stark shift as discussed in Sec. 6.1.5. Thus, this parameter is kept at 0. However, the power of the third tone which provides full AC Stark shift cancellation should be calibrated from time to time. Practically, we do not observe significant fluctuations of the power of the third tone.

⑤ **Gate amplitude for two-qubit gates: $\Omega_{j_1\text{-}j_2}$**

This parameter is closely related to parameter 2 and its calibration in our case is dependent on parameter 2. The parameter is ion-pair-dependent, partly due

to the reasons discussed in Sec. 6.1.6. The reason for fluctuations are the same as for parameter 2.

These parameters are deliberately ordered in this way since it makes sense to calibrate them in this order. For example, there is little point in calibration of the power for resonant single-qubit gates (parameter 2) if the laser frequency required to address the qubit transition (parameter 1) is not known. Hence, parameters depend on the previous ones in some cases. In the following we will go through the calibration procedures we use for these parameters.

6.2.2 Laser/qubit transition frequency

The energy levels of the ions are affected by the external magnetic field B. The main component of these shifts is the linear Zeeman shift [105]. Each level experiences an energy shift based on its component of the total angular momentum m_j along the field:

$$\Delta E = \mu_B g_J m_j B, \tag{6.27}$$

where μ_B is the Bohr magneton and g_J is the Landé g-factor. The transition frequencies between Zeeman sub-levels in $4^2\mathrm{S}_{1/2}$ and $3^2\mathrm{D}_{5/2}$ manifolds will change accordingly:

$$f_{\mathrm{S}_{1/2,m_j^{(\mathrm{S})}}\to\mathrm{D}_{3/2,m_j^{(\mathrm{D})}}} = f_{m_j^{(\mathrm{S})}\to m_j^{(\mathrm{D})}} = f_0 + \frac{1}{2\pi\hbar}\mu_B(g_J^{(D)}m_j^{(\mathrm{D})} - g_J^{(S)}m_j^{(\mathrm{S})})B, \tag{6.28}$$

where f_0 is the frequency of the transition at zero magnetic field. We will not be considering other less significant shifts, such as quadratic Zeeman shift or quadrupole shift, in this work, while they are taken into account in our experimental setup. A thorough analysis of those shifts can be found in the PhD thesis of Milena Guevara-Bertsch [106].

Resonant excitation of the qubit transition $\mathrm{S}_{1/2,-1/2} \to \mathrm{D}_{5/2,-1/2}$ would require the laser light to match the transition frequency, as described in Eq. (5.1):

$$f_{laser} + 2f_{DP} + f_{FAOM} + f_{AOD}^{(1)} - f_{AOD}^{(2)} = f_{-\frac{1}{2}\to-\frac{1}{2}}. \tag{6.29}$$

However, the laser frequency f_{laser} changes over time due to the reference cavity drift (5.2) and it is known precisely only immediately after calibrations.

Both unknown parameters, the magnetic field amplitude B and the laser frequency f_{laser}, can be determined if the frequencies of any two transitions are known, e.g. $f_{-\frac{1}{2}\to-\frac{5}{2}}$ and $f_{-\frac{1}{2}\to-\frac{1}{2}}$. The transition frequencies can be measured by means of Rabi or Ramsey spectroscopy. An example of such a measurement is shown in Fig. 6.14. The frequency of the DP AOM f_{DP} is scanned to find the resonances.

The magnetic field amplitude usually stays around $B \approx 5.95\,\mathrm{Gs}$ with long term fluctuations of around $0.02\,\mathrm{Gs}$. On the other hand, the laser frequency f_{laser} always changes due to the reference cavity drift as can be seen in Fig. 6.15. The long-term drift rate is around $\Delta f_{laser}/\Delta t \approx -5\,\mathrm{kHz/d}$.

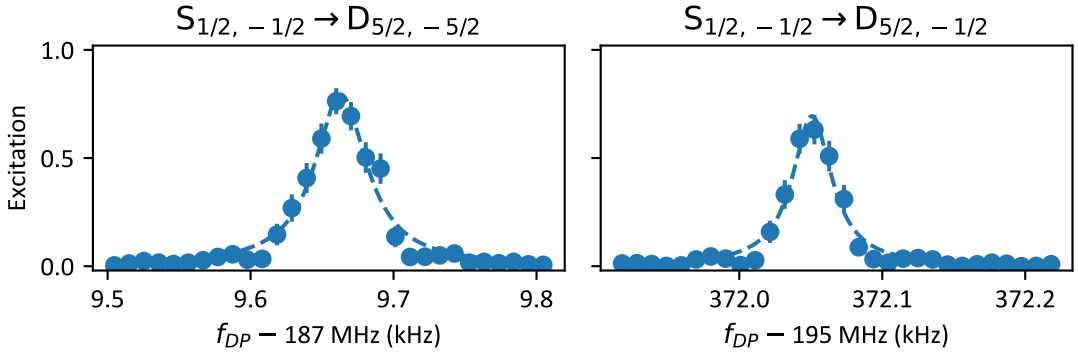

Figure 6.14: Measurement of two $S_{1/2} \rightarrow D_{5/2}$ transition frequencies using Rabi spectroscopy.

The spectroscopy measurement is repeated every 10–15 minutes. However, the laser frequency drift can be taken into account even between the measurements, given its linear nature. Every time a pulse sequence is applied the laser frequency f_{laser} is updated based on the linear extrapolation of the previous data in the last 3 hours (see Fig. 6.15 inset).

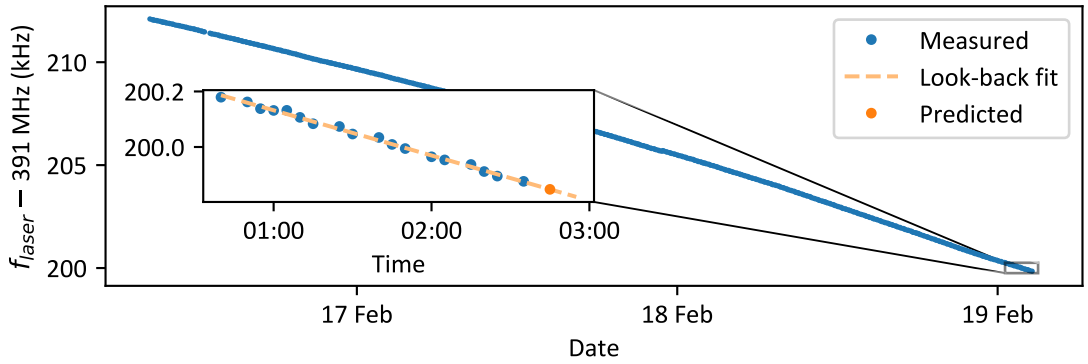

Figure 6.15: Laser frequency over time measured with spectroscopy (see Fig. 6.14). The linear drift of the reference cavity can be extrapolated to update the laser frequency until the next spectroscopy measurement is performed, see inset.

6.2.3 Addressing frequencies

Single- or two-qubit gates in our setup require the ability to address ions with laser light individually. Hence, the single-ion addressing system must be calibrated beforehand (see Sec. 5.3.1). Normally, an ion j can be addressed if the same frequency f_j is applied to both AODs:

$$f_{AOD}^{(1)} = f_j, \tag{6.30}$$

$$f_{AOD}^{(2)} = f_j. \tag{6.31}$$

Calibration is needed to determine the frequencies $\{f_j\}$ or adjust them if they have changed, for example due to temperature drifts. The calibration is performed by scanning the addressing frequencies:

$$f_{AOD}^{(1)} = f_0 + \Delta f_H, \tag{6.32}$$

$$f_{AOD}^{(2)} = f_0 + \Delta f_H, \tag{6.33}$$

$$f_0 = 100\,\text{MHz} \tag{6.34}$$

Changing Δf_H results in a horizontal displacement of the addressing beam, see Fig. 5.5. A typical result of the scan is given in Fig. 6.16 (left). The frequencies $\{f_j\}$ for each ion can be assigned after this scan. Typical values for $\{f_j\}$ are given in Fig. 6.17.

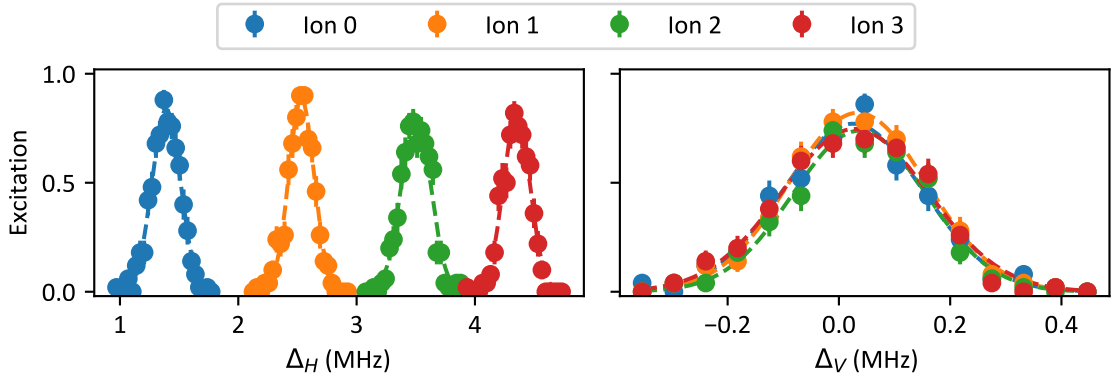

Figure 6.16: Scanning of the addressing frequencies horizontally (left) and vertically (right) in 16-ion chain. Data for the first four ions is shown. Highest excitation corresponds to the positions of the ions.

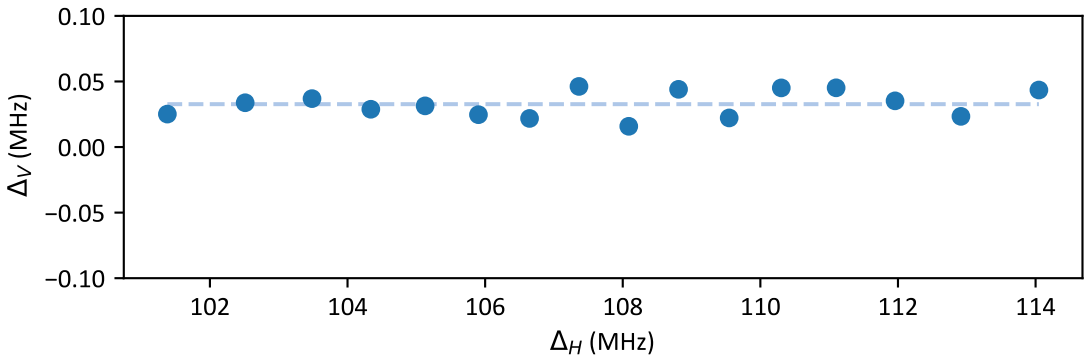

Figure 6.17: Typical horizontal and vertical addressing frequency shifts corresponding to the ions' positions in 16-ion chain.

The same scan can be done for the vertical component:

$$f_{AOD}^{(1)} = f_j + \Delta f_V, \tag{6.35}$$

$$f_{AOD}^{(2)} = f_j - \Delta f_V. \tag{6.36}$$

A typical scan is shown in Fig. 6.16 (right), while the values for each ion are given in Fig. 6.17. Vertical positions are roughly the same for all ions since the addressing system was aligned to minimize the tilt. This is required since having non-zero Δf_V will result in a frequency shift. If two ions are addressed simultaneously we can not use two different values for Δf_V because ions will be illuminated with light of different frequencies. This is usually not desired, so we use an average value for the vertical shift $\Delta f_{V,avg}$.

Scalability

The scalability aspect is important for this measurement. Let us assume that we roughly know the addressing frequencies $\{f_j\}$, so we need to perform a fine calibration. The most straightforward way to perform the scan for all ions would be (numbers on the right indicate how much time a single step approximately takes):

Addressing scan v1		
1.	**for** ion j **in** $\{1, \ldots, 16\}$:	
2.	**for** Δf_H **in** $[-0.5, 0.5]$ MHz:	
3.	Prepare ion chain (reset, cool)	15 ms
4.	Apply addressed pulse at $f_j + \Delta f_H$	30 µs
5.	Measure all ions	250 µs

A separate scan is done for each ion. Note that preparation of the ion chain and the measurement is done for each scan, i.e. 16 times (once per ion). That creates a substantial overhead and it scales poorly with the number of ions.

Alternatively, we can excite ions 'in parallel':

Addressing scan v2		
1.	**for** Δf_H **in** $[-0.5, 0.5]$ MHz:	
2.	Prepare ion chain (reset, cool)	15 ms
3.	**for** ion j **in** $\{1, \ldots, 16\}$:	
4.	Apply addressed pulse at $f_j + \Delta f_H$	30 µs
5.	Measure all ions	250 µs

Thus, we 'simultaneously' probe all ions in one scan, only one preparation and measurement is required. The time overhead here is almost constant since even with 100 ions total probing time is only 3 ms which is still much lower than the 15 ms preparation time. Note that this approach only works for fine tuning since each ion will only be excited by a single pulse.

A similar procedure is performed for the vertical shift. After these calibrations every ion j can be addressed at $(f_j, \Delta f_{V,avg})$. However, ions will see slightly different optical powers as can be seen in Fig. 6.17. The next calibration step handles this.

6.2.4 Single-qubit gates

The goal of single-qubit gates calibration is to be able to implement an R-gate with arbitrary rotation angle θ and phase ϕ (see Eq. (4.20)):

$$R(\theta,\phi) = e^{-iH_{sq}^{(j)}t/\hbar} = \begin{pmatrix} \cos\frac{\theta}{2} & -ie^{-i\phi}\sin\frac{\theta}{2} \\ -ie^{i\phi}\sin\frac{\theta}{2} & \cos\frac{\theta}{2} \end{pmatrix}. \tag{6.37}$$

The detuning Δ in Eq. (6.25) can already be set to 0 since it has been calibrated in Sec. 6.2.2. The phase ϕ can be set by the phase $\phi_{DP} = \phi/2$ of the signal going to the DP AOM. The first pulse in the quantum computing sequence sets the reference frame. The absolute phases of the pulses are not important, only the phase differences between the pulses matter. For a square pulse, the rotation angle $\theta = \Omega_j t$ is defined by the gate amplitude Ω_j and the length of the pulse t. The phase ϕ_{DP} and the length t of the electric pulse can be set precisely by the control electronics and do not need calibration. Hence, the only parameter which should be calibrated is the gate amplitude Ω_j induced for ion j.

We aim to calibrate amplitudes in such a way that every ion will have the same π-pulse time of $t_\pi = 30\,\mu s$, i.e. $\Omega_j = \Omega_0 = \pi/t_\pi, \forall j$. If this is achieved, the desired rotations θ can be set by the pulse time t for any ion:

$$t = \frac{\theta}{\pi} t_\pi. \tag{6.38}$$

Ideally, a perfectly aligned addressing system should provide the same illumination for all ions, i.e. $\Omega_{j_1} = \Omega_{j_2}, \forall j_1, j_2$ for the same AOM amplitudes. In the experiment, those values vary a little from ion to ion. The variation can be characterized in the following way.

Let us assume that the variation is small and we have established an approximate DP AOM amplitude providing a gate amplitude $\Omega_0 = 1/t_\pi$ to perform a π-pulse for a given $t_\pi = 30\,\mu s$. We can perform a sequence of measurements where we apply an $R(\theta_k, 0)$ in every measurement and measure the outcome [107]. The values for θ_k are chosen in the following way [108]:

$$\begin{aligned} \frac{\theta_k}{\pi} \in \{&\frac{1}{2}, \frac{1}{2}+\frac{1}{2}, \\ &1, 1+\frac{1}{2}, \\ &2, 2+\frac{1}{2}, \\ &\dots \\ &2^{\lfloor (k_{max}-1)/2 \rfloor}, 2^{\lfloor (k_{max}-1)_{max}/2 \rfloor} + \frac{1}{2}\}. \end{aligned} \tag{6.39}$$

We use 10 different θ_k values, so $k_{max} = 10$. The probability to find a qubit in the $|1\rangle$ state after $R(\theta_k, 0)$ is applied is:

$$P_{|1\rangle}(k) = \sin^2\frac{\theta_k}{2}. \tag{6.40}$$

Therefore, if indeed $\Omega_j = \Omega_0 = 1/t_\pi$ we should observe $P_{|1\rangle}(k) \in \{0, 0.5, 1\}$ for all ions. The experimental results are shown in Fig. 6.18. The exact values for Rabi frequencies and thus gate amplitudes for each ion $\{\Omega_j\}$ can be calculated from this data. Having a set of increasing values $\{\theta_k\}$ allows us to unambiguously determine the gate amplitudes precisely despite the periodic nature of Eq. (6.40).

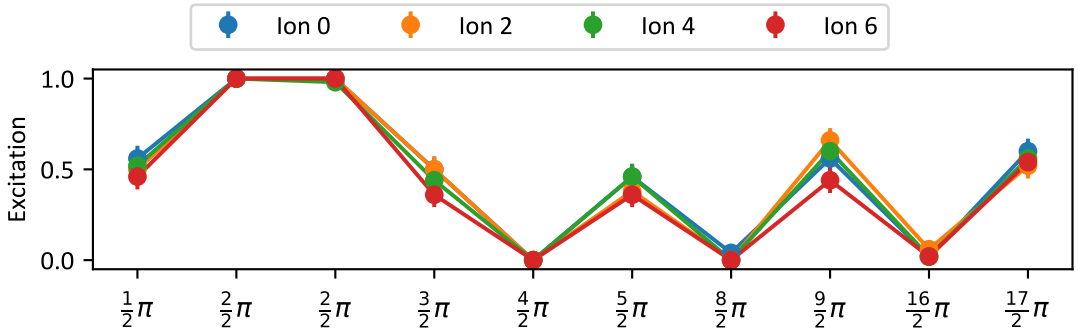

Figure 6.18: Application of $R(\theta_k, 0)$ with different θ_k to different ions. The data for the first four ions in the 16-ions chain is shown. The gate amplitudes for each ion can be determined from this data.

After this measurement, actual gate amplitudes $\{\Omega_j\}$ are know for each ion but we still want to equalize them. This is particularly important for two-qubit gates when two ions should be addressed simultaneously with the same gate amplitude. The gate amplitudes for each ion can be equalized by adjusting the AOD amplitudes for each ion. During the calibration procedure AODs were supplied with the same amplitude for all ions:

$$A^{(1)}_{AOD} = A^{(2)}_{AOD} = A_{AOD} = A_{AOD,0}. \tag{6.41}$$

We operate the AODs in the regime where the response is linear in Rabi frequency, i.e.

$$\Omega \sim A_{AOD}. \tag{6.42}$$

Therefore, we can adjust the AOD amplitude $A_{AOD,j}$ for ion j in the following way:

$$A_{AOD,j} = A_{AOD,0}\,\frac{\Omega_0}{\Omega_j}, \tag{6.43}$$

where Ω_j is the gate amplitude measured for ion j. Typical values for addressing amplitudes $A_{AOD,j}$ are within $[0.95, 1.05] \times A_{AOD,0}$. Now all ions will experience the same gate amplitude Ω_0 when addressed with AOD amplitude $A_{AOD,j}$. Thus, $R(\theta, \phi)$ can be implemented for any ion by adjusting the pulse time t and the phase of the DP AOM ϕ_{DP}.

Scalability

Similarly to the addressing scan this procedure can be implemented in a scalable way:

Rabi frequency scan		
1.	**for** ions to probe **in** {odd ions, even ions}:	
2.	**for** θ_k **in** Eq. (6.39):	
3.	Prepare ion chain (reset, cool)	15 ms
4.	**for** ion j **in** ions to probe:	
5.	Apply $R(\theta_k, 0)$ to ion j	15–255 µs
6.	Measure all ions	250 µs

Again, several ions are probed in one measurement to save time for preparation of the ion chain. However, here ions with odd numbers and even numbers are probed in separate scans. This method reduces the influence of addressing crosstalk on gate amplitudes.

6.2.5 Motional modes

High fidelity two-qubit gates require setting the detuning δ of the bichromatic tones precisely, as described in Sec. 6.1.6. The radial-y COM mode frequency should be determined for this. This can be done by means of sideband spectroscopy, i.e. one can excite the BSB transition of the radial-y COM mode and determine the frequency corresponding to maximal excitation. The scan should be done at low optical power to minimize AC Stark shifts. A representative scan is shown in Fig. 6.19.

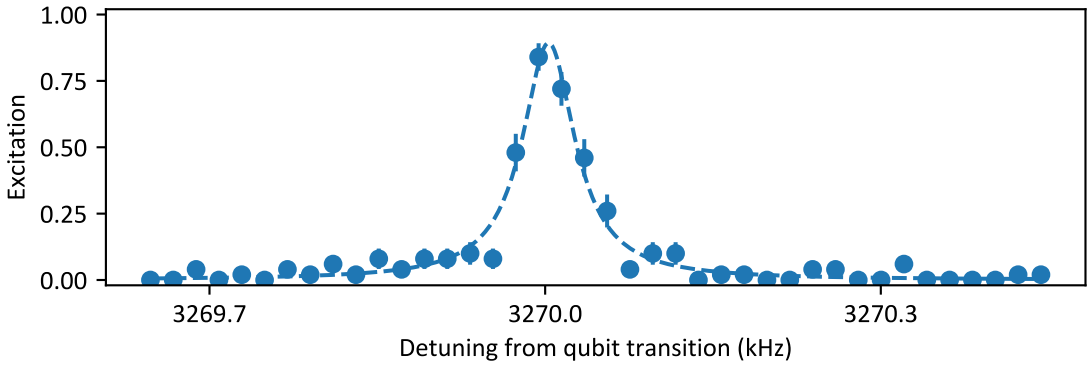

Figure 6.19: BSB spectroscopy of the radial-y COM mode. The mode frequency corresponds to the frequency of maximal excitation.

There are two ways how this can be handled from here:

1. **with feedback**

   The RF power going to the trap can be adjusted such that the radial-y COM mode frequency changes to the desired value. This requires some feedback loop (see Fig. 6.20), but the bichromatic tone frequencies will always stay the same.

2. **without feedback**

   The radial-y COM mode frequency can be simply updated in the control software system and the frequency of the bichromatic tones is changed accordingly for future two-qubit gates.

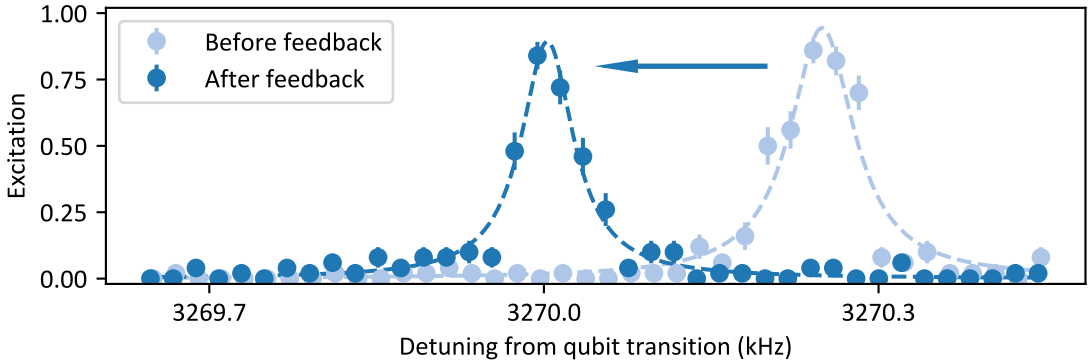

Figure 6.20: Feedback for the radial-y COM mode frequency, approach 1.

The RF power going to the trap is stabilized with a PID controller designed in-house by Matthias Bock [109]. The feedback loop in approach 1 can be implemented by changing the setpoint of the PID controller. Of course, this requires some prior calibration of how much the frequency changes per setpoint step. We find that both approaches work equally well in terms of maintaining high two-qubit gate fidelities. Therefore, we currently use approach 2 due to its technical simplicity; no feedback is needed. The stability of the radial-y COM mode in shown in Fig. 6.21 for both approaches.

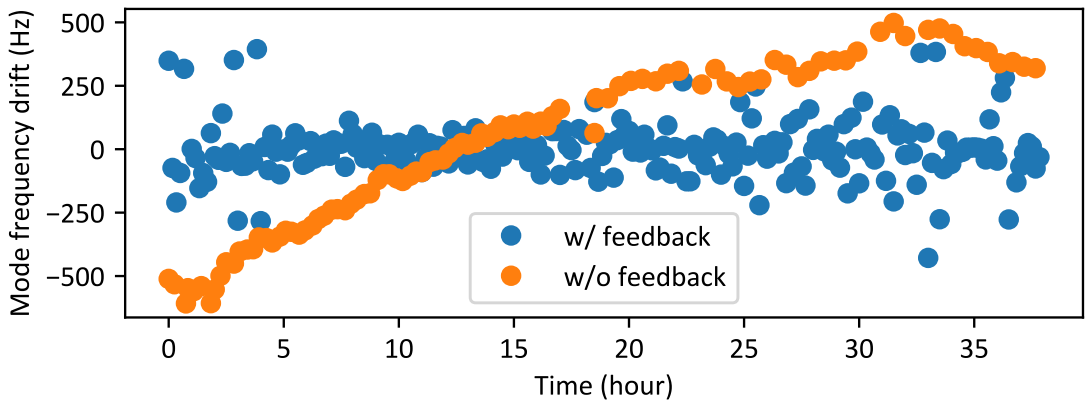

Figure 6.21: Stability of the radial-y COM mode frequency.

6.2.6 Two-qubit gates

All the previous calibrations ensure the following:

- The frequency of the qubit transition is known.
- The addressing frequencies required to optically address each ion are known.
- Each ion can be addressed with the same optical power ensuring 30 µs π-pulse time.
- The frequency of the radial-y COM mode is known.

What else is required for a two-qubit gate for any ion pair? The bichromatic tones frequencies can be calculated based on the qubit transition frequency and the radial-y COM mode frequency. The ions can be illuminated with the same optical power during the MS gate since the required addressing amplitudes are known.

However, the amplitude of the third tone (see Sec. 6.1.5) going to the FAOM canceling the AC Stark shift is not known and the DP AOM amplitude ensuring $-\pi/2$ rotation of the XX-gate is not known (see condition 2 in Sec. 6.1.6 or Eq. (6.18)).

Both of this parameters can be calibrated for any ion pair. The third tone amplitude does not depend on an ion pair as discussed in Sec. 6.1.5. The DP AOM can be calibrated for one pair and calculated for other pairs according to the power correction matrix (see Sec. 6.1.6). Typical experimental scans for pair 1-16 are shown in Fig. 6.22. The optimal third tone amplitude corresponds to the minimal population of $|01\rangle + |10\rangle$, since it indicates decoupling from the motional modes and consequently nullified AC Stark shift (see condition 1 in Sec. 6.1.6 or Eq. (6.18)). The optimal DP amplitude corresponds to equal populations of $|00\rangle$ and $|11\rangle$ since it indicates $-\pi/2$ rotation of the XX-gate.

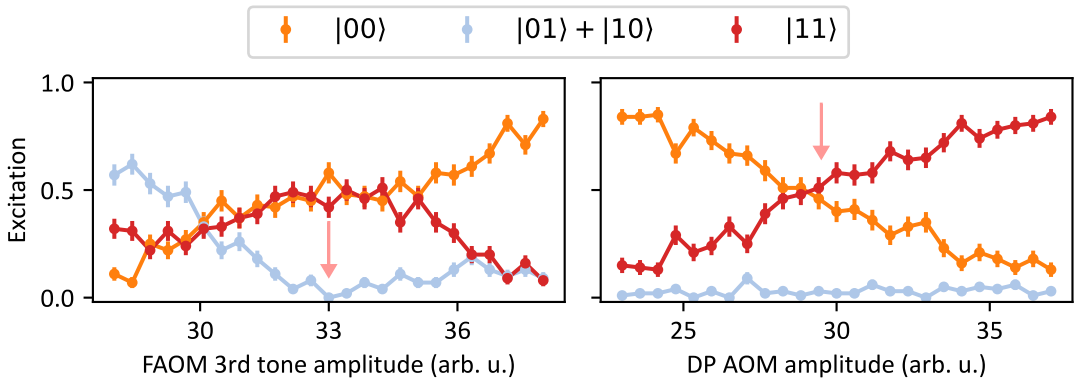

Figure 6.22: Populations of 2-ion states for pair 1-16 depending on two-qubits gate parameters: FAOM third tone amplitude and DP AOM amplitude. Arrows indicate optimal parameter values.

Alternatively, the calibration can involve several gates on different ions pairs at the same time. For example, the GHZ state of all 16 ions $(|0\ldots0\rangle + |1\ldots1\rangle)/\sqrt{2}$ can be

prepared with the circuit shown in Fig. 6.23. Preparation of the GHZ state uses two-qubit gates with different ion pairs: from 1-2 to 1-16. Therefore, such calibration cab be beneficial since it 'averages' over 15 pairs. The calibration is done already with power corrections applied, i.e. different DP amplitudes are used for different ion pairs but they are all scaled when the DP amplitude is scanned. Typical results are shown in Fig. 6.24. The optimal parameter values in both cases correspond to the highest sum of populations $P(|0\ldots0\rangle) + P(|1\ldots1\rangle)$. The optimal values correspond to the ones found in Fig. 6.22.

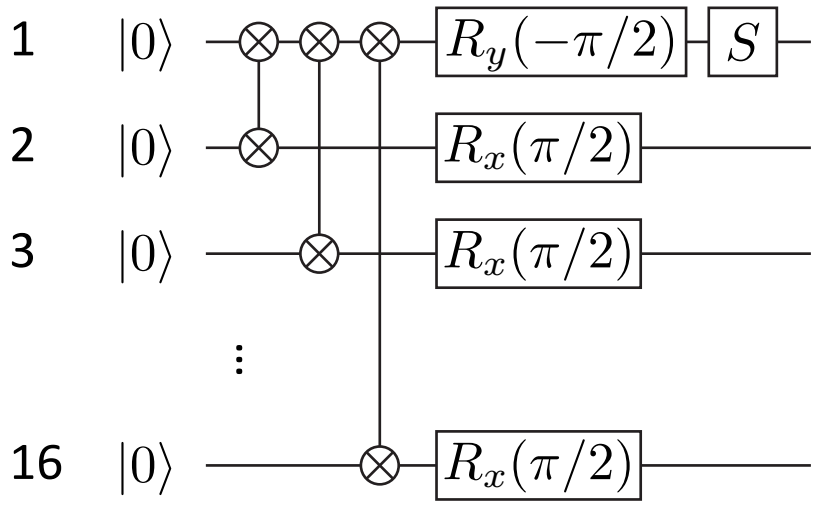

Figure 6.23: Quantum circuit to prepare a GHZ state of 16 qubits $(|0\ldots0\rangle + |1\ldots1\rangle)/\sqrt{2}$.

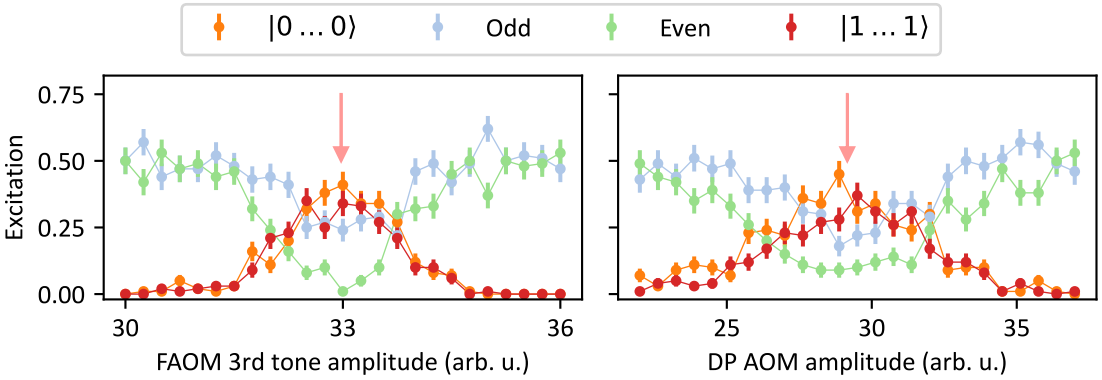

Figure 6.24: Populations of 16-ion states depending on two-qubit gate parameters: FAOM third tone amplitude and DP AOM amplitude. 'Odd' and 'Even' refers to states with odd (e.g. $|1110\ldots0\rangle$) and even (e.g. $|1100\ldots0\rangle$) number of excitations respectively. Arrows indicate optimal parameter values.

6.2.7 Time budget

All the calibration procedures provided above were designed keeping in mind the amount of time it would take to perform a procedure for a long ion chain. We tried to avoid repetitions of calibrations for every ion or ion pair if it increases the calibration time significantly.

In total, we periodically perform five calibration procedures. The procedures and the approximate amount of time they take are listed in Fig. 6.25. If we average these times including the repetition periods over a long period we get the bar chart in Fig. 6.25. It indicates that 80% of time the setup is not involved in any calibration procedures and can be used for running quantum computing circuits. We foresee this ratio not to change significantly with the number of ions in the chain since the calibration procedures are fairly scalable.

Calibration procedure	Time (s)	Repeat (min)
Laser/qubit transition frequency	13	7
Addressing frequencies	88	60
Single-qubit gates	44	15
Motional modes	22	10
Two-qubit gates	110	30

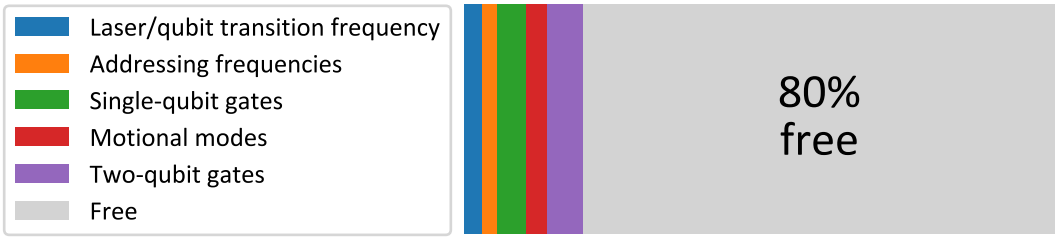

Figure 6.25: Table lists calibration procedures used in the AQTION setup, approximate amount of time they take and repetition periods. Bar chart shows relative time spent on each calibration procedure averaged over a long period of time.

6.2.8 Summary

The calibration procedures allow us to keep the setup performance at the same level over time. We usually monitor the performance based on the population of the full-register GHZ state $(|0\ldots0\rangle + |1\ldots1\rangle)/\sqrt{2}$. Preparation of this state includes addressed single- and two-qubit gates with different ions, so it tests the setup in many ways at the same time. Moreover, this procedure is short compared to full benchmarking procedures (e.g. randomized benchmarking [110]) which require a lot

of measurements. On the other hand, GHZ state population measurement does not provide detailed error characterization and it is entirely insensitive to some errors, e.g. errors on pairs not involved in the procedure.

The laser/qubit transition frequency calibration is a critical, but fast procedure. Hence, we repeat it frequently, here chosen as seven minute intervals. If there has been no data from this procedure in 15 minutes we send an alert to the setup operators. Usually, such an alert indicates some failure, e.g. software crash, laser unlocking or ion loss.

Other calibrated parameters are monitored in the software system. This is useful when looking for a source of hardware problems. The moment when the setup performance decayed can be clearly identified as well as the parameters it affected. A snapshot of the monitoring system is shown in Fig. 6.26.

Figure 6.26: A snapshot of the monitoring software system used to track the system performance.

6.3 High-level interface

The final goal of quantum computing is to be able to execute abstract quantum computing tasks no matter what the underlying system is. Quantum computing tasks are often formulated in the form of quantum circuits, listing an ordered sequence of gates and measurements. A modern quantum computer should be able to accept a quantum computing circuit in a hardware-agnostic form, interpret it into hardware commands, execute it, and return the result in a hardware-agnostic form. Part of the program for the AQTION project was to provide a high-level interface for this task.

Quantum circuits are usually formulated in terms of standard gates (see Sec. 2.2) such as H-gate, CNOT-gate and others. The AQTION setup can not natively implement some of these gates. Therefore, the direct execution of a given quantum circuit is not possible. An additional transpilation stage is required, i.e. the circuit has to be converted into an equivalent consisting only of the native gates of the setup. The native gate set of the AQTION setup includes the R-gate, the R_z-gate and the $XX(-\frac{\pi}{2})$-gate (see Sec. 4.4).

After the transpilation, the circuit must be compiled into a sequence of control pulses going to AOMs. The frequencies, amplitudes, and lengths of the pulses are defined based on the calibrations performed beforehand (see Sec. 6.2). In the end, the ion chain is detected and the fluorescence counts are reinterpreted as quantum states. The described concept is shown in Fig. 6.27.

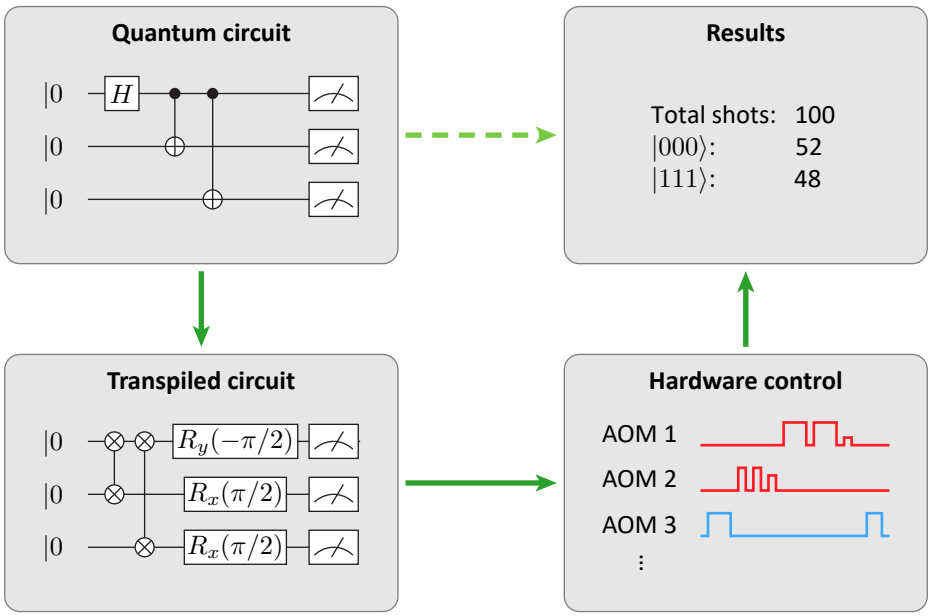

Figure 6.27: Conceptual illustration of the quantum computing via high-level interface. The initial task is submitted as a quantum circuit. The circuit must be transpiled into a native gate set and converted into AOM pulses. The result is returned in a hardware-agnostic form as quantum states.

We use the Qiskit software package by IBM [111] to describe the initial quantum

circuits for the high-level interface. A Qiskit circuit can be submitted as a task for the AQTION machine via a customized version [112] of the Qiskit backend developed by AQT [113]. The circuit is processed by the software, executed on the setup, and the result is returned as a Qiskit result object.

This high-level interface allows people not familiar with the technical details of the setup to prepare quantum computing tasks which can be executed on the AQTION machine. We have used this interface for several collaborations that resulted in the following publications [6, 7, 9, 114].

6.3.1 Transpilation

The main custom feature of our Qiskit backend is the transpilation step. The transpiler serves two purposes:

1. Decompose a given circuit into the native gate set of the device.
2. Optimize the circuit to minimize the number of gates to achieve better fidelities.

The first step is done via the Qiskit standard transpiler [115] (optimization_level = 3). The circuit is decomposed into R_x, R_y, and $XX(-\frac{\pi}{2})$. After that, we follow the logic described in Ref. 47:

2a. Move all R_x gates to the end of the circuit.

The idea is based on the following equalities:

$$R_y(\theta_y)R_x(\theta_x) = R_x(-\theta_x)R(\theta,\phi) \tag{6.44}$$

$$XX\left(-\frac{\pi}{2}\right)R_x(\theta_x) = R_x(\theta_x)XX\left(-\frac{\pi}{2}\right), \tag{6.45}$$

where $\theta = 2\arccos\left(\cos\theta_x\cos\frac{\theta_y}{2}\right)$, $\phi' = \arcsin\left(\frac{\sin\frac{\theta_y}{2}}{\sqrt{1-\cos^2\theta_x\cos^2\frac{\theta_y}{2}}}\right)$ and $\phi = \begin{cases}\phi', & \theta_x > 0\\ \pi-\phi', & \theta_x < 0\end{cases}$. The only two-qubit gate type in the native gate set is $XX(-\frac{\pi}{2})$ and it commutes with R_x (see Eq. (6.45)). Also, R_x can be moved through R_y as in Eq. (6.44). Hence, it follows that any R_x-gate can be moved all the way to the end of the circuit and be merged with other R_x-gates. This will reduce the amount of single-qubit gates in the transpiled circuit. The idea is illustrated in Fig. 6.28.

2b. Another step stems from the hardware limitation we have. Our current control electronics can not perform pulses shorter than 2 µs. Therefore, we can not implement $R(\theta,\phi)$-gates with $\theta_s < \frac{\pi}{15}$ using the described calibration procedures, since our π-pulse time is 30 µs. Instead, we can replace small angle rotation gate with two:

$$R(\theta_s,\phi) = R(\pi+\theta_s,\phi)R(\pi,\pi+\phi). \tag{6.46}$$

This replacement is implemented for $R(\theta_s,\phi)$ where $\frac{\pi}{20} < \theta_s < \frac{\pi}{15}$.

2c. Single-qubit gates have finite fidelity; we estimate it to be around 99.7% in our setup. If a rotation angle is very small, doing a gate will cause more error than not doing anything at all. Moreover, for small angles we need to perform two R-gates instead of one. In the end, doing $R(\theta_s, \phi)$ with $\theta_s < \frac{\pi}{20}$ causes more error, thus we just remove those gates from the transpiled circuit.

After these steps the transpiled circuit only contains gates native to the AQTION setup and has fewer single-qubit gates than after standard Qiskit transpilation.

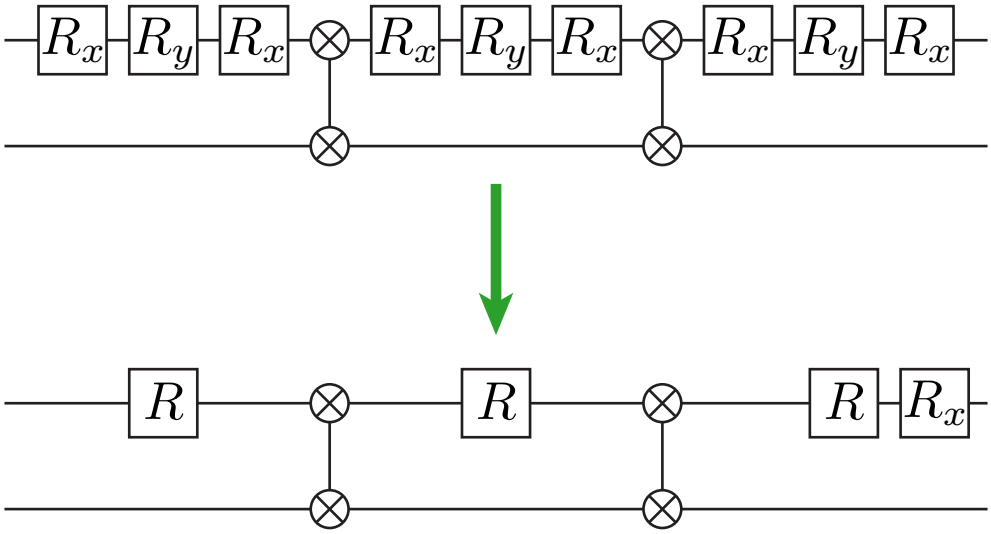

Figure 6.28: Step 2a of our custom transpiler – move all R_x-gates to the end of the circuit.

6.3.2 Usage example

The example below lists Python code to generate a Qiskit circuit preparing 3-ion GHZ state and to execute it on the AQTION setup as in Fig. 6.27.

```
from qiskit import QuantumCircuit
from qiskit_aqt_provider import AQTProvider, aqt_pass_manager

# Initialize AQTION backend and transpiler
aqtion_provider = AQTProvider('MY_TOKEN')
aqtion_backend = aqtion_provider.backends.aqtion_ms_minus
aqtion_transpiler = aqt_pass_manager()

# Generate Qiskit circuit for 3-ion GHZ state preparation
circuit = QuantumCircuit(3)
circuit.h(0)
circuit.cnot(0, 1)
```

```
circuit.cnot(0, 2)
circuit.measure_all()

# Transpile the circuit for AQTION setup
transpiled_circuit = aqtion_transpiler.run(qc)

# Execute the circuit and return the result
job = aqtion_backend.run(transpiled_circuit, shots=500)
result = job.get_counts()
```

6.4 Two-qubit gates fidelities

The principles described in Sec. 6.1 together with the calibration procedures from Sec. 6.2 allow us to achieve and maintain a certain level of two-qubit gate fidelities across the ion chain. This level can be quantified as follows.

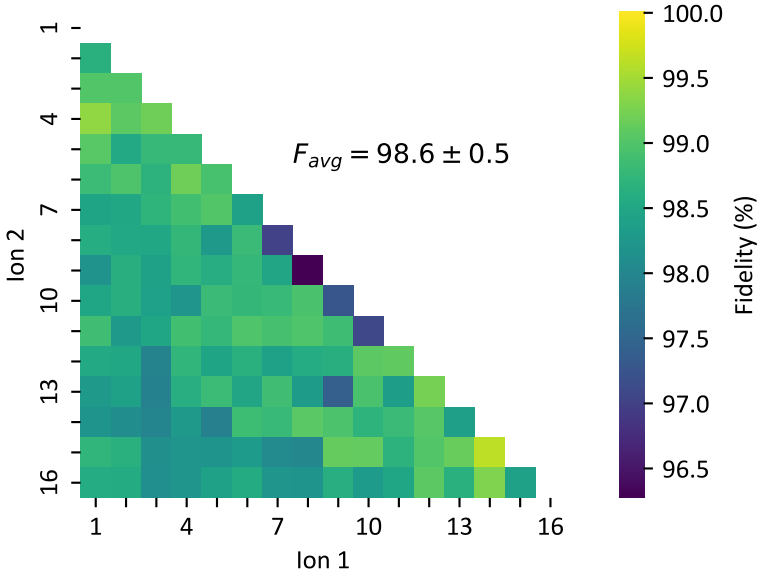

Figure 6.29: Fidelities of two-qubit gates for different ions pairs. The value for each pair is determined from population and parity scans, see example in Fig. 6.30. The results are averaged over nine runs for all pairs.

Currently, during the standard operation of the setup with auto-calibrations, two-qubit gates have a fidelity of around 98.5% when averaged over different pairs as shown in Fig. 6.29. Fidelity for each pair is measured in the following way. First, the 2-ion entangled state $(|00\rangle - i\,|11\rangle)/\sqrt{2}$ is prepared with application of an $XX(-\frac{\pi}{2})$ gate to an ion pair. The actual fidelity of the prepared state is measured with population and parity measurements [116]. The fidelity between the prepared and

the desired state F_{st} can be calculated as follows:

$$F = F_{pro} = F_{st} = \frac{F_{pop} + F_{par}}{2}. \tag{6.47}$$

In this case it is also equal to the process fidelity of the performed XX-gate, assuming that state preparation, measurement and single-qubit gates are error-free. Typical population and parity scans for pair 1-16 are shown in Fig. 6.30.

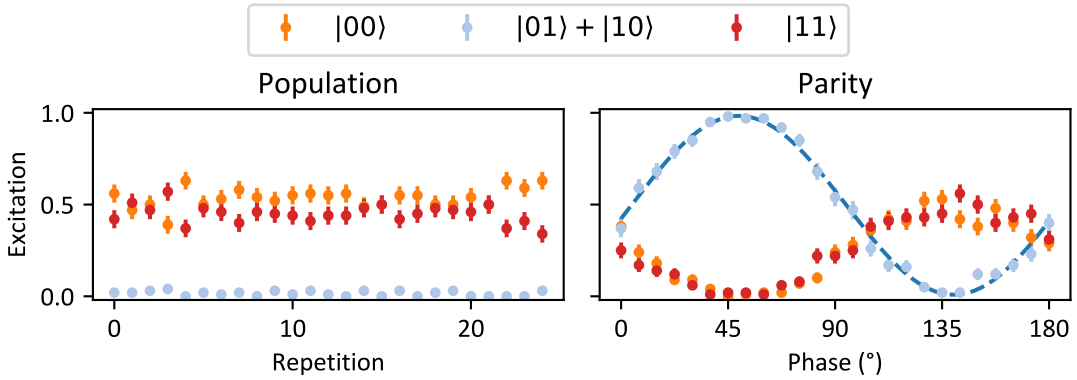

Figure 6.30: Population and parity scans for ion pair 1-16. The XX-gate fidelity is $98.0 \pm 1.3\%$ ($F_{pop} = 98.5 \pm 1.3\%, F_{par} = 97.5 \pm 2.2$ %).

Error sources

We estimate the main sources of infidelity for two-qubit gates in our setup to be:

1. Remaining coupling to radial modes (see Sec. 6.1.6 and Fig. 6.11).
2. Qubit coherence of 50 ms
3. Radial-y COM mode coherence of 50 ms
4. Radial-y COM mode heating rate of 3.6 ph/s.

The contribution of source 1 is estimated in Sec. 6.1.6. Contributions of sources 2–4 we estimate by means of Lindblad master equation simulations using the QuTiP package [117]. We simulate an MS-gate for two ions and one phonon mode (radial-y COM mode). The estimated contributions to infidelity are given in Tab. 6.2. An average experimental infidelity of 1.5% across different pairs is very reasonable for the current configuration of the setup.

The contribution from source 1 can be decreased by the use of modulated pulses. There are various approaches for MS gates with modulated pulses that can be tried [89–91, 101, 118]. Potentially, this contribution can be decreased to 0. Moreover, a modulated pulses approach no longer requires the bichromatic tones to be spectrally close the radial-y COM mode, which has higher heating rate compared to other radial modes. Therefore, the contribution of source 4 will be decreased as well.

Table 6.2: Contribution of different sources to two-qubit gate infidelity in the AQTION setup.

Error source	Contribution (%)
Remaining coupling to radial modes	up to 0.95
Qubit coherence 50 ms	0.6
Radial-y COM mode coherence 50 ms	0.4
Radial-y COM mode heating rate	0.05

The contribution from source 2 can be decreased by increasing the magnetic field stability. Currently, we are using coils to adjust the magnetic field in the setup. We are planning to fully transition to permanent magnets. A similar trapped-ion setup by AQT has demonstrated 400 ms qubit coherence time. We estimate the error from the qubit coherence time of 400 ms to be 0.07%.

The hardware modifications to mitigate these problem are currently being prepared for the AQTION setup. We aim to address sources 1 and 2 first. The further strategy will depend on the results of the upcoming modifications. For example, if source 3 becomes a limiting factor, the RF power stabilization circuit can be improved.

6.5 Summary

Overall, the setup reliably operates in an automated fashion with 16-ion chains following the described methods. Further development of the setup might include increasing the number of ions and fidelities of the two-qubit gates.

All things considered, two-qubit gates represent the main challenge for working with higher numbers of ions in our setup. The performance of the addressing system is still reasonably good even for a 50-ion chain. The calibration routines scale fairly well with the number of ions. However, the fidelities of two-qubit gates will decrease for longer chains, mainly due to the complexity of the radial spectrum and the remaining coupling to the radial modes. Therefore, a crucial next step for scaling the system is the implementation of modulated gate techniques to tackle this problem.

Chapter 7

Quantum error correction applications

Ultimately, quantum error correction should fight the errors affecting the logical information by means of redundant encoding and additional actions detecting and correcting some of the errors. However, a hardware setup should have a minimal level of fidelities for these additional actions to be beneficial. The rate of errors where it becomes beneficial is often referred to as the 'break-even' point (for a specific QEC code) [53, 119]. If the error rates in the experimental system are above break-even QEC procedures will do more harm than good and logical operation fidelities will be lower than the physical ones.

Nowadays, fidelities in state-of-the-art experimental setups including the AQTION setup are close to satisfying the break-even criterion for certain QEC codes [120–123]. While the AQTION setup can not be used for practically useful quantum computing with QEC, it has enough qubits and sufficiently high fidelities to experimentally test and explore intermediate-scale quantum error correction protocols. Such studies can reveal problems with the proposed QEC codes and inspire the development of new hardware-aware QEC codes and methods in QEC. This is a reasonable next step on the way toward useful large-scale quantum computing.

The setup built in this work was involved in three quantum error correction projects. Two of these projects are described in the PhD thesis of Lukas Postler [124]. Sec. 7.1 and Sec. 7.2 contain brief summaries of these projects. The third project is described in Sec. 7.3.

7.1 Steane error correction

The idea of fault tolerance of QEC protocols plays an important role in large-scale error-corrected quantum computing as discussed in Sec. 3.7. All the operations performed with encoded data should not proliferate errors. We have discussed a FT way to read out stabilizer expectation values using flag schemes in Sec. 3.7.4. For example, one of the most resource-efficient schemes for the $[[7, 1, 3]]$ code is a self-flagging scheme proposed in Ref. 73. This is one approach to make stabilizer mapping FT.

Other schemes that are not based on flag qubits have been proposed for FT stabilizer measurement [39, 125, 126]. The main idea of these schemes is to map a stabilizer to several auxiliary qubits instead of one as in flag schemes. Each auxiliary qubit is connected to a single data qubit with a CNOT-gate. Thus, the scheme is inherently FT. A drawback of these schemes is that they require more auxiliary qubits and the auxiliary register must be prepared is a specific state fault-tolerantly. More details

on these schemes can be found in Ref. 127.

Here we describe a scheme proposed by Andrew Steane [125] referred to as 'Steane error correction'. The stabilizers are mapped in such a way that several stabilizers are measured at once. Steane error correction can be applied to different QEC codes, but we will consider it for CSS codes and the $[[7,1,3]]$ code in particular.

7.1.1 Stabilizer measurements

Stabilizer measurements for X- and Z-stabilizers can be done separately for a CSS code. Steane error correction allows one to measure all stabilizers of the same type (e.g. X-stabilizers) simultaneously. The auxiliary register for this scheme is prepared as a specific logical state encoded in the same code as the data register; the $[[7,1,3]]$ in our case. The circuit for the stabilizers readout is shown in Fig. 7.1. Note that the logical state of the auxiliary register is not $|0\rangle_L$ or $|0\dots0\rangle$ as in the case of a single auxiliary qubit as in Fig. ??. Moreover, the auxiliary register must be prepared fault-tolerantly to ensure fault-tolerance of the whole scheme, e.g. as in Fig. 3.11.

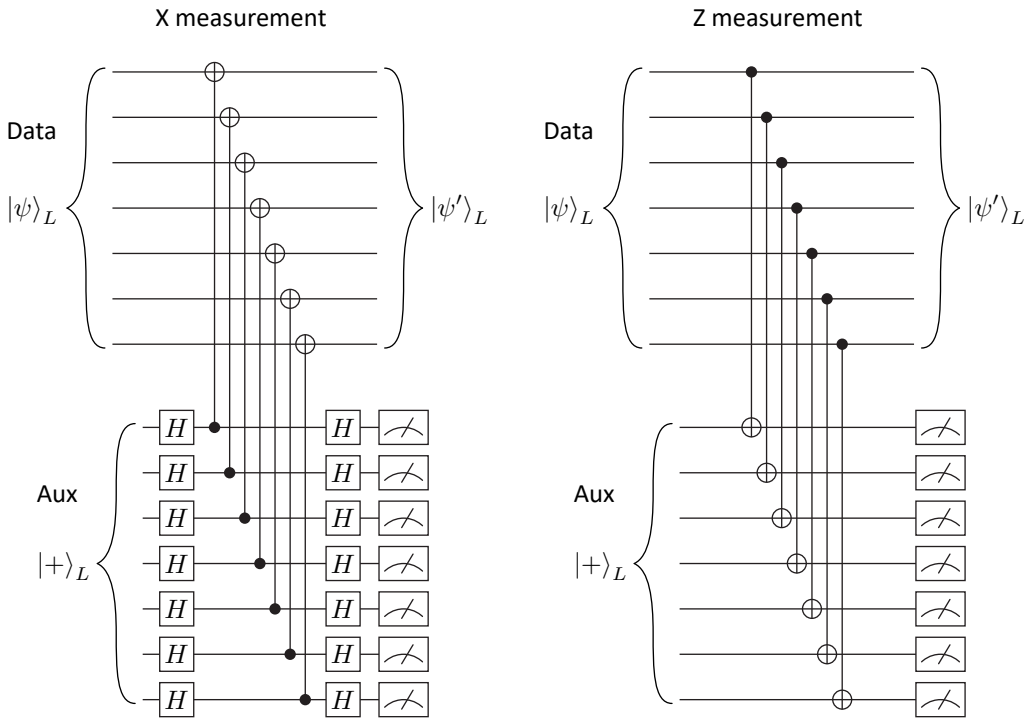

Figure 7.1: Steane error correction stabilizer readout for the $[[7,1,3]]$ code.

Let us consider the circuit for Z-stabilizer measurement (see Fig. 7.1 (right)). The input state for the circuit is a tensor product of the logical data state $|\psi\rangle_L$ and the auxiliary register state prepared in $|\psi_{aux}\rangle_L$:

$$|\psi\rangle_L |\psi_{aux}\rangle_L = \sum_{d\in D} c_d |d\rangle \otimes c_A \sum_{a\in A} |a\rangle . \tag{7.1}$$

Here we decomposed the logical state in the computational basis, e.g. $|1111000\rangle$; d and a are bit strings. Only some computational basis states can be present in the decomposition, namely the ones which are present in the decomposition of $|0\rangle_L$ and $|1\rangle_L$. The coefficients c_d of the logical data state are defined by the information encoded in the logical data state. On the other hand, the auxiliary logical state must be of a special form for Steane error correction: it must be an equal superposition of all states that are simultaneous eigenstates of the stabilizers we are reading, i.e. $S_Z^{(i)}$:

$$|\psi_{aux}\rangle_L = c_A \sum_{a\in A} |a\rangle\,, \qquad S_Z^{(i)}\,|a\rangle = |a\rangle\,, \forall a, \forall i. \tag{7.2}$$

The set A contains all possible computational basis states satisfying the condition. The states $|a\rangle$ should be eigenstates of the stabilizers since when we readout the auxiliary register in the error-free case it should satisfy all the parity checks for these stabilizers. At the same time, an equal superposition of these states is required to preserve the logical data state after the readout, as we will show below. For a CSS code the set A would be all computational basis states present in the $|0\rangle_L$ and the $|1\rangle_L$ decompositions since they are already the eigenstates of Z-stabilizers (see Eq. (3.43)). Hence,

$$|\psi_{aux}\rangle_L = c_A \sum_{a\in A} |a\rangle = (|0\rangle_L + |1\rangle_L)/\sqrt{2} = |+\rangle_L\,. \tag{7.3}$$

This state is notably different from $|0\ldots0\rangle$, which might intuitively seem as a suitable state for this task. $|0\ldots0\rangle$ would also allow us to readout the syndrome correctly, but the data register state will be corrupted after the measurement, as discussed in Ref. 127, while the equal superposition state $|\psi_{aux}\rangle_L$ will prevent this. The fact that the required auxiliary register state is $|+\rangle_L$ is a feature of CSS codes and it is not the case in general.

Now let us consider how the circuit in Fig. 7.1 (right) acts on the input state $|\psi\rangle_L\,|+\rangle_L$. Let us assume that the data register has an error with a bit string e, so the decomposition changes accordingly:

$$\begin{aligned}\mathrm{CNOT}_{1,1}\ldots\mathrm{CNOT}_{7,7}\,|\psi\rangle_L\,|+\rangle_L = \\ \mathrm{CNOT}_{1,1}\ldots\mathrm{CNOT}_{7,7}\sum_{d\in D} c_d\,|d\oplus e\rangle\, c_A \sum_{a\in A}|a\rangle = \\ \sum_{d\in D}\sum_{a\in A} c_d c_A\,|d\oplus e\rangle\,|a\oplus d\oplus e\rangle\,,\end{aligned} \tag{7.4}$$

where $\oplus$ represents bit-wise sum mod 2. The superposition $c_A\sum_{a\in A}|a\rangle$ has all computational basis states present in the logical states. Therefore, if we add $d\oplus e$ to each element of the sum, the new sum will have the same items for each value of d in $d\oplus e$. Consequently, we can take the sum out as a common factor:

$$\sum_{d\in D}\sum_{a\in A} c_d c_A\,|d\oplus e\rangle\,|a\oplus d\oplus e\rangle = \sum_{d\in D} c_d\,|d\oplus e\rangle\, c_A \sum_{a\in A}|a\oplus d\oplus e\rangle\,. \tag{7.5}$$

When we measure the auxiliary register we will project it into one of the states $|a\oplus d\oplus e\rangle$ and the logical data state will be left undisturbed $\sum_{d\in D}|d\oplus e\rangle$. The

stabilizer expectation values can be deduced from the parity of the respective substrings of the bit string $a \oplus d \oplus e$. If there is no error, i.e. $e = 0000000$, all the parity checks will be satisfied, while if there is a non-trivial error some of them will fail.

The full error syndrome is obtained by measuring X-stabilizers and Z-stabilizers sequentially. X-stabilizers can be measured analogously to Z-stabilizers by changing CZ to CX (see Fig. 7.1 (left)), similarly to Figs. 3.1, 3.2.

7.1.2 Publication: Demonstration of fault-tolerant Steane quantum error correction

We have experimentally implemented Steane error correction for the $[[7, 1, 3]]$ code and compared it to the self-flagged scheme from Ref. 73 in Ref. 5. The main result of the paper is shown in Fig. 7.2. Steane error correction demonstrates better performance compared to the flag-based approach. The Steane scheme for the $[[7, 1, 3]]$ code takes fewer two-qubit gates on average than the flag-based scheme. Hence, Steane error correction shows better performance given that two-qubit gates are the main error source in the AQTION setup. Apart from two-qubit gate errors, qubit decoherence and mid-circuit measurement errors are two other major error sources in this experiment. It can be seen from Fig. 7.2 that the advantage of the Steane method is less pronounced for $|+\rangle_L$. It can be explained by the 50 ms qubit coherence time in our setup and $|+\rangle_L$ being more susceptible to decoherence. We additionally studied the performance if all errors except for two-qubit gate errors are decreased by means of numerical simulations. The results in Ref. 5 show that the advantage of Steane error correction is even more pronounced in the case where two-qubit gate errors are dominant. Steane error correction can be very useful in certain hardware architectures, e.g. those where CNOT operations for Steane error correction stabilizer readout can be executed in parallel on two logical qubit registers [128].

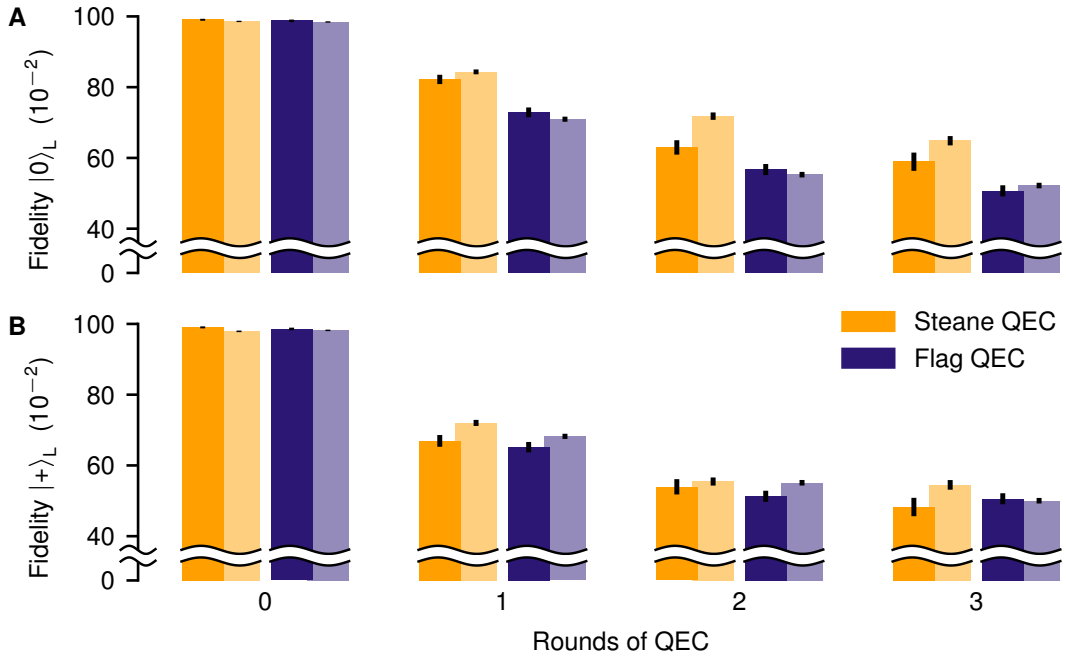

Figure 7.2: **(Fig. 4 from Ref. 5)** Logical fidelities for syndrome extraction on the seven-qubit color code. Logical fidelities obtained from Steane-type and flag-based QEC for the logical input state (**A**) $|0\rangle_L$ and (**B**) $|+\rangle_L$. Round 0 corresponds to the encoding of the logical state with no extra round of QEC. The experimental and simulation results are depicted with darker and lighter shades, respectively.

7.2 Universal logical gate set

Another important aspect of QEC is the implementation of a FT universal gate set with encoded logical qubits. A universal logical gate set opens a way to construction of arbitrary unitary operations (see Sec. 3.3) on a logical level. However, all gates in a universal gate set must be performed fault-tolerantly to avoid error spreading. This is not a trivial task since no QEC code allows for a transversal implementation of a universal gate set according to the Eastin-Knill theorem [68] (see Sec. 3.7.3). Therefore, some of the gates in a universal gate set must be implemented in some other, non-transversal way. Some of the possible options are magic state injection [69, 70], lattice surgery [71, 72] and code switching [61, 62].

In this section we will consider magic state injection for the $[[7, 1, 3]]$ code. We have already shown that the $[[7, 1, 3]]$ code has transversal implementations for the gates H, S, CNOT generating the Clifford group (see Sec. 3.6.1). Thus, adding a FT implementation of the T-gate will complete a universal gate set. This can be done by means of magic state injection.

7.2.1 Magic state injection

The term 'magic state' is usually used for a state having some special properties useful for implementation of non-Clifford gates fault-tolerantly [129, 130]. Such states are often hard to prepare and might require several repetitions of a repeat-until-success procedure [131] or a distillation procedure [132]. Once a magic state is prepared it can be 'injected' into the circuit and result in the application of a required gate. The injection procedure requires only Clifford gates and thus a non-Clifford gate can be implemented by means of Clifford gates if the specific magic state is available.

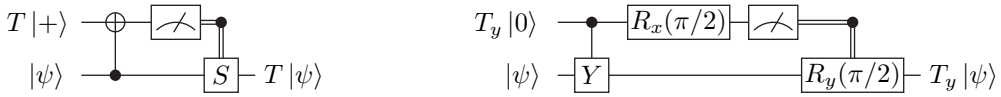

Figure 7.3: Magic state injection for T-gate (left) and T_y-gate (right).

Most frequently 'magic state' refers to a state used for FT implementation of the T-gate or the T-gate in a rotated basis. Let us consider a magic state injection implementing a T-gate with physical qubits as shown in Fig. 7.3 (left). The bottom qubit starts in a state $|\psi\rangle$:

$$|\psi\rangle = a|0\rangle + b|1\rangle \tag{7.6}$$

We want to apply the T-gate to it:

$$T|\psi\rangle = a|0\rangle + be^{i\pi/4}|1\rangle\,. \tag{7.7}$$

We can prepare the top qubit in a magic state $T|+\rangle$ and inject it into the bottom qubit as in the circuit diagram:

$$\mathrm{CNOT}_{2,1}\left[T|+\rangle|\psi\rangle\right] = \frac{1}{\sqrt{2}}\mathrm{CNOT}_{2,1}\left[(|0\rangle + e^{i\pi/4}|1\rangle)(a|0\rangle + b|1\rangle)\right] = \tag{7.8}$$

$$\frac{1}{\sqrt{2}}\left[a(|0\rangle + e^{i\pi/4}|1\rangle)|0\rangle + b(e^{i\pi/4}|0\rangle + |1\rangle)|1\rangle\right] = \tag{7.9}$$

$$\frac{1}{\sqrt{2}}[|0\rangle(a|0\rangle + be^{i\pi/4}|1\rangle) + \tag{7.10}$$

$$e^{i\pi/4}|1\rangle(a|0\rangle + be^{-i\pi/4}|1\rangle)] \tag{7.11}$$

We apply the S-gate based on the measurement results of the first qubit, i.e. the output state of the second qubit will be either

$$|\psi'\rangle = a|0\rangle + be^{i\pi/4}|1\rangle = T|\psi\rangle\,, \tag{7.12}$$

or

$$|\psi''\rangle = S(a|0\rangle + be^{-i\pi/4}|1\rangle) = a|0\rangle + be^{i\pi/4}|1\rangle = T|\psi\rangle\,. \tag{7.13}$$

The resulting state is $T|\psi\rangle$ in both cases. A similar protocol can be applied to implement the T_y-gate, i.e. a rotation by $\pi/4$ around the y-axis of the Bloch sphere:

$$T_y = R_y\left(\frac{\pi}{4}\right) = \begin{pmatrix} \cos\frac{\pi}{8} & -\sin\frac{\pi}{8} \\ \sin\frac{\pi}{8} & \cos\frac{\pi}{8} \end{pmatrix}. \tag{7.14}$$

The circuit for T_y-gate injection is shown in Fig. 7.3 (right). A T_y-gate together with the generators of the Clifford group is also sufficient to complete a universal gate set.

The same circuit can be implemented with logical qubits, encoded in the $[[7,1,3]]$ code in particular. All the gates used in these circuits have transversal implementation in the $[[7,1,3]]$ code: S, CNOT, CY, $R_x(\frac{\pi}{2})$, $R_y(\frac{\pi}{2})$. However, magic states like $T_L\left|+\right\rangle_L$ and $T_{y_L}\left|0\right\rangle_L$ are hard to prepare fault-tolerantly.

7.2.2 $T_{y_L}\left|0\right\rangle_L$ magic state preparation

We prepared the $T_{y_L}\left|0\right\rangle_L$ magic state for the $[[7,1,3]]$ code following the method proposed in Ref. 133. Let us denote

$$\left|H\right\rangle = T_y\left|0\right\rangle = \cos\frac{\pi}{8}\left|0\right\rangle + \sin\frac{\pi}{8}\left|1\right\rangle . \tag{7.15}$$

The state $\left|H\right\rangle$ is a $+1$ eigenstate of the H-gate:

$$H\left|H\right\rangle = \left|H\right\rangle . \tag{7.16}$$

Based on this fact the following scheme to fault-tolerantly prepare the $\left|H\right\rangle_L$ state is proposed:

1. Prepare $\left|H\right\rangle_L$ non-fault-tolerantly similarly to $\left|0\right\rangle_L$ preparation as in Fig. 3.7.
2. Measure the H_L operator to catch error propagation with the Hadamard test and discard '-1 outcomes'. $\left|H\right\rangle_L$ is a $+1$ eigenstate of the H_L-gate so it will not be altered after the Hamadard test while other states will be projected into $\left|H\right\rangle_L$. This is analogous to Z_L measurement for $\left|0\right\rangle_L$ as in Fig. 3.11.
3. Measure stabilziers of the $[[7,1,3]]$ code to catch other dangerous error propagation. The self-flagging scheme from Ref. 73 is used. Discard the state if the error syndrome is non-trivial.

The whole protocol is sketched in Fig. 7.4 a. The results are post-selected on the outcomes of eight flag qubits: two from the H_L measurement (step 2) and six from the stabilizer measurement (step 3). The fidelity of the resulting state is greatly boosted with each step of the procedure as indicated in Fig. 7.4 c at the cost of post-selection. This preparation procedure ensures that no error propagation will lead to uncorrectable errors.

7.2.3 Publication: Demonstration of fault-tolerant universal quantum gate operations

The ability to fault-tolerantly prepare the magic state $\left|H\right\rangle_L$ allows us to implement a universal logical gate set for the $[[7,1,3]]$ code fault-tolerantly. We have demonstrated this experimentally in Ref. 3 using the AQTION setup. The main components of a universal gate set were presented with two logical qubits encoded in the

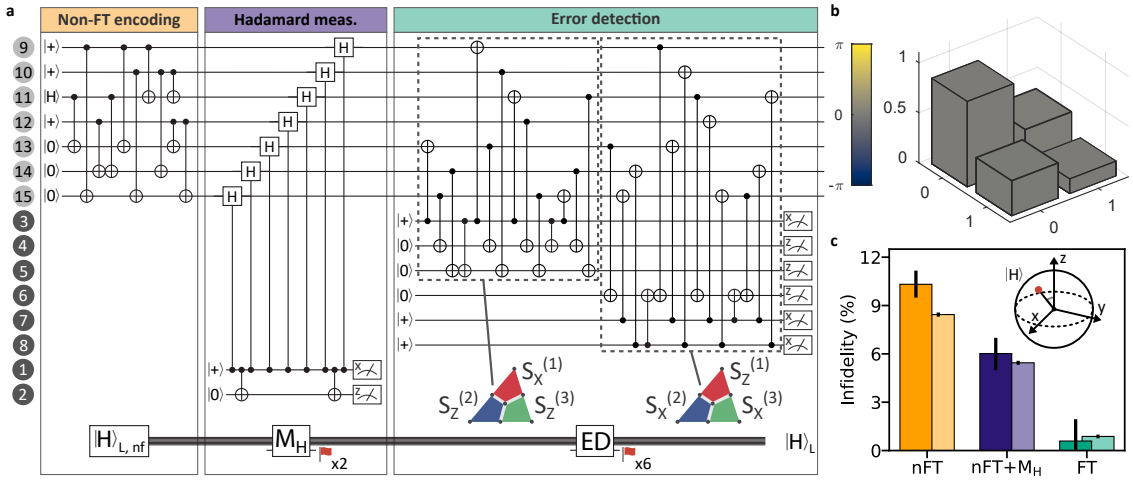

Figure 7.4: **(Fig. 4 from Ref. 3)** Fault-tolerant generation of a logical magic state $|H\rangle_L$. (a) The magic state is prepared non-fault-tolerantly in a first step, where a physical magic state $|H\rangle$ is mapped to the logical state $|H\rangle_{L,\mathrm{nf}}$ encoded in the data qubits at positions 9 to 15 in the ion string (see labels at left of circuit). Thereafter, a FT measurement of the Hadamard operator (M_H) is carried out. Two ancilla qubits herald that the prepared state is a $+1$ eigenstate of the Hadamard operator but also that no dangerous error occurred during the measurement. The magic state preparation is concluded with an error detection block that measures the three X- and Z-type stabilizers each in a fault-tolerant fashion. The first part of the error detection circuit (first dashed box), measures $S_X^{(1)}$, $S_Z^{(2)}$ and $S_Z^{(3)}$, whereas the second part measures $S_Z^{(1}$, $S_X^{(2)}$ and $S_X^{(2)}$. The magic state preparation is discarded and repeated in case of a non-trivial syndrome of the eight ancilla qubits 1 to 8. (b) Logical state tomography after FT magic state preparation. The phase of the complex amplitudes is encoded in the color of the 3D bar plot and the wireframes depict ideal results. Phase deviations from the ideal density matrix are smaller than 50 mrad while amplitude deviations are smaller than 0.07. (c) The decrease in infidelity of the logical magic state (red marker on Bloch sphere) after each step of the FT preparation procedure is observed experimentally and captured by depolarizing noise simulations (experimental/simulation results depicted darker/lighter).

$[[7, 1, 3]]$ code: different transversal single-qubit Clifford operations (Fig. 7.5), the transversal CNOT-gate (Fig. 7.6) and the T_{y_L} via magic state injection as discussed before (Fig. 7.7).

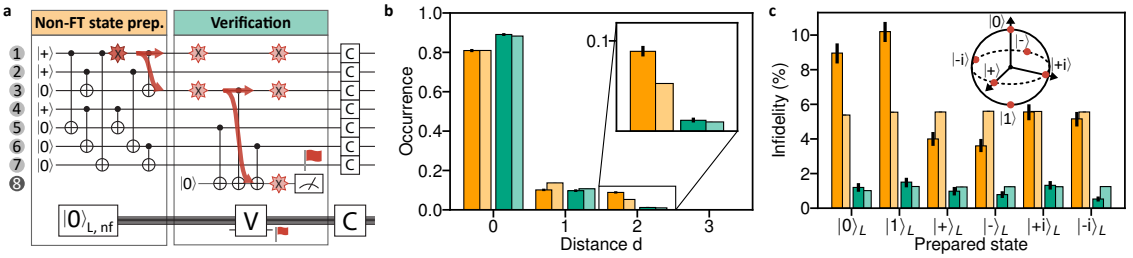

Figure 7.5: **(Fig. 2 from Ref. 3)** Fault-tolerant (FT) preparation of a logical basis state $|0\rangle_L$ and logical Clifford operations. (a) Logical Pauli states are prepared fault-tolerantly in three steps: First $|0\rangle_L$ is prepared by a non-fault-tolerant circuit. fault tolerance is ensured through verification (V) of the state by coupling to an additional flag ancilla qubit. This qubit, when measured as $|0\rangle$, signals that the correct state has been prepared fault-tolerantly, i.e. up to single-qubit errors. To prepare a logical Pauli eigenstate other than $|0\rangle_L$ an additional transversal Clifford gate needs to be applied. (b) Relative occurrence rates of logical output states of distance d to the target state $|0\rangle_L$ for non-FT (orange) and FT (turquoise) initialization. Example states of $d = 1, 2, 3$ are $X_0 |0\rangle_L$, $X_0X_1 |0\rangle_L$, $X_0X_1X_2 |0\rangle_L$. Simulation results are depicted by lighter colored bars. as described in the main text, all circuit elements are subject to depolarizing noise in numerical simulations. (c) Logical infidelities of all six logical Pauli eigenstates (red markers on Bloch sphere) including an ideal round of error correction performed in post-processing (experimental/simulation results depicted darker/lighter).

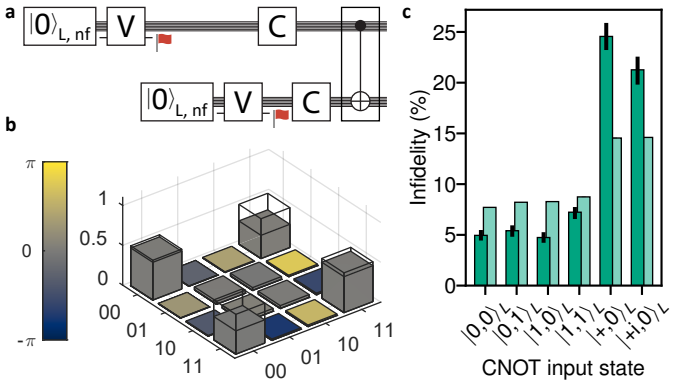

Figure 7.6: **(Fig. 3 from Ref. 3)** FT implementation of a logical entangling gate. (a) To estimate the performance of the logical CNOT-gate we fault-tolerantly prepare six different logical two-qubit input states and apply the transversal CNOT-gate (framed gate at the end of the circuit). (b) Logical state tomography after applying the CNOT-gate to the $|+, 0\rangle$ state. The phase of the complex amplitudes is encoded in the color of the 3D bar plot and the wireframes depict ideal results. (c) Logical infidelities for six different input states of the CNOT-gate (experimental/simulation results depicted darker/lighter).

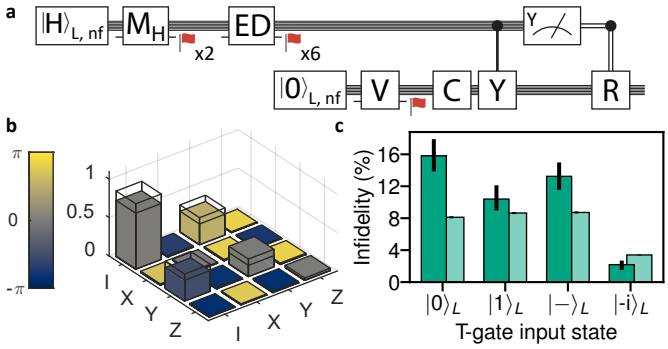

Figure 7.7: **(Fig. 5 from Ref. 3)** FT T-gate injection. (a) After performing the fully fault-tolerant three step procedure of preparing the logical magic state, the logical T-gate is applied via logical gate teleportation onto a second register that has a logical Pauli state prepared. Conditional application of $R \equiv R_Y(\pi/2)$ is done in post-processing. (b) Logical process matrix of the experimental logical T-gate. The phase of the complex amplitudes is encoded in the color of the 3D bar plot and the wireframes depict ideal results. (c) Infidelities of the data qubit state when applying the logical T-gate to several logical Pauli input states (experimental/simulation results depicted darker/lighter). Infidelity is the lowest for the $|+i\rangle_L$ state since it is an eigenstate of the T-gate. Infidelity is slightly larger for $|1\rangle_L$ and $|+\rangle_L$ than for $|0\rangle_L$ since preparation contains an additional transversal Clifford operation prone to errors.

7.3 Code switching

Magic state injection in not the only way to implement a universal logical gate set. The Eastin-Knill theorem forbids a transversal implementation of a universal gate set in a single QEC code. However, one can use two complementary QEC codes to form a transversal universal gate set together. For example, code A can have transversal $H_L, S_L, \mathrm{CNOT}_L$ and code B can have transversal T_L, CNOT_L. The information encoded in one code can be fault-tolerantly reencoded in another code with a procedure called 'code switching'. The computation can start in one code and once a non-transversal operation must be applied the code can be switched to another one to apply this operation transversally (see Fig. 7.8).

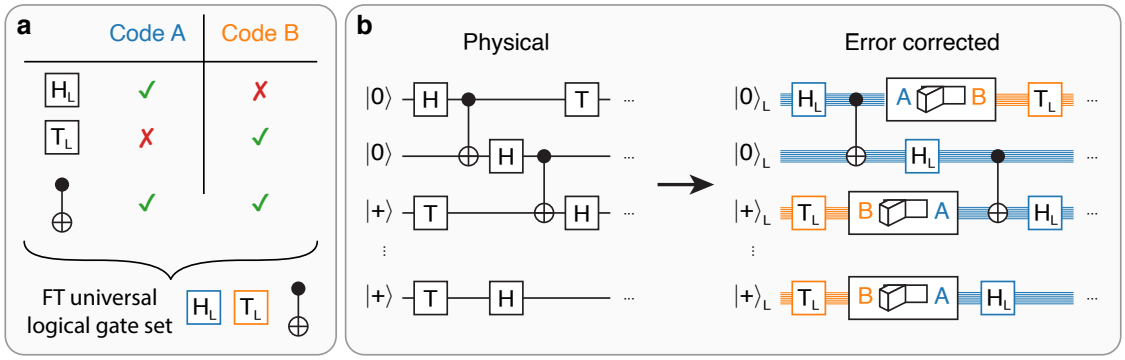

Figure 7.8: **(Fig. 1 from Ref. 2)** Quantum algorithms with universal gate set. (a) Two codes with complementary sets of FT gates in combination amount to a complete FT universal logical gate set $\{H_L, T_L, \mathrm{CNOT}_L\}$. (b) An algorithm running on physical qubits (left) can be run fault-tolerantly on logical qubits (right) by switching between two codes. If, for example, the FT T_L gate is only available in code B (orange), one has to switch to this code before applying the respective gate operation.

Aside from providing an avenue to complete a universal logical gate set, code switching can offer additional flexibility for quantum computing with logical qubits. For example, two codes might be used as a 'storage' code and a 'computational' code. A logical qubit can be switched to the storage code when it is not going to be used for some time to provide higher robustness against idling errors (e.g. decoherence). On the other hand, when a logical qubit is going to be involved in a lot of two-qubit gates it can be switched to the computational code which has higher robustness against gate errors or more efficient implementation of two-qubit gates.

Two stabilizer codes must obey certain conditions to make code switching between them available. It must be possible to represent logical operators in the same way for both codes and both stabilizer groups of these codes must include the stabilizer group of the same subsystems code (see Sec. 3.5.1). If we take the $[[7, 1, 3]]$ code as code A, a promising candidate for code B is the $[[15, 1, 3]]$ code.

7.3.1 The $[[15, 1, 3]]$ code

The $[[15, 1, 3]]$ code belongs to the 3D color code family [65]. It is a CSS code that encodes one logical qubit with 15 physical qubits. The stabilizers are supported on a tetrahedral structure as in Fig. 7.9. Hence, the code is sometimes referred to as 'the 15-qubit tetrahedral code'. Its X-type stabilizer generators are supported on four cells of the tetrahedral structure, while the Z-type stabilizer generators are supported on all faces (external and internal) of the tetrahedral structure.

Cells

$$S_X^{(1)} = S_Z^{(R)} = X_1X_2X_3X_4X_8X_{13}X_{14}X_{15}$$
$$S_X^{(2)} = S_Z^{(G)} = X_2X_3X_5X_6X_9X_{12}X_{14}X_{15}$$
$$S_X^{(3)} = S_Z^{(B)} = X_3X_4X_6X_7X_{10}X_{12}X_{13}X_{14}$$
$$S_X^{(4)} = S_Z^{(Y)} = X_8X_9X_{10}X_{11}X_{12}X_{13}X_{14}X_{15}$$

Faces

$$S_Z^{(1)} = S_Z^{(R)} = Z_1Z_2Z_3Z_4$$
$$S_Z^{(2)} = S_Z^{(G)} = Z_2Z_3Z_5Z_6$$
$$S_Z^{(3)} = S_Z^{(B)} = Z_3Z_4Z_6Z_7$$
$$S_Z^{(4)} = S_Z^{(Y)} = Z_8Z_9Z_{11}Z_{15}$$

$$S_Z^{(5)} = S_Z^{(RG)} = Z_2Z_3Z_{14}Z_{15}$$
$$\vdots$$
$$S_Z^{(10)} = S_Z^{(BY)} = Z_{10}Z_{12}Z_{13}Z_{14}$$

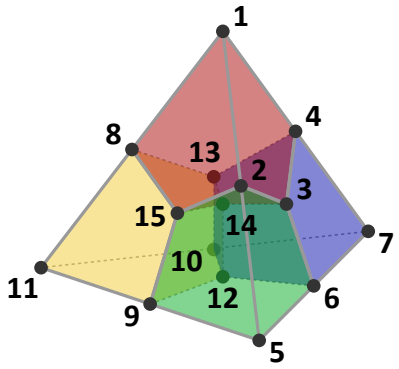

$$Z_L = Z_1 \dots Z_{15}$$
$$X_L = X_1 \dots X_{15}$$

Figure 7.9: $[[15, 1, 3]]$ code, its stabilizer generators and logical operators. The colors of the cells and the faces are labeled as R, G, B, Y. Double labels, e.g. RG, indicate a face between the cell of the respective colors.

The logical operators are defined on all 15 qubits as

$$Z_L = Z_1Z_2Z_3Z_4Z_5Z_6Z_7Z_8Z_9Z_{10}Z_{11}Z_{12}Z_{13}Z_{14}Z_{15}, \tag{7.17}$$
$$X_L = X_1X_1X_2X_3X_5X_6X_7X_8X_9X_{10}X_{11}X_{12}X_{13}X_{14}X_{15}. \tag{7.18}$$

The following operators are stabilizer-equivalent to the logical operators:

$$Z_L' = S_Z^{(1)}S_Z^{(4)}S_Z^{(10)}Z_L = Z_5Z_6Z_7, \tag{7.19}$$
$$X_L' = S_X^{(4)}X_L = X_1X_2X_3X_4X_5X_6X_7. \tag{7.20}$$

These are the minimal weight logical operators, so the code has $d_Z = 3$ for Z-errors and $d_X = 7$ for X-errors.

The $[[15, 1, 3]]$ code, as a CSS code, allows to implement the logical CNOT-gate transversally [63]. The logical Hadamard gate is not transversal in the $[[15, 1, 3]]$ code [63] since it is not a self-dual CSS code, X- and $Z-$stabilizers have different supports. However, it can be shown that the $[[15, 1, 3]]$ code is the smallest distance-three QEC code that has a transversal implementation of a non-Clifford gate [134]: the logical T-gate. The logical T-gate can be implemented as follows [62–64, 135] (see Fig. 7.10):

$$T_L = T_1 T_2^\dagger T_3 T_4^\dagger T_5 T_6^\dagger T_7 T_8^\dagger T_9^\dagger T_{10}^\dagger T_{11} T_{12} T_{13} T_{14}^\dagger T_{15}. \tag{7.21}$$

T is applied to eight qubits and $T^\dagger$ is applied to seven qubits.

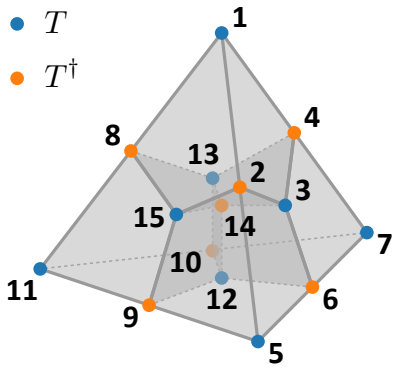

Figure 7.10: Transversal T_L implementation for the $[[15, 1, 3]]$ code. T is applied to blue qubits and $T^\dagger$ is applied to orange qubits.

The effect of this gate can be illustrated by applying it to $|0\rangle_L$ and $|1\rangle_L$. The $|0\rangle_L$ can be represented in the following way (see Eq. (3.43)):

$$|0\rangle_L = a \sum_{S_X \in \mathcal{S}_X} S_X |0 \dots 0\rangle , \tag{7.22}$$

where $\mathcal{S}_X$ is the set of all X-stabilizers of the $[[15, 1, 3]]$ code. The T-gate and the X-gate obey the following:

$$TX = e^{i\pi/4} XT^\dagger, \tag{7.23}$$

$$T^\dagger X = e^{-i\pi/4} XT. \tag{7.24}$$

Therefore, the action of T_L on $|0\rangle_L$ is as follows:

$$\begin{aligned} T_L |0\rangle_L &= a T_L \sum_{S_X \in \mathcal{S}_X} S_X |0 \dots 0\rangle = a \sum_{S_X \in \mathcal{S}_X} T_1 T_3 \dots T_{15} T_2^\dagger T_4^\dagger \dots T_{14}^\dagger S_X |0 \dots 0\rangle \\ &= a \sum_{S_X \in \mathcal{S}_X} e^{(\mathbf{4-4})\cdot i\pi/4} S_X T_1^\dagger T_3^\dagger \dots T_{15}^\dagger T_2 T_4 \dots T_{14} |0 \dots 0\rangle = a \sum_{S_X \in \mathcal{S}_X} S_X |0 \dots 0\rangle = |0\rangle_L . \end{aligned} \tag{7.25}$$

Note that factors $e^{i\pi/4}$ and $e^{-i\pi/4}$ appear four times (shown in bold) each since T_L overlaps with any X-stabilizer at eight sites: four sites have T acting on them and four sites have $T^\dagger$ acting on them. Consequently, in total, the factors cancel.

Similarly, for the $|1\rangle_L$ state we get:

$$T_L |1\rangle_L = T_L X_L |0\rangle_L = e^{(\mathbf{8-7})\cdot i\pi/4} X_L T_L^\dagger |0\rangle_L = e^{i\pi/4} X_L |0\rangle_L = e^{i\pi/4} |1\rangle_L . \tag{7.26}$$

T_L overlaps with X_L at all 15 sites: eight sites have T acting on then and seven sites have $T^\dagger$ acting on them (shown in bold). Therefore, we get a factor of $e^{i\pi/4}$.

Overall, T_L has the desired action on the logical states:

$$T_L |0\rangle_L = |0\rangle_L , \tag{7.27}$$
$$T_L |1\rangle_L = e^{i\pi/4} |1\rangle_L . \tag{7.28}$$

7.3.2 Code switching $[[7, 1, 3]] \leftrightarrow [[15, 1, 3]]$

The $[[7, 1, 3]]$ code and the $[[15, 1, 3]]$ code are valid candidates for code switching [63, 64, 136–138] according to the conditions discussed in Sec. 3.5.1. The $[[7, 1, 3]]$ code is considered together with the eight qubits from the tetrahedral structure that are not used in the $[[7, 1, 3]]$ code, i.e. qubits 8–15. We will call these eight qubits 'bulk' (see Fig. 7.11). Z-stabilizers supported on the faces connecting qubits 1–7 to the bulk are not stabilizers in this code. On the other hand, X-stabilizers supported on the other faces are stabilizers, according to the definition of the $[[7, 1, 3]]$ code.

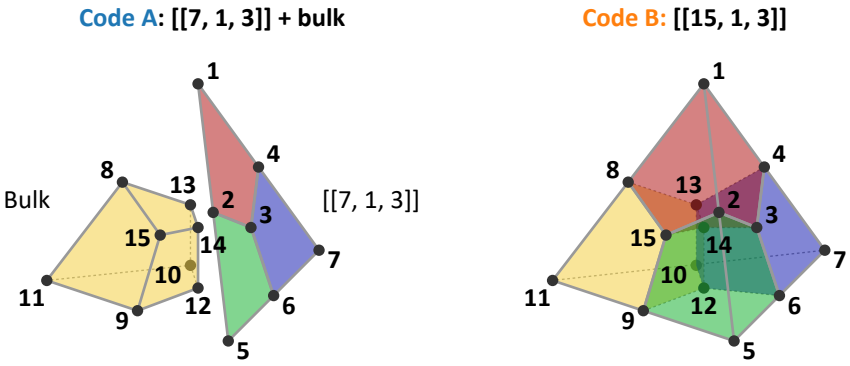

Figure 7.11: The $[[7, 1, 3]]$ code with the bulk and the $[[15, 1, 3]]$ code.

We can define a subsystem code $\mathcal{G}$ on the tetrahedral structure using all faces as X- and Z-gauge operators. The center of $\mathcal{G}$ will contain X- and Z-stabilizers with the support on cells. We denote the center as $\mathcal{S}$. The stabilizers of all three codes are given in Tab. 7.1. It can be seen that:

$$\mathcal{S} \subset \mathcal{S}_A \tag{7.29}$$
$$\mathcal{S} \subset \mathcal{S}_B. \tag{7.30}$$

Moreover, the logical operators of the codes have a common representation:

$$Z_L = Z_1 Z_2 Z_3 Z_4 Z_5 Z_6 Z_7, \tag{7.31}$$
$$X_L = X_1 X_1 X_2 X_3 X_5 X_6 X_7. \tag{7.32}$$

Table 7.1: Stabilizers of the $[[7,1,3]]$, the $[[15,1,3]]$ and the subsystem code $\mathcal{G}$ used for switching between the first two codes.

	$\mathcal{S}_A$: $[[7,1,3]]$ + bulk	$\mathcal{S}$ / $\mathcal{G}$	$\mathcal{S}_B$: $[[15,1,3]]$
X-cells	✓	✓ / ✓	✓
Connecting X-faces: 'RG': $X_2X_3X_{14}X_{15}$ 'RB': $X_3X_4X_{13}X_{14}$ 'BG': $X_3X_6X_{12}X_{14}$	✗	✗ / ✓	✗
Other X-faces:	✓	✗ / ✓	✗
Z-cells	✓	✓ / ✓	✓
Connecting Z-faces: 'RG': $Z_2Z_3Z_{14}Z_{15}$ 'RB': $Z_3Z_4Z_{13}Z_{14}$ 'BG': $Z_3Z_6Z_{12}Z_{14}$	✗	✗ / ✓	✓
Other Z-faces:	✓	✗ / ✓	✓

Therefore, code switching can be performed between these two codes.

The switching $[[7,1,3]] \to [[15,1,3]]$ can be performed in the following way (see Sec. 3.5.1):

- The stabilizers in $\mathcal{S}_B \setminus \mathcal{S}_A$ are measured, i.e. Z-stabilizers supported on the connecting faces. The switching syndrome is obtained.
- Operators from $\mathcal{G} \setminus \mathcal{S}$ can be applied to fix the gauge. In this case, X-stabilizers of the $[[7,1,3]]$ code should be applied to fix the values for Z-stabilizers supported on the connecting faces.

The example is illustrated in Fig. 7.12. Switching in the other direction is done analogously: the X-stabilizers of the $[[7,1,3]]$ code are measured and Z-stabilizers supported on the connecting faces are applied for gauge fixing.

The whole switching procedure can be made FT if additional checks and flag qubits are added, see Ref. 64, 138 for details. FT code switching has a substantial overhead compared to nFT. However, FT code switching between $[[7,1,3]]$ and $[[15,1,3]]$ can be performed deterministically, unlike the magic state preparation discussed in Sec. 7.2.

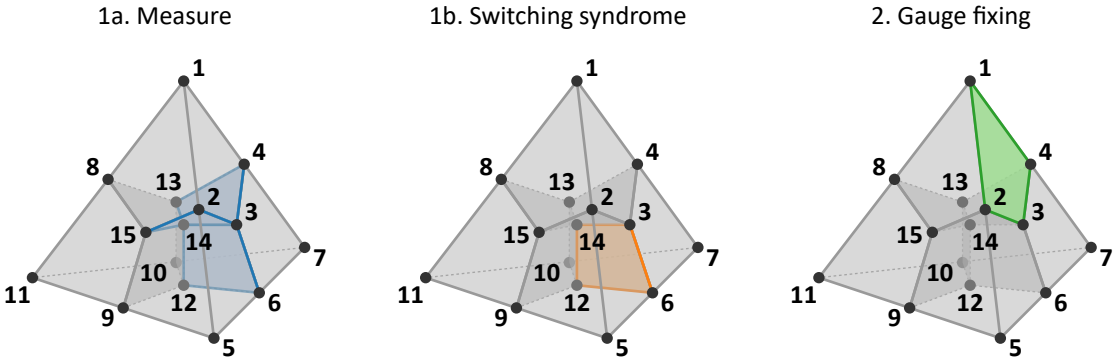

Figure 7.12: $[[7,1,3]] \rightarrow [[15,1,3]]$ code switching example. (1a) $\mathcal{S}_B \setminus \mathcal{S}_A$ stabilizers are measured, i.e. Z-stabilizers supported on the faces shown in blue. (1b) The stabilizer $Z_3Z_6Z_{12}Z_{14}$ measurement outcome is -1, i.e. the switching syndrome is $(0,0,1)$. (2) Gauge fixing is performed according to the switching syndrome, i.e. stabilizer $X_1X_2X_3X_4$ is applied to fix the value of stabilizer $Z_3Z_6Z_{12}Z_{14}$.

7.3.3 The $[[10,1,2]]$ code

One way to minimize the required number of gates and qubits at the cost of non-determinism is code morphing [139]. Code morphing allows to generate new QEC codes from existing ones. A stabilizer code $\mathcal{S}_p$ (parent code) can have a smaller stabilizer code $\mathcal{S}_c$ (child code) contained inside it. This is the case if the parent stabilizer group $\mathcal{S}_p$ has a subgroup $\mathcal{S}_c$ supported on the subset of qubits of the parent code. For example, the $[[15,1,3]]$ code has a smaller $[[8,3,2]]$ code [140] as a child code. The $[[8,3,2]]$ code can be supported on the bulk qubits (see Fig. 7.11) and encodes three logical qubits. The idea of morphing is to replace the logical qubits encoded in the child code with physical qubits. For example, the $[[8,3,2]]$ code can be replaced by only three physical qubits and the five other physical qubits are removed entirely (see Fig. 7.13). This morphs the $[[15,1,3]]$ code into the $[[10,1,2]]$ code. More details on the morphing procedure can be found in Ref. 64, 138, 139.

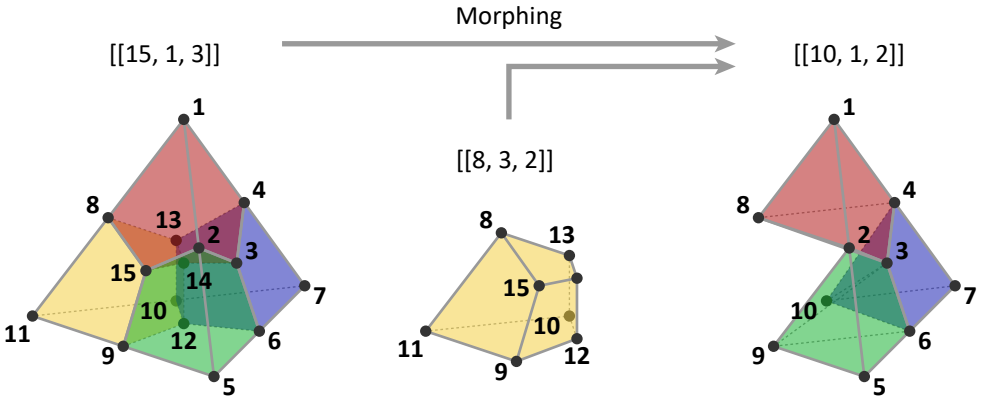

Figure 7.13: The $[[15,1,3]]$ code morphing into the $[[10,1,2]]$ code.

The morphed code $[[10,1,2]]$ keeps some of the properties of the parent code $[[15,1,3]]$. The Z-stabilizers supported on the faces not involved in the bulk remain the same.

The X-stabilizers supported on the cells are now weight-5 instead of weight-8. Z-stabilizers supported on the faces connecting the bulk to the rest change to weight-3. In summary, the $[[10, 1, 2]]$ code is defined by the following stabilizers:

$$\begin{aligned} S_Z^{(1)} &= Z_1Z_2Z_3Z_4, & S_X^{(1)} &= X_1X_2X_3X_4X_8 \\ S_Z^{(2)} &= Z_2Z_3Z_5Z_6, & S_X^{(2)} &= X_2X_3X_5X_6X_9 \\ S_Z^{(3)} &= Z_3Z_4Z_6Z_7, & S_X^{(3)} &= X_3X_4X_6X_7X_{10} \\ S_Z^{(4)} &= Z_3Z_6Z_8, \\ S_Z^{(5)} &= Z_3Z_4Z_9, \\ S_Z^{(6)} &= Z_2Z_3Z_{10}. \end{aligned} \tag{7.33}$$

The logical operators have the same representations as for $[[7, 1, 3]]$ and $[[15, 1, 3]]$:

$$\begin{aligned} Z_L &= Z_1Z_2Z_3Z_4Z_5Z_6Z_7, \\ X_L &= X_1X_2X_3X_4X_5X_6X_7. \end{aligned} \tag{7.34}$$

The minimal weight logical operators are

$$Z_L' = S_Z^{(2)}S_Z^{(3)}S_Z^{(4)}Z_L = Z_1Z_8, \tag{7.35}$$

$$X_L' = S_X^{(1)}X_L = X_5X_6X_7X_8. \tag{7.36}$$

The $[[10, 1, 2]]$ code has $d_Z = 2$ for Z-errors and $d_X = 4$ for X-errors. Therefore, the code is only error-detecting because some Z-error cannot be distinguished, e.g. Z_1 and Z_8.

The $[[10, 1, 2]]$ code has a fault-tolerant implementation of the logical T-gate [64, 138]:

$$T_L = T_1T_2^\dagger T_3T_4^\dagger T_5T_6^\dagger T_7\mathrm{CC}Z_{8,9,10} \tag{7.37}$$

The implementation is not transversal anymore since it contains CCZ between physical qubits of the same logical qubit. However, it is fault-tolerant since all errors that can propagate are detectable.

Summarizing, the morphed code $[[10, 1, 2]]$ has lower-weight stabilizers and requires fewer qubits than the parent $[[15, 1, 3]]$ code, i.e. the requirements for the experimental setup are lower. On the other hand, the distance of the $[[10, 1, 2]]$ code is lower; it is only an error-detecting code. If certain Z-errors happen, the logical state can not be corrected and should be discarded which results in non-determinism of the switching protocols. However, unlike the $[[15, 1, 3]]$ code, the $[[10, 1, 2]]$ code is within reach of the capabilities of the AQTION setup and can be used to study code switching protocols experimentally.

7.3.4 Code switching $[[7, 1, 3]] \leftrightarrow [[10, 1, 2]]$

The $[[7, 1, 3]]$ code and the $[[10, 1, 2]]$ code are also valid candidates for code switching [64, 138]. The logic is very similar to the $[[7, 1, 3]] \leftrightarrow [[15, 1, 3]]$ switching. We can

define a subsystem code $\mathcal{G}$ such that it includes all stabilizers of both codes, i.e. weight-5 X-cells, weight-4 X-faces, weight-3 Z-faces and weight-4 Z-faces. The center $\mathcal{S}$ of the gauge group $\mathcal{G}$ contains weight-5 X-cells and weight-4 Z-faces. The stabilizers of all three codes are shown in the Tab. 7.2.

Table 7.2: Stabilizers of the $[[7,1,3]]$, the $[[10,1,2]]$ and the subsystem code $\mathcal{G}$ used for switching between the first two codes.

	$\mathcal{S}_A$: $[[7,1,3]]$ + bulk	$\mathcal{S}$ / $\mathcal{G}$	$\mathcal{S}_B$: $[[10,1,2]]$
Weight-5 X-cells $X_1X_2X_3X_4X_8$ $X_2X_3X_5X_6X_9$ $X_3X_4X_6X_7X_{10}$	✓	✓ / ✓	✓
Weight-4 X-faces: $X_1X_2X_3X_4$ $X_2X_3X_5X_6$ $X_3X_4X_6X_7$	✓	✗ / ✓	✗
Single-qubit bulk X: X_8 X_9 X_{10}	✓	✗ / ✓	✗
Weight-4 Z-faces: $Z_1Z_2Z_3Z_4$ $Z_2Z_3Z_5Z_6$ $Z_3Z_4Z_6Z_7$	✓	✓ / ✓	✓
Weight-3 Z-faces: $Z_3Z_6Z_8$ $Z_3Z_4Z_9$ $Z_2Z_3Z_{10}$	✗	✗ / ✓	✓

Both codes share a representation of the logical operators:

$$Z_L = Z_1Z_2Z_3Z_4Z_5Z_6Z_7, \tag{7.38}$$
$$X_L = X_1X_1X_2X_3X_5X_6X_7. \tag{7.39}$$

The switching procedure for $[[7,1,3]] \to [[10,1,2]]$ is also similar:

- The stabilizers in $\mathcal{S}_B \setminus \mathcal{S}_A$ are measured, i.e. Z-stabilizers supported on the weight-3 faces. The switching syndrome is obtained.
- Operators from $\mathcal{G} \setminus \mathcal{S}$ can be applied to fix the gauge. In this case, X-stabilizers of the $[[7, 1, 3]]$ code should be applied to fix the values for Z-stabilizers supported on the weight-3 faces.

An example is given in Fig. 7.14. The opposite switching direction is done analogously: weight-4 X-faces are measured, weight-3 Z-faces are applied for gauge fixing.

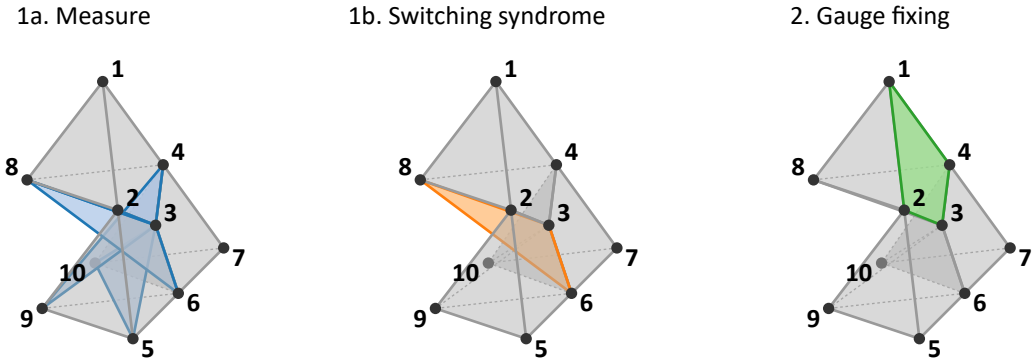

Figure 7.14: $[[7, 1, 3]] \to [[10, 1, 2]]$ code switching example. (1a) $\mathcal{S}_B \setminus \mathcal{S}_A$ stabilizers are measured, i.e. Z-stabilizers supported on the weight-3 face shown in blue. (1b) The stabilizer $Z_3Z_6Z_8$ measurement outcome is -1, i.e. the switching syndrome is $(1, 0, 0)$. (2) Gauge fixing is performed according to the switching syndrome, i.e. stabilizer $X_1X_2X_3X_4$ is applied to fix the value of stabilizer $Z_3Z_6Z_8$.

The whole procedure can be conducted fault-tolerantly if additional checks are introduced [2, 64, 138]. The overhead is lower than for the $[[7, 1, 3]] \leftrightarrow [[15, 1, 3]]$ switching, making the $[[7, 1, 3]] \leftrightarrow [[10, 1, 2]]$ switching more feasible for near-term quantum computers.

7.3.5 Publication: Experimental fault-tolerant code switching

We have demonstrated experimental fault-tolerant code switching between $[[7, 1, 3]]$ and $[[10, 1, 2]]$ in Ref. 2; the publication is provided below. We have shown different building blocks of the code switching approach: logical state preparation for both codes, switching in both directions, logical Clifford gates in $[[7, 1, 3]]$ and the logical T-gate in $[[10, 1, 2]]$. All these blocks together provide a flexible framework for quantum computing with logical qubits. We illustrate it by running a minimal example of a logical circuit including all elements of the universal logical gate set: T_L, H_L, CNOT_L.

Code switching provides a viable alternative to magic state injection. It is not yet clear which option is more efficient for large-scale quantum computing with encoded qubits [137, 138] given that both approaches have been barely studied experimentally. Theoretically, code switching might need fewer auxiliary qubits since it does not require an additional logical auxiliary qubit as magic state injection does. Moreover, code switching can be done deterministically. On the other hand, magic state injection can have lower overhead in gate count. Any comparison of these two concepts heavily depends on the QEC code and the experimental platform with its error profile and the benefits of both approaches are yet to be studied for large-scale quantum computing.

Experimental fault-tolerant code switching

Ivan Pogorelov,[1,*] Friederike Butt,[2,3,*] Lukas Postler,[1] Christian D. Marciniak,[1]
Philipp Schindler,[1] Markus Müller,[2,3] and Thomas Monz[1,†]

[1] *Universität Innsbruck, Institut für Experimentalphysik, Innsbruck, Austria*
[2] *Institute for Quantum Information, RWTH Aachen University, Aachen, Germany*
[3] *Institute for Theoretical Nanoelectronics (PGI-2), Forschungszentrum Jülich, Jülich, Germany*

(Dated: March 21, 2024)

Quantum error correction is a crucial tool for mitigating hardware errors in quantum computers by encoding logical information into multiple physical qubits. However, no single error-correcting code allows for an intrinsically fault-tolerant implementation of all the gates needed for universal quantum computing [1–3]. One way to tackle this problem is to switch between two suitable error-correcting codes, while preserving the encoded logical information, which in combination give access to a fault-tolerant universal gate set [4–6]. In this work, we present the first experimental implementation of fault-tolerant code switching between two codes. One is the seven-qubit color code [7], which features fault-tolerant CNOT and H quantum gates, while the other one, the 10-qubit code [8], allows for a fault-tolerant T-gate implementation. Together they form a complementary universal gate set. Building on essential code switching building blocks, we construct logical circuits and prepare 12 different logical states which are not accessible natively in a fault-tolerant way within a single code. Finally, we use code switching to entangle two logical qubits employing the full universal gate set in a single logical quantum circuit. Our results experimentally open up a new route towards deterministic control over logical qubits with low auxiliary qubit overhead, not relying on the probabilistic preparation of resource states.

I. INTRODUCTION

Quantum computers offer the prospect of performing certain computational tasks more efficiently than any known classical algorithm [9, 10]. However, the accuracy of quantum computations is limited by noise, arising from the interaction of qubits with their environment [11]. Quantum error correction (QEC) addresses this challenge by encoding quantum information across multiple physical qubits, thereby adding redundancy and allowing errors to be localized and corrected without destroying the encoded information [12, 13]. QEC is performed by physical operations which are themselves faulty. Operations on these error-corrected logical qubits therefore have to be performed without proliferating local errors uncontrollably across the encoded qubit. This can be achieved by means of fault-tolerant (FT) circuit designs [2, 14–16] for example by using very resource-efficient transversal gates. Transversal gate operations perform logical operations by qubitwise application of the physical operations. Generally, it is not possible to implement an arbitrary logical operation transversally in a given QEC code. Computations on qubits can be approximated to arbitrary precision using only a finite set of gates forming a so-called universal gate set [3, 13], as for example the gate set consisting of the Hadamard-gate (H), T-gate, and two-qubit entangling CNOT-gate would allow for universal quantum computing. However, at least one of these gates cannot be transversal for encoded qubits [1]. Consequently, at least one logical gate must be implemented through alternative methods to achieve universal FT computation, which often implies a substantial resource overhead [1].

Two well-known methods to complete a universal gate set are magic state injection and code switching. With magic state injection, it is possible to implement a non-Clifford gate by preparing a magic resource state fault-tolerantly on a logical auxiliary qubit [17, 18] and injecting this auxiliary state onto the encoded data qubit [19]. Magic states have been prepared on superconducting architectures [20], as well as on ion trap quantum processors [21], and a full universal gate set has recently been realized on an ion-trap quantum processor [22]. However, producing high-fidelity magic states poses a significant challenge and presents a large overhead [23]. As an alternative method, switching between two codes with complementary sets of transversal gates also enables the implementation of a full universal gate set [4–6], as illustrated in Fig. 1. Here, the key idea is to transfer encoded information from one encoding to another by measuring a set of operators and applying local Pauli operations. These are chosen in a way that fixes the state into the desired codespace but also preserves the encoded information. An experimental demonstration of this route to fault-tolerance has so far not been achieved.

In previous theoretical work we developed FT code switching protocols utilizing the concept of flag qubits, as introduced by [17, 24, 25], and found schemes that reach a level of performance competitive with magic state injection [26]. In this work we present the first experimental implementation of such FT code switching protocols. We characterize the performance of essential building blocks for switching between the seven-qubit color code, encod-

* These authors contributed equally
† Also at Alpine Quantum Technologies GmbH, Innsbruck, Austria; Email to thomas.monz@uibk.ac.at

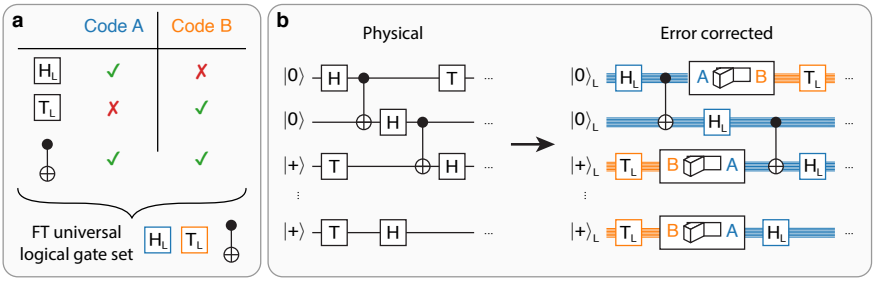

FIG. 1: **Quantum algorithms with universal gate set.** (a) Two codes with complementary sets of FT gates in combination amount to a complete FT universal logical gate set $\{H_L, T_L, \mathrm{CNOT}_L\}$. (b) An algorithm running on physical qubits (left) can be run fault-tolerantly on logical qubits (right) by switching between two codes. If, for example, the FT T_L gate is only available in code B (orange), one has to switch to this code before applying the respective gate operation.

ing a single logical qubit and capable of correcting a single error, and an error-detecting 10-qubit code [8] on an ion-trap quantum processor. We prepare 12 different states on the seven-qubit color code, which can not be obtained transversally using a single error-correcting code. We furthermore extend these protocols to entangling logical operations and implement minimal logical algorithms using all gates of a universal gate set $\{H, T, \mathrm{CNOT}\}$.

II. FT CODE SWITCHING PROCEDURE

The seven-qubit color code encodes $k = 1$ logical qubit in $n = 7$ physical qubits and has a code distance $d = 3$, allowing the correction of any single error [7, 27]. A valid logical state is the simultaneous $+1$-eigenstate of the stabilizer generators $A_\sigma^{(i)}$, which are shown in Fig. 2 on the left and given explicitly in App. A. The logical Pauli operators of this code correspond to applying Pauli X- and Z- operations to all seven qubits $X_L = X^{\otimes 7}$ and $Z_L = Z^{\otimes 7}$. A logical Hadamard gate H_L can be implemented transversally by bitwise application of single-qubit Hadamard-gates and, similarly, the phase gate S_L can be realized in a transversal manner by applying single-qubit $S^\dagger$-gates to all qubits. As introduced in [8], the $[[10, 1, 2]]$ code encodes a single logical qubit in 10 physical qubits and, with distance $d = 2$, can *detect* any single error. The logical qubit of the $[[10, 1, 2]]$ code is defined by the stabilizer generators $B_\sigma^{(i)}$, shown in Fig. 2 on the right and given in App. A, and the logical Pauli-operators coincide with those of the seven-qubit color code. X- and Z-stabilizer generators are not defined on the same support, meaning that the $[[10, 1, 2]]$ code is not self-dual, and consequently does not have a transversal Hadamard-gate. It is generated from the larger 15-qubit tetrahedral code, inheriting its FT non-Clifford T-gate, which can be implemented with [8]

$$T_L = T_1 T_2^\dagger T_3 T_4^\dagger T_5 T_6^\dagger T_7 \, \mathrm{CCZ}_{8,9,10}, \qquad (1)$$

which includes the controlled-controlled-Z-gate on qubits 8, 9, and 10. This implementation of the logical T_L-gate is not transversal anymore but FT in the sense that all possible errors resulting from a single fault are still detectable. The $[[10, 1, 2]]$ code is the smallest known code that has a FT T-gate [8].

We implement a FT universal gate set by switching between the seven-qubit color code $[[7, 1, 3]]$ and the $[[10, 1, 2]]$ code [7, 8, 27]. We can transfer encoded information between these two codes by first measuring those stabilizers of the target code which differ from the stabilizers of the initial code. This measurement randomly projects the logical state onto a ± 1-eigenstate of the measured stabilizers. In a second step, we force the state into the $+1$-eigenstate of the measured stabilizers without changing the logical state [4, 6, 28] by applying a combination of Pauli-generators. Here, these generators directly correspond to stabilizer operators of the initial code and, therefore, do not affect the logical state.

Specifically, we measure the three Z-stabilizers $(B_Z^{(4)}, B_Z^{(5)}, B_Z^{(6)})$, shown in Fig. 2 to switch from $[[7, 1, 3]]$ to $[[10, 1, 2]]$. Then, we apply a combination of the weight-4 X-generators of the $[[7, 1, 3]]$ code $(A_X^{(1)}, A_X^{(2)}, A_X^{(3)})$. For example, if the random projection onto the Z-stabilizers yields $(0, 0, 1)$, where 0 corresponds to a $+1$-eigenvalue and 1 to a -1-eigenvalue of the measured operator, we would apply $A_X^{(3)} = X_3 X_4 X_6 X_7$. $A_X^{(3)}$ overlaps at an even number of sites with the first and second Z-stabilizer and only at a single site with $B_X^{(6)}$ and, therefore, this operation fixes the state into the $+1$-eigenstate of all Z-stabilizers $(B_Z^{(4)}, B_Z^{(5)}, B_Z^{(6)})$ of the ten-qubit code. For switching in the inverse direction from $[[10, 1, 2]]$ to $[[7, 1, 3]]$, we employ the same scheme but interchange the sets of stabilizers: we measure $(A_X^{(1)}, A_X^{(2)}, A_X^{(3)})$ and apply a combination of $(B_Z^{(4)}, B_Z^{(5)}, B_Z^{(6)})$. The lookup table with possible measurement outcomes and switching operations for both directions is summarized in App. Tab. I.

To achieve fault tolerance, we repeat measurements

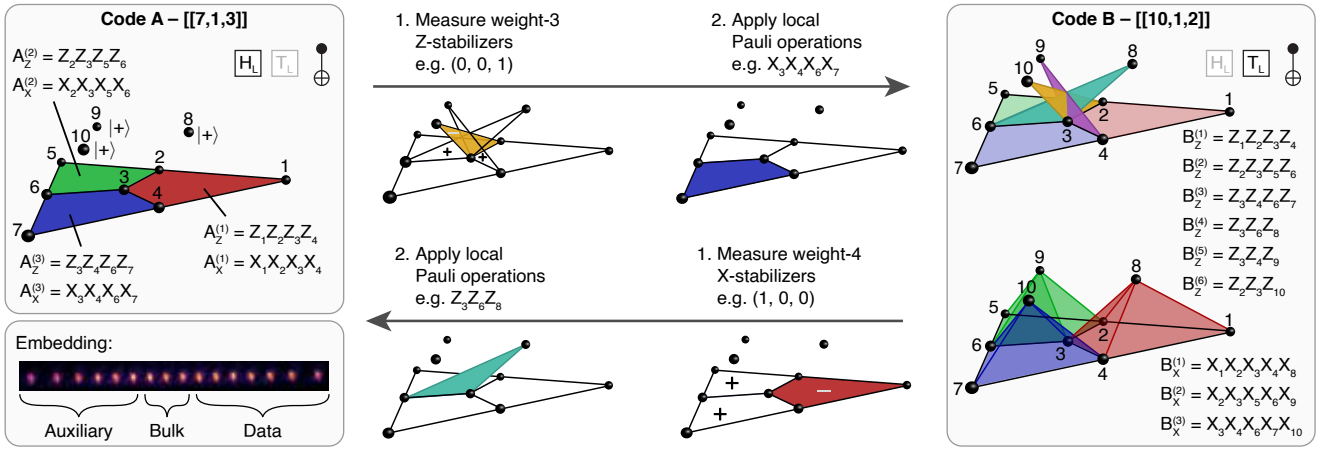

FIG. 2: **Switching between** $[[7,1,3]]$ **and** $[[10,1,2]]$**.** A valid codestate of the $[[7,1,3]]$ code (left) is a $+1$-eigenstate of the X- and Z-stabilizers $A_X^{(i)}$ and $A_Z^{(i)}$ which are defined symmetrically on the weight-4 plaquettes (red, green, blue). In contrast to that, the X- and Z-stabilizers of the $[[10,1,2]]$ code (right) differ: Z-stabilizers are defined on the three weight-4 plaquettes in the triangular plane (red, green blue), as well as on the three weight-3 plaquettes connecting the triangular plane with the bulk qubits 8, 9, and 10 (orange, turquoise, purple). The X-stabilizers of the $[[10,1,2]]$ code have support on the weight-5 pyramids (red, green, blue). To switch from the $[[7,1,3]]$ code to the $[[10,1,2]]$ code, we measure the three weight-3 Z-stabilizers which connect the encoded $[[7,1,3]]$ on qubits 1–7 with the bulk qubits 8, 9 and 10. Based on the obtained switching syndrome, a combination of the weight-4 plaquettes $(A_X^{(1)}, A_X^{(2)}, A_X^{(3)})$ is applied, which fixes the logical state into the desired codespace while preserving the encoded information. The inverse switching direction is implemented analogously: first, the three weight-4 X-stabilizers are measured, followed by the application of a combination of $(B_Z^{(4)}, B_Z^{(5)}, B_Z^{(6)})$.

to correct for single measurement faults. We use flag-qubits for stabilizer measurements in order to prevent faults on auxiliary qubits from propagating uncontrollably [17, 24–26, 29], and we perform additional stabilizer measurements to detect potentially dangerous errors on data qubits. Whenever a potentially dangerous error is detected, the corresponding run is discarded. The full FT protocols for switching in both directions are discussed and summarized in App. A.

III. EXPERIMENTAL SETUP

The experiment was performed with a 16-ion chain of $^{40}Ca^+$ ions trapped in a linear Paul trap. We utilize an optical qubit encoded in $|0\rangle = |4^2S_{1/2}, m_J = -1/2\rangle$ and $|1\rangle = |3^2D_{5/2}, m_J = -1/2\rangle$ Zeeman sub-levels. An optical addressing system for 729 nm laser light driving the qubit transition allows for individual qubit control. In addition, ion-ion interaction through common motional modes of the trap provides all-to-all connectivity for two-qubit gates based on the Mølmer-Sørensen (MS) interaction [30]. A more detailed description of the experimental setup is given in [22, 31, 32].

The setup features detection of the ion chain using the electron shelving technique such that only a desired subset of qubits is detected while the state of the other qubits is preserved. Subsequent recooling of the ion chain and reinitialization of the detected qubits allow for applying high-fidelity gates after the detection procedure. This procedure is used here for mid-circuit measurements of the auxiliary qubits for flag-based stabilizer readout. A comprehensive overview of the procedure can be found in [33]. The error rates for the basic experimental qubit manipulation operations are given in App. Tab. II.

IV. RESULTS

We characterize each building block essential for implementing the universal gate set based on code switching: the initialization of $[[10,1,2]]$ logical states, the logical T-gate, and switching back and forth between the $[[10,1,2]]$ and the $[[7,1,3]]$ codes. We perform logical quantum process tomography, as specified in App. C, for all building blocks and compare the results to the respective ideal process. All experimental results are accompanied by numerical simulations using a multi-parameter noise model described in App. B which is using experimental error rates given in App. Tab. II. The resulting logical process fidelities are shown in Fig. 3. All obtained fidelities and acceptance rates are given in App. Tab. IV.

We find that the fidelities for the initialization in the nFT case are similar to those in the FT case, since the FT overhead for an additional verification is small and errors do not propagate in a dangerous way for the nFT proto-

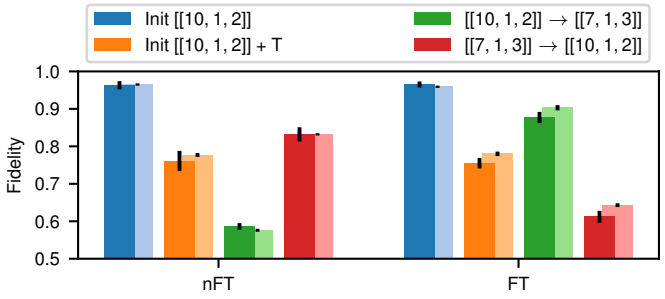

FIG. 3: **Fidelities for code switching building blocks.** Logical process fidelities for nFT (left) and FT (right) protocols for the initialization of $[[10, 1, 2]]$ logical states (blue), a logical T-gate (orange), switching from $[[10, 1, 2]]$ to $[[7, 1, 3]]$ (green) and in the inverse direction (red). The values obtained in the experiment/simulation are depicted in darker/lighter colors, respectively. The error bars show standard deviations, determined as discussed in App. E, and explicit values are summarized in App. Tab. IV.

col. Only if further operations are performed on the logical state afterward, previously correctable errors can become uncorrectable even for transversal operations due to different code distances for X- and Z-errors. For the T-gate on the $[[10, 1, 2]]$ code we observe a similar feature as the fidelity does not change significantly when employing the FT scheme. The FT T-gate on the $[[10, 1, 2]]$ code includes one additional minimal error detection (ED) block before applying the logical T-gate, which is reflected in a decreasing acceptance rate: 81% are accepted for the nFT protocol while 51% are accepted for the FT version, as summarized in App. Tab. IV. We can identify a clear advantage of the FT scheme over the nFT scheme for switching from $[[10, 1, 2]]$ to $[[7, 1, 3]]$, as we can achieve fault tolerance with only a small increase of the two-qubit gate count as discussed in Sec. II. However, the FT switching protocol does not provide an advantage over the nFT one for $[[7, 1, 3]] \rightarrow [[10, 1, 2]]$. This is not unexpected due to the complexity of the protocol with a large circuit depth and the current error rates, which are discussed in detail in App. D.

As a next step, we combine the aforementioned building blocks to prepare a variety of different states fault-tolerantly, which are inaccessible with natively FT gate implementations in the seven-qubit color code. The protocol is shown in Fig. 4**a**: initially, $|+\rangle_L$ of the $[[10, 1, 2]]$ is prepared followed by the application of FT gates of the $[[10, 1, 2]]$ code which includes any combinations of gates from the set $\{Z, S, T\}$. This enables the preparation of the four cardinal states as well as four additional states, which require a T-gate, on the equator of the Bloch sphere, as shown in Fig. 4**b**. After switching to the seven-qubit color code, we can lastly apply an H-gate. This allows us to prepare logical states on the 45th parallels of the Bloch sphere, which are not reachable with a single code with a natively FT implementation. We implement this protocol experimentally and numerically and perform logical quantum state tomography for each obtained state. The reconstructed Bloch vectors for all prepared logical states are shown in Fig. 4**b**. Circuits including the non-Clifford T-gate have decreased fidelity relative to purely Clifford circuits. This can be attributed to the additional two-qubit gates required for the ED block before the application of the T-gate, and the mid-circuit measurement which does not have to be performed for the Clifford circuits. We identify dephasing on idling qubits as a major contribution to the total logical state infidelity and take further measures to improve the fidelities of the states, prepared with the protocol in Fig. 4, which is discussed further in App. G. We can effectively increase the fidelities by up to 0.08 for Clifford states and up to 0.04 for non-Clifford states by simply reassigning the X- and Z- stabilizers, which is shown in App. Fig. 10.

We extend the demonstrated set of logical gates by entangling two-qubit operations with the goal of exploring small logical circuits with gates from the universal gate set. We again start in the logical $|+\rangle_L$ of the $[[10, 1, 2]]$ code and may apply a FT T-gate before switching to $[[7, 1, 3]]$ as shown in Fig. 5**a**. On the target code, we can apply an additional H-gate. Afterward, a second logical qubit is prepared on the $[[7, 1, 3]]$ code in $|0\rangle_L$ and the two logical qubits are entangled with a logical CNOT. Utilizing the full universal gate set, we prepare three entangled states with this protocol and analyze these states by means of logical quantum state tomography, as shown in Fig. 5**b, c** and explicitly given in App. E. Again, experimental results and the numerically obtained fidelities agree within one standard deviation. All three logical states are entangled with $> 99\%$ confidence despite a large circuit depth and circuit complexity, involving up to 61 two-qubit gates and two mid-circuit measurements.

V. DISCUSSION

In our experimental demonstration of FT code switching we operate all gates directly at the logical level - code switching between error-correcting codes does not rely on probabilistic preparation of resource states. This fact is important in light of the observation that a deterministic code execution empowered by code switching rather than a probabilistic protocol via state injection can become advantageous over probabilistic execution via state preparation and injection, as overall device capabilities improve. [32].

We find experimentally that fault-tolerant code switching schemes can significantly improve fidelities in certain situations compared to their non-fault-tolerant counterparts. However, this advantage does currently not yet extend to protocols with large circuit depth or many mid-circuit measurements. These primary bottlenecks in our implementation fidelity can be mitigated with

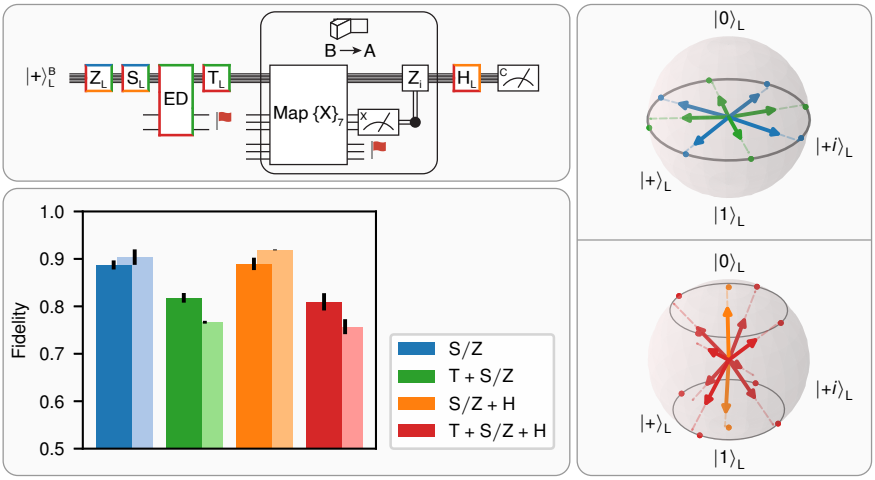

FIG. 4: **Spanning logical states on the Bloch sphere.** (a) Circuit used in the experiment to produce different logical states on the Bloch sphere. The colored lines around gates indicate if the gate was executed to prepare the state of the respective color, e.g. the T-gate was only performed when producing 'green' or 'red' states. First, a logical $|+\rangle_L$ is initialized for the $[[10, 1, 2]]$ code, followed by operations from the gate set $\{Z, S, T\}$. The T-gate is made FT by including an additional error-detection block before applying the T-gate. We then switch to the $[[7, 1, 3]]$ code by measuring three weight-4 X-stabilizers and applying a Z-type switching operation based on the obtained measurement outcomes. Finally, we can perform $\pi/2$ rotations about the X- or Y-axis, which correspond to a transversal logical H-gate. (b) Bloch vectors for all states that are reachable with the different gate combinations of the protocol shown in (a). These include the four cardinal states on the equator of the Bloch sphere (blue), as well as those four states which are rotated by 45° about the Z-axis (green). The north and south poles (orange) are reached by rotating about the Y-axis. By applying a combination of all operations, i.e. the initial (non-)Clifford gates $\{S, Z, T\}$ and the final rotation, we can reach various points on 45^{th} parallels (gray circles) of the Bloch sphere (red). (c) State fidelities for different logical states with the circuit in (a). These are averaged over groups of states with the same number of physical operations. For example, the blue bar corresponds to the fidelity averaged over the blue Bloch vectors in (b). Experimental results are shown in darker and simulated results in lighter colors. The error bars show standard deviations, determined as discussed in App. E, and the values are summarized in App. Tab. V.

technical or logical changes. In our particular implementation we may benefit mostly from independently-demonstrated technical improvements such as extended coherence times [34–36] and more robust composite pulse sequences during mid-circuit measurements [37, 38]. Furthermore, tailoring QEC protocols to systems with biased noise [39–42] promises the possibility of reaching higher fidelities for experimental setups with these noise characteristics. The present case of Z-bias makes selecting a code like the rotated $[[10,1,2]]_X$ which is more resilient to Z-noise beneficial, as demonstrated by the improved performance under this exchange of stabilizers.

In the near future code switching can be beneficial in hardware systems where the cost of mid-circuit measurements is low compared to the cost of having additional auxiliary qubits for the magic state injection. Contemporary superconducting quantum computers with limited connectivity [43–48] and QCCD-based trapped-ion architectures [29, 49–51] might fall into this category.

Here, we have considered the experimental implementation of code switching for the smallest possible instances of the respective classes of codes, namely the $[[10, 1, 2]]$ and the $[[7, 1, 3]]$ code. Future work will include the extension from the error-detecting $[[10, 1, 2]]$ code to the deterministic error-correcting $[[15, 1, 3]]$ code, which has been explored theoretically [4, 26], as well as larger-distance codes, which promise the implementation of a deterministic set of universal gates, without the need for large-scale magic-state factories.

VI. ACKNOWLEDGEMENTS

We gratefully acknowledge support by the European Union's Horizon Europe research and innovation program under Grant Agreement Number 101114305 ("MILLENION-SGA1" EU Project), the US Army Research Office through Grant Number W911NF-21-1-0007, the European Union's Horizon Europe research and innovation program under Grant Agreement Number 101046968 (BRISQ), the ERC Starting Grant QCosmo under Grant Number 948893, the ERC Starting Grant QNets through Grant Number 804247, the Austrian Science Fund (FWF Grant-DOI 10.55776/F71) (SFB BeyondC), the Austrian Research Promotion Agency under Contracts Number 896213 (ITAQC) and 897481 (HPQC)

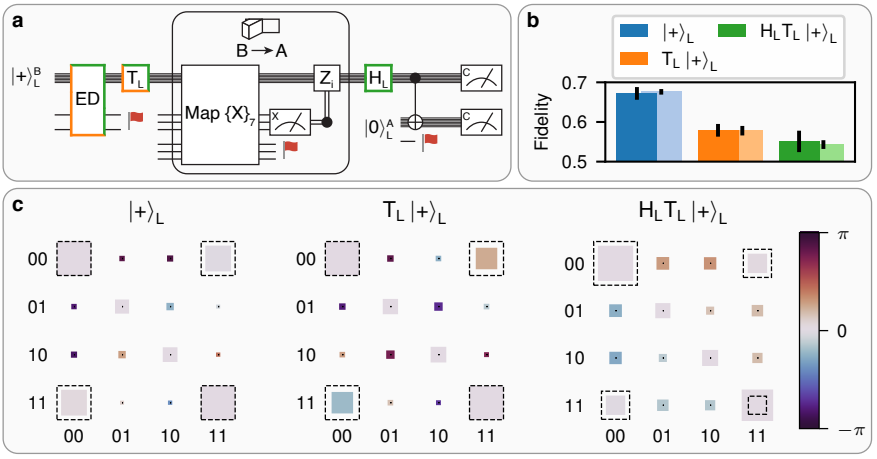

FIG. 5: **Entangled states with non-Clifford gates by means of code switching.** (a) Protocol for the preparation of entangled logical qubits. A logical Bell-state $\frac{1}{\sqrt{2}}(|00\rangle_L+|11\rangle_L)$ is prepared by encoding a qubit on the $[[10,1,2]]$ code and FT switching to $[[7,1,3]]$. A second qubit is then initialized in $|0\rangle_L$ on the seven-qubit color code and coupled to the initial logical qubit by applying a transversal CNOT-gate. $\frac{1}{\sqrt{2}}(|00\rangle_L + e^{i\frac{\pi}{4}}|11\rangle_L)$ and $\cos\frac{\pi}{8}|00\rangle_L + \sin\frac{\pi}{8}|11\rangle_L$ are prepared by including the FT T-gate on the initial 10-qubit code and the $\pi/2$ rotations about the X-axis on the $[[7,1,3]]$ code, which corresponds to a transversal logical H-gate. Colored lines around gates indicate which gates were used to prepare the state of the corresponding color. (b) Fidelities for the entangled logical states which can be prepared with the different gate combinations of protocol (a). Experiment/simulation results are shown in darker/lighter colors. The error bars show standard deviations, determined as discussed in App. E, and the values are summarized in App. Tab. V. (c) Logical state tomography result for the three entangled states. The dashed black boxes indicate the ideal values which correspond to the fault-free case.

supported by the European Union – NextGenerationEU, the Office of the Director of National Intelligence (ODNI), Intelligence Advanced Research Projects Activity (IARPA), under the Entangled Logical Qubits program through Cooperative Agreement Number W911NF-23-2-0216. This research is also part of the Munich Quantum Valley (K-8), which is supported by the Bavarian state government with funds from the Hightech Agenda Bayern Plus. We further receive support from the IQI GmbH, and by the German ministry of science and education (BMBF) via the VDI within the project IQuAn, and by the Deutsche Forschungsgemeinschaft (DFG, German Research Foundation) under Germany's Excellence Strategy 'Cluster of Excellence Matter and Light for Quantum Computing (ML4Q) EXC 2004/1' 390534769.

The views and conclusions contained in this document are those of the authors and should not be interpreted as representing the official policies, either expressed or implied, of IARPA, the Army Research Office, or the U.S. Government. The U.S. Government is authorized to reproduce and distribute reprints for Government purposes notwithstanding any copyright notation herein.

We acknowledge computing time provided at the NHR Center NHR4CES at RWTH Aachen University (Project No. p0020074). This is funded by the Federal Ministry of Education and Research and the state governments participating on the basis of the resolutions of the GWK for national high-performance computing at universities.

Data availability

The data provided in the figures in this article and the circuits used in the experiment are available at https://doi.org/10.5281/zenodo.10812902. Full measurement data can be provided by the corresponding author upon reasonable request.

Authors contribution:

I.P. carried out the experiments. I.P., L.P., C.D.M. contributed to the experimental setup. I.P., F.B. analyzed the data. F.B. developed the protocols and underlying quantum circuits, performed the numerical simulations, characterization, and theory modeling. I.P., F.B., and C.D.M. wrote the manuscript, with contributions from all authors. P.S., M.M., and T.M. supervised the project.

Competing interests:

T.M. is connected to Alpine Quantum Technologies GmbH, a commercially oriented quantum computing company.

[1] B. Eastin and E. Knill, Restrictions on transversal encoded quantum gate sets, Phys. Rev. Lett. **102**, 110502 (2009).

[2] A. Y. Kitaev, Quantum computations: algorithms and error correction, Russ. Math. Surv. **52**, 1191 (1997).

[3] R. Solovay, Lie groups and quantum circuits, 2000 (1995).

[4] J. T. Anderson, G. Duclos-Cianci, and D. Poulin, Fault-tolerant conversion between the Steane and Reed-Muller quantum codes, Phys. Rev. Lett. **113**, 080501 (2014).

[5] H. Bombín, Dimensional jump in quantum error correction, NJP **18**, 043038 (2016).

[6] A. Kubica and M. E. Beverland, Universal transversal gates with color codes: A simplified approach, Phys. Rev. A **91**, 032330 (2015).

[7] A. Steane, Multiple-particle interference and quantum error correction, Proc. R. Soc. London, Ser. A **452**, 2551 (1996).

[8] M. Vasmer and A. Kubica, Morphing quantum codes, Phys. Rev. X Quantum **3**, 030319 (2022).

[9] P. W. Shor, Algorithms for quantum computation: discrete logarithms and factoring, in *Proceedings 35th annual symposium on foundations of computer science* (Ieee, 1994) p. 124.

[10] L. K. Grover, Quantum computers can search arbitrarily large databases by a single query, Phys. Rev. Lett. **79**, 4709 (1997).

[11] J. Preskill, Quantum computing in the NISQ era and beyond, Quantum **2**, 79 (2018).

[12] D. Gottesman, *Stabilizer Codes and Quantum Error Correction*, Ph.D. thesis, California Institute of Technology (1997).

[13] M. A. Nielsen and I. L. Chuang, *Quantum Computation and Quantum Information: 10th Anniversary Edition* (Cambridge University Press, 2010).

[14] P. Aliferis, D. Gottesman, and J. Preskill, Quantum accuracy threshold for concatenated distance-3 codes, Quantum Inf. Comput. **6**, 97 (2006).

[15] E. Knill, R. Laflamme, and W. H. Zurek, Resilient quantum computation, Science **279**, 342 (1998).

[16] D. Aharonov and M. Ben-Or, Fault-tolerant quantum computation with constant error rate, SIAM Journal on Computing **38**, 1207 (2008).

[17] H. Goto, Minimizing resource overheads for fault-tolerant preparation of encoded states of the Steane code, Sci. Rep. **6**, 1 (2016).

[18] C. Chamberland and A. W. Cross, Fault-tolerant magic state preparation with flag qubits, Quantum **3**, 143 (2019).

[19] S. Bravyi and A. Kitaev, Universal quantum computation with ideal Clifford gates and noisy ancillas, Phys. Rev. A **71**, 022316 (2005).

[20] R. S. Gupta, N. Sundaresan, T. Alexander, C. J. Wood, S. T. Merkel, M. B. Healy, M. Hillenbrand, T. Jochym-O'Connor, J. R. Wootton, T. J. Yoder, *et al.*, Encoding a magic state with beyond break-even fidelity, Nature **625**, 259 (2024).

[21] L. Egan, D. M. Debroy, C. Noel, A. Risinger, D. Zhu, D. Biswas, M. Newman, M. Li, K. R. Brown, M. Cetina, *et al.*, Fault-tolerant control of an error-corrected qubit, Nature **598**, 281 (2021).

[22] L. Postler, S. Heußen, I. Pogorelov, M. Rispler, T. Feldker, M. Meth, C. D. Marciniak, R. Stricker, M. Ringbauer, R. Blatt, P. Schindler, M. Müller, and T. Monz, Demonstration of fault-tolerant universal quantum gate operations, Nature **605**, 675 (2022).

[23] C. Gidney and A. G. Fowler, Efficient magic state factories with a catalyzed $|CCZ\rangle$ to 2 $|T\rangle$ transformation, Quantum **3**, 135 (2019).

[24] R. Chao and B. W. Reichardt, Quantum error correction with only two extra qubits, Phys. Rev. Lett. **121**, 050502 (2018).

[25] C. Chamberland and M. E. Beverland, Flag fault-tolerant error correction with arbitrary distance codes, Quantum **2**, 53 (2018).

[26] F. Butt, S. Heußen, M. Rispler, and M. Müller, Fault-tolerant code switching protocols for near-term quantum processors, arXiv preprint arXiv:2306.17686 (2023).

[27] H. Bombin and M. A. Martin-Delgado, Topological quantum distillation, Phys. Rev. Lett. **97**, 180501 (2006).

[28] D. Poulin, Stabilizer formalism for operator quantum error correction, Phys. Rev. Lett. **95**, 230504 (2005).

[29] J. Hilder, D. Pijn, O. Onishchenko, A. Stahl, M. Orth, B. Lekitsch, A. Rodriguez-Blanco, M. Müller, F. Schmidt-Kaler, and U. Poschinger, Fault-tolerant parity readout on a shuttling-based trapped-ion quantum computer, Phys. Rev. X **12**, 011032 (2022).

[30] A. Sørensen and K. Mølmer, Entanglement and quantum computation with ions in thermal motion, Phys. Rev. A **62**, 022311 (2000).

[31] I. Pogorelov, T. Feldker, C. D. Marciniak, L. Postler, G. Jacob, O. Krieglsteiner, V. Podlesnic, M. Meth, V. Negnevitsky, M. Stadler, B. Höfer, C. Wächter, K. Lakhmanskiy, R. Blatt, P. Schindler, and T. Monz, Compact ion-trap quantum computing demonstrator, Phys. Rev. X Quantum **2**, 020343 (2021).

[32] S. Heußen, L. Postler, M. Rispler, I. Pogorelov, C. D. Marciniak, T. Monz, P. Schindler, and M. Müller, Strategies for a practical advantage of fault-tolerant circuit design in noisy trapped-ion quantum computers, Phys. Rev. A **107**, 042422 (2023).

[33] L. Postler, F. Butt, I. Pogorelov, C. D. Marciniak, S. Heußen, R. Blatt, P. Schindler, M. Rispler, M. Müller, and T. Monz, Demonstration of fault-tolerant Steane quantum error correction, arXiv preprint arXiv:2312.09745 (2023).

[34] T. P. Harty, D. T. C. Allcock, C. J. Ballance, L. Guidoni, H. A. Janacek, N. M. Linke, D. N. Stacey, and D. M. Lucas, High-fidelity preparation, gates, memory, and readout of a trapped-ion quantum bit, Phys. Rev. Lett. **113**, 220501 (2014).

[35] T. Ruster, C. T. Schmiegelow, H. Kaufmann, C. Warschburger, F. Schmidt-Kaler, and U. G. Poschinger, A long-lived Zeeman trapped-ion qubit, Appl. Phys. B **122**, 254 (2016).

[36] P. Wang, C.-Y. Luan, M. Qiao, M. Um, J. Zhang, Y. Wang, X. Yuan, M. Gu, J. Zhang, and K. Kim, Single ion qubit with estimated coherence time exceeding one hour, Nat. Commun. **12**, 233 (2021).

[37] S. Wimperis, Composite pulses with rectangular excitation and inversion profiles, J. Magn. Reson. **83**, 509 (1989).

[38] S. Wimperis, Broadband, narrowband, and passband composite pulses for use in advanced NMR experiments, J. Magn. Reson. **109**, 221 (1994).
[39] J. P. Bonilla Ataides, D. K. Tuckett, S. D. Bartlett, S. T. Flammia, and B. J. Brown, The XZZX surface code, Nat. Commun. **12**, 2172 (2021).
[40] Q. Xu, N. Mannucci, A. Seif, A. Kubica, S. T. Flammia, and L. Jiang, Tailored XZZX codes for biased noise, Phys. Rev. Res. **5**, 013035 (2023).
[41] E. Huang, A. Pesah, C. T. Chubb, M. Vasmer, and A. Dua, Tailoring three-dimensional topological codes for biased noise, Phys. Rev. X Quantum **4**, 030338 (2023).
[42] A. K. Pal, P. Schindler, A. Erhard, Á. Rivas, M.-A. Martin-Delgado, R. Blatt, T. Monz, and M. Müller, Relaxation times do not capture logical qubit dynamics, Quantum **6**, 632 (2022).
[43] S. Krinner, N. Lacroix, A. Remm, A. Di Paolo, E. Genois, C. Leroux, C. Hellings, S. Lazar, F. Swiadek, J. Herrmann, *et al.*, Realizing repeated quantum error correction in a distance-three surface code, Nature **605**, 669 (2022).
[44] J. Kelly, R. Barends, A. G. Fowler, A. Megrant, E. Jeffrey, T. C. White, D. Sank, J. Y. Mutus, B. Campbell, Y. Chen, *et al.*, State preservation by repetitive error detection in a superconducting quantum circuit, Nature **519**, 66 (2015).
[45] Y. Zhao, Y. Ye, H.-L. Huang, Y. Zhang, D. Wu, H. Guan, Q. Zhu, Z. Wei, T. He, S. Cao, *et al.*, Realization of an error-correcting surface code with superconducting qubits, Phys. Rev. Lett. **129**, 030501 (2022).
[46] G. Q. AI, Exponential suppression of bit or phase errors with cyclic error correction, Nature **595**, 383 (2021).
[47] K. Satzinger, Y.-J. Liu, A. Smith, C. Knapp, M. Newman, C. Jones, Z. Chen, C. Quintana, X. Mi, A. Dunsworth, *et al.*, Realizing topologically ordered states on a quantum processor, Science **374**, 1237 (2021).
[48] M. Takita, A. W. Cross, A. D. Córcoles, J. M. Chow, and J. M. Gambetta, Experimental demonstration of fault-tolerant state preparation with superconducting qubits, Phys. Rev. Lett. **119**, 180501 (2017).
[49] J. M. Pino, J. M. Dreiling, C. Figgatt, J. P. Gaebler, S. A. Moses, M. Allman, C. Baldwin, M. Foss-Feig, D. Hayes, K. Mayer, *et al.*, Demonstration of the trapped-ion quantum CCD computer architecture, Nature **592**, 209 (2021).
[50] C. Ryan-Anderson, J. Bohnet, K. Lee, D. Gresh, A. Hankin, J. Gaebler, D. Francois, A. Chernoguzov, D. Lucchetti, N. Brown, *et al.*, Realization of real-time fault-tolerant quantum error correction, Phys. Rev. X **11**, 041058 (2021).
[51] Y. Wan, R. Jördens, S. D. Erickson, J. J. Wu, R. Bowler, T. R. Tan, P.-Y. Hou, D. J. Wineland, A. C. Wilson, and D. Leibfried, Ion transport and reordering in a 2D trap array, Adv. Quantum Technol. **3**, 2000028 (2020).
[52] D. Kribs, R. Laflamme, and D. Poulin, Unified and generalized approach to quantum error correction, Phys. Rev. Lett. **94**, 180501 (2005).
[53] J. Preskill, Fault-tolerant quantum computers (1998).
[54] Qiskit, Quantum information, `https://docs.quantum.ibm.com/api/qiskit/quantum_info`.
[55] N. Kanazawa, D. J. Egger, Y. Ben-Haim, H. Zhang, W. E. Shanks, G. Aleksandrowicz, and C. J. Wood, Qiskit Experiments: A Python package to characterize and calibrate quantum computers, Journal of Open Source Software **8**, 5329 (2023).
[56] S. Huang, K. R. Brown, and M. Cetina, Comparing Shor and Steane error correction using the Bacon-Shor code, arXiv preprint arXiv:2312.10851 (2023).
[57] D. Bluvstein, S. J. Evered, A. A. Geim, S. H. Li, H. Zhou, T. Manovitz, S. Ebadi, M. Cain, M. Kalinowski, D. Hangleiter, *et al.*, Logical quantum processor based on reconfigurable atom arrays, Nature **626**, 58 (2024).

Appendix A: FT code switching between $[[7,1,3]]$ and $[[10,1,2]]$

Stabilizer definitions

The stabilizer generators of the seven-qubit color code $[[7,1,3]]$ are given by

$$\begin{aligned} A_X^{(1)} &= X_1X_2X_3X_4, \quad A_Z^{(1)} = Z_1Z_2Z_3Z_4 \\ A_X^{(2)} &= X_2X_3X_5X_6, \quad A_Z^{(2)} = Z_2Z_3Z_5Z_6 \\ A_X^{(3)} &= X_3X_4X_6X_7, \quad A_Z^{(3)} = Z_3Z_4Z_6Z_7. \end{aligned} \tag{A1}$$

The logical qubit of the $[[10,1,2]]$ code is defined by the stabilizer generators

$$\begin{aligned} B_X^{(1)} &= X_1X_2X_3X_4X_8 \\ B_X^{(2)} &= X_2X_3X_5X_6X_9 \\ B_X^{(3)} &= X_3X_4X_6X_7X_{10} \end{aligned} \tag{A2}$$

and

$$\begin{aligned} B_Z^{(1)} &= Z_1Z_2Z_3Z_4, \quad B_Z^{(4)} = Z_3Z_6Z_8 \\ B_Z^{(2)} &= Z_2Z_3Z_5Z_6, \quad B_Z^{(5)} = Z_3Z_4Z_9 \\ B_Z^{(3)} &= Z_3Z_4Z_6Z_7, \quad B_Z^{(6)} = Z_2Z_3Z_{10}. \end{aligned} \tag{A3}$$

For both codes, the logical Pauli operators can be implemented by applying

$$\begin{aligned} X_L &= X_1X_2X_3X_4X_5X_6X_7, \\ Z_L &= Z_1Z_2Z_3Z_4Z_5Z_6Z_7. \end{aligned} \tag{A4}$$

Switching operations

We measure stabilizer operators and apply local Pauli operations that correspond to so-called gauge operators of the subsystem code [28, 52] to switch between the seven-qubit color code $[[7,1,3]]$ and the $[[10,1,2]]$ code. The lookup tables for switching in both directions are shown in App. Tab. I. Fig. 2 exemplarily illustrates the scheme for switching between $[[10,1,2]]$ and $[[7,1,3]]$.

Measured syndrome $(A_X^{(1)}, A_X^{(2)}, A_X^{(3)})$	Switching operation
$(0,0,0)$	–
$(1,0,0)$	$Z_3Z_6Z_8$
$(0,1,0)$	$Z_3Z_4Z_9$
$(0,0,1)$	$Z_2Z_3Z_{10}$
$(1,1,0)$	$Z_4Z_6Z_8Z_9$
$(1,0,1)$	$Z_2Z_6Z_8Z_{10}$
$(0,1,1)$	$Z_2Z_4Z_9Z_{10}$
$(1,1,1)$	$Z_2Z_3Z_4Z_6Z_8Z_9Z_{10}$

Measured syndrome $(B_Z^{(4)}, B_Z^{(5)}, B_Z^{(6)})$	Switching operation
$(0,0,0)$	–
$(1,0,0)$	$X_1X_2X_3X_4$
$(0,1,0)$	$X_2X_3X_5X_6$
$(0,0,1)$	$X_3X_4X_6X_7$
$(1,1,0)$	$X_1X_4X_5X_6$
$(1,0,1)$	$X_1X_2X_6X_7$
$(0,1,1)$	$X_2X_4X_5X_7$
$(1,1,1)$	$X_1X_3X_5X_7$

TABLE I: **Lookup tables for switching between $[[7,1,3]]$ and $[[10,1,2]]$.** For switching from $[[10,1,2]]$ to $[[7,1,3]]$ (top) we measure the three X-stabilizers $(A_X^{(1)}, A_X^{(2)}, A_X^{(3)})$ and apply a Pauli Z-operation that fixes the state into the codespace of the seven-qubit color code while preserving the encoded information. For the inverse direction (bottom), we measure the three weight-3 Z-stabilizers of the $[[10,1,2]]$ code $(B_Z^{(4)}, B_Z^{(5)}, B_Z^{(6)})$ and apply a suitable Pauli X-operation.

FT switching protocols

The following two algorithms summarize the protocols for FT switching between $[[10,1,2]]$ and $[[7,1,3]]$, which are described in Sec. II. The graphical representation of the protocols is also given in Fig. 11.

Stabilizers can be measured by coupling a physical auxiliary qubit to the data qubits that belong to the operator to be measured [53]. However, this scheme is not FT because single faults on auxiliary qubits can directly result in a logical failure. This is avoided by making use of flag-qubits [17, 18, 24]. In addition, we also need to be able to identify errors on data qubits that invert the projective measurement with random outcomes [26]. For example, consider the case where a Z-error occurs on qubit 1: If we originally would have directly (randomly) projected onto the correct target codespace and measured the trivial switching syndrome (0, 0, 0), we would now measure the same one as illustrated in Fig. 2. This would cause us to apply the same gauge operator $Z_3Z_6Z_8$ as before, which in total amounts to a logical $Z_L = Z_1Z_3Z_6$ on the target Steane code. There are different strategies for detecting these dangerous errors on data qubits for each switching direction. For switching from $[[7,1,3]]$ to $[[10,1,2]]$, we identify the potentially dangerous positions and perform additional stabilizer measurements to check if an error has occurred at one of these. For the inverse direction, we can detect these dangerous errors on data qubits without additional stabilizer measurements. After switching in this direction, we measure qubits 8, 9, and 10 in the X-basis and compare this outcome to their op-

Protocol: FT switching $[[10,1,2]] \to [[7,1,3]]$

Input: Logical state in $[[10,1,2]]$

Output: Logical state in $[[7,1,3]]$

Measure $\sigma = (A_X^{(1)}, A_X^{(2)}, A_X^{(3)})$ with flags

    If a circuit flags: discard

Measure qubits 8, 9 and 10 in the X-basis

Check agreement of opposing X-operators

    $a = [(A_X^{(1)}, A_X^{(2)}, A_X^{(3)}) + (X_8, X_9, X_{10})] \mod 2$

    If $a \neq (0,0,0)$: discard

Apply switching operation according to lookup table using switching syndrome σ

Protocol: FT switching $[[7,1,3]] \to [[10,1,2]]$

Input: Logical state in $[[7,1,3]]$

Output: Logical state in $[[10,1,2]]$

Measure $\sigma_1 = (B_Z^{(4)}, B_Z^{(5)}, B_Z^{(6)})$

Measure $\sigma_2 = (B_Z^{(4)}, B_Z^{(5)}, B_Z^{(6)})$

If 1 and 2 agree:

    Measure $(B_Z^{(2)}, B_Z^{(3)})$

    If $(B_Z^{(2)}, B_Z^{(3)}) \neq (0,0)$: discard

    $\sigma_{\text{final}} = \sigma_2$

If 1 and 2 disagree:

    Measure $\sigma_3 = (B_Z^{(4)}, B_Z^{(5)}, B_Z^{(6)})$ and $(B_Z^{(2)}, B_Z^{(3)})$

    If $(B_Z^{(2)}, B_Z^{(3)}) \neq (0,0)$: discard

    $\sigma_{\text{final}} = \sigma_3$

Apply switching operation according to lookup table using switching syndrome σ_{final}

posing stabilizer plaquette. For example, we compare the outcome of qubit 8 to the outcome of $A_X^{(1)} = X_1X_2X_3X_4$. Since we started in a +1-eigenstate of the weight-5 cell, we know that pairs of these opposing operators have to agree so that, in total, they amount to 0 mod 2.

Appendix B: Noise model and simulation methods

We determine the expected fidelities of the implemented code switching protocols by performing Monte Carlo (MC) simulations. In the numerical simulations, every ideal circuit component is followed by an error E with a specified probability p, that is in particular the probability of an error occurring $p \in [0,1]$. We include a depolarizing channel on all single- and two-qubit gates, which is defined by the error rates p_1 and p_2 with which one of the errors in the error sets E_1 and E_2 is applied.

Operation	Error rate	Duration
Two-qubit gate	$p_2 = 0.027$	322.5 µs
Single-qubit gate	$p_1 = 0.0036$	25 µs
Measurement	$p_{\text{meas}} = 0.003$	
Preparation	$p_{\text{init}} = 0.003$	
Mid-circuit detection	$p^{(x)}_{\text{mid-circ}} = 0.011$ $p^{(y)}_{\text{mid-circ}} = 0.024$ $p^{(z)}_{\text{mid-circ}} = 0.035$	
Coherence time	$T_2 = 50\,\text{ms}$	

TABLE II: **Depolarizing error rates and duration of operations on a trapped-ion quantum processor [33].**

The error channel is defined as

$$\mathcal{E}_1(\rho) = (1-p_1)\rho + \frac{p_1}{3}\sum_{i=1}^{3} E_1^i \rho E_1^i \tag{B1}$$

$$\mathcal{E}_2(\rho) = (1-p_2)\rho + \frac{p_2}{15}\sum_{i=1}^{15} E_2^i\, \rho\, E_2^i.$$

with the error sets $E_1 \in \{X, Y, Z\}$ for $k = 1,2,3$ and $E_2 \in \{IX, XI, XX, IY, YI, YY, IZ, ZI, ZZ, XY, YX, XZ, ZX, YZ, ZY\}$ for $k = 1, ..., 15$. Qubits are initialized and measured in the computational basis and faults on these two operations are simulated by applying X-flips after and before the respective operation with probabilities p_{init} and p_{meas}. Furthermore, idling qubits experience dephasing due to environmental fluctuations. We model this dephasing of idling qubits with the error channel

$$\mathcal{E}_{\text{idle}}(\rho) = (1-p_{\text{idle}})\rho + p_{\text{idle}} Z\rho Z. \tag{B2}$$

Here, a Z-fault is placed on each idling qubit with probability p_{idle}, which depends on the execution time t of the performed gate and the coherence time $T_2 \approx 50\,\text{ms}$

$$p_{\text{idle}} = \frac{1}{2}\left[1 - \exp\left(-\frac{t}{T_2}\right)\right]. \tag{B3}$$

Lastly, we perform mid-circuit detections, where auxiliary qubits are measured while the data qubits are kept intact, as discussed in Sec. III. Based on single qubit process tomography, we estimate the error rates of X- Y- and Z-faults on the idling data qubits [33] and model the mid-circuit detection with an asymmetric depolarizing channel which is specified by individual Pauli $p^{(x)}_{\text{inseq}}, p^{(y)}_{\text{inseq}}, p^{(z)}_{\text{inseq}}$ error rates. All error rates and relevant gate durations are summarized in App. Tab. II.

We determine the state fidelity between two states ρ_1 and ρ_2 as

$$F(\rho_1, \rho_2) = \text{Tr}\left[\sqrt{\sqrt{\rho_1}\rho_2\sqrt{\rho_1}}\right]^2. \tag{B4}$$

	TQ gates	Mid-circ
$\|0\rangle_L^B$	15	0
$\|+\rangle_L^B$	13	0
T_L	12	0
$\|\psi\rangle_L^B \rightarrow \|\psi\rangle_L^A$	18	0
$\|\psi\rangle_L^A \rightarrow \|\psi\rangle_L^B$	26/35	1/2
$\mathrm{T}_L\|+\rangle_L^B \rightarrow \mathrm{T}_L\|+\rangle_L^A$	43	1
Clifford CNOT-protocol	49	1
non-Clifford CNOT-protocol	61	2

TABLE III: **Number of two-qubit gates and mid-circuit measurements for different FT protocols.** Code B corresponds to $[[10,1,2]]$ and code A to $[[7,1,3]]$. The CNOT-protocol includes the FT initialization of $|+\rangle_L^B$, FT switching to the seven-qubit color code, the initialization of a second logical qubit $|0\rangle_L^A$ and a transversal CNOT-gate, and has the highest number of two-qubit gates and mid-circuits measurements.

The process fidelity is calculated similarly with

$$F_{\mathrm{pro}}(\mathcal{E},\mathcal{F}) = F(\rho_{\mathcal{E}},\rho_{\mathcal{F}}), \tag{B5}$$

where F is the state fidelity, and $\rho_{\mathcal{E}}$ the normalized Choi matrix for channel $\mathcal{E}$. We use Qiskit's Quantum Information package to calculate fidelities [54].

Appendix C: Experimental methods

1. Mid-circuit measurement

The mid-circuit measurement in our implementation setup is a significant technical source of errors with the current parameters (see App. Tab. II). Therefore, we aim at constructing our circuits in a way that minimizes the required number of mid-circuit detections. Stabilizers and flags mapped to auxiliary qubits are measured all in one mid-circuit measurement whenever possible, an example of which is shown in Fig. 6. When not all of the auxiliary qubits are used we aim at mapping information to the auxiliary qubits spatially far away from the data qubits to avoid optical cross-talk on data qubits. It is also beneficial to leave idle buffer qubits between auxiliary qubits to avoid cross-talk between auxiliary qubits. However, minimizing the number of mid-circuit measurements takes priority.

We specify the number of mid-circuit measurements for each protocol presented here in App. Tab. III.

2. Flag bunching

FT code switching $[[10,1,2]] \rightarrow [[7,1,3]]$ includes the measurement of three stabilizers with flags, which requires six auxiliary qubits in total. Preparing the logical $|0\rangle_L$ state of the $[[10,1,2]]$ also requires one auxiliary qubit as a flag for fault-tolerance. Therefore, seven auxiliary qubits are required to map all the required stabilizers and flags if $[[10,1,2]] \rightarrow [[7,1,3]]$ code switching is done immediately after the state preparation, which is the case for building block characterization (see Fig. 3, App. Tab. IV). In the current experimental configuration we are limited to no more than six auxiliary qubits in addition to 10 data qubits, hence we map two flags to the same auxiliary qubits to reduce the number of mid-circuit measurements. Bunching together the preparation flag and one of the stabilizer flags still preserves fault tolerance in this particular case: if only one error takes place, no dangerous error propagation can happen in such a way that both flags should be raised at the same time. Such flag bunching only takes place in this protocol.

3. Branching post-selection

FT code switching $[[7,1,3]] \rightarrow [[10,1,2]]$ requires mid-circuit decision making to choose which set of stabilizers should be measured based on the result of the first mid-circuit measurement (see step 3a,b in the description of the protocol in App. A). The current hardware electronics configuration does not allow for fast communication between the camera and the control electronics so mid-circuit decision making within the qubits' lifetime is currently not feasible. Thus, we assume we know the result of the measurement and act accordingly instead of making a decision based on the result of the mid-circuit measurement. We discard this experimental shot if during the analysis it turns out that our assumption about the measurement result was incorrect. This effectively decreases the acceptance rate for $[[7,1,3]] \rightarrow [[10,1,2]]$ by a factor of two compared to the protocol with mid-circuit decision making.

4. Switching operation

Both code switching procedures require the application of a switching operation based on the outcome of the measurement of the stabilizers of the target code (see App. Tab. I). This switching operation cannot be applied mid-circuit since the setup is currently missing a mid-circuit decision-making feature. Therefore, we apply switching operations in classical processing with Pauli frame updates. This is possible if all the gates after the switching operation belong to the Clifford group, which is the case for all of our circuits.

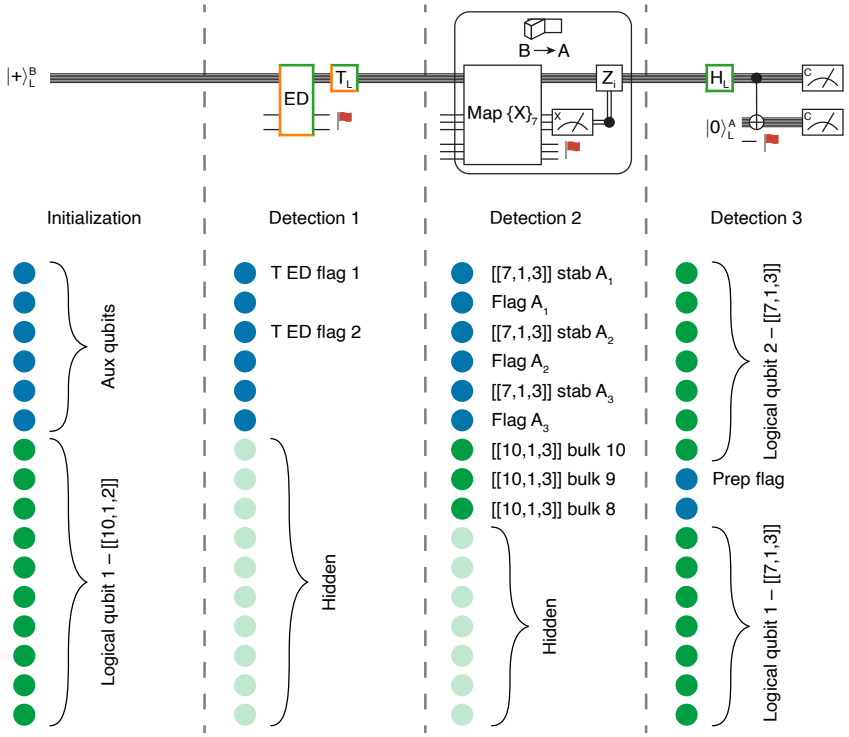

FIG. 6: **Auxiliary qubits mapping for the entangled states generation circuit.** Data qubits encoding logical states are shown in green, while auxiliary qubits used for stabilizers/flags mapping are shown in blue. There are three detections happening during the circuit, two of which are mid-circuit detections. All auxiliary qubits are detected during mid-circuit detections while some data qubits are hidden (shown in light green). The information mapped to auxiliary qubits during each detection is shown next to qubits, no label means that the qubit is not used but still detected. After any mid-circuit detection all detected qubits are reinitialized as $|0\rangle$. All the qubits are detected during the last detection.

5. Number of measurements

The total numbers of measurements performed for different protocols before post-selection are the following. Building blocks: 30000 shots per measurement basis for each input state for [[7,1,3]] → [[10,1,2]] switching protocol and 12500 shots for the other protocols. Bloch sphere states: 5000 shots per measurement basis for each prepared state. CNOT protocol: 15000 shots per measurement basis for each configuration of the protocol.

Appendix D: FT code switching building blocks

App. Tab. IV summarizes the obtained process fidelities for all code switching building blocks that we implemented experimentally and numerically.

We observe that the fidelity for nFT switching from $[[7,1,3]]$ to $[[10,1,2]]$ is higher than for FT switching. This has two main reasons: The first is that for the nFT protocol, we only measure weight-3 Z-stabilizers. This means that there are no dangerous faults on auxiliary qubits that could result in a logical error. Any error propagating from the auxiliary qubits to the data qubits is only equivalent to a weight-1 Z-error and at least detectable on the target code. The nFT protocol therefore only requires nine two-qubits gates and there are few possible single-fault positions on data qubits that can cause a logical failure [26]. Furthermore, we require almost twice as many two-qubit gates for the FT implementation of this direction than for the inverse one and have to perform a mid-circuit measurement, as summarized in App. Tab. III. This overhead in noisy operations in the FT protocol leads to a decrease in fidelity with the current level of noise in gate operations.

For switching from $[[10,1,2]]$ to the $[[7,1,3]]$ code, the FT scheme consists of two features: first, the flag-based stabilizer measurement schemes and, second, the agreement check of opposing pairs of operators, as discussed in Sec. II [26]. The latter does not require any additional qubits or measurements, since it can be done completely in classical post-processing. We estimate the contributions of these two features to the observed increase in fidelity by performing a partially FT experiment (pFT): we only add the agreement check to the nFT scheme and again, determine the fidelity, which is shown in Fig. 7. We

	Experiment			Simulation		
	nFT	FT	AR (%)	nFT	FT	AR (%)
$\|\psi\rangle_L^B$	0.963(11)	0.965(8)	86 / 78	0.965(3)	0.959(3)	85 / 76
$T_L\|\psi\rangle_L^B$	0.761(27)	0.755(14)	81 / 51	0.777(5)	0.780(6)	81 / 49
$\|\psi\rangle_L^B \to \|\psi\rangle_L^A$	0.586(9)	0.877(15)	100 / 23	0.576(4)	0.903(7)	100 / 27
$\|\psi\rangle_L^A \to \|\psi\rangle_L^B$	0.832(19)	0.612(16)	79 / 14	0.832(3)	0.643(5)	80 / 31

TABLE IV: **Process fidelities and acceptance rates of code switching building blocks.** Code A refers to the seven-qubit color code $[[7,1,3]]$ and code B to the 10-qubit code $[[10,1,2]]$. We determine the fidelities for each code switching building block experimentally and numerically for the nFT as well as the FT protocol version using the methods described in Apps. B and C. The numbers in brackets indicate the uncertainty on the obtained value of the fidelity, which are determined as discussed in App. E. The acceptance rates (AR) are given for the nFT and the FT protocols, as for example for the initialization of a logical states on code B, 86% of the runs are accepted in the nFT case.

find that the agreement check contributes significantly more to the infidelity than adding flag qubits for FT stabilizer measurements.

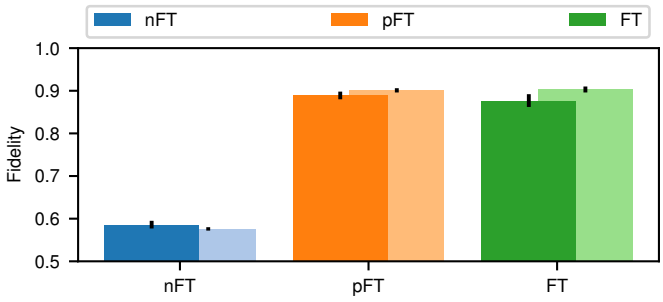

FIG. 7: **Fidelities for partially FT code switching.** Logical process fidelities of switching from the $[[10,1,2]]$ to the $[[7,1,3]]$ code, using a non-FT (blue), a partially FT (orange) and FT (green) scheme. Partially FT switching does not require additional measurements or auxiliary qubits and only includes the agreement check of opposing pairs of operators. For FT switching, we add flag qubits for fully FT stabilizer measurements.

Appendix E: Quantum state and process tomography

The numbers given in Sec. IV were obtained with logical quantum state/process tomography via linear inversion using the Qiskit Experiments package [55]. For each protocol in Figs. 3, 5**b** all data was collected in five experimental runs. Experimental runs were performed on different days and the setup's performance differed slightly. The results' spread caused by the difference in the setup's performance is more substantial than the one coming from the finite number of shots taken for each protocol. Hence, to estimate errors we performed logical quantum state/process tomography for each experimental run separately and then averaged the results. The resulting values are mean and standard deviation over fidelities obtained from each run. For Fig. 4**c** logical quantum state tomography was performed for each state from Fig. 4**b** and the results were averaged over the states belonging to the same group (color). The data from five experimental runs was joined to obtain the average density matrices in Fig. 5**c**, which were reconstructed by means of logical quantum state tomography. The reconstructed matrices are the following:

$$\mathrm{CNOT}_L(|+\rangle_L \otimes |0\rangle_L) = \begin{pmatrix} 0.447 & -0.003-0.002i & -0.005-0.002i & 0.231+0.022i \\ -0.003+0.002i & 0.057 & 0.007+0.007i & 0.001 \\ -0.005+0.002i & 0.007-0.007i & 0.064 & -0.001i \\ 0.231-0.022i & 0.001 & 0.001i & 0.432 \end{pmatrix},$$

$$\mathrm{CNOT}_L(T_L\,|+\rangle_L \otimes |0\rangle_L) = \begin{pmatrix} 0.429 & -0.005-0.003i & 0.003+0.003i & 0.117-0.101i \\ -0.005+0.003i & 0.07 & -0.01+0.01i & 0.004+0.002i \\ 0.003-0.003i & -0.01-0.01i & 0.074 & -0.001-0.002i \\ 0.117+0.101i & 0.004-0.002i & -0.001+0.002i & 0.427 \end{pmatrix},$$

$$\mathrm{CNOT}_L(H_L T_L\,|+\rangle_L \otimes |0\rangle_L) = \begin{pmatrix} 0.477 & 0.029-0.035i & 0.025-0.035i & 0.125-0.009i \\ 0.029+0.035i & 0.07 & 0.012-0.006i & 0.03-0.018i \\ 0.025+0.035i & 0.012+0.006i & 0.081 & 0.023-0.013i \\ 0.125+0.009i & 0.03+0.018i & 0.023+0.013i & 0.373 \end{pmatrix}.$$

Appendix F: Additional post-selection

The logical fidelity of the output state of the circuits can be additionally boosted without any extra measurements or operations by post-selecting for the trivial syndrome [56, 57]. The final measurement of the data qubits in every circuit yields stabilizer values for the corresponding QEC code. If all results with non-trivial stabilizer syndromes are discarded, the logical fidelity increases while the acceptance rate decreases. In doing so, a fraction of runs with error configurations of weight >1 is sorted out. The resulting logical fidelities and acceptance rates with additional post-selection on trivial stabilizer syndromes for some protocols are given in App. Tab. V.

Appendix G: Error budget and rotated $[[10, 1, 2]]$

1. Individual error contributions

We perform numerical simulations of the non-Clifford CNOT protocol with a reduced error model where we set to zero all error sources except for one in order to estimate and compare contributions to the logical infidelity from the different individual error sources present, as shown in Fig 8. Note that the single contributions are not additive, as is expected, since errors propagate and the different noise processes influence each other. Decoherence and mid-circuit measurements have a significant impact on the fidelity, which is comparable to that of two-qubit gate errors. While improving two-qubit gate fidelities in a large ion chain is a complex problem, we anticipate improved coherence and mid-circuit measurement performance pending near-term hardware changes.

2. Impact of two-qubit entangling gate errors

We investigate the impact of the different noise processes further by simulating the scaling of the logical infidelity as a function of the two-qubit error rate p_2. We consider both nFT and FT switching in both directions for three different settings of the noise parameters to determine how an improvement of the two-qubit error rate would affect the total infidelity as shown in Fig. 9. Already for the current noise parameters, FT switching from $[[10, 1, 2]]$ to $[[7, 1, 3]]$ outperforms the nFT protocol, but the infidelity quickly reaches a regime where there is no qualitative change with further improvement of p_2. This is in stark contrast to the behavior found with magic state injection [32]. However, this changes if the dephasing error rate on idling qubits p_{idle} and on the mid-circuit detections $p_{\mathrm{mid-circ}}$ is reduced tenfold. In this case, the infidelity decreases by more than an order of magnitude, even for small values of p_2. When switching from $[[7, 1, 3]]$ to $[[10, 1, 2]]$, nFT switching outperforms the FT protocol for the complete range of considered values of p_2. This is inverted for a tenfold improvement of p_{idle} and $p_{\mathrm{mid-circ}}$. FT switching now achieves smaller infidelities than the nFT scheme, even for the current value of p_2. Note that these reduced values for the error rates are within reach as extended coherence times have been demonstrated [34–36] and composite pulse sequences have been shown to be more robust against crosstalk and laser amplitude noise [37, 38], which can be applied in the mid-circuit measurements.

3. Rotated more dephasing-robust encoding

It has been shown that QEC protocols tailored to experimental systems with biased noise can improve performance on these setups [39–42]. Due to dephasing of

	no PS		PS	
	Fidelity	AR (%)	Fidelity	AR (%)
$\|\psi\rangle_L^A \rightarrow \|\psi\rangle_L^B$	0.597(15)	14	0.75(4)	4
$\mathrm{T}_L\|+\rangle_L^B \rightarrow \mathrm{T}_L\|+\rangle_L^A$	0.887(10)	27	0.963(4)	19
	0.818(10)	15	0.919(11)	10
	0.890(13)	27	0.959(9)	19
	0.810(18)	12	0.918(17)	8
CNOT-protocol	0.672(16)	22	0.934(7)	6
	0.579(16)	10	0.795(15)	3
	0.551(27)	10	0.80(5)	2

TABLE V: **Fidelities without and with additional post-selection.** Code A refers to the seven-qubit color code $[[7,1,3]]$ and code B to the 10-qubit code $[[10,1,2]]$. Additional post-selection (PS) on trivial stabilizer syndrome can be done to boost the logical fidelity at the cost of the acceptance rate. The values for logical state/process fidelities and acceptance rates (AR) with additional post-selection are given for three protocols, as presented in Fig. 5. Different rows within one cell refer to different states prepared.

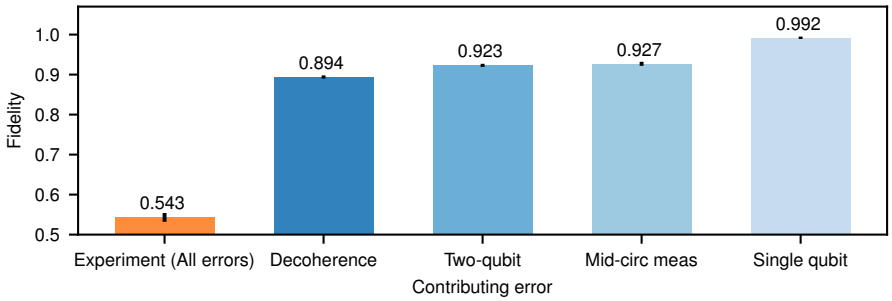

FIG. 8: **Estimated isolated error contributions to the total infidelity.** Fidelities for the non-Clifford CNOT-protocol obtained with numerical simulations. The orange column shows the fidelity for the system with realistic experimental error rates from App. Tab. II. The blue columns show the results for the reduced error model where all the errors were set to zero except for one with the corresponding fidelity indicated on top of the columns. The non-zero error source varies between blue columns and is specified below. *Decoherence* corresponds to the dephasing of idling qubits while gates are carried out on different sets of qubits, *two-qubit* to the physical two-qubit MS-gate error rate, *mid-circ meas* to the idling of data qubits during the measurement of auxiliary qubits and *single-qubit* to all single-qubit noise processes, including faulty initializations, measurements as well as single-qubit gates.

idling qubits and during mid-circuit detections, the noise in our experimental setup is strongly Z-biased. We can reduce the sensitivity to dephasing by simply interchanging the X- and Z-type stabilizers of the initial $[[10,1,2]]$ code, thereby exploiting EC properties which are advantageous given strongly Z-biased noise. The $[[10,1,2]]$ code as described in App. A is capable of correcting up to three X-errors but can only detect at most one Z-error. This is an unfortunate combination for the current experimental setup since decoherence of our qubits is one of the dominant error sources. However, the $[[10,1,2]]$ can be modified by exchanging the support of X- and Z-stabilizers (A2), (A3). We refer to the initial code as $[[10,1,2]]_Z$ and to the modified one as $[[10,1,2]]_X$ or the rotated $[[10,1,2]]$ code. The rotated code has its X/Z error-correcting properties exchanged, i.e. it is capable of correcting up to three Z-errors, but can only detect at most one X-error. By effectively exchanging the support of the X- and Z-stabilizers of the $[[10,1,2]]_Z$ code, the logical T-gate now becomes a rotation about the X-axis instead of the Z-axis and the physically executed operation includes additional H-gates before and after the

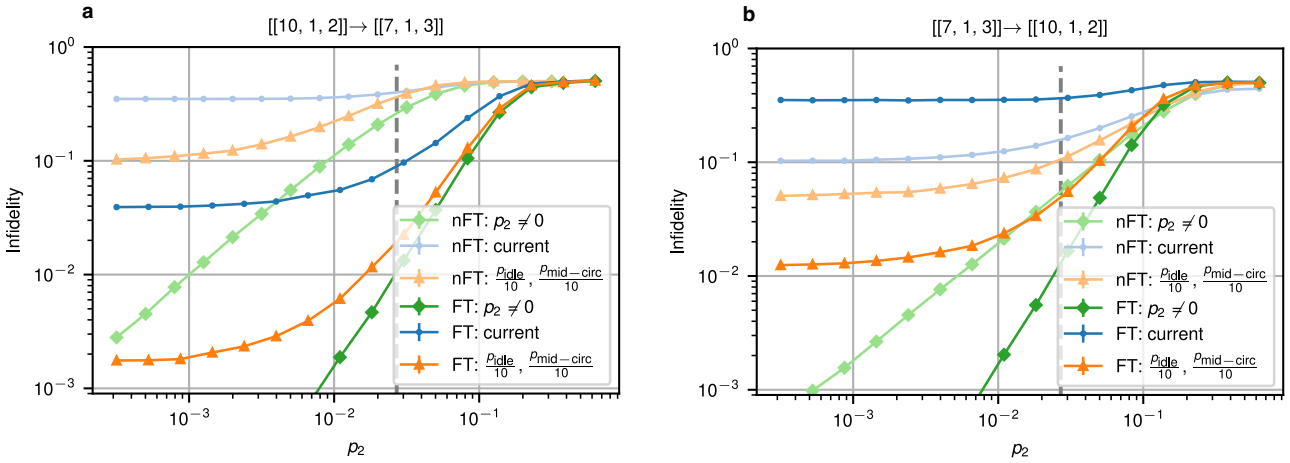

FIG. 9: **Projected performance of FT code switching between** $[[10, 1, 2]]$ **and** $[[7, 1, 3]]$**.** We scale the two-qubit error rate p_2 for three different scenarios: first, for the current set of noise parameters (blue), second, for a modified set of parameters, where only the idling dephasing rate p_{idle} and the mid-circuit detection error rate $p_{\text{mid-circ}}$ is reduced by a factor of 10 (orange) and, third, setting all error rates to 0, except for the two-qubit error rate p_2 (green). We consider the FT and nFT switching protocols for switching (a) from $[[10, 1, 2]]$ to $[[7, 1, 3]]$ and (b) in the inverse direction. The grey dashed line corresponds to the current value of p_2.

previous T-gate

$$T_L^X = H^{\otimes 10} T_L^Z H^{\otimes 10}.$$

We use the $[[10, 1, 2]]_X$ code to span different states on the Bloch sphere, similar to Fig. 4, and compare its performance to the $[[10, 1, 2]]_Z$ code, which is shown in Fig 10. We now initially prepare $|0\rangle_L$ of the $[[10, 1, 2]]_X$ code and apply an X-rotation to create various states in the YZ-plane of the Bloch sphere (blue, green). Then, we switch to the $[[7, 1, 3]]$ code by measuring the three Z-stabilizers of the $[[7, 1, 3]]$ code and apply $\pi/2$ rotations about the Y- or Z-axis since these are not available transversally in the $[[10, 1, 2]]_X$ code. In doing so, we prepare eight additional states requiring non-Clifford gates (red) and two cardinal states (orange). By using this rotated $[[10, 1, 2]]$ code, fidelities improve on average by 0.046 for the states shown in blue and 0.027 for the green states.

This is due to the fact that the qubits spend less time in a decoherence-sensitive state and, during switching from $[[10, 1, 2]]$, Z-faults on data qubits cannot propagate to the auxiliary qubits and corrupt the switching syndrome. Therefore, it can be beneficial to adjust the theoretically constructed codes based on the knowledge of the setup's intrinsic error profile. However, for longer circuits with several mid-circuit measurements, as for the CNOT protocols shown in Fig. 5, the difference is less pronounced.

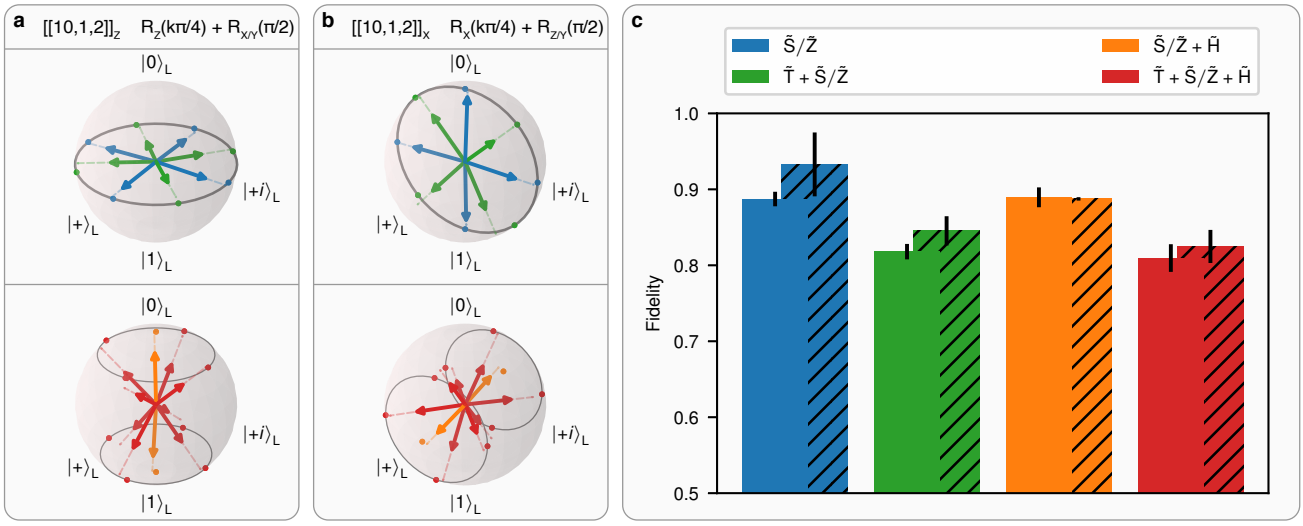

FIG. 10: **Bloch states and fidelities for the rotated** $[[10, 1, 2]]$ **code.** (a) Bloch states that were obtained for the original $[[10, 1, 2]]$ code, as shown in Fig. 4. (b) States within the Bloch sphere that were prepared with the rotated $[[10, 1, 2]]_X$ code using the analogous protocol. (c) Fidelities averaged over groups of states that require the same number of logical operations. The filled bars correspond to the Bloch states for the original code and the hatched bars to those of the rotated version. On average, fidelities are higher for the rotated code, which is less sensitive to the dephasing. The error bars show standard deviations, determined as discussed in App. E.

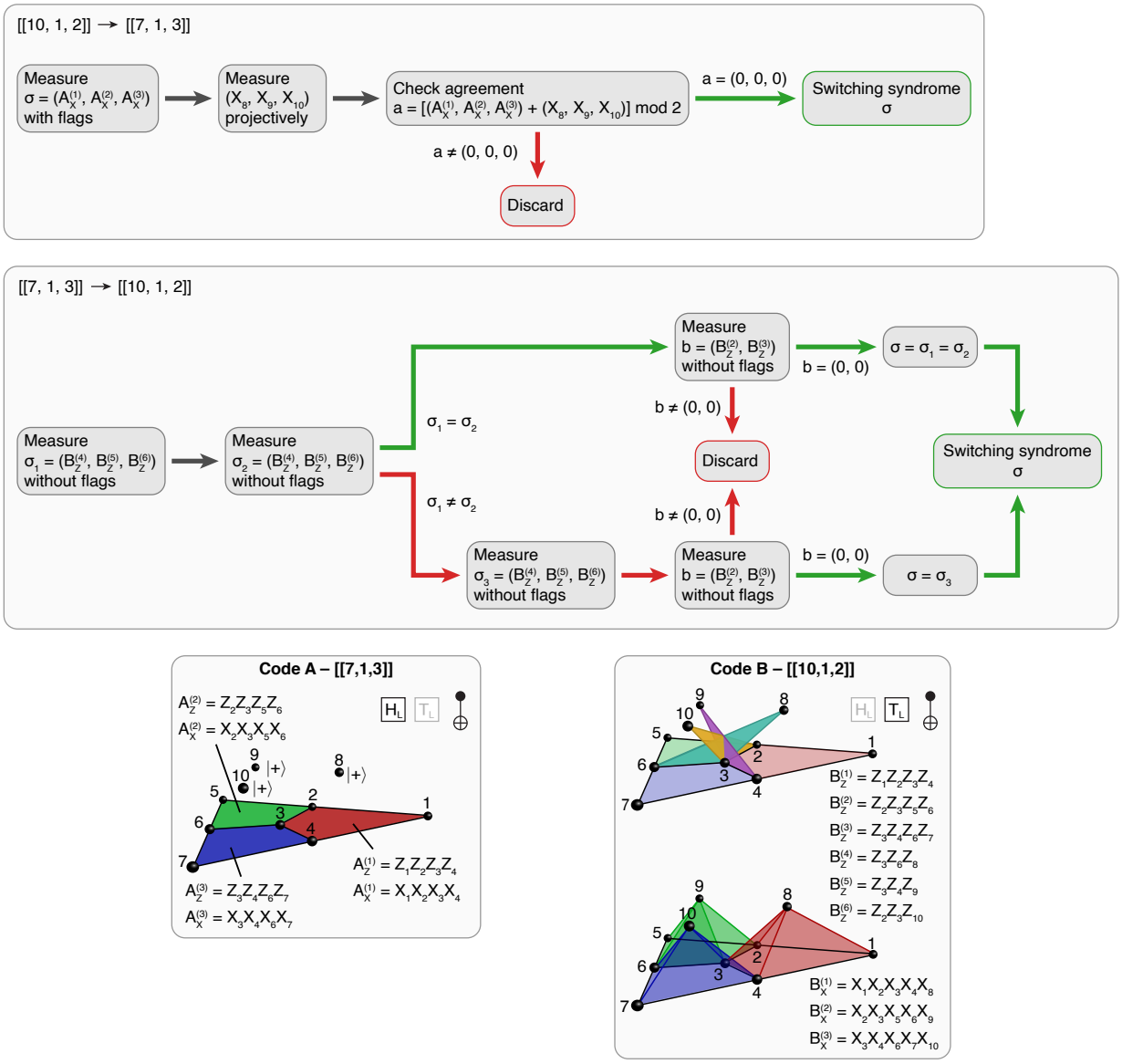

FIG. 11: **Protocols for switching between [[7, 1, 3]] and [[10, 1, 2]] codes.** Stabilizers of the target code are measured to obtain the switching syndrome σ. If an error happens (indicated with red arrows), the run must be discarded or additional measurements must be taken.

Chapter 8

Outlook

The present work describes a compact trapped-ion quantum computing setup capable of working with 16 qubits. The setup is highly automated and can operate independently for a long period of time. Currently, a major limitation for the system is the fidelity of two-qubit operations. There are several modifications that can be implemented to the hardware to improve the performance of the system (see Sec. 6.4), e.g. increasing the coherence times or introducing modulated pulses for MS gates. Therefore, the number of the available qubits and fidelities still can be increased in the described device.

It is worth mentioning that at some point the setup will be limited by the properties of the optical qubit in $^{40}Ca^{+}$, mainly the qubit lifetime of 1 s. This effect can already be seen in long gate sequences, e.g. 100 two-qubit gates will take around $100 \times 300\,\mu s$ and result in $\approx 2.5\%$ decay for idle qubits. The lifetime can be increased by switching to optical qubits in Ba^{+} (30 s) or Yb^{+} (> days), switching to Zeeman ground state qubits or switching to hyperfine qubits e.g. in $^{43}Ca^{+}$, $^{137}Ba^{+}$ or $^{171}Yb^{+}$.

On the other hand, the long-term scalability of quantum computers based on a single trapped-ion chain is questionable. The number of ions in the presented setup can be certainly extended to 30 [141] or even 50, but scaling this architecture further would have some substantial problems. First of all, adding more ions to a linear chain while keeping the same motional spectrum spacing would require more RF power. Generally, this is not desired due to the higher heat load and high-power electronic components being more noisy. Alternatively, the axial confinements can be decreased resulting in the motional spectrum becoming more crowded which is not desired either. Secondly, the increasing complexity of the motional mode spectrum of long ion chains makes two-qubit gate implementation harder. Theoretically, modulated pulse approaches can mitigate this issue but it is yet to be explored experimentally how these techniques work in ion chains with more than 50 ions. Finally, optical single-ion addressing in a long chain represents a significant engineering challenge. There is always a trade-off between the optical crosstalk (at some point diffraction limited) and the field of view of the addressing system. This becomes more critical if one tries to fit a lot of ions in one chain. Moreover, ions at the ends of a long chain can have significant aberrations and therefore higher crosstalk.

An alternative to single-chain trapped-ion systems are so-called QCCD architectures [142–145] and integrated trap architectures [146–151]. These platforms are being studied and developed more and more these days. However, there are still a lot of technical challenges to overcome, despite the flexibility these architectures offer for scaling the systems.

Today, quantum computing platforms are at the stage where capabilities of ex-

perimental apparatuses are high enough for QEC to start becoming beneficial and provide utility [3, 152–154]. QEC seems like an inevitable step on the way toward practically-useful quantum computing. Therefore, it is sensible to explore QEC primitives theoretically and experimentally, as it has been demonstrated in this work. Hardware progress like improved fidelities and increasing the number of available qubits allows for working with larger-distance QEC codes and concatenated codes. Such experimental QEC studies can inspire new hardware architectures to tailor them for specific QEC codes [155], resulting in a better performance for practical quantum computing in the future.

Bibliography

[1] **I. Pogorelov**, T. Feldker, C. D. Marciniak, et al., 'Compact Ion-Trap Quantum Computing Demonstrator', PRX Quantum **2**, 020343 (2021).

[2] **I. Pogorelov**, F. Butt, L. Postler, et al., 'Experimental fault-tolerant code switching', Nature Physics **21**, 298 (2025).

[3] L. Postler, S. Heußen, **I. Pogorelov**, et al., 'Demonstration of fault-tolerant universal quantum gate operations', Nature **605**, 675 (2022).

[4] S. Heußen, L. Postler, M. Rispler, et al., 'Strategies for a practical advantage of fault-tolerant circuit design in noisy trapped-ion quantum computers', Physical Review A **107**, 042422 (2023).

[5] L. Postler, F. Butt, **I. Pogorelov**, et al., 'Demonstration of Fault-Tolerant Steane Quantum Error Correction', PRX Quantum **5**, 030326 (2024).

[6] N. Sadoune, **I. Pogorelov**, C. L. Edmunds, et al., 'Learning symmetry-protected topological order from trapped-ion experiments', arXiv.2408.05017 (2024).

[7] C. Sanz-Fernandez, R. Hernandez, C. D. Marciniak, et al., 'Quantum portfolio value forecasting', arXiv.2111.14970 (2021).

[8] C. D. Marciniak, T. Feldker, **I. Pogorelov**, et al., 'Optimal metrology with programmable quantum sensors', Nature **603**, 604 (2022).

[9] L. O. Conlon, T. Vogl, C. D. Marciniak, et al., 'Approaching optimal entangling collective measurements on quantum computing platforms', Nature Physics **19**, 351 (2023).

[10] J. Eisert, M. Ringbauer, M. Hinsche, et al., 'Verifiable measurement-based quantum random sampling with trapped ions', rs.3.rs-3936332/v1 (2024).

[11] D. Miller, K. Levi, L. Postler, et al., 'Experimental measurement and a physical interpretation of quantum shadow enumerators', arXiv.2408.16914 (2024).

[12] P. Benioff, 'The computer as a physical system: A microscopic quantum mechanical Hamiltonian model of computers as represented by Turing machines', Journal of Statistical Physics **22**, 563 (1980).

[13] Y. Manin, 'Computable and uncomputable' (Sovetskoye Radio, Moscow, 1980).

[14] R. P. Feynman, 'Simulating physics with computers', International Journal of Theoretical Physics **21**, 467 (1982).

[15] S. Jordan, 'Quantum Algorithm Zoo', https://quantumalgorithmzoo.org/, 2024.

[16] P. Shor, 'Algorithms for quantum computation: discrete logarithms and factoring', sfcs.1994.365700 (1994).

[17] L. K. Grover, 'A fast quantum mechanical algorithm for database search', STOC '96, 237814.237866 (1996).

[18] S. Lloyd, 'Universal Quantum Simulators', Science **273**, 1073 (1996).

[19] P. Treutlein, P. Hommelhoff, T. Steinmetz, et al., 'Coherence in Microchip Traps', Physical Review Letters **92**, 203005 (2004).

[20] F. Schmidt-Kaler, S. Gulde, M. Riebe, et al., 'The coherence of qubits based on single Ca+ ions', Journal of Physics B: Atomic, Molecular and Optical Physics **36**, 623 (2003).

[21] J. Benhelm, G. Kirchmair, C. F. Roos, et al., 'Towards fault-tolerant quantum computing with trapped ions', Nature Physics **4**, 463 (2008).

[22] C. Langer, R. Ozeri, J. Jost, et al., 'Long-Lived Qubit Memory Using Atomic Ions', Physical Review Letters **95**, 060502 (2005).

[23] E. Knill, D. Leibfried, R. Reichle, et al., 'Randomized benchmarking of quantum gates', Physical Review A **77**, 012307 (2008).

[24] D. Leibfried, B. DeMarco, V. Meyer, et al., 'Experimental demonstration of a robust, high-fidelity geometric two ion-qubit phase gate', Nature **422**, 412 (2003).

[25] C. A. Ryan, M. Laforest, and R. Laflamme, 'Randomized benchmarking of single- and multi-qubit control in liquid-state NMR quantum information processing', New Journal of Physics **11**, 013034 (2009).

[26] M. Neeley, M. Ansmann, R. C. Bialczak, et al., 'Process tomography of quantum memory in a Josephson-phase qubit coupled to a two-level state', Nature Physics **4**, 523 (2008).

[27] E. Lucero, M. Hofheinz, M. Ansmann, et al., 'High-Fidelity Gates in a Single Josephson Qubit', Physical Review Letters **100**, 247001 (2008).

[28] M. Steffen, M. Ansmann, R. C. Bialczak, et al., 'Measurement of the Entanglement of Two Superconducting Qubits via State Tomography', Science **313**, 1423 (2006).

[29] J. A. Schreier, A. A. Houck, J. Koch, et al., 'Suppressing charge noise decoherence in superconducting charge qubits', Physical Review B **77**, 180502 (2008).

[30] J. M. Chow, L. DiCarlo, J. M. Gambetta, et al., 'Detecting highly entangled states with a joint qubit readout', Physical Review A **81**, 062325 (2010).

[31] L. DiCarlo, J. M. Chow, J. M. Gambetta, et al., 'Demonstration of two-qubit algorithms with a superconducting quantum processor', Nature **460**, 240 (2009).

[32] P. Bertet, I. Chiorescu, G. Burkard, et al., 'Dephasing of a Superconducting Qubit Induced by Photon Noise', Physical Review Letters **95**, 257002 (2005).

[33] J. H. Plantenberg, P. C. de Groot, C. J. P. M. Harmans, et al., 'Demonstration of controlled-NOT quantum gates on a pair of superconducting quantum bits', Nature **447**, 836 (2007).

[34] J. R. Petta, A. C. Johnson, J. M. Taylor, et al., 'Coherent Manipulation of Coupled Electron Spins in Semiconductor Quantum Dots', Science **309**, 2180 (2005).

[35] A. Greilich, D. R. Yakovlev, A. Shabaev, et al., 'Mode Locking of Electron Spin Coherences in Singly Charged Quantum Dots', Science **313**, 341 (2006).

[36] D. Press, T. D. Ladd, B. Zhang, et al., 'Complete quantum control of a single quantum dot spin using ultrafast optical pulses', Nature **456**, 218 (2008).

[37] C. Monroe, D. M. Meekhof, B. E. King, et al., 'Demonstration of a Fundamental Quantum Logic Gate', Physical Review Letters **75**, 4714 (1995).

[38] L. M. K. Vandersypen, M. Steffen, G. Breyta, et al., 'Experimental realization of Shor's quantum factoring algorithm using nuclear magnetic resonance', Nature **414**, 883 (2001).

[39] P. Shor, 'Fault-tolerant quantum computation', SFCS-96, 56 (1996).

[40] A. Steane, 'Multiple-particle interference and quantum error correction', Proceedings of the Royal Society of London. Series A: Mathematical, Physical and Engineering Sciences **452**, 2551 (1996).

[41] M. A. Nielsen and I. L. Chuang, 'Quantum Computation and Quantum Information', URL (Cambridge University Press, 2012).

[42] Y. Wang, Z. Hu, B. C. Sanders, et al., 'Qudits and High-Dimensional Quantum Computing', Frontiers in Physics **8**, fphy.2020.589504 (2020).

[43] P. A. M. Dirac, 'A new notation for quantum mechanics', Mathematical Proceedings of the Cambridge Philosophical Society **35**, 416 (1939).

[44] M. Born, 'Quantenmechanik der Stoßvorgänge', Zeitschrift für Physik **38**, 803 (1926).

[45] A. Barenco, C. H. Bennett, R. Cleve, et al., 'Elementary gates for quantum computation', Physical Review A **52**, 3457 (1995).

[46] A. Sørensen and K. Mølmer, 'Entanglement and quantum computation with ions in thermal motion', Physical Review A **62**, 022311 (2000).

[47] D. Maslov, 'Basic circuit compilation techniques for an ion-trap quantum machine', New Journal of Physics **19**, 023035 (2017).

[48] P. Boykin, T. Mor, M. Pulver, et al., 'On Universal and Fault-Tolerant Quantum Computing', SFCS-99, 486 (1999).

[49] M.-D. Choi, 'Completely positive linear maps on complex matrices', Linear Algebra and its Applications **10**, 285 (1975).

[50] A. Jamiołkowski, 'Linear transformations which preserve trace and positive semidefiniteness of operators', Reports on Mathematical Physics **3**, 275 (1972).

[51] I. H. Kim, Y.-H. Liu, S. Pallister, et al., 'Fault-tolerant resource estimate for quantum chemical simulations: Case study on Li-ion battery electrolyte molecules', Physical Review Research **4**, 023019 (2022).

[52] D. Gottesman, 'An introduction to quantum error correction and fault-tolerant quantum computation', Quantum Information Science and Its Contributions to Mathematics **68**, 13 (2010).

[53] S. J. Devitt, W. J. Munro, and K. Nemoto, 'Quantum error correction for beginners', Reports on Progress in Physics **76**, 076001 (2013).

[54] D. E. Gottesman, 'Stabilizer Codes and Quantum Error Correction', URL, PhD thesis (California Institute of Technology, 1997).

[55] P. W. Shor, 'Scheme for reducing decoherence in quantum computer memory', Physical Review A **52**, 2493 (1995).

[56] A. M. Steane, 'Error Correcting Codes in Quantum Theory', Physical Review Letters **77**, 793 (1996).

[57] D. Gottesman, 'The Heisenberg Representation of Quantum Computers', arXiv.quant-ph/9807006 (1998).

[58] D. Kribs, R. Laflamme, and D. Poulin, 'Unified and Generalized Approach to Quantum Error Correction', Physical Review Letters **94**, 180501 (2005).

[59] D. Poulin, 'Stabilizer Formalism for Operator Quantum Error Correction', Physical Review Letters **95**, 230504 (2005).

[60] N. Breuckmann, 'Quantum Subsystem Codes: Their Theory and Use', URL, MSc thesis (RWTH Aachen University, 2011).

[61] H. Bombín, 'Gauge color codes: optimal transversal gates and gauge fixing in topological stabilizer codes', New Journal of Physics **17**, 083002 (2015).

[62] A. Kubica and M. E. Beverland, 'Universal transversal gates with color codes: A simplified approach', Physical Review A **91**, 032330 (2015).

[63] A. M. Kubica, 'The ABCs of the Color Code: A Study of Topological Quantum Codes as Toy Models for Fault-Tolerant Quantum Computation and Quantum Phases Of Matter', URL, PhD thesis (California Institute of Technology, 2017).

[64] F. Butt, 'Fault-Tolerant Code Switching Protocols for Near-Term Quantum Processors', MSc thesis (RWTH Aachen University, 2022).

[65] H. Bombin and M. A. Martin-Delgado, 'Topological Quantum Distillation', Physical Review Letters **97**, 180501 (2006).

[66] A. R. Calderbank and P. W. Shor, 'Good quantum error-correcting codes exist', Physical Review A **54**, 1098 (1996).

[67] R. Chao and B. W. Reichardt, 'Quantum Error Correction with Only Two Extra Qubits', Physical Review Letters **121**, 050502 (2018).

[68] B. Eastin and E. Knill, 'Restrictions on Transversal Encoded Quantum Gate Sets', Physical Review Letters **102**, 110502 (2009).

[69] D. Gottesman and I. L. Chuang, 'Demonstrating the viability of universal quantum computation using teleportation and single-qubit operations', Nature **402**, 390 (1999).

[70] B. W. Reichardt, 'Quantum Universality from Magic States Distillation Applied to CSS Codes', Quantum Information Processing **4**, 251 (2005).

[71] D. Horsman, A. G. Fowler, S. Devitt, et al., 'Surface code quantum computing by lattice surgery', New Journal of Physics **14**, 123011 (2012).

[72] A. G. Fowler, M. Mariantoni, J. M. Martinis, et al., 'Surface codes: Towards practical large-scale quantum computation', Physical Review A **86**, 032324 (2012).

[73] B. W. Reichardt, 'Fault-tolerant quantum error correction for Steane's seven-qubit color code with few or no extra qubits', Quantum Science and Technology **6**, 015007 (2020).

[74] T. D. Ladd, F. Jelezko, R. Laflamme, et al., 'Quantum computers', Nature **464**, 45 (2010).

[75] D. P. DiVincenzo, 'Topics in Quantum Computers', arXiv.cond-mat/9612126 (1996).

[76] P. K. Ghosh, 'Ion Traps', URL (Oxford University Press, 1995).

[77] D. Leibfried, R. Blatt, C. Monroe, et al., 'Quantum dynamics of single trapped ions', Reviews of Modern Physics **75**, 281 (2003).

[78] A. Erhard, 'Towards scalable quantum computation with trapped ions', URL, PhD thesis (University of Innsbruck, 2021).

[79] C. Marquet, F. Schmidt-Kaler, and D. James, 'Phonon-phonon interactions due to non-linear effects in a linear ion trap', Applied Physics B: Lasers and Optics **76**, 199 (2003).

[80] A. Steane, 'The ion trap quantum information processor', Applied Physics B: Lasers and Optics **64**, 623 (1997).

[81] D. James, 'Quantum dynamics of cold trapped ions with application to quantum computation', Applied Physics B: Lasers and Optics **66**, 181 (1998).

[82] D. G. Enzer, M. M. Schauer, J. J. Gomez, et al., 'Observation of Power-Law Scaling for Phase Transitions in Linear Trapped Ion Crystals', Physical Review Letters **85**, 2466 (2000).

[83] P. Schindler, D. Nigg, T. Monz, et al., 'A quantum information processor with trapped ions', New Journal of Physics **15**, 123012 (2013).

[84] D. T. C. Allcock, W. C. Campbell, J. Chiaverini, et al., 'omg blueprint for trapped ion quantum computing with metastable states', Applied Physics Letters **119**, 5.0069544 (2021).

[85] D. C. McKay, C. J. Wood, S. Sheldon, et al., 'Efficient Z gates for quantum computing', Physical Review A **96**, 022330 (2017).

[86] C. F. Roos, 'Ion trap quantum gates with amplitude-modulated laser beams', New Journal of Physics **10**, 013002 (2008).

[87] G. Kirchmair, J. Benhelm, F. Zähringer, et al., 'Deterministic entanglement of ions in thermal states of motion', New Journal of Physics **11**, 023002 (2009).

[88] A. R. Milne, 'Construction of a linear ion trap and engineering controlled spin-motional interactions', URL, PhD thesis (University of Sydney, 2021).

[89] A. R. Milne, C. L. Edmunds, C. Hempel, et al., 'Phase-Modulated Entangling Gates Robust to Static and Time-Varying Errors', Physical Review Applied **13**, 024022 (2020).

[90] C. D. B. Bentley, H. Ball, M. J. Biercuk, et al., 'Numeric Optimization for Configurable, Parallel, Error-Robust Entangling Gates in Large Ion Registers', Advanced Quantum Technologies **3**, 2000044 (2020).

[91] R. Blümel, N. Grzesiak, N. Pisenti, et al., 'Power-optimal, stabilized entangling gate between trapped-ion qubits', npj Quantum Information **7**, 147 (2021).

[92] M. Kang, Q. Liang, B. Zhang, et al., 'Batch Optimization of Frequency-Modulated Pulses for Robust Two-Qubit Gates in Ion Chains', Physical Review Applied **16**, 024039 (2021).

[93] B. P. Ruzic, M. N. H. Chow, A. D. Burch, et al., 'Frequency-robust Mølmer-Sørensen gates via balanced contributions of multiple motional modes', arXiv.2210.02372 (2022).

[94] S. G. Gulde, 'Experimental realization of quantum gates and the Deutsch-Josza algorithm with trapped 40Ca+-ions', URL, PhD thesis (University of Innsbruck, 2003).

[95] M. Riebe, 'Preparation of entangled states and quantum teleportation with atomic qubits', URL, PhD thesis (University of Innsbruck, 2005).

[96] M. Chwalla, 'Precision spectroscopy with 40Ca+ ions in a Paul trap', URL, PhD thesis (University of Innsbruck, 2009).

[97] T. Monz, 'Quantum information processing beyond ten ion-qubits', URL, PhD thesis (University of Innsbruck, 2010).

[98] D. Nigg, 'Towards fault tolerant quantum computation', URL, PhD thesis (University of Innsbruck, 2017).

[99] M. Guggemos, 'Precision spectroscopy with trapped 40Ca+ and 27Al+ ions', URL, PhD thesis (University of Innsbruck, 2017).

[100] E. Laird, 'Scaling Quantum Computers with Long Chains of Trapped Ions', URL, PhD thesis (University of Maryland, 2021).

[101] Y. Shapira, L. Peleg, D. Schwerdt, et al., 'Fast design and scaling of multi-qubit gates in large-scale trapped-ion quantum computers', arXiv.2307.09566 (2023).

[102] F. Diedrich, J. C. Bergquist, W. M. Itano, et al., 'Laser Cooling to the Zero-Point Energy of Motion', Physical Review Letters **62**, 403 (1989).

[103] C. Maier, 'A quantum simulator with long strings of trapped ions', URL, PhD thesis (University of Innsbruck, 2021).

[104] ISOMET, 'Application Note: Acousto-Optic Modulation', URL, 2014.

[105] W. Jook, 'Atomic Physics Lectures', URL, 2020.

[106] M. Guevara Bertsch, 'Optical clocks with trapped ions', URL, PhD thesis (University of Innsbruck, 2023).

[107] S. Kimmel, G. H. Low, and T. J. Yoder, 'Robust calibration of a universal single-qubit gate set via robust phase estimation', Physical Review A **92**, 062315 (2015).

[108] K. Rudinger, S. Kimmel, D. Lobser, et al., 'Experimental Demonstration of a Cheap and Accurate Phase Estimation', Physical Review Letters **118**, 190502 (2017).

[109] D. Kiesenhofer, H. Hainzer, A. Zhdanov, et al., 'Controlling Two-Dimensional Coulomb Crystals of More Than 100 Ions in a Monolithic Radio-Frequency Trap', PRX Quantum **4**, 020317 (2023).

[110] E. Knill, D. Leibfried, R. Reichle, et al., 'Randomized benchmarking of quantum gates', Physical Review A **77**, 012307 (2008).

[111] A. Javadi-Abhari, M. Treinish, K. Krsulich, et al., 'Quantum computing with Qiskit', arXiv.2405.08810 (2024).

[112] **I. Pogorelov**, 'Qiskit AQT provider - AQTION version', URL, 2021.

[113] E. Wodey, M. Treinish, P. Nation, et al., 'qiskit-community/qiskit-aqt-provider: v0.19.0', version v0.19.0, URL, 2023.

[114] L. Nützel, A. Gresch, L. Hehn, et al., 'Solving an Industrially Relevant Quantum Chemistry Problem on Quantum Hardware', arXiv.2408.10801 (2024).

[115] A. Javadi-Abhari, M. Treinish, K. Krsulich, et al., 'Qiskit transpiler', URL.

[116] T. Monz, P. Schindler, J. T. Barreiro, et al., '14-Qubit Entanglement: Creation and Coherence', Physical Review Letters **106**, 130506 (2011).

[117] J. Johansson, P. Nation, and F. Nori, 'QuTiP: An open-source Python framework for the dynamics of open quantum systems', Computer Physics Communications **183**, 1760 (2012).

[118] B. P. Ruzic, M. N. Chow, A. D. Burch, et al., 'Leveraging motional-mode balancing and simply parametrized waveforms to perform frequency-robust entangling gates', Physical Review Applied **22**, 014007 (2024).

[119] C. Chamberland, T. Jochym-O'Connor, and R. Laflamme, 'Thresholds for Universal Concatenated Quantum Codes', Physical Review Letters **117**, 010501 (2016).

[120] V. V. Sivak, A. Eickbusch, B. Royer, et al., 'Real-time quantum error correction beyond break-even', Nature **616**, 50 (2023).

[121] N. Berthusen, J. Dreiling, C. Foltz, et al., 'Experiments with the 4D Surface Code on a QCCD Quantum Computer', arXiv.2408.08865 (2024).

[122] M. P. da Silva, C. Ryan-Anderson, J. M. Bello-Rivas, et al., 'Demonstration of logical qubits and repeated error correction with better-than-physical error rates', arXiv.2404.02280 (2024).

[123] R. Acharya, L. Aghababaie-Beni, I. Aleiner, et al., 'Quantum error correction below the surface code threshold', arXiv.2408.13687 (2024).

[124] L. Postler, 'Towards keeping a qubit alive', PhD thesis (University of Innsbruck, 2025).

[125] A. M. Steane, 'Active Stabilization, Quantum Computation, and Quantum State Synthesis', Physical Review Letters **78**, 2252 (1997).

[126] E. Knill, 'Fault-Tolerant Postselected Quantum Computation: Schemes', arXiv.quant-ph/0402171 (2004).

[127] J. Preskill, 'Fault-tolerant quantum computation', in *Introduction to Quantum Computation and Information* (World Scientific, 1998), pp. 213–269.

[128] D. Bluvstein, S. J. Evered, A. A. Geim, et al., 'Logical quantum processor based on reconfigurable atom arrays', Nature **626**, 58 (2023).

[129] S. Bravyi and A. Kitaev, 'Universal quantum computation with ideal Clifford gates and noisy ancillas', Physical Review A **71**, 022316 (2005).

[130] E. T. Campbell, 'Magic states', E. T. Campbell's blog, URL.

[131] K. Mayer, C. Ryan-Anderson, N. Brown, et al., 'Benchmarking logical three-qubit quantum Fourier transform encoded in the Steane code on a trapped-ion quantum computer', arXiv.2404.08616 (2024).

[132] S. Bravyi and A. Kitaev, 'Universal quantum computation with ideal Clifford gates and noisy ancillas', Physical Review A **71**, 022316 (2005).

[133] C. Chamberland and A. W. Cross, 'Fault-tolerant magic state preparation with flag qubits', Quantum **3**, 143 (2019).

[134] S. Koutsioumpas, D. Banfield, and A. Kay, 'The Smallest Code with Transversal T', arXiv.2210.14066 (2022).

[135] H. Bombin, 'Transversal gates and error propagation in 3D topological codes', arXiv.1810.09575 (2018).

[136] J. T. Anderson, G. Duclos-Cianci, and D. Poulin, 'Fault-Tolerant Conversion between the Steane and Reed-Muller Quantum Codes', Physical Review Letters **113**, 080501 (2014).

[137] M. E. Beverland, A. Kubica, and K. M. Svore, 'Cost of Universality: A Comparative Study of the Overhead of State Distillation and Code Switching with Color Codes', PRX Quantum **2**, 020341 (2021).

[138] F. Butt, S. Heußen, M. Rispler, et al., 'Fault-Tolerant Code-Switching Protocols for Near-Term Quantum Processors', PRX Quantum **5**, 020345 (2024).

[139] M. Vasmer and A. Kubica, 'Morphing Quantum Codes', PRX Quantum **3**, 030319 (2022).

[140] E. T. Campbell, 'The smallest interesting colour code', E. T. Campbell's blog, URL, 2016.

[141] J.-S. Chen, E. Nielsen, M. Ebert, et al., 'Benchmarking a trapped-ion quantum computer with 29 algorithmic qubits', arXiv.2308.05071 (2023).

[142] D. Kielpinski, C. Monroe, and D. J. Wineland, 'Architecture for a large-scale ion-trap quantum computer', Nature **417**, 709 (2002).

[143] J. M. Pino, J. M. Dreiling, C. Figgatt, et al., 'Demonstration of the trapped-ion quantum CCD computer architecture', Nature **592**, 209 (2021).

[144] S. A. Moses, C. H. Baldwin, M. S. Allman, et al., 'A Race-Track Trapped-Ion Quantum Processor', Physical Review X **13**, 041052 (2023).

[145] C. Mordini, A. R. Vasquez, Y. Motohashi, et al., 'Multi-zone trapped-ion qubit control in an integrated photonics QCCD device', arXiv.2401.18056 (2024).

[146] K. K. Mehta, C. Zhang, M. Malinowski, et al., 'Integrated optical multi-ion quantum logic', Nature **586**, 533 (2020).

[147] R. J. Niffenegger, J. Stuart, C. Sorace-Agaskar, et al., 'Integrated multi-wavelength control of an ion qubit', Nature **586**, 538 (2020).

[148] S. L. Todaro, V. B. Verma, K. C. McCormick, et al., 'State Readout of a Trapped Ion Qubit Using a Trap-Integrated Superconducting Photon Detector', Physical Review Letters **126**, 010501 (2021).

[149] C. W. Hogle, D. Dominguez, M. Dong, et al., 'High-fidelity trapped-ion qubit operations with scalable photonic modulators', npj Quantum Information **9**, s41534-023-00737-1 (2023).

[150] J. Kwon, W. J. Setzer, M. Gehl, et al., 'Multi-site integrated optical addressing of trapped ions', Nature Communications **15**, s41467-024-47882-5 (2024).

[151] F. W. Knollmann, E. Clements, P. T. Callahan, et al., 'Integrated photonic structures for photon-mediated entanglement of trapped ions', Optica Quantum **2**, 230 (2024).

[152] S. Krinner, N. Lacroix, A. Remm, et al., 'Realizing repeated quantum error correction in a distance-three surface code', Nature **605**, 669 (2022).

[153] C. Ryan-Anderson, J. G. Bohnet, K. Lee, et al., 'Realization of Real-Time Fault-Tolerant Quantum Error Correction', Physical Review X **11**, 041058 (2021).

[154] M. P. da Silva, C. Ryan-Anderson, J. M. Bello-Rivas, et al., 'Demonstration of logical qubits and repeated error correction with better-than-physical error rates', arXiv.2404.02280 (2024).

[155] M. Valentini, M. W. van Mourik, F. Butt, et al., 'Demonstration of two-dimensional connectivity for a scalable error-corrected ion-trap quantum processor architecture', arXiv.2406.02406 (2024).